

*Signatures of Neutrino mass models in
current and future experiments*

A THESIS

submitted for the Award of Ph.D. degree of

MOHANLAL SUKHADIA UNIVERSITY

in the

Faculty of Science

by

Gulab Bambhaniya



Under the Supervision of

Prof. Srubabati Goswami

Professor

Theoretical Physics Division

Physical Research Laboratory

Ahmedabad, India.

DEPARTMENT OF PHYSICS
MOHANLAL SUKHADIA UNIVERSITY
UDAIPUR

Year of submission: 2015

To
My Parents

DECLARATION

*I, Mr. Gulab Bambhaniya, S/o Mr. Gopalbhai Bambhaniya, resident of Room No. 012, PRL Thaltej Hostel, Sindhubhawan road, Ahmedabad, Gujarat 380054, hereby declare that the research work incorporated in the present thesis entitled, “**Signatures of Neutrino mass models in current and future experiments**” is my own work and is original. This work (in part or in full) has not been submitted to any University for the award of a Degree or a Diploma. I have properly acknowledged the material collected from secondary sources wherever required. I solely own the responsibility for the originality of the entire content.*

Date:

(Gulab Bambhaniya)

CERTIFICATE

I feel great pleasure in certifying that the thesis entitled, “**Signatures of Neutrino mass models in current and future experiments**” embodies a record of the results of investigations carried out by Mr. Gulab Bambhaniya under my guidance. He has completed the following requirements as per Ph.D regulations of the University.

- (a) Course work as per the university rules.
- (b) Residential requirements of the university.
- (c) Regularly submitted six monthly progress reports.
- (d) Presented his work in the departmental committee.
- (e) Published minimum of one research papers in a refereed research journal.

I am satisfied with the analysis, interpretation of results and conclusions drawn. I recommend the submission of thesis.

Date:

Prof. Srubabati Goswami
(Thesis Supervisor)
Professor, THEPH,
Physical Research Laboratory,
Ahmedabad - 380 009

Countersigned by
Head of the Department

Acknowledgements

It has been a privilege to be here in PRL for five years during the course of this thesis. I thank PRL for providing me all the facilities to carry out my research work smoothly.

I would like to express my sincere gratitude and warm appreciation to my thesis supervisor Prof. Srubabati Goswami for her guidance throughout the work. I am extremely benefited from her expertise and insight into the subject, and her ability to explain the physics in a lucid manner. I am thankful to her for introducing me to the fascinating world of neutrinos and developing an interest in it. It was a great experience to work under her guidance. I am very much thankful for her continuous support and patience for my Ph.D. study and related issues. I am also very grateful to her for encouraging me to attend the schools and conferences in India and abroad, and to collaborate with others from which I benefited a lot. Her suggestions will always help me in my future research career.

I wish to express my sincere appreciation to Dr. Partha Konar for his valuable collaboration. I enjoyed discussing with him due to his friendly nature and have learnt many aspects of physics. I am very pleased to acknowledge Dr. Joydeep Chakraborty, for his collaboration and also giving me an opportunity to collaborate with the research group of Prof. Gluza. His enthusiasm is really motivating to keep going. I am grateful to Partha and Joydeep for their immense support to learn various tools of particle physics, which have been very helpful for me to learn the subject of collider physics.

I have been lucky to be able to collaborate with various people from within and outside the PRL. It gives me a pleasure to thank all my collaborators, in alphabetical order (as we follow in the particle physics community!): Sumeet K. Dagaonkar, Dr. Bhupal Dev, Prof. Janusz Gluza, Dr. Tomek Jeliński, Dr. Subrata Khan, Magdalena Kordiaczyńska, Dr. Manimala Mitra, Tanmoy Mondal and Dr. Robert Szafron. It has been a very good experience to work with them and I have learned a lot from them on different aspects of particle physics.

I am very grateful to Dr. Namit Mahajan and Dr. Raghvan Rangarajan for

sparing the time to read and examine this thesis.

I warmly acknowledge Prof. Jitesh Bhatt, Prof. Abhijeet Chakraborty, Prof. Srubabati Goswami, Dr. Bhuwan Joshi, Dr. Partha Konar, Dr. Namit Mahajan, Dr. Kuljeet Kaur Marhas, Prof. Hiranmaya Mishra, Prof. Raghavan Rangarajan, Prof. R. Ramesh, Dr. Bijaya Sahoo, Prof. M M Sarin, Dr. Varun Sheel, for teaching the nice courses during the coursework. I would like to thank Prof. Subhendra Mohanty for taking the advanced courses. I am thankful to Prof. Jay Banerji for the communication skills course. I also thank Prof. Mohanty and Dr. Santosh Vadawale for allowing me to do short term projects under them during the coursework. I thank Prof. Anjan Joshipura, Prof. Saurabh Rindani and Dr. Namit Mahajan for useful discussions.

I am thankful to the professors in my Bachelor and Master, in particular, Prof. K N Joshipura, Prof. P C Vinodkumar, Prof. Udeshi, Prof. Arun Bhide and Prof. Mahesh Oza for developing my interest in the field of theoretical particle physics.

I am thankful to Prof. J. N. Goswami, former director of PRL, Prof. Utpal Sarkar, the director of PRL, the dean Prof. Janardhan Padmanabhan, former academic committee chairman Prof. Shyam Lal, academic committee chairman Prof. Ramachandran. I thank academic committee for reviewing my work and commenting for improvements. I thank Dr. Bhushit Vaishnav for his help. I also thank the staff members of the director's office, the dean's office, the registrar's office for their help related to the administrative aspects of the thesis.

I am grateful to past and present area chairmen of the theoretical physics division, Prof. Mohanty and Prof. Mishra, for their support to attend the schools and the conferences. I thank theory division secretaries Raza and Sujathaben for their help.

I am very grateful to my officemates: Monojit, Tanmoy, Abhaya, and Ujjal, for the nice discussions on physics and also on general issues. I have benefited a lot from them.

Many thanks to my batch-mates: Aadhi, Anjali, Arko, Avdhesh, Bhavya, Damodar, Dileep, Dinesh, Gangi, Gaurav Sharma, Gaurav Tomar, Girish, Lek-

shmy, Midhun, Monojit, Priyanka, Tanmoy, Upendra, Wagheesh and Yashpal, for their support during the course work and during my tenure.

I am thankful to my seniors: Ketanbhai, Bhavikbhai, Soumya Rao, Pankaj Sharma, Shivani Gupta, Vimal Kishore, Vishal Joshi, Ujjal Dey, Tanushree Basak, Ila Garg, Mansi Dhuria, Vineet Goswami, Arvind Singh, Ananta Mishra, Siddharth, Zeen, Bhaswar, Anjishnu, Chinmay, Sunil, Arun A, Sushant Bishoi, Ranjita, Fazlul, Sashi, Sushant Raut and Gaurav Goswami. I am very much thankful to Ketanbhai, Subrata and Tanushree for the useful discussions. I learned many things in the area of their expertise.

I thank my juniors: Girish, Newton, Vishnudatt, Chandan H, Chandan G, Arun P, Guru, Manu, Ikshu, Shraddha, Anirban, Lalit, Subhanand and Subhadyouti.

I would like to thank all the staff members of the administration, the computer center, the library, the account section and the dispensary for their support. I also thank canteen staffs at both the places main campus as well as Thaltej campus, for providing nice food.

I thank the head of the department of physics and the dean of MLSU, for their support and positive response whenever we go to Udaipur. I thank staff members of the physics department and the dean's office.

Special thanks to my friends Manish Sanghani and Vijayan for the nice meals with them. I am very thankful to Manish for various discussions on spiritual topics lasting late night, in Vallabh Vidyanagar as well as in Ahmedabad. Thanks to my other friends in Ahmedabad for the social activities.

Finally, I would like to thank my parents, who have encouraged me for the study and supported constantly, without whom I could not have completed my study. I also thank my brother and sisters for their kind support.

In short, I am extremely grateful to all who have helped me directly or indirectly in my study and to complete this thesis.

ABSTRACT

Neutrinos are neutral fundamental fermions, which interact only via weak interactions in the Standard Model (SM). The SM presumes neutrinos to be massless. However, the observation of the phenomenon of neutrino oscillations has conclusively established the fact that neutrinos are massive and therefore the SM is not the complete description of nature. Neutrino mass is the first direct evidence of the existence of new physics beyond the SM. The Large Hadron Collider (LHC) has found the last missing piece of the SM, the Higgs boson, but no hint of any new physics is observed in the first run with center of mass energies $\sqrt{s} = 7$ and 8 TeV. At the time of writing of this thesis the second run of the LHC has already started. The energy scale of the LHC motivated us to study the TeV scale beyond Standard Model (BSM) scenarios, which have new particles with masses within the reach of the LHC energy. The new physics models can have enlarged particle content keeping the gauge group same as that of the SM or with a gauge extension.

We have studied both types of models: (1) particle extended scenarios, which include models like the Babu-Nandi-Tavartkiladze model (BNTM) and the minimal linear seesaw model (MLSM), and (2) gauge extended models in which we have analyzed the minimal Left-Right symmetric model (MLRSM).

First we consider the BNTM, in which naturally small neutrino masses arise from a dimension-7 operator at the tree level. Such a term can arise in the presence of a scalar quadruplet and a pair of vectorlike fermion triplets and enables one to obtain small neutrino masses through the TeV scale linear seesaw mechanism. We study the phenomenology of the charged scalars of this model, in particular, the multilepton signatures coming from their decays, at the LHC. Of special importance is the presence of the same-sign-tri-lepton signatures originating from the triply charged scalars. The Standard Model background for such processes is small, and hence this is considered as a confirming evidence of new physics. We also looked for events with three, four, five, and six leptons that have negligible contamination from the Standard Model. We further point out

the spectacular lepton flavor violating four-lepton signal that can be the hallmark for these types of models. We also compute the added contributions to the rate for the Standard Model Higgs decaying to two photons via the charged scalars of this model.

In the next part of the thesis, we study the production of heavy neutrinos at the LHC through the dominant s-channel production mode as well as the vector boson fusion process. We consider the TeV scale MLSM containing two heavy singlets with opposite lepton numbers. This model is fully reconstructible from neutrino oscillation data apart from an overall normalization constant which can be constrained from the metastability of the electroweak vacuum and bounds coming from lepton flavor violation searches. The Dirac nature of heavy neutrinos in this model implies suppression of the conventional same-sign-dilepton signal at the LHC. We analyze the collider signatures with the tri-lepton final state and missing transverse energy as well as vector boson fusion type signals which are characterized by two additional forward tagged jets. Our investigation reveals that due to stringent constraints on light-heavy mixing coming from lepton flavor violation and metastability bounds, the model can be explored only for a light to moderate mass range of heavy neutrinos. We also note that in the case of a positive signal, flavor counting of the final tri-lepton channel can give information about the mass hierarchy of the light neutrinos.

In the later part of the thesis, we do a comprehensive investigation of the charged scalar sector of the MLRSM. First, the constraints on the scalar masses from the collider experiments and from theoretical considerations are discussed. We explore the scenarios where the amplified signals due to relatively light charged scalars dominate against heavy neutral gauge boson Z_2 and charged gauge boson W_2 as well as heavy neutral Higgs boson signals which are suppressed due to the large vacuum expectation value v_R of the right-handed scalar triplet. Consistency with flavor changing neutral current (FCNC) effects implies masses of the two neutral Higgs bosons A_1^0, H_1^0 to be at least of order 10 TeV, which in turn implies that in MLRSM only three of the four charged Higgs bosons, namely $H_{1,2}^{\pm\pm}$ and H_1^\pm , can be simultaneously light. The doubly charged Higgs

bosons $H_{1,2}^{\pm\pm}$ would undoubtedly be clear messengers of new physics. We discuss their mass spectrum and show how experimental data and relations between scalar masses put limits on it. In particular, both the masses of the particles H_1^0, A_1^0 , that play a crucial role in FCNC effects and the masses of the additional gauge bosons W_2, Z_2 are notably important. In contrast, due to the freedom in the parameter space of the full scalar potential, there is no lower limit on the mass of $H_2^{\pm\pm}$. When we demand vacuum stability of the scalar potential in addition to other available constraints, we find that the stability of the potential constrains the splitting ($M_{H_1^{\pm\pm}} - M_{H_1^\pm}$). We discuss and summarize the main processes within MLRSM where heavy charged Higgs bosons can be produced at the LHC. The decays of the charged scalars lead to multilepton signals. In particular, the tri- and four-lepton final states for different benchmark points are analyzed in our study. Kinematic cuts are chosen in order to strengthen the leptonic signals and decrease the Standard Model (SM) background. The results are presented using dilepton invariant mass and lepton-lepton separation distributions for the same-sign-dilepton (SSDL) and opposite-sign-dilepton (OSDL) as well as the charge asymmetry in the tri-lepton signals. We find that for the considered MLRSM processes, tri-lepton and four-lepton signals are most important for their detection when compared to the SM background. Both the signals can be detected at 14 TeV collisions at the LHC with integrated luminosity at the level of 300 fb^{-1} with doubly charged Higgs bosons up to approximately 600 GeV. Finally, the possible extra contribution of the charged MLRSM scalar particles to the measured Higgs to diphoton ($H_0^0 \rightarrow \gamma\gamma$) decay is computed.

Production and decays of doubly charged Higgs bosons of the MLRSM, at the LHC and future hadron colliders triggered by the vector boson fusion mechanism are also discussed. Though the parity breaking scale v_R is large (\sim few TeV) and scalar masses which contribute to FCNC effects are even larger, a consistent Higgs boson mass spectrum still allows us to keep doubly charged scalar masses below 1 TeV which is an interesting situation for the LHC and future circular collider (FCC). Assuming that doubly charged Higgs bosons decay predominantly into a pair of same-sign leptons through the process $pp \rightarrow H_{1/2}^{\pm\pm} H_{1/2}^{\mp\mp} jj \rightarrow \ell^\pm \ell^\pm \ell^\mp \ell^\mp jj$,

we find that even for LHC operating at $\sqrt{s} = 14$ TeV with an integrated luminosity at the level of 3000 fb^{-1} (*i.e.*, High Luminosity LHC (HL-LHC)) there is practically no chance to detect such particles at a reasonable significance level through this channel. However, 33 TeV High Energy LHC (HE-LHC) and(or) 100 TeV Future Circular Hadron-Hadron Collider (FCC-hh) open up a wide region for the doubly charged Higgs boson mass spectrum to be explored. In FCC-hh doubly charged Higgs boson masses upto 1 TeV can be probed easily.

Apart from colliders, TeV scale seesaw models can have interesting implications for neutrinoless double beta decay ($0\nu\beta\beta$) and lepton flavor violation (LFV). We perform a detailed study of the scalar triplet contribution to the low-energy rare processes of lepton flavor violation and $0\nu\beta\beta$ within a TeV-scale Left-Right Symmetric framework. We show that in both Type-I and Type-II seesaw dominance limit for the light neutrino masses, if the triplet is lighter than the right-handed (RH) neutrinos or the RH gauge bosons, its contribution to the LFV processes could be sizable, irrespective of the uncertainties in the Dirac and Majorana CP phases in the neutrino mixing matrix, except when the light neutrinos are quasi-degenerate. In particular, a combination of the constraints from $\mu \rightarrow e\gamma$ and $\mu \rightarrow 3e$ either already rules out these scenarios or can probe these in the next generation experiments. Similarly, the triplet contribution to $0\nu\beta\beta$ is also accessible to the next generation ton-scale experiments for relatively light triplets, which is complementary to the direct searches for these exotic particles at the LHC. Finally, we also examine the implications of the triplet contribution for the scenario with $M_{W_2} \sim 2$ TeV and $g_R \sim 0.4 - 0.5$, which provides a plausible explanation of the recent diboson anomaly at the LHC.

Keywords : Neutrino Mass, Beyond the Standard Model, Large Hadron Collider, Gauge Extension, Left-Right Symmetry, Charged Scalars, Heavy Neutrinos, Neutrinoless Double Beta Decay, Lepton Flavor Violation

LIST OF PUBLICATIONS

Publications contributing to this thesis :

1. “*Generation of neutrino mass from new physics at TeV scale and multilepton signatures at the LHC*”
Gulab Bambhaniya, J. Chakrabortty, S. Goswami and P. Konar, Phys. Rev. D **88**, no. 7, 075006 (2013) [arXiv:1305.2795 [hep-ph]]. [SPIRES entry](#)
2. “*Left-Right Symmetry and the Charged Higgs Bosons at the LHC*”
Gulab Bambhaniya, J. Chakrabortty, J. Gluza, M. Kordiaczyńska and R. Szafron, JHEP **1405**, 033 (2014) [arXiv:1311.4144 [hep-ph]]. [SPIRES entry](#)
3. “*Lowest limits on the doubly charged Higgs boson masses in the minimal left-right symmetric model*”
Gulab Bambhaniya, J. Chakrabortty, J. Gluza, T. Jeliński and M. Kordiaczynska, Phys. Rev. D **90**, no. 9, 095003 (2014) [arXiv:1408.0774 [hep-ph]]. [SPIRES entry](#)
4. “*Looking for hints of a reconstructible seesaw model at the Large Hadron Collider*”
Gulab Bambhaniya, S. Goswami, S. Khan, P. Konar and T. Mondal, Phys. Rev. D **91**, no. 7, 075007 (2015) arXiv:1410.5687 [hep-ph]. [SPIRES entry](#)
5. “*Search for doubly charged Higgs bosons through VBF at the LHC, and beyond*”
Gulab Bambhaniya, J. Chakrabortty, J. Gluza, T. Jelinski and R. Szafron, Phys. Rev. D **92**, no. 1, 015016 (2015) arXiv:1504.03999 [hep-ph]. [SPIRES entry](#)
6. “*Scalar Triplet Contribution to Lepton Flavor Violation and Neutrinoless Double Beta Decay in Left-Right Symmetric Model*”

Gulab Bambhaniya, P. S. B. Dev, S. Goswami, M. Mitra, (Manuscript under preparation).

Other publications :

1. *“Rare meson decay through off-shell doubly charged scalars”*
Gulab Bambhaniya, J. Chakrabortty and S. K. Dagaonkar, Phys. Rev. D **91**, no. 5, 055020 (2015). [SPIRES entry](#)
2. *“Constraints on a seesaw model leading to Quasi-Degenerate neutrinos and signatures at the LHC”*
Gulab Bambhaniya, S. Khan, P. Konar and T. Mondal, Phys. Rev. D **91**, no. 9, 095007 (2015) arXiv:1411.6866 [hep-ph]. [SPIRES entry](#)

List of Abbreviations

SM	Standard Model
BSM	Beyond Standard Model
SUSY	Supersymmetry
MSSM	Minimal Supersymmetric Standard Model
RH	Right-Handed
LH	Left-Handed
VEV	Vacuum Expectation Value
EW	Electroweak
EWSB	Electroweak Symmetry Breaking
LHC	Large Hadron Collider
BR	Branching Ratio
MLRSM	Minimal Left-Right Symmetric Model
MLSM	Minimal Linear Seesaw Model
BNTM	Babu-Nandi-Tavartkiladze Model
LFV	Lepton Flavor Violation
LNV	Lepton Number Violation
GUT	Grand Unified Theory
LHE	Les Houches Event
ISR	Initial State Radiation
FSR	Final State Radiation
SSDL	Same-Sign-Dilepton
OSDL	Opposite-Sign-Dilepton
QD	Quasi-Degenerate
C.L.	Confidence Level
$0\nu\beta\beta$	Neutrinoless Double Beta Decay

Contents

Acknowledgements	i
Abstract	v
List of Publications	ix
List of Abbreviations	xi
Contents	xiii
List of Tables	xix
List of Figures	xxi
1 Introduction	1
1.1 The Standard Model	1
1.2 A brief history of parity violation	4
1.3 Generation of gauge boson and fermion masses in the SM	4
1.4 The neutrinos	6
1.5 Neutrino oscillations	7
1.6 Absolute neutrino masses	10
1.7 Generation of neutrino masses	11
1.8 The Large Hadron Collider (LHC)	12
1.9 Phenomenological implications of neutrino masses	13
1.9.1 $0\nu\beta\beta$ decay	13
1.9.2 Lepton flavor violation	16

1.9.3	Vacuum stability	17
1.10	Objectives	18
1.11	Thesis overview	18
2	Mechanisms of neutrino mass generation	19
2.1	Generation of neutrino mass: seesaw mechanism	20
2.2	Origin of seesaw mechanism	22
2.3	Type-I seesaw	23
2.4	Type-II seesaw mechanism	26
2.5	Type-III seesaw mechanism	27
2.6	Neutrino masses in Left-Right Symmetric Model	27
2.7	TeV scale models for neutrino mass generation	31
2.7.1	Singlet seesaw models	33
2.7.1.1	Inverse seesaw model	34
2.7.1.2	Linear seesaw model	34
2.7.1.3	Minimal Linear Seesaw Model (MLSM)	35
2.7.2	Seesaw models with higher dimensional operator	38
2.7.3	Babu-Nandi-Tavartkiladze Model (BNTM)	40
2.7.3.1	The model	40
2.7.3.2	Generation of neutrino masses	43
2.7.3.3	Origin of neutrino mass	45
3	Probing neutrino mass models at colliders	49
3.1	Simulations and event selection	52
3.2	Babu-Nandi-Tavartkiladze-model (BNTM)	56
3.2.1	Production and decay of isospin 3/2 Scalar	56
3.2.1.1	Signatures of new physics	59
3.2.1.2	Background estimation	60
3.2.1.3	Multilepton signatures	61
3.2.1.4	Lepton flavor violating signal	64
3.2.2	New contributions to $H \rightarrow \gamma\gamma$	66
3.2.3	Summary: BNTM	67

3.3	Minimal Linear Seesaw Model (MLSM)	68
3.3.1	Phenomenology at the LHC	72
3.3.2	Simulations and results	75
3.3.3	Selection criteria	75
3.3.4	Background	76
3.3.4.1	For s-channel signal	76
3.3.4.2	For VBF signal	77
3.3.5	Signal	77
3.3.5.1	Signal for s-channel	78
3.3.5.2	Signal for VBF	79
3.3.6	Discovery potential	80
3.3.7	Summary: MLSM	81
3.4	Collider Phenomenology of scalar fields within the Minimal Left-Right Symmetric Model (MLRSM)	83
3.4.1	Constraints in the MLRSM: experimental and theoretical	85
3.4.2	Constraints from FCNC, SM Higgs boson mass, perturbativity	87
3.4.3	Scalar sector of the MLRSM and the lowest limit for the doubly charged scalar $H_1^{\pm\pm}$ mass	89
3.4.4	Constraints on α_3 and $\delta\rho$: adding vacuum stability condition	95
3.4.5	Multilepton signal from the charged scalars in MLRSM	98
3.4.5.1	Primary production of heavy charged Higgs bosons at the LHC	101
3.4.5.2	$pp \rightarrow H_1^+ H_1^-$ and $pp \rightarrow H_2^+ H_2^-$	102
3.4.5.3	$pp \rightarrow H_1^{++} H_1^{--}$ and $pp \rightarrow H_2^{++} H_2^{--}$	103
3.4.5.4	$pp \rightarrow H_1^{\pm\pm} H_1^\mp$ and $pp \rightarrow H_2^{\pm\pm} H_2^\mp$	105
3.4.6	Primary production of a heavy Higgs and gauge bosons	108
3.4.6.1	$pp \rightarrow W_{1/2}^\mp H_{1/2}^\pm$, $pp \rightarrow Z_{1/2} H_{1/2}^\pm$ and $pp \rightarrow \gamma H_{1/2}^\pm$	108
3.4.7	Simulations and results for final lepton signals	108
3.4.7.1	Events selection criteria	109

3.4.7.2	Signal events for doubly charged Higgs particles in MLRSM	109
3.4.7.3	$pp \rightarrow H_1^{++}H_1^{--}$ and $pp \rightarrow H_2^{++}H_2^{--}$	109
3.4.7.4	$pp \rightarrow H_1^{\pm\pm}H_1^\mp$ and $pp \rightarrow H_2^{\pm\pm}H_2^\mp$	113
3.4.8	Background estimation and significance of signals	116
3.4.9	MLRSM charged Higgs bosons contribution to $H_0^0 \rightarrow \gamma\gamma$	119
3.4.10	MLRSM VBF signal	122
3.4.10.1	Possible processes which identify doubly charged Higgs through VBF in the MLRSM	123
3.4.10.2	Predictions for $pp \rightarrow H_{1/2}^{\pm\pm}H_{1/2}^{\mp\mp}jj \rightarrow \ell^\pm\ell^\pm\ell^\mp\ell^\mp jj$ in the MLRSM	124
3.5	Summary: MLRSM	130
4	Phenomenological implications of neutrino mass models	135
4.1	Lepton flavor violation	137
4.1.1	Moderate value of r	141
4.1.2	Smaller value of r	144
4.1.3	Larger value of r	146
4.2	Neutrinoless double beta decay	147
4.3	Diboson excess, LFV and $0\nu\beta\beta$	152
4.4	Summary	156
5	Conclusion and future prospects	157
A	Feynman rules in the BNTM	165
A.1	Quadruplet scalar kinetic term	165
A.2	Yukawa interactions of fermion triplets	166
A.3	Neutrino mass through dimension-7 effective vertex	166
A.4	Lepton flavor violating effective vertex	168
A.5	Feynman rules	168
B	Potential in the MLRSM	171
B.1	Scalar potential of the MLRSM	171

C FCNC in the MLRSM	173
C.1 Reconciling FCNC effects and large ν_R with relatively light charged Higgs mass spectrum within MLRSM	173
Bibliography	177
Publications attached with the thesis	199

List of Tables

1.1	Quantum numbers of the SM particles. Charges of the individual particles can be calculated using the formula $Q = T_{3L} + \frac{Y}{2}$ [1].	3
1.2	The best-fit values and 3σ ranges of neutrino oscillation parameters from global analysis of current data [19].	9
2.1	Natural seesaw models with a Majorana mass insertion.	39
2.2	Natural seesaw models with a Dirac mass insertion.	40
2.3	Order of neutrino mass for $v = 174$ GeV, $M_\Sigma = 3500$ GeV, $M_{\Phi^0} = 400$ GeV.	44
3.1	The cuts used to estimate SM backgrounds and signal events. For complete set of selection criteria, see the text.	53
3.2	Choice of parameter v_Φ for $M_{\Phi^0} = 400$ GeV and $\Delta M = -2.8$ GeV. Here \dagger denotes all the three charged leptons (e, μ, τ).	59
3.3	Dominant SM background contributions to the multilepton channels at the LHC with $\sqrt{S} = 14$ TeV after all the cuts.	60
3.4	Neutrino mass hierarchy dependency in four-lepton signal in $\dagger W$ dominant region.	64
3.5	Lepton flavor violating four-lepton signals at different dominant decay regions for normal and inverted hierarchies at the LHC.	65
3.6	Allowed 3σ ranges of oscillation parameters and benchmark values of these parameters used in our analysis to get the signal allowed by LFV and vacuum metastability.	69

3.7	Dominant Standard Model background cross sections contributing to tri-lepton and missing transverse energy.	76
3.8	Dominant Standard Model background cross section contributing to tri-lepton and missing transverse energy associated with two forward jets.	77
3.9	Cross section for IH case. Final tri-lepton signal cross section through s-channel heavy neutrino production at the 14 TeV LHC for the benchmark point $M_N = 100$ GeV.	78
3.10	Final tri-lepton signal through VBF production of heavy neutrino for the benchmark point $M_N = 100$ GeV at 14 TeV LHC for IH after all event selection cuts.	80
3.11	Minimal masses of a doubly charged Higgs boson $H_1^{\pm\pm}$ as a function of the parity breaking scale v_R of the right sector of the model and the mass of neutral Higgs bosons $\{A_1^0, H_1^0\}$ which contribute to the FCNC effects.	92
3.12	Phenomenologically interesting MLRSM processes at the LHC with primarily produced charged scalar particles and possible final signals.	99
3.13	Dominant Standard Model background contributions (in fb) for tri- and four-lepton signals at the LHC with $\sqrt{s} = 14$ TeV.	116
3.14	Number of background and signal events at 25 fb^{-1} and 300 fb^{-1} as an anticipated integrated luminosity at next 14 TeV run of LHC.	117
3.15	The significance of the signals for 300 fb^{-1} integrated luminosity.	118
3.16	Selection criteria for the forward jets. The two highest p_T jets $p_{T_{j_1}}, p_{T_{j_2}}$ are chosen as the VBF forward jets.	125
3.17	Standard Model cross section in fb for $\ell^+\ell^-\ell^+\ell^-jj$ final state and $\sqrt{s} = 14, 33, 100$ TeV LHC.	129

List of Figures

1.1	The building blocks of the SM with their mass, electric charge and spin.	2
1.2	Neutrino mass hierarchies.	10
1.3	(a) $2\nu\beta\beta$ process (b) $0\nu\beta\beta$ process (c) Spectra for the summed energy of emitted two β -particles. The figure is adapted from Moe et al. [45]	14
2.1	Schematic diagram showing various mechanisms of neutrino mass generation.	20
2.2	Diagram generating neutrino masses in Type-I seesaw. The diagram is drawn using Jaxodraw package [65].	24
2.3	Generic tree-level diagram for generation of small neutrino mass from heavy fermion exchange when lepton-number symmetry is broken by the (Majorana) mass insertion.	38
2.4	Generic tree-level diagram for generation of small neutrino mass for Dirac type mass insertion.	39
2.5	Tree level diagram (left panel) generating dimension-7 seesaw operator and 1-loop diagram (right panel) generating dimension-5 operator for neutrino masses.	46
2.6	Contour plot of the ratio $m_\nu^{loop}/m_\nu^{tree}$ in the $(M_\Phi - M_\Sigma)$ plane.	46
3.1	Representative diagrams for production and decay of doubly- and triply-charged scalars at hadron collider leading to multilepton (≥ 3) final states.	56

3.2	Figure (a): Production cross sections for the processes $pp \rightarrow \Phi^{+++}\Phi^{---}, \Phi^{++}\Phi^{--}, \Phi^{\pm\pm\pm}\Phi^{\mp\mp\mp}$ at the LHC with $\sqrt{s}=14$ TeV and $\Delta M = -2.8$ GeV. Figure (b): Dependence of decay Branching Ratio (BR) of $\Phi^{\pm\pm\pm}$ on v_Φ for IH and NH. Here \dagger implies all three charged leptons (e, μ, τ).	58
3.3	The colored histograms for a specific n-lepton signal show the number of events after implementing successive cuts in (a) $\dagger W$, (b) $\dagger W - WWW$ and (c) WWW dominant modes in the case of <i>Inverted Hierarchy</i>	62
3.4	The colored histograms for a specific n-lepton signal show the number of events after implementing successive cuts in (a) $\dagger W$, (b) $\dagger W - WWW$ and (c) WWW dominant modes in the case of <i>Normal Hierarchy</i>	63
3.5	New diagrams that contribute in Higgs to diphoton decay through charged components of Φ . Here Φ^i represents singly, doubly and triply-charged scalars.	66
3.6	Iso-contour of $R_{\gamma\gamma}$ in the $M_\Phi - \lambda_3$ plane.	66
3.7	Bound on y_ν/M_N as a function of Majorana phase α , varying the oscillation parameters in the allowed 3σ range.	70
3.8	(Left plot) Leading order s-channel diagram for heavy neutrino production at hadron colliders, and (Right plot) representative diagram for one of the decay mode of the heavy neutrino. These two figures lead to tri-lepton + \cancel{E}_T signal considered in the analysis.	71
3.9	Representative parton level diagrams contributing to $N\ell jj$ production through vector boson fusion at hadron colliders.	72
3.10	The total cross section is shown for production of heavy neutrino associated with light lepton ($pp \rightarrow N\ell$, where $\ell = e, \mu$) at the 14 TeV LHC through the leading order s-channel process, while dotted lines represent VBF production cross section.	73

3.11	The decay branching ratios of the heavy neutrino (N) in different channels as a function of its mass in the case of the normal hierarchy, Case-I, (left) and inverted hierarchy (right).	74
3.12	(Left) The variation of significance $S/\sqrt{S+B}$ for the s-channel production signal for benchmark point $M_N = 100$ GeV with the integrated luminosity available for the low luminosity option at 14 TeV LHC. (Right) The lines for 3σ (red) and 5σ (blue) significance in terms of heavy neutrino mass and integrated luminosity.	80
3.13	<u>On left:</u> an example of 20 Higgs mass spectra obtained by randomly chosen Higgs potential parameters. <u>On right:</u> cumulative distribution function P of the lowest mass of singly and doubly charged and next to lightest neutral scalars.	88
3.14	Dependence of the $H_1^{\pm\pm}$ mass on $\delta\rho \equiv \rho_3 - 2\rho_1$ for $v_R = 8$ TeV and various masses of flavor changing neutral Higgs scalars H_1^0 and A_1^0	91
3.15	Dependence of the $H_1^{\pm\pm}$ mass (in TeV) on $\delta\rho$ and α_3 for $v_R = 8$ TeV.	93
3.16	Exclusion limits on the masses of doubly charged scalars from ATLAS analysis, depending on their leptonic branching ratios.	96
3.17	Dependence of the $H_1^{\pm\pm}$ mass (in TeV) on $\delta\rho$ and α_3 for $v_R = 8$ TeV.	98
3.18	Branching ratios for the decay modes $(e^+e^+ + \mu^+\mu^+)$ and $\tau^+\tau^+$ of the doubly charged scalars as a function of ΔM	100
3.19	Production cross sections for $pp \rightarrow H_1^+H_1^-$ and $pp \rightarrow \tilde{H}_2^+\tilde{H}_2^-$ processes without imposing kinematic cuts.	102
3.20	Scenario I. Cross sections for $pp \rightarrow H_1^{++}H_1^{--}$ and $pp \rightarrow H_2^{++}H_2^{--}$ processes without imposing kinematic cuts.	103
3.21	Scenario II. Contour plots for the $pp \rightarrow (H_1^{++}H_1^{--} + H_2^{++}H_2^{--})$ cross section. $\sqrt{s} = 14$ TeV, no kinematic cuts imposed.	105
3.22	Production cross sections for $pp \rightarrow H_1^{++}H_1^-$ and $pp \rightarrow H_2^{++}\tilde{H}_2^-$ processes at $\sqrt{s} = 14$ TeV and no kinematic cuts are imposed.	107
3.23	Summary of various MLRSM LHC production cross sections considered in the study is shown with charged scalars at $\sqrt{s} = 14$ TeV and without kinematic cuts.	108

- 3.24 Invariant mass for SSDL and OSDL for $(pp \rightarrow H_{1,2}^{++} H_{1,2}^{--} \rightarrow 4l)$
with $M_{H_1^{++}} = M_{H_2^{++}} = 400$ GeV for $\sqrt{s} = 14$ TeV and $L = 300 \text{ fb}^{-1}$. 110
- 3.25 Lepton - lepton separations for the same-sign lepton pairs ($\Delta R_{\ell^\pm \ell^\pm}$)
and opposite-sign lepton pairs ($\Delta R_{\ell^\pm \ell^\mp}$) for $(pp \rightarrow H_{1,2}^{++} H_{1,2}^{--} \rightarrow 4l)$ within the degenerate scenario with $M_{H_1^{++}} = M_{H_2^{++}} = 400$
GeV for $\sqrt{s} = 14$ TeV and $L = 300 \text{ fb}^{-1}$ 112
- 3.26 Invariant mass for SSDL and OSDL signals in the $(pp \rightarrow H_{1,2}^{++} H_{1,2}^{--} \rightarrow 4l)$ process in the non-degenerate mass scenario with $M_{H_1^{\pm\pm}} = 400$
GeV and $M_{H_2^{\pm\pm}} = 500$ GeV for $\sqrt{s} = 14$ TeV and $L = 300 \text{ fb}^{-1}$. . 112
- 3.27 Lepton - lepton separations for same-sign lepton pairs ($\Delta R_{\ell^\pm \ell^\pm}$)
and opposite-sign lepton pairs ($\Delta R_{\ell^\pm \ell^\mp}$) in the $(pp \rightarrow H_{1,2}^{++} H_{1,2}^{--} \rightarrow 4l)$ process for non-degenerate mass scenario having $M_{H_1^{\pm\pm}} = 400$
GeV and $M_{H_2^{\pm\pm}} = 500$ GeV with $\sqrt{s} = 14$ TeV and $L = 300 \text{ fb}^{-1}$. 113
- 3.28 Invariant mass plots for SSDL and OSDL for the signals $\ell^\pm \ell^\pm \ell^\mp$
+ missing p_T , at the LHC with $\sqrt{s} = 14$ TeV and integrated
luminosity 300 fb^{-1} 114
- 3.29 Lepton-lepton separation plot for same-sign leptons ($\Delta R_{\ell^\pm \ell^\pm}$) and
opposite-sign leptons ($\Delta R_{\ell^\pm \ell^\mp}$) in the process $(pp \rightarrow (H_1^{\pm\pm} H_1^\mp + H_2^{\pm\pm} H_2^\mp) \rightarrow 3\ell)$. Here $\sqrt{s} = 14$ TeV and integrated luminosity
 300 fb^{-1} at the LHC. 115
- 3.30 Cross section σ for the pair production of doubly charged scalars
 $H_i^{\pm\pm}$ decaying to four-leptons for $\sqrt{s} = 8, 14$ and 100 TeV at the
LHC. 119
- 3.31 Charged scalar contribution to the $H_0^0 \rightarrow \gamma\gamma$ channel at the LHC.
In the loop there are three contributions coming from the charged
scalars $H_i^q \equiv H_1^{\pm\pm}, H_2^{\pm\pm}, H_1^\pm$ 120
- 3.32 $R_{\gamma\gamma}$ with the variation of charged scalar masses. 121
- 3.33 Basic processes which lead to $H^{\pm\pm}$ pair production. 123

3.34	Dependence of cross sections (σ) with the masses of doubly charged scalars for the process $pp \rightarrow H^{++}H^{--}jj$ for different center of mass energies: 14 TeV (red-solid), 33 TeV (green-dashed), and 100 TeV (blue-dotted) respectively.	125
3.35	Variations of significance of <i>signal</i> with integrated luminosities for different energies of pp colliders and various doubly charged Higgs boson masses.	129
4.1	Feynman diagrams for $\mu \rightarrow e\gamma$ in the MLRSM.	138
4.2	Feynman diagrams for $\mu \rightarrow 3e$ in the MLRSM.	139
4.3	The predicted branching ratios of $\mu \rightarrow e\gamma$ and $\mu \rightarrow 3e$ processes as a function of the lightest neutrino mass for NH and IH in Type-I and Type-II seesaw dominance. Here $r = 0.707$	140
4.4	Variation of G_L^γ , G_R^γ , the branching ratio of $\mu \rightarrow e\gamma$ process and the branching ratio of $\mu \rightarrow 3e$ process as a function of the light neutrino mass.	142
4.5	The predicted branching ratios of $\mu \rightarrow e\gamma$ (blue points) and $\mu \rightarrow 3e$ (red points) processes, when experimental bounds on the branching ratios of both are simultaneously satisfied, as a function of the Majorana phase α_2 for Type-I and NH case.	143
4.6	The predicted branching ratios of $\mu \rightarrow e\gamma$ and $\mu \rightarrow 3e$ processes as a function of the lightest neutrino mass for NH and IH in Type-I and Type-II seesaw dominance. Here $r = 0.1414$	144
4.7	The predicted branching ratios of $\mu \rightarrow e\gamma$ and $\mu \rightarrow 3e$ processes as a function of the lightest neutrino mass for NH and IH in Type-I and Type-II seesaw dominance. Here $r = 1.414$	145
4.8	The dominant LH and RH current contributions to the $0\nu\beta\beta$ process in our model.	146
4.9	The variation of the effective neutrino mass as a function of the lightest neutrino mass for Type-I dominance with NH.	147

4.10	The variation of the effective mass as a function of the lightest neutrino mass for Type-I dominance and IH.	149
4.11	The variation of the effective mass as a function of the light neutrino mass for Type-II dominance and NH.	150
4.12	The variation of the effective mass as a function of the lightest neutrino mass for Type-II dominance and IH.	151
4.13	The branching ratio of $\mu \rightarrow e\gamma$ and $\mu \rightarrow 3e$ vs light neutrino mass, for the right-handed gauge boson mass $M_{W_R} = 2$ TeV and $\frac{M_N}{M_\Delta} = 0.707$	153
4.14	The effective mass m_{ee} vs light neutrino mass, for the right-handed gauge boson mass $M_{W_R} = 2$ TeV and $\frac{M_N}{M_\Delta} = 0.707$	154
4.15	The allowed region in the M_N vs M_Δ plane that is experimentally allowed by LFV processes, as well as $0\nu\beta\beta$	155
A.1	The tree-level diagram for the generation of the dimension-7 effective vertex is shown on the left-hand side. The right-hand figure shows the effective vertex in the low energy approximation.	167
A.2	Effective vertex of $\Phi^{++}\ell_i^-\ell_j^-$ coupling.	168
A.3	Feynman rules for the production and decays of charged scalars.	169
A.4	Feynman rules for Yukawas in the Lagrangian.	170
A.5	Feynman rules for the effective vertices.	170

Chapter 1

Introduction

Neutrinos are the most elusive particles in the Standard Model (SM). The SM presumes neutrinos to be massless, but neutrino oscillation experiments have already established that the neutrinos are massive¹. This demands physics beyond the SM. In this chapter we introduce the Standard Model of particle physics. Then we discuss a brief history of the neutrinos, why they are massless in the SM and the phenomenon of neutrino oscillation which implies that neutrinos are massive. We also outline the mechanisms of neutrino mass generation. Phenomenological consequences of neutrino masses, like neutrinoless double beta ($0\nu\beta\beta$) decay and lepton flavor violation (LFV) are also introduced in this chapter. Finally, we give a thesis overview.

1.1 The Standard Model

The Standard Model [1] of particle physics is a mathematical framework based on the principle of invariance of the Lagrangian under local gauge transformations. The gauge group of the SM is $G_{SM} \equiv SU(3)_c \otimes SU(2)_L \otimes U(1)_Y$. Generators of these individual groups are associated with the gauge bosons needed for local gauge invariance. These gauge bosons are mediators of the fundamental forces. In nature there are four fundamental interactions which have been

¹The Nobel prize in physics for the year 2015 is shared by two experimental physicists, Prof. Takaaki Kajita and Prof. Arthur B. McDonald, for the discovery of neutrino oscillations which shows that neutrinos have mass.

identified: strong interaction, electromagnetic interaction, weak interaction and gravitational interaction. The SM includes the elementary particles and their interactions except the gravitational interaction. It has been a successful model in explaining wide range of experimental observations in high energy physics. The discovery of the Higgs boson by the ATLAS [2] and the CMS [3] collaborations has further consolidated it.

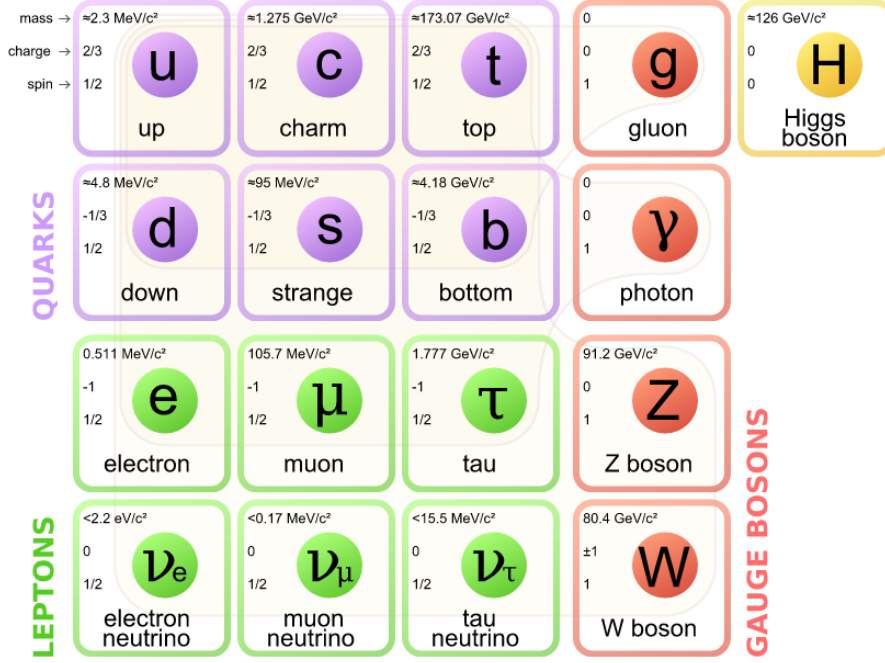


Figure 1.1: The building blocks of the SM with their mass, electric charge and spin. The first three columns show the three generations of fermions with the upper half having quarks and the lower half with leptons, while the fourth column represents gauge bosons of the strong, electromagnetic, and weak interactions. The top right square is for the scalar particle called the Higgs boson. The figure is taken from Wikipedia.

The field content of the Standard Model is as follows:

$$\begin{aligned}
 \text{Fermions :} & \quad [Q_L = (u_L, d_L)^T, u_R, d_R, L_L = (\nu_L, e_L)^T, e_R] \times 3 \\
 \text{Gauge Bosons :} & \quad \gamma, W^\pm, Z, \text{ gluons} \\
 \text{Scalar :} & \quad H = (H^+, H^0)^T.
 \end{aligned} \tag{1.1}$$

Quarks (Q_L, u_R, d_R) and leptons (L_L, e_R) are fermions since they have half integer spins and they follow Fermi-Dirac statistics, while gauge bosons are medi-

Particles	Color multiplicity $SU(3)_c$	Third component of isospin, T_{3L} $SU(2)_L$	Hypercharge $U(1)_Y$	Electric charge $Q = T_{3L} + \frac{Y}{2}$
$Q_L = \begin{pmatrix} u_L \\ d_L \end{pmatrix}$	$\begin{pmatrix} 3 \\ 3 \end{pmatrix}$	$\begin{pmatrix} +1/2 \\ -1/2 \end{pmatrix}$	+1/3	$\begin{pmatrix} +2/3 \\ -1/3 \end{pmatrix}$
u_R	3	0	+4/3	+2/3
d_R	3	0	-2/3	-1/3
$l_L = \begin{pmatrix} \nu_L \\ e_L \end{pmatrix}$	$\begin{pmatrix} 1 \\ 1 \end{pmatrix}$	$\begin{pmatrix} +1/2 \\ -1/2 \end{pmatrix}$	-1	$\begin{pmatrix} 0 \\ -1 \end{pmatrix}$
e_R	1	0	-2	-1
$H = \begin{pmatrix} H^+ \\ H^0 \end{pmatrix}$	$\begin{pmatrix} 1 \\ 1 \end{pmatrix}$	$\begin{pmatrix} +1/2 \\ -1/2 \end{pmatrix}$	+1	$\begin{pmatrix} +1 \\ 0 \end{pmatrix}$

Table 1.1: Quantum numbers of the SM particles. Charges of the individual particles can be calculated using the formula $Q = T_{3L} + \frac{Y}{2}$ [1].

ators of the fundamental forces and they have integer spin and obey Bose-Einstein statistics. In Table 1.1 quantum numbers of the SM particles are given. In nature there are three copies of fermions termed as three generations or three families and each quark comes in three colors². The electron, the electron-neutrino, the up-quark and the down-quark are collectively known as the first generation of fermions. In the Eq. 1.1 and Table 1.1 only the first family of fermions is shown. In Fig. 1.1 the building blocks of the SM including the fermions of all the families, are shown with their masses, electrical charges and spins. As we can read from the figure, γ (photon) is the massless gauge boson which mediates the electromagnetic interaction, while W^\pm, Z are the massive force carriers for the weak interaction, and massless gluons (g) mediate the strong interaction.

In the SM the left-handed fermion fields transform as doublets, while the right-handed fermion fields transform as singlets under $SU(2)_L$. However, the right-handed neutrino (ν_R) is not present in the SM. This Left-Right asymmetry is the implication of maximal parity violation observed in the weak interactions. The SM neutrinos take part only in the weak interactions.

²Here color does not mean the color in our usual sense, but it means some charge corresponding to the non-abelian $SU(3)_c$ gauge group, like the electrical charge corresponding to the $U(1)_Q$ abelian gauge group.

1.2 A brief history of parity violation

A brief history of parity violation in the weak interactions is as follows: conservation of parity was observed firmly in the electromagnetic and strong interactions and therefore it was thought that parity conservation is a general law of nature. But $\theta - \tau$ puzzle led Lee and Yang to propose parity violation in the processes involving weak interactions. The τ and θ mesons were known to have the same life-time and the same mass, but it was found that τ decays to 3 pions and θ decays to 2 pions. Dalitz had shown that τ had parity -1 and θ had parity +1. So either τ and θ were two different particles and there was no violation of parity, or τ and θ were the same particle but parity was violated. Lee and Yang in their classic paper on parity violation, also suggested some experiments to check whether parity is violated in the weak interactions [4]. The first observation of parity violation was obtained by Wu and collaborators by observing angular distribution of electrons in the β -decay of Co^{60} nuclei [5].

1.3 Generation of gauge boson and fermion masses in the SM

A mass term for a gauge boson, of the form $M^2 A_a^\mu A_{a\mu}$ breaks the gauge invariance, where μ is a Lorentz index and a is a gauge index. So, a bare (direct) mass term for the gauge boson would not respect the symmetry of the Lagrangian. This forces the gauge bosons in the SM to be massless. However, to explain the short-range nature of the weak interactions, massive gauge bosons are needed. Because of the gauge invariance, fermion mass term $m\bar{\psi}_L\psi_R$ is also not allowed, since ψ_L transforms as a doublet and ψ_R transforms as a singlet under $SU(2)_L$, and thus the term is not invariant under $SU(2)_L$. So, the fermions are also massless before the symmetry breaking. Therefore, before the electroweak ($SU(2)_L \otimes U(1)_Y$) symmetry breaking, all the particles in the SM are massless. In general, masses of the particles in the SM arise by the Higgs mechanism [6–10], in which the gauge symmetry is broken spontaneously by the electroweak

vacuum as the neutral component of the Higgs doublet gets vacuum expectation value (VEV), $\langle H^0 \rangle = v/\sqrt{2}$. The symmetry breaking pattern is as follows:

$$\begin{array}{c} \underbrace{SU(2)_L \otimes U(1)_Y}_{\langle H^0 \rangle \downarrow Q=T_{3L}+\frac{Y}{2}} \\ U(1)_Q. \end{array}$$

Here the electroweak symmetry $SU(2)_L \otimes U(1)_Y$ breaks to $U(1)_Q$ which is the abelian gauge group representing electromagnetic interactions. The charge (Q), in terms of T_{3L} and hypercharge (Y), is given as $Q = T_{3L} + \frac{Y}{2}$. Once the symmetry breaks down spontaneously, the gauge bosons (W^\pm, Z^0) and fermions become massive through the Higgs mechanism. Photon and gluon still remain massless as they are gauge bosons of the (manifestly residual) unbroken symmetries. The Higgs mechanism also gives rise to a physical neutral scalar called the Higgs boson, which has been found at the Large Hadron Collider (LHC) [2, 3].

Once the Higgs doublet is introduced, we can write a gauge invariant mass term $y\bar{\psi}_L\psi_R H + \text{h.c.}$ for the fermions, where y is the Yukawa coupling. The fermion mass term, after SSB, becomes $m_f\bar{\psi}_L\psi_R + \text{h.c.}$ with $m_f = y\langle H^0 \rangle = yv/\sqrt{2}$. But even after the Higgs mechanism, the neutrinos still remain massless, due to the non-existence of right-handed neutrinos in the SM.

Though the SM at present gives a very good account of most of the observed phenomena, there are several reasons which compel one to go beyond the SM. Some of the theoretical drawbacks of the SM are the instability of the Higgs mass under radiative correction also known as the hierarchy problem, no explanation of hierarchy amongst fermion masses, presence of large number of free parameters, non-inclusion of gravitation, etc. The experimental drawbacks are inability to explain masses of neutrinos, no explanation for dark matter, etc. There are several attempts at formulating a more fundamental theory at a higher scale and the SM can be a low energy realization of this. The observation of non-zero neutrino mass puts an emphasis on beyond the SM (BSM) scenarios which could successfully generate neutrino masses.

1.4 The neutrinos

Neutrinos are fermions with no electrical charge. The history of neutrino goes back to the famous letter of Pauli, sent to a conference, in which he postulated neutrinos in 1930 to explain the continuous energy spectrum of electrons in the nuclear β -decay process. Based on the neutrino hypothesis Fermi built a theory to explain the energy spectrum of the β -decay process, $n \rightarrow p e \bar{\nu}_e$ [11]. In 1956 Goldhaber, Grodzins and Sunyar gave the first experimental evidence for negative helicity³ of the neutrinos[12]. Anti-neutrino ($\bar{\nu}_e$) was first discovered in the reactor experiments conducted by Cowan and Reines[13–15]. In these experiments anti-neutrinos from the Savannah River reactor were detected through the inverse β -decay process,

$$\bar{\nu}_e + p \rightarrow e^+ + n. \quad (1.2)$$

There are three types of neutrinos observed in various experiments. The second type of neutrino, called as muon neutrino (ν_μ), was found in the Brookhaven neutrino experiment led by Lederman[16]. The third generation neutrino ν_τ , dubbed as the tau neutrino, was discovered by the DONUT collaboration at Fermilab[17]. These three neutrinos ν_l ($l = e, \mu, \tau$) are termed as three flavors of neutrinos and they are associated with the three charged leptons in the SM e , μ , and τ , respectively. Measurement of the decay-width of the Z boson at LEP experiment gives important information about the number of neutrino species. It is found that the number of species of neutrinos, with the SM interactions, are $n_\nu = 2.984 \pm 0.008$ [1]. Therefore it was established that there are three types of active neutrinos. For a historical overview of neutrinos, see for instance [18].

As mentioned earlier, fermion mass is the coupling between a left chiral state and a right chiral state. For the fermions two types of mass terms are possible. One is called the Dirac mass term, $m_D \bar{\psi}_R \psi_L$, where $m_D = yv/\sqrt{2}$, which

³Helicity of a particle is defined as the (normalized) spin projection along the momentum direction of that particle: $\mathcal{H} \equiv \frac{\vec{\sigma} \cdot \vec{p}}{|\vec{\sigma}| |\vec{p}|}$. This is same as the chirality operator when the mass of the particle is zero or can be neglected. In such cases, a particle with $\mathcal{H} = -1(+1)$ is called *left-handed (right-handed)*.

conserves the lepton number. For neutral fermions like neutrino, there is also the possibility of coupling between the left-handed neutrino with right-handed anti-neutrino, $\frac{1}{2}m_L\bar{\psi}_L^c\psi_L$. This term is called Majorana mass term and violates any charge (like lepton number) by 2 units. Since electric charge is conserved, this term is prohibited for the charged fermions. Thus, electrically neutral particles can have both, the Dirac as well as the Majorana mass term, while charged particles can have only the Dirac mass term. In the Majorana case particles and antiparticles are the same.

In the SM, neutrinos are massless. This is because the Dirac mass term $\bar{\nu}_R m_D \nu_L$ is not possible in the SM due to the absence of right-handed neutrino ν_R . Majorana mass term $\frac{1}{2}\bar{\nu}_L^c M_L \nu_L$ is also not allowed within the SM as it breaks the gauge symmetry. It also breaks the lepton number which is an accidental symmetry of the SM. But the discovery of neutrino oscillations gave a breakthrough establishing that neutrinos are massive. This implies that the SM is incomplete. It is interesting to note that the evidence of neutrino mass coming from neutrino oscillation provides the first direct testimony of physics beyond the SM.

1.5 Neutrino oscillations

Neutrino oscillation is a quantum mechanical interference phenomenon in which one flavor of neutrino is converted to another. This phenomenon is possible if neutrinos are massive. For massive neutrinos, neutrino flavor states (ν_l) are superpositions of neutrino mass eigenstates (propagation eigenstates) (ν_i),

$$\nu_l = \sum_{i=1}^3 U_{li} \nu_i, \quad l = e, \mu, \tau \quad , \quad (1.3)$$

where ν_l are the states with definite flavors and ν_i are the states with definite masses. Here U is neutrino mixing matrix, also known as the Pontecorvo-Maki-Nakagawa-Sakata (PMNS) matrix, which relates the mass-eigenstates with the flavor-eigenstates. In the standard parametrization, neutrino mixing matrix U

is given as [1]

$$U \equiv U_{\text{PMNS}} = \begin{pmatrix} c_{12} c_{13} & s_{12} c_{13} & s_{13} e^{-i\delta} \\ -c_{23} s_{12} - s_{23} s_{13} c_{12} e^{i\delta} & c_{23} c_{12} - s_{23} s_{13} s_{12} e^{i\delta} & s_{23} c_{13} \\ s_{23} s_{12} - c_{23} s_{13} c_{12} e^{i\delta} & -s_{23} c_{12} - c_{23} s_{13} s_{12} e^{i\delta} & c_{23} c_{13} \end{pmatrix} P, \quad (1.4)$$

where $c_{ij} = \cos \theta_{ij}$, $s_{ij} = \sin \theta_{ij}$, θ_{ij} are mixing angles and δ denotes the Dirac CP phase. Here $P = \{e^{i\alpha_1}, e^{i\alpha_2}, 1\}$ is the Majorana phase matrix.

U_{PMNS} is a 3×3 unitary matrix with 3 angles and 3 observable phases, if the neutrinos are Majorana particles. If the neutrinos are Dirac particles, then there are 3 mixing angles and only one observable phase⁴.

Due to their masses and flavor mixing, during their flight neutrinos can oscillate from one flavor state to another. The probability of oscillation of one flavor of neutrino (ν_α) to another (ν_β) in vacuum, is given as

$$P(\nu_\alpha \rightarrow \nu_\beta) = \delta_{\alpha\beta} - 4 \sum_{i>j} \text{Re}(U_{\alpha i}^* U_{\beta i} U_{\alpha j} U_{\beta j}^*) \sin^2(\Delta m_{ij}^2 \frac{L}{4E}) + 2 \sum_{i>j} \text{Im}(U_{\alpha i}^* U_{\beta i} U_{\alpha j} U_{\beta j}^*) \sin(\Delta m_{ij}^2 \frac{L}{2E}). \quad (1.5)$$

Here L is the distance between the source and the detector, E is the energy of the neutrino⁵.

As can be seen from Eq. 1.5, neutrino oscillation probability is sensitive to mass squared differences and the mixing angles, but not to the absolute masses. So we can infer only about the mass squared differences and mixing angles from the neutrino oscillation experiments. Neutrino oscillations have been observed

⁴For an $N \times N$ unitary matrix there are $2N^2$ real parameters. Unitarity conditions reduce them to N^2 independent parameters, out of which there are $\frac{N(N-1)}{2}$ moduli (angles) and $\frac{N(N+1)}{2}$ phases. So for $N = 3$, there are 3 independent mixing angles and 6 phases. Now, $2N - 1$ phases can be absorbed by redefining the fields. Finally, we have $\frac{N(N-1)}{2}$ moduli (angles) and $\frac{N(N+1)}{2} - (2N - 1) = \frac{(N-1)(N-2)}{2}$ phases. So out of 6 phases, 5 are not observable (physical), but only one phase, known as the Dirac phase, δ , is physical. In case of Majorana neutrinos, there are two additional physical phases, if all the three neutrinos are massive. If one of the neutrinos is massless, then there is only one additional phase.

⁵Note that when neutrinos propagate through matter then interactions with the ambient electrons can change the masses and mixings. In such cases one needs to solve the propagation equation, assuming appropriate density profile, to get the probabilities.

in solar, atmospheric, accelerator and reactor experiments. Recent experimental bounds on the mass squared differences and the mixing angles, from the global analysis of neutrino oscillation data [19], are presented in Table 1.2. In the table, best-fit values and 3σ ranges of the neutrino oscillation parameters are given. We can see from the table that Dirac phase δ is allowed in its full range for 3σ . Majorana phases do not appear in the oscillation probability formula. At present there are no bounds on these phases as well.

parameter	best-fit	3σ range
$\Delta m_{21}^2 [10^{-5} \text{ eV}^2]$	7.60	7.11 – 8.18
$\sin^2 \theta_{12}$	0.323	0.278 – 0.375
$ \Delta m_{31}^2 [10^{-3} \text{ eV}^2]$	2.48 (NH)	2.30 – 2.65 (NH)
	2.38 (IH)	2.20 – 2.54 (IH)
$\sin^2 \theta_{23}$	0.567 (NH)	0.393 – 0.643 (NH)
	0.573 (IH)	0.403 – 0.640 (IH)
$\sin^2 \theta_{13}$	0.0226 (NH)	0.0190 – 0.0262 (NH)
	0.0229 (IH)	0.0193 – 0.0265 (IH)
δ	1.41π (NH)	$0 - 2\pi$
	1.48π (IH)	

Table 1.2: The best-fit values and 3σ ranges of neutrino oscillation parameters from global analysis of current data [19].

Sign of the solar mass squared difference is positive *i.e.*, $\Delta m_{21}^2 > 0$, as inferred from the matter effect of solar neutrinos in the Sun [20]. As the sign of the other mass squared difference Δm_{32}^2 , known as the atmospheric mass squared difference, is not yet known from the experiments, there is the possibility of two neutrino mass hierarchies as follows:

- ◇ Normal Hierarchy (NH) : $m_1 \approx m_2 \ll m_3$

$$m_1, \quad m_2 = \sqrt{m_1^2 + \Delta m_{sol}^2}, \quad m_3 = \sqrt{m_1^2 + \Delta m_{sol}^2 + \Delta m_{atm}^2}, \quad (1.6)$$

- ◇ Inverted Hierarchy (IH) : $m_3 \ll m_1 \approx m_2$

$$m_3, \quad m_1 = \sqrt{m_3^2 + \Delta m_{atm}^2}, \quad m_2 = \sqrt{m_3^2 + \Delta m_{atm}^2 + \Delta m_{sol}^2}. \quad (1.7)$$

Fig. 1.2 shows the two possible mass hierarchies for neutrinos. The colors in the mass-eigenstates denote the proportions of the neutrino flavor eigenstates. Another possibility of neutrino mass spectrum is non-hierarchical mass spectrum *i.e.*, the quasi-degenerate (QD) spectrum: $m_1 \approx m_2 \approx m_3 \gg \sqrt{\Delta m_{atm}^2}$.

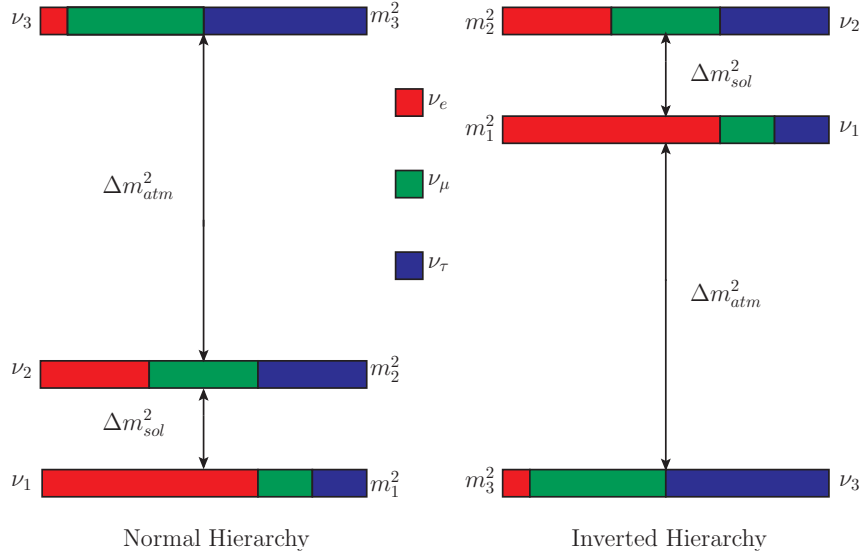


Figure 1.2: Neutrino mass hierarchies.

1.6 Absolute neutrino masses

There are experiments which look for absolute neutrino masses, like tritium β -decay experiments. They put bounds on the effective electron neutrino mass $m_{\nu_e} = \sqrt{\sum_i U_{ei}^2 m_i^2}$. Two past tritium experiments have put the following upper limits on the electron neutrino mass at 95% confidence level (C.L.): $m_{\nu_e} < 2.05$ eV by the Troitsk nu-mass experiment [21] and $m_{\nu_e} < 2.3$ eV by the Mainz experiment [22]. The next generation experiment KATRIN at the Karlsruhe Institute of Technology, is expected to start taking data in 2016. The experiment can achieve a sensitivity for the electron neutrino mass, m_{ν_e} , of ~ 0.2 eV (at 90% C.L.), with a discovery potential of ~ 0.3 eV at 3σ level [23, 24]. If neutrinos are Majorana particle then it is in principle possible to have neutrinoless double beta decay ($0\nu\beta\beta$) which violates lepton number. $0\nu\beta\beta$ decay experiments put bound on the effective neutrino mass defined as $m_{ee} = \sum_i U_{ei}^2 m_i$ which we discuss

in 1.9.1. Bound on the sum of the neutrino masses from cosmology is $\sum m_i \leq 0.17$ eV [25]. Oscillation data together with the cosmological mass bound imply that the neutrinos have very tiny (< 0.1 eV) masses, much less compared to the charged leptons. In a minimal model at least two of the three light neutrinos must be massive to explain the two non-zero mass squared differences coming from the neutrino oscillation data.

1.7 Generation of neutrino masses

Neutrino masses are many orders of magnitudes lower as compared to their charged companions. It is a challenging problem in theoretical physics to generate such small masses. Moreover, in the quark sector the mixing angles, governed by the Cabibbo-Kobayashi-Maskawa (CKM) matrix, are small. On the other hand the observed mixing patterns of the neutrinos consist of two large and one small mixing angles. Any theory/model beyond the SM should explain these features along with other established facts of the SM. Therefore neutrinos provide an important avenue to look beyond the SM and lots of experimental and theoretical efforts are geared towards unraveling the origin of neutrino mass and mixing which may lead to a better understanding of the nature.

There are various mechanisms to generate light neutrino masses: seesaw mechanism, radiative mass generations, etc. Seesaw mechanism is a generic mechanism to generate non-zero mass of neutrino and it naturally explains the smallness of this mass. This mechanism requires introduction of heavier particles. The smallness of neutrino masses can be ascribed to the heaviness of these particles. After integrating out the heavy particles, we can get small neutrino masses via the effective dimension-5 Weinberg operator, $\frac{\kappa}{M} L_L L_L H H$. Here κ is the effective coupling and M is the mass of the heavy particle which sets the scale of new physics. Once the electroweak symmetry is broken spontaneously, neutrino masses are generated as $m_\nu = \kappa v^2/M$. The seesaw mechanism can be implemented in more fundamental Grand Unified Theories (GUT) which enhances the theoretical appeal of this scenario. For the GUT-seesaw with $M \sim 10^{14}$ GeV,

correct neutrino mass is generated if $\kappa \sim \mathcal{O}(1)$. Note that as M increases, m_ν is lowered and hence the nomenclature of seesaw mechanism comes.

There are three ways to generate the Weinberg operator at tree level, leading to the ultra-violet (UV) completion of the theory. The minimal extension of the SM to realize seesaw mechanism and give three non-zero light neutrino masses, is to add one right-handed neutrino (ν_R) per generation, which transform trivially *i.e.*, they are singlets under the SM gauge group. This mechanism is called Type I seesaw mechanism [26–30]. Dimension 5 operators can also be generated by the Feynman diagrams mediated by a triplet scalar or a fermion triplet. These mechanisms are known as Type-II [31–34] and Type-III [35] seesaw mechanisms, respectively.

Currently, testing of BSM physics has got an unprecedented momentum because of the LHC. As discussed in the context of GUT seesaw, to generate small neutrino masses naturally the scale of the heavy particles is very high which is not accessible to the present colliders. However neutrino mass also imply BSM physics and hence it is only natural to ask if it is possible to get signature of neutrino mass models, in particular seesaw models at the LHC. This has led to the proliferation of the study of TeV scale neutrino mass models in which the scale of the new physics is not very high and can be probed at the LHC. In this thesis we investigate collider signatures of some of these models.

1.8 The Large Hadron Collider (LHC)

The LHC [36] is a collider, installed in a 17 mile long tunnel buried ~ 100 meter underground. The LHC is located at the European Organization for Nuclear Research (CERN) which sits at the border of France and Switzerland, near the city of Geneva. The tunnel was originally built between 1984 and 1989 for the CERN LEP machine [37].

Various steps are followed for proton-proton collisions to occur at the LHC. In the first stage of the acceleration, the proton beam obtained from hydrogen atoms is accelerated by Linac2 up to 50 MeV. Then the beam is injected into

the Proton Synchrotron(PS) booster, which accelerates it up to 1.4 GeV. The PS further accelerates the beam up to 25 GeV and then it is injected into the SPS to gain an energy of 450 GeV. Finally, it is injected to the LHC, where the final energy is achieved. Inside the LHC tunnel two proton beams travel in the opposite directions in separate beam pipes. These beams are guided by strong superconducting magnets and the beams collide at four different places, corresponding to the four locations of LHC experiments: ATLAS [38] and LHCf [39], CMS [40] and TOTEM [41], LHCb [42] and MoEDAL [43], and ALICE [44]. ATLAS and CMS experiments have general-purpose detectors to investigate the largest range of physics possible, while all other experiments have detectors specialized for focusing on specific phenomena.

The LHC was envisaged as a Higgs discovery machine. It has succeeded in achieving this goal. The next step at the LHC will be finding a signature of BSM physics and lot of effort is being seen worldwide to examine this possibility from various angles.

1.9 Phenomenological implications of neutrino masses

Masses of neutrinos can have other phenomenological implications like $0\nu\beta\beta$, LFV. The heavy particles introduced for generating neutrino masses, can also affect the stability of the electroweak vacuum if seesaw mechanism is operative. In this section we discuss some phenomenological implications of the massive neutrinos.

1.9.1 $0\nu\beta\beta$ decay

Lepton number conserving double beta decay, $2\nu\beta\beta$, is the process in which two beta particles (electrons) are emitted simultaneously with two anti-neutrinos. In general such a process can be described by the following decay equation and the

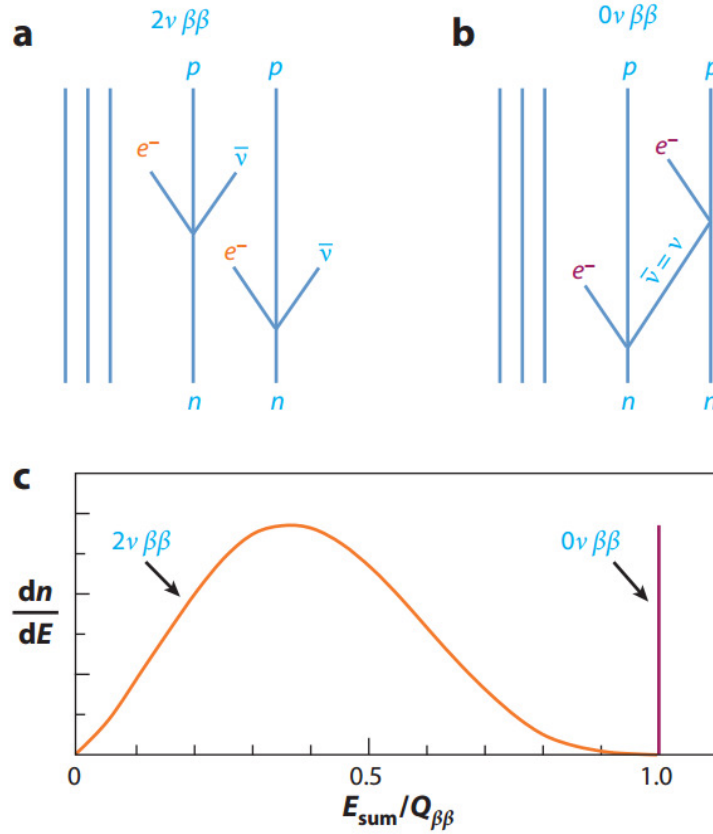


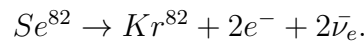
Figure 1.3: (a) $2\nu\beta\beta$ process (b) $0\nu\beta\beta$ process (c) Spectra for the summed energy of emitted two β -particles. The figure is adapted from Moe et al. [45]

Feynman diagram in Fig. 1.3(a):

$$(A, Z) \rightarrow (A, Z + 2) + 2e^- + 2\bar{\nu}_e. \quad (1.8)$$

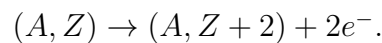
Here Z is the proton number and A is the nucleon (proton + neutron) number of the decaying nucleus. Experimental approaches to double beta decay can broadly be classified into two categories: direct experiments and indirect experiments. In the direct experiments two electrons are measured by detector in real time, while in the indirect experiments focus on counting the excess of daughter isotopes containing the parent isotopes that can undergo double beta decay. Indirect experiments do not distinguish in two neutrino and zero neutrino modes of the decay. Therefore, the main focus of the current double beta decay research is on the direct experiments. There are two types of indirect experiments: Geo-

chemical and Radiochemical. In geochemical experiments one searches for an abnormal isotopic abundance of the daughter nuclei in an ore containing double beta decay candidates, *e.g.* the double beta decay transition $Te^{130} \rightarrow Xe^{130}$. The radiochemical experiments are similar to the geochemical ones but daughter nuclei are unstable and can be identified by their decay, *e.g.* the double beta decay transition $U^{238} \rightarrow Pu^{238}$. $2\nu\beta\beta$ process was first observed in 1987 in the “direct” experiment (not geochemical or radiochemical) by Moe et al [46] in a Selenium nucleus decaying to a Krypton nucleus:



$2\nu\beta\beta$ decay can only occur if the single beta decay of the initial nucleus is forbidden. This process is a second order weak process. These facts make the process very rare to occur. After 1987 many other nuclei have been observed to undergo $2\nu\beta\beta$ decay.

Seesaw mechanism implies neutrinos to be Majorana particles and Majorana nature of neutrinos can be established by observing $0\nu\beta\beta$ decay process. The $0\nu\beta\beta$ decay process is a lepton number violating (LNV) nuclear transition, which can occur if neutrinos have mass and they are their own antiparticles. This process is almost similar to the $2\nu\beta\beta$ decay, and can be described by the following decay equation:



Feynman diagram for this process is shown in Fig. 1.3(b), in which only two beta particles but no anti-neutrinos are emitted. The $0\nu\beta\beta$ process is rarest compared to the $2\nu\beta\beta$ process due to the additional suppression because of the tiny Majorana neutrino mass. Fig. 1.3(c) shows decay spectrum for both the processes: $2\nu\beta\beta$ and $0\nu\beta\beta$. As can be seen from the figure, $2\nu\beta\beta$ process has continuous spectrum as in the case for single β decay spectrum, while $0\nu\beta\beta$ spectrum is monochromatic .

The formula for the half-life of the $0\nu\beta\beta$ decay is

$$\frac{1}{T_{1/2}^{0\nu}} = G^{0\nu} |M^{0\nu}|^2 |m_{ee}|^2, \quad (1.9)$$

where $G^{0\nu}$ is the phase space factor, $M^{0\nu}$ is the nuclear matrix element coming from nuclear physics. m_{ee} is the effective Majorana mass of neutrinos which comes from particle physics and for the standard case (only light neutrino contribution) it is given as

$$m_{ee} \equiv m_{eff} = \sum_i U_{ei}^2 m_i, \quad (1.10)$$

U_{ei} being elements of the PMNS matrix, U .

The best lower bound for the half life of $0\nu\beta\beta$ process at present is $T_{1/2}^{0\nu} > 3.0 \times 10^{25}$ (2.6×10^{25}) years coming from the GERDA+Heidelberg Moscow+IGEX (KamLAND-Zen) experiments using Ge^{76} (Xe^{136}). This constraint can be translated to a bound on the effective neutrino mass $m_{eff} \leq 0.18-0.22$ ($0.12-0.18$) eV, where the range is due to the uncertainty in the nuclear matrix element (NME) calculation [47].

1.9.2 Lepton flavor violation

Another interesting phenomenon is lepton flavor violation. Individual quark and lepton are assigned a quantum number known as flavor. Flavor is conserved at tree level by neutral current interactions mediated by gluons, Z boson and photon, but it is violated in charged current interactions mediated by W^\pm . The flavor changing neutral currents are highly suppressed and there are severe constraints from the experiments. In LFV processes individual lepton flavor number, like electron number, muon number, tau number are not conserved. For more details on LFV, see, *e.g.* [48]. Neutrino oscillation experiments already proved that neutrino flavors are not conserved (as neutrinos oscillate from one flavor to another). This leads to searches for lepton flavor violation in the charged-lepton processes like, *e.g.* $\mu^- \rightarrow e^- \gamma$, $\mu^- \rightarrow e^- e^- e^+$, etc. The experiments put stringent bounds from non-observation of these processes. The current limits are: $BR(\mu \rightarrow e\gamma) < 5.7 \times 10^{-13}$ from MEG [49] and $BR(\mu \rightarrow 3e) < 1.0 \times 10^{-12}$ from SINDRUM [50] experiments. The reach of future experiments, such as MEG-II [51], PRISM/PRIME [52] and Mu3e [53] will be $BR(\mu \rightarrow e\gamma) < 10^{-14}$, $BR(\mu \rightarrow e\gamma) < 10^{-16}$ and $BR(\mu \rightarrow 3e) < 10^{-16}$, respectively.

1.9.3 Vacuum stability

An important consequence of a TeV scale seesaw model is significant modification towards the stability of the electroweak vacuum [54, 55]. Because of the quantum corrections, the Higgs self-coupling, λ , diverges for higher values of Higgs mass and becomes negative for low values of Higgs mass near the Planck-scale ($M_{pl} = 1.2 \times 10^{19}$ GeV). Assuming the absence of any new physics between SM and the Planck scale, Higgs mass was found to lie in the range 126 – 171 GeV for λ (at M_{pl}) to be in the range $[0, \pi]$ [56, 57]. The upper bound is called the “triviality” bound and essentially portrays the perturbativity of the theory. The lower bound known as the “vacuum stability bound”, is obtained from the fact that a negative λ makes the potential unbounded from below and renders the vacuum unstable [58, 59]. The presence of new Yukawa couplings in seesaw models changes the β function of Higgs self-coupling. In the conventional Type-I seesaw model, generation of small neutrino mass needs the mass scale of the singlet to be of the order of 10^{14} GeV for $y_\nu \sim \mathcal{O}(1)$. It was observed in [54] that the presence of this extra coupling increases the lower bound of the Higgs mass coming from the vacuum stability constraints, gradually reaching the perturbativity bound. But, for canonical Type-I seesaw mechanism, the window of the new physics effect (from 10^{14} GeV to the Planck scale) towards the running of λ is small. Hence, the electroweak vacuum is less likely to get destabilized. For TeV scale models (with not very small y_ν), as the running of Yukawa starts affecting the running of λ from TeV scale up to the Planck scale, vacuum is more likely to get destabilized. Thus, it is possible to put bound on y_ν from the requirement of stability of the electroweak vacuum.

The possibility of a synergistic study of collider phenomenology with other phenomenological implications of seesaw, like $0\nu\beta\beta$, LFV and stability of the electroweak vacuum, makes the issue of TeV scale mechanisms of neutrino mass generation a very interesting field of research at present. All these together would guide us towards the new fundamental theory beyond the SM.

1.10 Objectives

The objectives of our work are as follows:

- ◇ To study neutrino mass models
- ◇ To investigate signatures of these models at hadron colliders and also to examine the Higgs sectors.
- ◇ To examine other phenomenological implications of the neutrino mass, like $0\nu\beta\beta$ decay, LFV, etc.

1.11 Thesis overview

The thesis is organized as follows: In Chapter 2 we discuss the various mechanisms to generate neutrino mass. In particular, we discuss the popular seesaw mechanisms including Type-I, Type-II and Type-III seesaws. We also discuss radiative neutrino mass models in which neutrino masses are generated at the loop level. The model part of the mechanisms whose signatures are studied in this thesis, are also discussed in details in Chapter 2. These models are: Babu-Nandi-Tavartkiladze Model (BNTM), Minimal Left-Right Symmetric Model (MLRSM) and Minimal Linear Seesaw Model (MLSM).

Chapter 3 contains the details of collider phenomenology of these models. We will discuss the collider signatures, in particular multilepton signatures, of these models in detail. In the study of the BNTM and the MLRSM, we have considered multilepton signatures of the charged scalars, while in the case of the MLSM the signals come from the decays of the heavy neutrinos.

Next, in Chapter 4, we discuss some phenomenological implication of neutrino mass including correlation between LFV and $0\nu\beta\beta$ in the context of the MLRSM.

We summarize and give future prospects in Chapter 5.

Chapter 2

Mechanisms of neutrino mass generation

As discussed in the introduction, it is now established that neutrinos have tiny masses, which are much smaller as compared to those of the charged leptons. The SM can not accommodate masses of the neutrinos. Thus to have a non-zero neutrino mass, one needs to go beyond the SM. This can be done either by just extending the particle content keeping the gauge group same as that of the SM or by extending the gauge group. To explain the tiny neutrino masses, various extensions of the SM have been proposed in the literature. This includes models in which neutrino mass is generated at the tree level, models with neutrino mass generation at the loop level, and the third category of models in which one can have neutrino mass at the tree level as well as loop level. This is pictorially represented by the Venn diagram in Fig. 2.1. The first category represents the popular seesaw mechanism, while the second represents the radiative neutrino mass models. The models of the third category are not purely seesaw models, nor are they purely radiative models, but instead they are in between. In the third type of models, both mechanisms are always present, with the tree-level mass being dominant in some regions of parameter space and the radiative mass being dominant in the other regions.

The most popular among these are the seesaw models which are presented in the next section. Then we discuss the origin of the dimension-5 Weinberg

operator and the generation of this in the Type-I seesaw mechanism. We also discuss neutrino masses in Type-II and III seesaw models. Subsequently, realization of the seesaw mechanism in the context of the Left-Right symmetric models is discussed. As mentioned in the previous chapter, seesaw implies introduction of particles at a much higher energy scale. This scale is usually $\sim 10^{14}$ GeV to account for the smallness of the neutrino mass. But in the context of LHC, TeV scale seesaw models have become relevant. In the subsequent section we discuss various TeV scale models for neutrino mass generation.

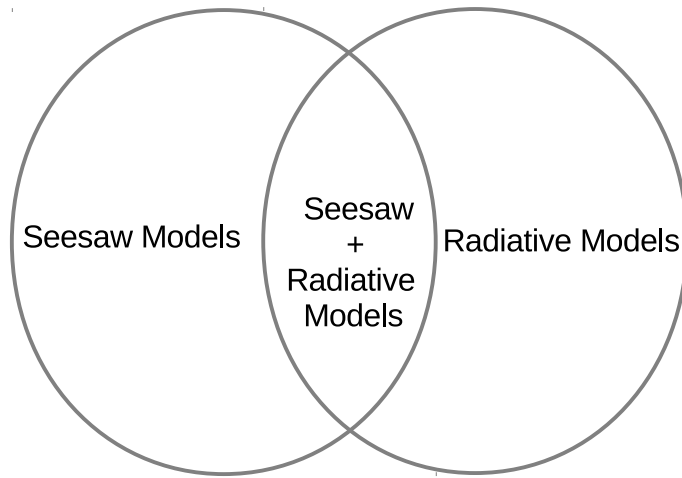


Figure 2.1: Schematic diagram showing various mechanisms of neutrino mass generation.

2.1 Generation of neutrino mass: seesaw mechanism

There are two possible mass terms for fermions. In the first possibility, known as Dirac mass term, the left- and right-handed fields are independent:

$$\mathcal{L}_{Dirac} = -m_D \bar{\psi} \psi = -m_D (\bar{\psi}_L \psi_R + \bar{\psi}_R \psi_L), \quad (2.1)$$

where $\psi = \psi_L + \psi_R$, $\psi_{L,R} = P_{L,R} \psi$ and $P_{L,R} = \frac{1 \mp \gamma_5}{2}$ are the chirality projection operators.

The second possibility called Majorana mass term, is only possible for neutral fermions. In this case, the charge conjugated field $\psi_L^C = (\psi^C)_R$ serves as the right-handed partner. This violates lepton number conservation, which is an accidental symmetry of the SM, by two units. Therefore the Majorana mass terms can be written as

$$\mathcal{L}_{Majorana} = -\frac{1}{2}m_L(\bar{\psi}_L^C\psi_L + \bar{\psi}_L\psi_L^C) - \frac{1}{2}M_R(\bar{\psi}_R^C\psi_R + \bar{\psi}_R\psi_R^C). \quad (2.2)$$

Note that, for the most general scenario we consider presence of two independent fields ψ_L and ψ_R . In the absence of ψ_R also, a Majorana mass term, $-\frac{1}{2}m_L(\bar{\psi}_L^C\psi_L + \bar{\psi}_L\psi_L^C)$, can be written. Also note that the Majorana mass matrices have to be symmetric¹ *i.e.*, $m_L^\top = m_L$ and $M_R^\top = M_R$. If we consider only one generation then m_D , m_L and M_R are just numbers, but if more than one generation are considered then these are no longer numbers but matrices. By including all the possible mass terms, the most general Lagrangian for fermion masses can be written as

$$\begin{aligned} \mathcal{L}_{Mass} &= \mathcal{L}_{Majorana,L} + \mathcal{L}_{Dirac} + \mathcal{L}_{Majorana,R} + h.c. \\ &= -\frac{1}{2}\bar{\psi}_L^C m_L \psi_L - \bar{\psi}_R m_D \psi_L - \frac{1}{2}\bar{\psi}_R M_R \psi_R^C + h.c. \\ &= -\frac{1}{2}\bar{\psi}_L^C m_L \psi_L - \frac{1}{2}\bar{\psi}_R m_D \psi_L - \frac{1}{2}\bar{\psi}_L^C m_D^\top \psi_R^C - \frac{1}{2}\bar{\psi}_R M_R \psi_R^C + h.c. \\ &= -\frac{1}{2}\bar{n}_L^C M n_L + h.c., \end{aligned} \quad (2.3)$$

where

$$n_L \equiv \begin{pmatrix} \psi_L \\ \psi_R^C \end{pmatrix} \quad (2.4)$$

¹This can be proved, using antisymmetry of C and anticommutation property of fermion fields, as follows: Since the Lagrangian is a scalar, $(\bar{\psi}_L^C m_L \psi_L)^\top = \bar{\psi}_L^C m_L \psi_L$. But $(\bar{\psi}_L^C m_L \psi_L)^\top = (-\psi_L^\top C^{-1} m_L \psi_L)^\top = \bar{\psi}_L^C m_L^\top \psi_L$. Therefore, $\bar{\psi}_L^C m_L^\top \psi_L = \bar{\psi}_L^C m_L \psi_L$, which implies $m_L^\top = m_L$. Hence, a Majorana mass matrix must be a symmetric matrix.

and

$$M \equiv \begin{pmatrix} m_L & m_D^\top \\ m_D & M_R \end{pmatrix}. \quad (2.5)$$

Here we consider a special case $m_L \ll m_D \ll M_R$, which leads to the seesaw mechanism. Then the mass-matrix M can be block-diagonalized by a unitary matrix W [60], as

$$M_{BD} = W^\top \begin{pmatrix} m_L & m_D^\top \\ m_D & M_R \end{pmatrix} W = \begin{pmatrix} M_{light} & 0 \\ 0 & M_{heavy} \end{pmatrix} \quad (2.6)$$

where M_{light} and M_{heavy} are not yet diagonal and given as

$$M_{light} \equiv m_\nu \sim m_L - m_D^\top M_R^{-1} m_D, \quad (2.7)$$

and

$$M_{heavy} \sim M_R. \quad (2.8)$$

In Type-I seesaw mechanism, $m_L = 0$ and hence the light neutrino mass is

$$M_{light} \equiv m_\nu \sim -m_D^\top M_R^{-1} m_D. \quad (2.9)$$

This is the seesaw mechanism in which a high M_R can give a low value for the neutrino mass naturally.

2.2 Origin of seesaw mechanism

Seesaw mechanism is a generic mechanism to explain tiny observed values of neutrino masses. Renormalizability criterion does not allow the operators in the SM Lagrangian to have larger than four mass dimension. The light neutrino masses arise from the effective higher dimensional operator ($d > 4$) generated once the heavy intermediate fields are integrated out. Origin of the seesaw mechanisms is

from the dimension-5 Weinberg operators given as [61]

$$\mathcal{L}_5 = -\frac{1}{8} \frac{a_{ji}^{(5)}}{M} \left(\overline{l_{Lj}^c} \epsilon \tau^a l_{Li} \right) \left(H^T \epsilon \tau^a H \right) + \text{h.c.} \quad (2.10)$$

where $a_{ji}^{(5)}$ is $\mathcal{O}(1)$ effective coupling and $\tau^a/2$ ($a = 1, 2, 3$) are the $SU(2)$ generators. Here l_L is the SM lepton doublet, H is the scalar doublet and ϵ being the antisymmetric $SU(2)$ tensor.

This type of operator is obtained by integrating out intermediate heavy fields of mass scale M , which sets the energy scale of new physics. After electroweak symmetry breaking neutral component of H field acquires VEV and consequently such an operator leads to the mass term for the neutrinos. Representation of the intermediate heavy fields can be obtained by $SU(2)$ group multiplication, $2 \otimes 2 = 1 \oplus 3$. Hence, there are four possible ways to form a dimension-5 gauge singlet term given in Eq. 2.10 at low energy through the tree-level exchange of a heavy particle at the high energy: (i) each l_L - H pair forms a fermion singlet, (ii) each of the l_L - l_L and H - H pair forms a scalar triplet, (iii) each l_L - H pair forms a fermion triplet, and (iv) each of the l_L - l_L and H - H pair forms a scalar singlet. Seesaw mechanism involving singlet fermion as in scenario (i), is known as Type-I seesaw [26, 30]. Seesaw mechanism mediated through triplet scalar as in scenario (ii), is known as Type-II seesaw [31–34, 62] and by triplet fermion as in scenario (iii), is known as Type-III seesaw [35, 63, 64]. Scenario (iv) gives gauge singlet terms only of the form $\overline{\nu_L^c} e_L$, which cannot generate a neutrino mass. Type-I, II and -III seesaws are the only three realizations of the dimension-5 effective operator at tree level.

2.3 Type-I seesaw

In Type-I seesaw mechanism, the additional part of the Lagrangian including the heavy neutrino field N_j to the SM Lagrangian is given by

$$\mathcal{L}_{\text{ext}} = -(Y_\nu)_{ji} \epsilon_{\alpha\beta} H_\beta \overline{N}_j P_L l_{\alpha i} - \frac{1}{2} M_{ji} \overline{N}_j P_R N_i^c + \text{h.c.} \quad (2.11)$$

with $\tilde{H} = \epsilon H^*$, and i and j being the generation indices, α and β are the $SU(2)$ indices. For m generation of light neutrinos and n generation of heavy neutrinos, i and j run from 1 to m and 1 to n respectively. The Yukawa coupling matrix, Y_ν , is a complex-valued $m \times n$ matrix in general. After SSB one gets the Dirac mass matrix as $m_D = \frac{v}{\sqrt{2}} Y_\nu$. The Majorana mass matrix M is an $n \times n$ complex symmetric matrix.

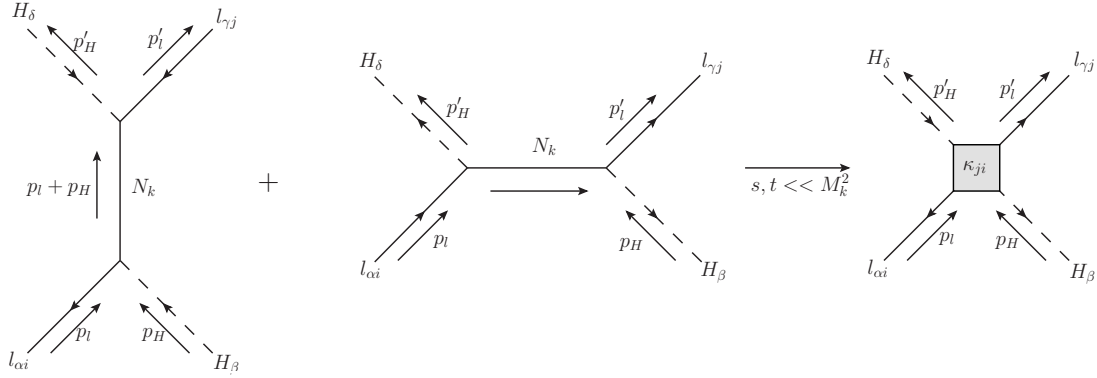


Figure 2.2: Diagram generating neutrino masses in Type-I seesaw. The diagram is drawn using Jaxodraw package [65].

With the Lagrangian 2.11, one can construct two possible dimension-5 operators in the context of $lH \rightarrow l^c H^*$ and $\bar{l}H^* \rightarrow \bar{l}^c H$. Here we present only one of them, as the other one can be obtained by just reversing the fermion lines. In diagram 2.2, in l.h.s. there are two possible diagrams from the renormalizable Lagrangian. To illustrate the connection between the effective and the full theory, consider the low energy limit, $s, t \ll M_k^2$, of these scattering diagrams, then we get the tree level amplitude as

$$i \left[\epsilon_{\gamma\delta} \epsilon_{\alpha\beta} \left(Y_\nu^\top (M^{-1}) Y_\nu \right)_{ji} + \epsilon_{\gamma\beta} \epsilon_{\alpha\delta} \left(Y_\nu^\top (M^{-1}) Y_\nu \right)_{ji} \right] P_L. \quad (2.12)$$

The right-hand side diagram of Fig. 2.2 corresponds to the dimension-5 operator with effective coupling κ ,

$$\mathcal{L}^{(5)} = \frac{1}{4} \kappa_{ji} \left(\bar{l}_{Lj}^c \epsilon H \right) \left(H^\top \epsilon^\top l_{Li} \right) + \text{h.c.}, \quad (2.13)$$

and the amplitude for this diagram is written as

$$\frac{i}{2} \kappa_{ji} (\epsilon_{\gamma\delta} \epsilon_{\alpha\beta} + \epsilon_{\gamma\beta} \epsilon_{\alpha\delta}) P_L. \quad (2.14)$$

By matching amplitudes of both the sides, we get the effective coupling κ in terms of parameters of the full theory (SM + N_j). Therefore, the effective theory emerges from the extended SM, at low energy where the momenta of the heavy particles are negligible compared to their mass. In terms of Feynman diagrams, this correspond to replacing Majorana neutrino line by the effective vertex, whose coupling is determined by the matching condition.

Tree level matching of both side amplitudes *i.e.*, Eqs. 2.12 and 2.14, gives

$$\begin{aligned} & i \left[\epsilon_{\gamma\delta} \epsilon_{\alpha\beta} \left(Y_\nu^\top (M^{-1}) Y_\nu \right)_{ji} + \epsilon_{\gamma\beta} \epsilon_{\alpha\delta} \left(Y_\nu^\top (M^{-1}) Y_\nu \right)_{ji} \right] P_L \\ &= \frac{i}{2} \kappa_{ji} (\epsilon_{\gamma\delta} \epsilon_{\alpha\beta} + \epsilon_{\gamma\beta} \epsilon_{\alpha\delta}) P_L. \end{aligned} \quad (2.15)$$

From Eq. 2.15, we identify

$$\kappa = 2 Y_\nu^\top M^{-1} Y_\nu. \quad (2.16)$$

Note that κ is symmetric. Here $s = (p_l + p_H)^2$ and $t = (p_l - p'_H)^2$. After SSB, the Higgs field receives VEV, v , as

$$H \equiv \begin{pmatrix} H^+ \\ H^0 \end{pmatrix} \longrightarrow \begin{pmatrix} 0 \\ \frac{v}{\sqrt{2}} \end{pmatrix}, \quad (2.17)$$

consequently the dimension five operator in Eq. 2.13 becomes

$$-\frac{1}{2} \cdot \left(-\frac{1}{4} \kappa_{ji} v^2 \right) \overline{\nu_{Lj}^c} \nu_{Li}. \quad (2.18)$$

The above expression is rearranged with $-ve$ sign as fermion mass term comes with a $-ve$ sign in the Lagrangian. The $1/2$ factor taken out to the front as it is a Majorana mass term. Then the light neutrino mass, using Eqs. 2.18 and 2.16,

is being identified as

$$m_\nu = -\frac{1}{4} \kappa v^2 = -m_D^\top M^{-1} m_D. \quad (2.19)$$

Since M is very large, the mass eigenvalues are naturally suppressed. The Majorana mass matrix m_ν is symmetric and can in general be diagonalized by unitary matrix ($U_\nu = U_{PMNS}$), parameterized as in Eq. 1.4.

2.4 Type-II seesaw mechanism

In Type-II seesaw mechanism, $SU(2)$ triplet scalar field is added to the SM particle spectra. The extra part of the Lagrangian containing this field is given by [66, 67]

$$\begin{aligned} \mathcal{L}_{\text{ext}}^{\text{II}} = & - (Y_\Delta^r)_{ji} \overline{l_{\beta j}^c} \epsilon_{\beta\gamma} \Delta_{\gamma\alpha}^r P_L l_{\alpha i} + \mu_\Delta^r H_\beta \epsilon_{\beta\gamma} \Delta_{\gamma\alpha}^r H_\alpha \\ & - (M_\Delta^{rs})^2 \text{Tr} [\Delta^{r\dagger} \Delta^s] + \text{h.c.} \end{aligned} \quad (2.20)$$

where the triplet Higgs field, Δ in adjoint representation, is given by

$$\Delta = \begin{pmatrix} \frac{1}{\sqrt{2}} \Delta^+ & \Delta^{++} \\ \Delta^0 & -\frac{1}{\sqrt{2}} \Delta^+ \end{pmatrix}, \quad (2.21)$$

r, s are the number of triplet Higgs fields which is at least two for successful leptogenesis [68]. Apart from the above Lagrangian, the SM potential receives additional terms due to the presence of the extra Higgs field. After symmetry breaking, the neutral component of Δ^r also receives VEV, $v_\Delta^r = (\mu_\Delta^r)^* v^2 / (M_\Delta^r)^2$. Then the light neutrino mass matrix in Type-II seesaw is given as

$$m_\nu = m_L = 2 (Y_\Delta^r v_\Delta^r). \quad (2.22)$$

For $\mu_\Delta \sim M_\Delta \sim 10^{12} - 10^{14}$ GeV, $v_\Delta \sim v^2 / M_\Delta$ which is of the form of seesaw suppression. For $\mathcal{O}(1)$ Yukawa coupling, this would naturally give the correct light neutrino mass term.

2.5 Type-III seesaw mechanism

In Type-III seesaw model one adds $SU(2)$ triplet fermions in place of singlet fermions of Type-I seesaw. These fermions have gauge interaction in contrast to the singlet fermions. The additional part of the Lagrangian contributing to neutrino mass is given as

$$\mathcal{L}_{\text{ext}}^{\text{III}} = - (Y_{\Sigma})_{ji} \tilde{H}^{\dagger} \bar{\Sigma}_j P_L l_i - \frac{1}{2} (M_{\Sigma})_{ji} \text{Tr} [\bar{\Sigma}_j P_R \tilde{\Sigma}_i] + \text{h.c.} \quad (2.23)$$

where Σ and $\tilde{\Sigma}$ are given by

$$\Sigma = \begin{pmatrix} \frac{1}{\sqrt{2}}\Sigma^0 & \Sigma^+ \\ \Sigma^- & -\frac{1}{\sqrt{2}}\Sigma^0 \end{pmatrix}, \quad \tilde{\Sigma} = \epsilon \mathcal{C} \bar{\Sigma}^T \epsilon, \quad (2.24)$$

and \mathcal{C} stands for the charge conjugation operator. The light neutrino mass matrix is the same as in Type-I seesaw mechanism with Y_{ν} and M replaced by Y_{Σ} and M_{Σ} respectively.

Type III seesaw mechanism can naturally be obtained in $SU(5)$ GUT model [35, 63, 64]. On the other hand, Type I and Type II seesaw mechanism naturally arise in both Left-Right Symmetric Model (MLRSM) and $SO(10)$ GUT models. In the next section we elaborate on generation of neutrino masses in LR symmetric model.

2.6 Neutrino masses in Left-Right Symmetric Model

In the SM, both, left-handed neutrinos and the charged leptons transform as doublets of the $SU(2)_L$ gauge group. Similarly, left-handed up and down quarks transform as doublets. However, right-handed fields of quarks and leptons are not treated on the same footing as the left-handed fields: they are singlet fields with respect to the $SU(2)_L$ gauge group. In the Left-Right symmetric models both left-handed and right-handed fields are treated on the same footing - they

transform as doublets under $SU(2)_L$ and $SU(2)_R$ gauge groups, respectively. The full gauge group of the LRSM is $G_{LRSM} = SU(3)_c \otimes SU(2)_L \otimes SU(2)_R \otimes U(1)_{B-L}$. In what follows we concentrate on the $SU(2)_L \otimes SU(2)_R \otimes U(1)_{B-L}$ sector. Note that $SU(3)_c$ is an intact symmetry and hence the breaking pattern does not involve this. Left-right symmetry gauge group can be embedded in the $SO(10)$ GUT group.

Attractive features of the LRSM are as following:

- ◇ It naturally generates tiny masses of light neutrinos via the seesaw mechanism,
- ◇ Parity violation is not an ad-hoc assumption, but comes naturally from spontaneous breaking of Left-Right symmetry,
- ◇ Hypercharge (Y) is no more ad-hoc, but is given in terms of more physical charges like baryon number (B) and lepton number (L).

The matter field content of the LRSM is as follows:

$$L_{iL} = \begin{pmatrix} \nu'_i \\ l'_i \end{pmatrix}_L : (2, 1, -1), \quad L_{iR} = \begin{pmatrix} \nu'_i \\ l'_i \end{pmatrix}_R : (1, 2, -1), \quad (2.25)$$

$$Q_{iL} = \begin{pmatrix} u'_i \\ d'_i \end{pmatrix}_L : (2, 1, 1/3), \quad Q_{iR} = \begin{pmatrix} u'_i \\ d'_i \end{pmatrix}_R : (1, 2, 1/3). \quad (2.26)$$

$i = 1, 2, 3$ runs over number of generations. The numbers $(n_L, n_R, B - L)$ in parenthesis characterize the $SU(2)_L$, $SU(2)_R$ and $U(1)_{B-L}$ charges, respectively. $n_{L,R}$ denote dimensions of the $SU(2)_L$ and $SU(2)_R$ representations. Note that here we need three heavy neutrinos for Left-Right symmetry.

The SM scalar sector consists of a doublet of complex scalar fields. There are four real scalar fields, three of them are responsible for giving masses to the three gauge bosons W^\pm, Z^0 through the Higgs mechanism. The remaining scalar is associated with the neutral Higgs boson which has been discovered at the LHC. However, if we go beyond the SM, we may need to deal with more complex scalar systems, for instance $SU(2)$ triplet which contains charged (singly and(or)

doubly) scalar particles. These particles are naturally embedded in the Left-Right symmetric models where a new characteristic energy scale exists and the symmetry between left and right $SU(2)$ gauge sectors is broken spontaneously [69, 70]. Here we focus on the so-called minimal and manifest version of the model (MLRSM), see *e.g.* [69–72].

In the MLRSM, to break the Left-Right symmetry, scalar triplets Δ_L and Δ_R are added², which transform as $(3, 1, 2)$ and $(1, 3, 2)$, respectively and can be written as

$$\Delta_{L,R} = \begin{pmatrix} \delta_{L,R}^+/\sqrt{2} & \delta_{L,R}^{++} \\ \delta_{L,R}^0 & -\delta_{L,R}^+/\sqrt{2} \end{pmatrix}. \quad (2.27)$$

SM symmetry breaking can be achieved by introducing a Higgs bi-doublet,

$$\phi = \begin{pmatrix} \phi_1^0 & \phi_2^+ \\ \phi_1^- & \phi_2^0 \end{pmatrix} : (2, 2, 0), \quad (2.28)$$

This is also responsible for the masses of the SM fermions and gauge bosons. Neutral components of the triplets and the two neutral components of the bi-doublet get VEVs and symmetries are broken at two stages. The symmetry breaking pattern for the MLRSM is as follows:

$$\begin{array}{c} SU(2)_L \otimes \underbrace{SU(2)_R \otimes U(1)_{B-L}} \\ \langle \delta_R^0 \rangle \Big| \frac{Y}{2} = T_{3R} + \frac{B-L}{2} \\ \hline \underbrace{SU(2)_L \otimes U(1)_Y} \\ \langle \phi_1^0 \rangle, \langle \phi_2^0 \rangle \Big| Q = T_{3L} + \frac{Y}{2} \\ \hline U(1)_Q \end{array}$$

Therefore, in the MLRSM, $U(1)_Q$ symmetry of the Lagrangian is reached by spontaneous symmetry breaking in two steps. In the first step LR symmetry breaks to the SM gauge group, while second step leads to the breaking of the SM gauge group in to $U(1)_Q$ gauge group.

²One can also introduce scalar doublets $\chi_{L,R}$ instead of $\Delta_{L,R}$, but that will not be minimal to generate neutrino mass as extra fermion singlets are also needed to be introduced [73].

The gauge symmetry $SU(2)_R \times U(1)_{B-L}$ is broken down to the SM group $U(1)_Y$ by the vacuum expectation value (VEV) of the neutral component of the $SU(2)_R$ triplet Δ_R : $\langle \delta_R^0 \rangle = \frac{v_R}{\sqrt{2}}$. This generates the Majorana masses of the RH neutrinos N_R , as well as the masses of the RH gauge bosons W_R and Z_R . The other Higgs triplet Δ_L acquires a small VEV $\langle \delta_L^0 \rangle = \frac{v_L}{\sqrt{2}}$ and contributes to the generation of light neutrino masses. The standard electroweak symmetry is broken by the VEV of the Higgs bi-doublet field ϕ : $\langle \phi \rangle = \text{diag}(\frac{\kappa_1}{\sqrt{2}}, \frac{\kappa_2}{\sqrt{2}})$, which generates masses for the charged fermions, as well as the SM W and Z bosons. The mixing between the LH and RH gauge bosons is given by $\tan 2\xi \simeq -2\kappa_1\kappa_2/v_R^2$. Notice that in the case of no mixing ($\xi \rightarrow 0$) the mass eigenstates will exactly be $M_{W_1} = M_{W_L}$ and $M_{W_2} = M_{W_R}$.

The current experimental constraints on the mass of the RH gauge boson $M_{W_R} \simeq g_R v_R / \sqrt{2} \gtrsim 3$ TeV (assuming the equality of the $SU(2)_L$ and $SU(2)_R$ gauge couplings, *i.e.*, $g_L = g_R$) from direct LHC searches [74, 75], as well as from quark flavor changing neutral current (FCNC) processes [76–79], imply that $v_R \gtrsim 10$ TeV. Similarly, the constraints from the electroweak ρ -parameter [1] restrict $v_L \lesssim 2$ GeV. On the other hand, since the VEVs of the Φ field break the electroweak symmetry, we have $\kappa_1^2 + \kappa_2^2 = k^2$, where $k \simeq 246$ GeV is the electroweak VEV in the SM. Thus we expect to have the following hierarchy of VEVs:

$$v_L \ll \kappa_1, \kappa_2 \ll v_R. \quad (2.29)$$

Without loss of generality, we can choose κ_1 and v_R as real parameters, while κ_2 and v_L can be, in general, complex parameters.

The Yukawa Lagrangian in the lepton sector is given by

$$\begin{aligned} -\mathcal{L}_Y &= h_{ij} \bar{\psi}_{L,i} \Phi \psi_{R,j} + \tilde{h}_{ij} \bar{\psi}_{L,i} \tilde{\Phi} \psi_{R,j} + f_{L,ij} \psi_{L,i}^\top C i \tau_2 \Delta_L \psi_{L,j} \\ &\quad + f_{R,ij} \psi_{R,i}^\top C i \tau_2 \Delta_R \psi_{R,j} + \text{H.c.}, \end{aligned} \quad (2.30)$$

where $C = i\gamma_2\gamma_0$ is the charge conjugation operator, $\tilde{\Phi} = \tau_2 \Phi^* \tau_2$, τ_2 is the second Pauli matrix and γ_μ are the Dirac matrices. After electroweak symmetry breaking, the above Yukawa Lagrangian leads to the following 6×6 neutrino

mass matrix in the (ν, N) basis,

$$\mathcal{M}_\nu = \begin{pmatrix} m_L & m_D \\ m_D^\top & M_R \end{pmatrix}, \quad (2.31)$$

where the 3×3 Dirac and Majorana mass matrices are given by

$$m_D = \frac{1}{\sqrt{2}} (\kappa_1 h + \kappa_2 \tilde{h}), \quad m_L = \sqrt{2} v_L f_L, \quad M_R = \sqrt{2} v_R f_R. \quad (2.32)$$

In the seesaw approximation, using Eq. 2.29, the 3×3 light neutrino mass matrix becomes

$$m_\nu \simeq m_L - m_D M_R^{-1} m_D^\top = \sqrt{2} v_L f_L - \frac{\kappa^2}{\sqrt{2} v_R} h_D f_R^{-1} h_D^\top, \quad (2.33)$$

where $h_D \equiv (\kappa_1 h + \kappa_2 \tilde{h})/(\sqrt{2}\kappa)$ and $\kappa \equiv (|\kappa_1|^2 + |\kappa_2|^2)^{1/2}$.

In the scalar sector of the MLRSM, there are 20 real degrees of freedom: 8 from the bi-doublet and 6 each from the LH and RH triplets. After spontaneous symmetry breaking, 6 of them are Goldstone bosons, which give masses to the LH and RH gauge bosons in both charged and neutral sectors. Thus, there remain 14 physical real scalar fields, one of which (H_0^0) should be identified as the SM-like Higgs boson with mass proportional to k , independent of the triplet VEVs, for more details, see Appendix C. The remaining 13 scalar fields are as follows: three neutral scalars H_1^0, H_2^0 and H_3^0 , two pseudoscalars A_1^0 and A_2^0 , four singly charged scalars H_1^\pm and H_2^\pm , and four doubly charged scalars $H_1^{\pm\pm}$ and $H_2^{\pm\pm}$. In the next chapter we will discuss the collider signatures of the charged scalars of the MLRSM.

2.7 TeV scale models for neutrino mass generation

To have signatures of seesaw models at the LHC, the heavy neutrino (N) mass needs to be $\sim \mathcal{O}$ (TeV). However, if one lowers the scale of seesaw to TeV, then

to generate neutrino mass ($m_\nu \sim y_\nu^2 v^2/M$), the neutrino Yukawa couplings required are much smaller $\sim y_\nu \sim 10^{-6}$. Such small Yukawa couplings lead to suppression of the production of the heavy neutrinos in natural TeV scale Type-I seesaw models. Therefore, small y_ν implies that there are no other observable consequences at low energy except neutrino oscillations. This leads to the question whether it is possible to achieve both the requirements simultaneously, *i.e.*, having TeV scale heavy neutrinos along with large Yukawa coupling leading to large light-heavy mixing.

For such models, additional suppression mechanism for the neutrino masses are required and some possibilities are as follows:

(1) Texture models: in some specific texture models, where texture means a specific configuration of a mass matrix, heavy neutrino mass scale can be at TeV scale and also light-heavy mixing can be sizable to produce at the LHC.

(2) The neutrino mass is generated at tree level in which additional suppression comes from the small lepton number violating contribution e.g R-parity violating SUSY, singlet seesaw models *e.g.* inverse seesaw, linear seesaw .

(3) Seesaw models with higher dimensional operator: The neutrino mass can be generated from the operators having dimensions larger than 5.

(4) The neutrino mass is generated radiatively (loop correction). In this case the additional suppression comes from loop calculation. *e.g.* Zee model[80], etc.

TeV scale physics can also be probed in the context of the left-right symmetric model in which the gauge group is extended to $SU(3)_c \otimes SU(2)_L \otimes SU(2)_R \otimes U(1)_{B-L}$. The MLRSM can lead to various observable consequences in colliders, LFV and $0\nu\beta\beta$, if the scale of parity restoration is in the TeV range. This leads to heavy gauge bosons and heavy neutrinos of mass TeV. To generate small neutrino masses, the Yukawa coupling needs to be small (10^{-6}), so that the light-heavy mixing is small unless specific textures are evoked [81]. Note that the canonical seesaw models require large light-heavy mixing to have any observable consequences in the above processes. However, in LR models even if this mixing small, the TeV scale RH sector can give significant contribution.

For a review on TeV scale models, see [82]. Below we discuss few such models

that are relevant for the work carried out in this thesis. We have already discussed the various features of the MLRSM in Section 2.6.

2.7.1 Singlet seesaw models

As already mentioned, in seesaw models motivated by GUT, the mass scale of the heavy fields is near the GUT scale $i.e \sim 10^{12} - 10^{14}$ GeV. One option to generate TeV scale seesaw is to add extra singlets with mass \sim TeV, as is done in inverse seesaw and linear seesaw models. Below its mass scale, the heavy fields get integrated out and give rise to dimension five operator similar to Type-I seesaw.

The Yukawa part of the most general Lagrangian involving extra singlet states can be written as

$$-\mathcal{L} = \bar{N}_R Y_\nu \tilde{\phi}^\dagger l_L + \bar{S} Y_S \tilde{\phi}^\dagger l_L + \bar{S} M_R N_R^c + \frac{1}{2} \bar{S} \mu S^c + \frac{1}{2} \bar{N}_R M_N N_R^c + \text{h.c.}, \quad (2.34)$$

where $l_L = (\nu_x, x)_L^\top$, $x = e, \mu, \tau$. Here l_L and N have lepton number +1, while S has lepton number -1. The terms with Y_S , M_N and μ are lepton number violating. When all these parameters vanish, lepton number symmetry is restored and hence the t'Hooft naturalness criterion [83] is satisfied.

The neutral fermion mass matrix from the above Lagrangian can be written as

$$\mathcal{M}_\nu = \begin{pmatrix} 0 & m_D^\top & m_S^\top \\ m_D & M_N & M_R^\top \\ m_S & M_R & \mu \end{pmatrix}, \quad (2.35)$$

in the (ν_L, N_R^c, S^c) basis. Here $m_D = y_\nu v / \sqrt{2}$ and $m_S = y_s v / \sqrt{2}$.

From the general singlet seesaw mass matrix one can obtain variants of the model by choosing some parameters to be zero which can be done with no loss of generality: like inverse seesaw model, linear seesaw model etc.

Type-I seesaw is a special case of singlet seesaw models and can be realized, if only Y_ν and M_N are non-zero. In Type-I seesaw also, heavy neutrino mass can be at TeV scale, for some specific structure of Yukawa matrix as already

mentioned.

2.7.1.1 Inverse seesaw model

In the inverse seesaw mechanism a small lepton number violating parameter μ is responsible for the smallness of the neutrino mass. If μ vanishes, lepton number conservation is restored. Hence a small value of μ satisfies t'Hooft naturalness criterion. The seesaw is called inverse seesaw, because in this case the smallness of neutrino mass is due to a small lepton number violating parameter in the numerator. In contrast, in conventional Type-I seesaw the smallness is explained through very high mass scale in the denominator. The mass matrix for inverse seesaw is given as

$$\mathcal{M}_\nu = \begin{pmatrix} 0 & m_D^\top & 0 \\ m_D & 0 & M_R^\top \\ 0 & M_R & \mu \end{pmatrix}, \quad (2.36)$$

in the (ν_L, N_R^c, S^c) basis. After block-diagonalization, light neutrino mass is given as

$$m_\nu = m_D (M_R^\top)^{-1} \mu (M_R)^{-1} m_D^\top. \quad (2.37)$$

We can make an order of magnitude estimate of the parameters in the inverse seesaw model to get $m_\nu \sim 0.1$ eV. Assuming typical value $m_D = 100$ GeV and $M_R = 1$ TeV, one needs $\mu \sim 10^{-8}$ GeV.

2.7.1.2 Linear seesaw model

In the linear seesaw models [84–86] one assumes m_S to be small and non-zero while the μ and the M_N terms are set to zero. This can be done since they contribute towards light neutrino mass in the sub-leading orders [87]. Since lepton number violating mass terms are set to zero, the heavy neutrinos are purely Dirac type. Then the mass matrix takes the form

$$\mathcal{M}_\nu = \begin{pmatrix} 0 & m_D^\top & m_S^\top \\ m_D & 0 & M_R^\top \\ m_S & M_R & 0 \end{pmatrix}, \quad (2.38)$$

in the (ν_L, N_R^c, S^c) basis. After block-diagonalization, light neutrino mass is given as

$$m_\nu = m_D^T M_R^{-1} m_S + m_S^T M_R^{-1} m_D. \quad (2.39)$$

In the linear seesaw the light neutrino mass is proportional to one power (linearly) of m_D and hence the nomenclature. In general, three singlets are needed to give 3 non-zero light neutrino masses. However, low energy phenomenology can be explained with only two light neutrinos to be massive, which can be achieved by adding just two singlets as in the minimal linear seesaw model (MLSM), discussed next. We can make an order of magnitude estimate of the parameters to get $m_\nu \sim 0.1$ eV, assuming typical value $m_D \sim 100$ GeV and $M_R \sim 1$ TeV, one needs $y_S \sim 10^{-11}$. Hence, smallness of the neutrino mass can be attributed to the tiny lepton number violating parameter y_S .

2.7.1.3 Minimal Linear Seesaw Model (MLSM)

The minimal model which can successfully generate two light neutrinos with non-zero mass is when only two extra heavy singlets are added to the SM Lagrangian. This is called the Minimal Linear Seesaw Model (MLSM) [88, 89]. This is a variant of the singlet seesaw model but in this case the minimal scheme consists of adding just two heavy singlets with opposite lepton number as opposed to four heavy neutrinos in canonical minimal inverse seesaw models [90]. It was shown in [88] that the Yukawa couplings matrices for this model can be fully reconstructed in terms of the oscillation parameters apart from an overall normalization factor. It was further shown in [89] that this normalization constant can be constrained from consideration of the meta-stability of the electroweak vacuum and lepton flavor violation bounds.

The full mass matrix has dimension 5×5 and can be written as ,

$$\mathcal{M}_\nu = \begin{pmatrix} 0 & m_D'^T \\ m_D' & M \end{pmatrix}, \quad (2.40)$$

where $m_D'^T = (m_D^T, m_S^T)$ and

$$M = \begin{pmatrix} 0 & M_R \\ M_R & 0 \end{pmatrix}. \quad (2.41)$$

For the minimal case M_R is just a number, not a matrix. \mathcal{M}_ν can be diagonalized by a 5×5 unitary matrix U_0 as

$$U_0^T \mathcal{M}_\nu U_0 = \mathcal{M}_\nu^{diag}, \quad (2.42)$$

where $\mathcal{M}_\nu^{diag} = \text{diag}(m_1, m_2, m_3, M_1, M_2)$. Following a two-step diagonalization procedure [60], U_0 can be expressed as,

$$U_0 = \begin{pmatrix} \left(1 - \frac{1}{2}\epsilon\right) U_\nu & m_D^\dagger (M^{-1})^* U_R \\ -M^{-1} m_D U_\nu & \left(1 - \frac{1}{2}\epsilon'\right) U_R \end{pmatrix} \equiv \begin{pmatrix} U_L & V \\ S & U_H \end{pmatrix}, \quad (2.43)$$

where, U_L is the U_{PMNS} mixing matrix, and V, S are the light-heavy mixing matrices. Interaction of heavy neutrinos with the SM fields are determined by the mixing matrix V , whose elements will be denoted as V_{lN} hereafter. We would notice afterwards that the strong constraints on some elements of this matrix *i.e.*, V_{eN} and $V_{\mu N}$ would restrict the production signal. The diagonalizing matrix is now non-unitary which is characterized by the factor $(1 - \epsilon/2)$. The non-unitary corrections ϵ and ϵ' are given, *e.g.* in [60, 91]. U_ν is the unitary component of U_{PMNS} which is same as U_{PMNS} for $\epsilon \ll 1$. We use the standard parametrization for U_{PMNS} as given in Eq. 1.4. The Majorana phase matrix P is expressed as $P = \text{diag}(e^{-i\alpha}, e^{i\alpha}, 1)$, there is only one Majorana phase because one of the mass eigenvalues is zero. In Table 1.2, we have presented the 3σ allowed ranges of oscillation parameters. Note that the phases are completely unconstrained at present.

Using the seesaw approximation one obtains the light neutrino mass matrix,

$$m_\nu = m_D'^T M^{-1} m_D'. \quad (2.44)$$

This being a rank 2 matrix the light neutrinos belonging to this model are hierarchical. After diagonalizing m_ν by U_{PMNS} , we get the light neutrino mass matrix in mass eigen-basis.

In the MLSM, Y_ν and Y_S are 3×1 matrices (*cf.* Eq. 2.34) and can be considered as two independent vectors [88]

$$Y_\nu \equiv y_\nu \hat{\mathbf{a}}; \quad Y_S \equiv y_s \hat{\mathbf{b}}, \quad (2.45)$$

where $\hat{\mathbf{a}}$ and $\hat{\mathbf{b}}$ denotes complex vectors with unit norm while y_ν and y_s represent the norms of the Yukawa matrices Y_ν and Y_S , respectively. Using Eq. 2.44 and 2.45 one can reconstruct the Yukawa matrices Y_ν and Y_S in terms of the oscillation parameters barring an overall normalization factor. The parametrization of the Yukawa matrices depend on the mass hierarchy and can be expressed as [88, 89],

$$\begin{aligned} Y_\nu &= \frac{y_\nu}{\sqrt{2}} \left(\sqrt{1+\rho} U_j^\dagger + e^{i\frac{\pi}{2}} \sqrt{1-\rho} U_k^\dagger \right), \\ Y_S &= \frac{y_s}{\sqrt{2}} \left(\sqrt{1+\rho} U_j^\dagger - e^{i\frac{\pi}{2}} \sqrt{1-\rho} U_k^\dagger \right), \end{aligned} \quad (2.46)$$

where, $j = 2, k = 3$ for NH and $j = 2, k = 1$ for IH. U_j 's denote the columns of the unitary matrix U_ν that diagonalizes the light neutrino mass matrix m_ν in Eq. 2.44. The parameter ρ is given as,

$$\rho = \frac{\sqrt{1+r} - \sqrt{r}}{\sqrt{1+r} + \sqrt{r}} \quad (NH), \quad \rho = \frac{\sqrt{1+r} - 1}{\sqrt{1+r} + 1} \quad (IH). \quad (2.47)$$

Here r denotes the ratio of the solar and atmospheric mass squared differences, $r = \Delta m_{sol}^2 / \Delta m_{atm}^2$, with $\Delta m_{sol}^2 \equiv m_2^2 - m_1^2$ and $\Delta m_{atm}^2 \simeq m_3^2 - m_1^2$ ($m_2^2 - m_3^2$) for NH (IH).

The overall coupling y_ν can be constrained from the metastability of the electroweak vacuum and LFV [89]. We have discussed these bounds in detail in Chapter 3.

2.7.2 Seesaw models with higher dimensional operator

One of the ways to generate neutrino mass via new physics at TeV scale is through higher dimensional operators [92–100]. These operators typically contain the factor $\sim \frac{v^2}{M}(\frac{v}{M})^{d-5}$ in the expression of neutrino mass. This implies the suppression factor M^{d-4} in the denominator, where d is the dimension of the operator. Consequently, the cutoff scale of new physics can be lowered to TeV without making the Yukawa couplings minuscule. Such operators can arise at tree as well as loop level and requires extension of the SM field content by new fermions and scalars belonging to higher representations of $SU(2)$. Since the scale of new physics in these models is at TeV, it is conceivable that these new particles can be produced and studied at the LHC.

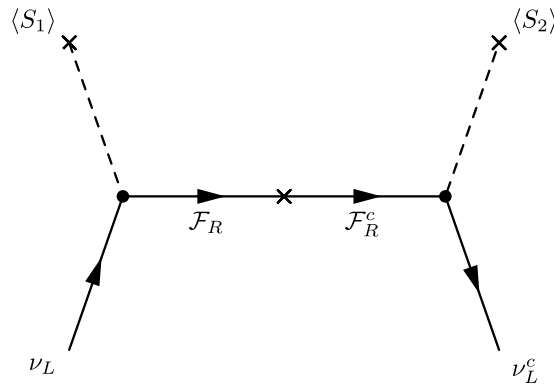


Figure 2.3: Generic tree-level diagram for generation of small neutrino mass from heavy fermion exchange when lepton-number symmetry is broken by the (Majorana) mass insertion. The simplest realizations are the Type-I and Type-III seesaws, with $\mathcal{F}_R \sim (1, 1, 0)$ and $\mathcal{F}_R \sim (1, 3, 0)$, respectively, and with $S_1 = S_2 = H \sim (1, 2, 1)$. Figure is adapted from Ref. [100]

Figs. 2.3 and 2.4 are generic diagrams representing Majorana and Dirac mass insertion in the propagator, respectively [100]. Various possibilities of higher dimensional ($d \geq 5$) models for neutrino mass generation are tabulated in Table 2.1 and Table 2.2. In the tables, minimal models refer to the models in which neutrino mass is generated by only one higher dimensional operator at tree level. Model (A) in Table 2.2 is the BNTM. The question marks in the tables indicate that those models are introduced for the first time in Ref. [100]. However, to

Model	S_1	\mathcal{F}_R	S_2	$[\mathcal{O}_\nu]$	Ref.
(a)	(1, 2, 1)	(1, 1, 0)	–	$d = 5$	Type-I seesaw
(b)	(1, 2, 1)	(1, 3, 0)	–	$d = 5$	Type-III seesaw
(c)	(1, 4, 1)	(1, 5, 0)	–	$d = 9$	[99]
(d)	(1, 2, 1)	(1, 3, 0)	(1, 4, 1)	$d = 5, 7, 9$	[101]
(e)	(1, 4, 1)	(1, 5, 0)	(1, 6, 1)	$d = 9, 11, 13$?

Table 2.1: Natural seesaw models with a Majorana mass insertion. The first three entries are minimal while last two entries are not; model (d)/(e) is essentially model (b)/(c) with an additional field. Table is taken from Ref. [100].

the best of our knowledge, no detailed studies have been performed so far.

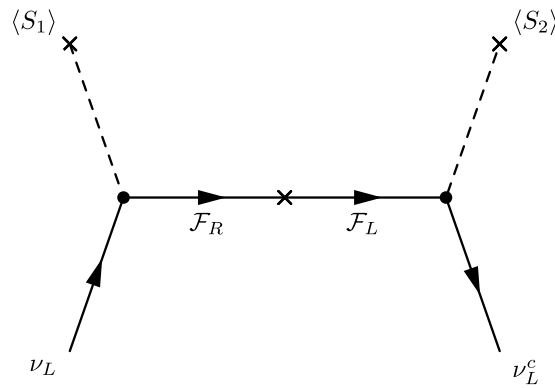


Figure 2.4: Generic tree-level diagram for generation of small neutrino mass for Dirac type mass insertion. In the simplest realization, one of the scalars is the SM doublet, $S_1 = H \sim (1, 2, 1)$, and the quantum numbers for the new fields are uniquely determined, with $\mathcal{F}_{L,R} \sim (1, 3, -2)$, and $S_2 \sim (1, 4, -3)$. Figure is adapted from Ref. [100]

Model	S_1	\mathcal{F}_R	S_2	$[\mathcal{O}_\nu]$	Ref.
(A)	(1, 2, 1)	(1, 3, -2)	(1, 4, -3)	$d = 7$	[93]
(B)	(1, 3, 0)	(1, 4, -1)	(1, 5, -2)	$d = 9$?
(C)	(1, 4, 1)	(1, 5, -2)	(1, 4, -3)	$d = 9$	[97]
(D)	(1, 6, 1)	(1, 5, -2)	(1, 4, -3)	$d = 11$?
(E)	(1, 4, 1)	(1, 5, -2)	(1, 6, -3)	$d = 11$?
(F)	(1, 4, 1)	(1, 3, -2)	(1, 4, -3)	$d = 7, 9$?

Table 2.2: Natural seesaw models with a Dirac mass insertion. The first five entries are minimal while last one is not; model (F) is essentially model (A) with an additional field. Model (A) is the BNTM. Table is taken from Ref. [100].

2.7.3 Babu-Nandi-Tavartkiladze Model (BNTM)

This model is an example of neutrino mass generation through higher dimensional operators. In this type of mass generation, suppression come from the higher power of the new physics mass scale.

In particular, BNTM was proposed in Ref. [93]. In this model neutrino mass is generated at the tree level through dimension-7 operator and at the loop level via dimension-5 operator. Charged lepton flavor violation in this model has been considered in [96]. The model contains a pair of vector-like triplet fermions with hypercharge of 2 units and a scalar with isospin 3/2.

2.7.3.1 The model

Prime aim of this model is to generate light neutrinos without making the Dirac Yukawa couplings minuscule and at the same time having the scale of new physics

at TeV. This requires introduction of exotic fermions and scalars, heavier than the SM fields. The gauge group of the model under consideration is the same as that of the SM: $G = SU(3)_c \otimes SU(2)_L \otimes U(1)_Y$ with an enlarged particle content that includes the following fields: an isospin 3/2 scalar

$$\Phi = \left(\begin{array}{cccc} \Phi^{+++} & \Phi^{++} & \Phi^+ & \Phi^0 \end{array} \right)_{Y=3}, \quad (2.48)$$

and a pair of vector-like fermion triplets³

$$\Sigma_{R,L} = \left(\begin{array}{ccc} \Sigma_{R,L}^{++} & \Sigma_{R,L}^+ & \Sigma_{R,L}^0 \end{array} \right)_{Y=2}. \quad (2.49)$$

Note that although the above fermionic representations have a non-zero hypercharge, the chiral anomaly gets canceled as they are vector-like by nature. The scalar kinetic and potential terms involving the field Φ read as

$$\mathcal{L}_{scalar} = (D^\mu \Phi)^\dagger (D_\mu \Phi) + (D^\mu H)^\dagger (D_\mu H) + V(H, \Phi), \quad (2.50)$$

where

$$D_\mu S = \left(\partial_\mu - ig\vec{T} \cdot \vec{W}_\mu - ig' \frac{Y}{2} B_\mu \right) S. \quad (2.51)$$

In the above expression S can be either H or Φ . The generators T_a 's are the Pauli matrices for H , whereas for Φ these are the $SU(2)$ generators in the isospin 3/2 representation, see Appendix A.1 for details. The interactions of the new scalar field Φ with the gauge bosons originate from the above term. The scalar potential is given as

$$\begin{aligned} V(H, \Phi) = & \mu_H^2 H^\dagger H + \mu_\Phi^2 \Phi^\dagger \Phi + \frac{\lambda_1}{2} (H^\dagger H)^2 + \frac{\lambda_2}{2} (\Phi^\dagger \Phi)^2 \\ & + \lambda_3 (H^\dagger H) (\Phi^\dagger \Phi) + \lambda_4 (H^\dagger \tau_a H) (\Phi^\dagger T_a \Phi) + \{\lambda_5 H^3 \Phi^* + h.c.\}. \end{aligned} \quad (2.52)$$

The electroweak symmetry is broken spontaneously once the Higgs acquires the vacuum expectation value (VEV), v . As the other scalar Φ is also non-singlet

³Scalar quadruplet and vector-like fermion triplet but with different hypercharges are studied in the literature, see for instance, Ref. [101, 102].

under $SU(2)_L \otimes U(1)_Y$, the VEV of Φ , *i.e.*, v_Φ can also be responsible for this breaking and affects the ρ parameter of the SM. Thus, v_Φ gets constrained from the ρ parameter which gets modified as $\rho \approx (1 - 6v_\Phi^2/v^2)$. In order to satisfy the 3σ range of this parameter $\rho = 1.0004_{\pm 0.0009}^{-0.0012}$ [103], v_Φ must be less than 2.01 GeV. Minimization of potential in Eq. 2.52 leads to the induced VEV $v_\Phi = -\lambda_5 \frac{v^3}{M_{\Phi^0}^2}$, where $v = \sqrt{\frac{-\mu_H^2}{\lambda_1}}$ is VEV of the SM Higgs. The mass of the neutral scalar Φ^0 comes out to be

$$M_{\Phi^0}^2 = \mu_\Phi^2 + \lambda_3 v^2 + \frac{3}{4} \lambda_4 v^2. \quad (2.53)$$

The mass of i^{th} component of the quadruplet field Φ with absolute value of electric charge q_i can be expressed as⁴

$$M_{\Phi^i}^2 = M_{\Phi^0}^2 - q_i \frac{\lambda_4}{2} v^2 = M_{\Phi^0}^2 - q_i \Delta M^2. \quad (2.54)$$

ΔM^2 denotes the difference of squared masses between any two successive components in the scalar quadruplet.

Note that the mass degeneracy between the members of heavy scalar are lifted by the λ_4 coupling once the symmetry is broken. Choice of this free coupling within the perturbative limit can produce successive scalar states from a near degenerate to a mass difference of as large as few tens of GeV. Depending on the *sign* of λ_4 , we get two hierarchies in masses of the Φ field⁵:

$$\begin{aligned} M_{\Phi^0} > M_{\Phi^\pm} > M_{\Phi^{\pm\pm}} > M_{\Phi^{\pm\pm\pm}} & \text{for positive sign of } \lambda_4 \text{ and } \Delta M - \text{ve}, \\ M_{\Phi^{\pm\pm\pm}} > M_{\Phi^{\pm\pm}} > M_{\Phi^\pm} > M_{\Phi^0} & \text{for negative sign of } \lambda_4 \text{ and } \Delta M + \text{ve}, \end{aligned} \quad (2.55)$$

where the mass difference between two successive members is constrained as $1.4 \text{ GeV} < |\Delta M| < 38 \text{ GeV}$. The lower bound comes from precision electroweak

⁴Note that we get the splitting parameter (ΔM^2) as $\frac{\lambda_4}{2} v^2$ instead of $\frac{\lambda_4}{4} v^2$ in Ref. [93].

⁵One can find that both choices of λ_4 (positive and negative) are compatible from the boundedness of the scalar potential since this scalar coupling need not be positive definite for the stability of the scalar potential. This can be perceived easily by neglecting the λ_5 term from the potential. Note that λ_5 is required to be very small to generate correct order of light neutrino masses (*cf.* Eq. 2.59).

corrections [104] and the upper bound is for compliance with the ρ parameter bound [105]. The physical scalar spectrum in this model consists of one triply-charged scalar, one doubly and one singly charged scalars (all with their charge conjugated counterparts) as well as three neutral scalars (two CP even and one CP odd).

2.7.3.2 Generation of neutrino masses

In this model the neutrino mass (m_ν) comes from the renormalizable Lagrangian

$$\mathcal{L}_{m_\nu} = Y_i \overline{l_{iL}^C} H^* \Sigma_L + Y'_i \overline{\Sigma_R} \Phi l_{iL} + \overline{\Sigma_R} M_\Sigma \Sigma_L + h.c., \quad (2.56)$$

where Y_i , Y'_i are Yukawa coupling matrices and i is generation index. The detailed structure of the Yukawa interactions are given in Appendix A.2. From the Lagrangian (2.56) the neutral lepton mass matrix can be written in the $(\nu_L, \Sigma_L^0, (\Sigma_R^0)^C)$ basis as

$$M_0 = \begin{pmatrix} 0 & m & m'^T \\ m^T & 0 & M_\Sigma \\ m' & M_\Sigma & 0 \end{pmatrix}. \quad (2.57)$$

In terms of the Yukawa couplings, $m = -Yv$ and $m'^T = Y'v_\Phi$. Here m and m'^T are 3×1 matrices, while the $(1, 1)$ element of the matrix M_0 is the 3×3 null matrix.

Since we have introduced a vector-like fermion pair, the above mass matrix is 5×5 and is of rank 4 with determinant zero. Therefore, out of five fields one will have zero mass. Thus, the neutral fermion spectrum consists of two nearly degenerate heavy neutrinos, one massless neutrino as well as two massive light neutrinos. With these two light neutrinos the model satisfies the neutrino oscillation data for hierarchical neutrinos. However, as also noted in Ref. [93] one can extend this model by adding more pairs of fermions to get all the light neutrinos to be massive. This will of course increase the number of unknown parameters in the model.

This model contains $SU(2)$ triplet fermions as in the Type-III seesaw model. However, here they have a hypercharge $Y = 2$, whereas the Type-III seesaw model contains triplet fermion with $Y = 0$. These two models are different in the way neutrino masses are being generated and lepton number is being violated. In general, the presence of light Majorana neutrinos demands lepton number violation by two units, *i.e.*, $\Delta L = 2$. In conventional Type-III seesaw mechanism, the triplet fermions which are being integrated out during the seesaw process have Majorana mass term and the violation of lepton number is directly reflected from the mass insertion in the propagator. But in this case the triplet fermions have $Y = 2$ and have Dirac type mass term. However, lepton number violation can come from the $\bar{\Sigma}\Phi l$ term in the Lagrangian if we assign a lepton number of +1 to the l field and -1 to the vector-like Σ_L and Σ_R fields⁶.

v_Φ (GeV)	y	y'	m_ν (eV)
5×10^{-6}	10^{-1}	10^{-3}	0.05
5.1×10^{-5}	10^{-1}	10^{-4}	0.05
4.3×10^{-5}	10^{-1}	10^{-4}	0.04
0.5	10^{-3}	10^{-6}	0.04

Table 2.3: Order of neutrino mass for $v = 174$ GeV, $M_\Sigma = 3500$ GeV, $M_{\Phi^0} = 400$ GeV.

Note that with the above assignment of lepton number the matrix in Eq. 2.57 has the form of the linear seesaw mass matrix [84, 86, 106]. Naturally small neutrino masses can be generated in this model assuming small lepton number violation.

The above matrix can be diagonalized in the limit $M_\Sigma \gg m, m'$ to generate the light neutrino mass matrix m_ν using the seesaw approximation. To the leading order this can be expressed as,

$$m_\nu = -m \frac{1}{M_\Sigma} m' - m'^T \frac{1}{M_\Sigma} m^T. \quad (2.58)$$

⁶It is also possible to assign lepton number +1 to the Σ_L and Σ_R fields, in which case lepton number will be violated at the $\bar{l}^C H^* \Sigma$ vertex.

Then the expression for m_ν can be written as,

$$(m_\nu)_{ij} = \frac{(Y_i Y'_j + Y'_i Y_j) v_\Phi v}{M_\Sigma} = -\frac{\lambda_5 (Y_i Y'_j + Y'_i Y_j) v^4}{(M_\Sigma M_{\Phi^0}^2)}. \quad (2.59)$$

Overall coupling strengths of the Yukawa matrices Y and Y' are denoted as y and y' , respectively. Note that the neutrino mass goes to zero in the limit the lepton number violating coupling y' goes to zero. Thus, a naturally small neutrino mass can be generated assuming small lepton number violation. Along with the lepton number violation it is also possible to have lepton flavor violation in this model. This is reflected in the effective vertex $(\Phi \ell \ell)$, as shown in Appendix A.4.

In our analysis we consider v_Φ and M_{Φ^0} to be independent parameters with $\lambda_5 < 0$. In Table 2.3 we present the typical values of v_Φ used in our analysis and the corresponding values of y and y' in order to generate correct order of magnitude for the neutrino mass for the representative values of M_{Φ^0} and M_Σ .

2.7.3.3 Origin of neutrino mass

The tree level diagram from which the neutrino mass originates is given in Fig. 2.5(left panel). After integrating out heavy fermion fields Σ , $\bar{\Sigma}$ and scalar field Φ , this diagram gives rise to a dimension-7 effective Lagrangian

$$\mathcal{L}_\kappa = -\kappa_{ij} \left(\bar{l}_{La}^i H_{a'} l_{Lg'}^j H^b H_b H_g \right) \varepsilon_{aa'} \varepsilon_{gg'} + \text{h.c.} \quad , \quad (2.60)$$

where

$$\kappa_{ij} = -\frac{(Y_i Y'_j + Y'_i Y_j) \lambda_5}{M_\Sigma M_{\Phi^0}^2}, \quad (2.61)$$

which after spontaneous symmetry breaking generates the neutrino mass given in Eq. 2.59. The details of the calculation for obtaining Eq. 2.61 are given in Appendix A.3.

It is interesting to note that the dominant contribution for neutrino mass is obtained from the dimension-7 operator at the tree level. This is ensured by the absence of singlet fermions, $Y = 0$ triplet fermions and triplet scalars in the model. However, dimension-5 operator can arise at the 1-loop level through

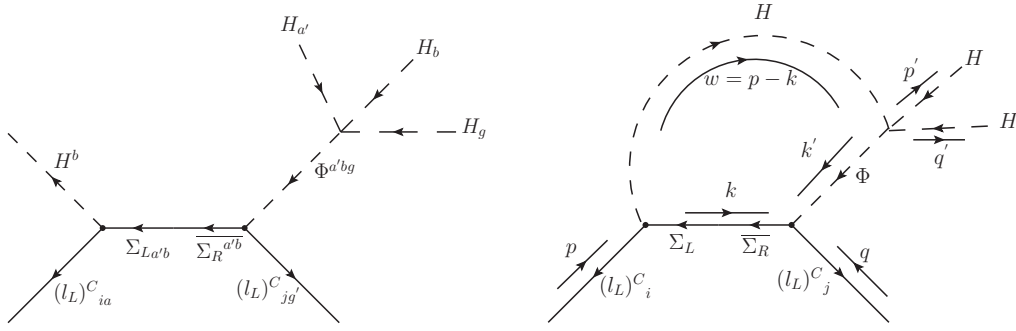


Figure 2.5: Tree level diagram (left panel) generating dimension-7 seesaw operator and 1-loop diagram (right panel) generating dimension-5 operator for neutrino masses.

diagram depicted in the right panel of Fig. 2.5. One can redefine the λ_5 coupling to account for the loop contribution to the neutrino mass in the parameter range for which it is significant.

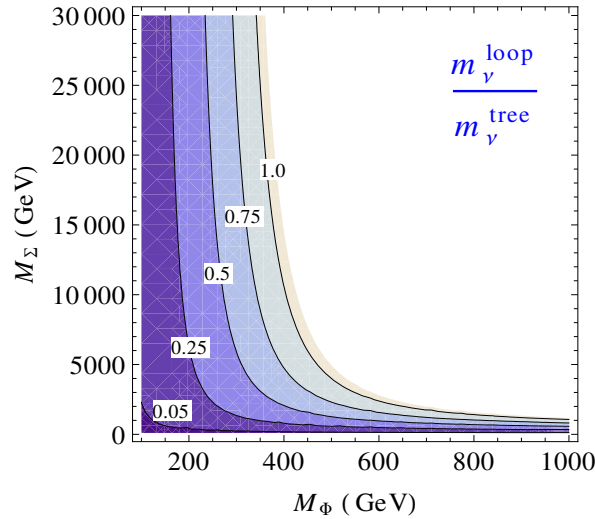


Figure 2.6: Contour plot of the ratio $m_\nu^{\text{loop}}/m_\nu^{\text{tree}}$ in the $(M_\Phi - M_\Sigma)$ plane.

Including the above diagram the total contribution to m_ν becomes $m_\nu^{\text{total}} = m_\nu^{\text{tree}} + m_\nu^{\text{loop}}$, where m_ν^{tree} is given by Eq. 2.59. The loop contribution to the

neutrino mass, m_ν^{loop} , can be computed as

$$(m_\nu)_{ij}^{loop} = \frac{(3 + \sqrt{3}) \lambda_5 v^2 M_\Sigma (Y_i Y'_j + Y'_i Y_j)}{16\pi^2 (M_\Phi^2 - M_H^2)} \left(\frac{M_\Phi^2 \log\left(\frac{M_\Sigma^2}{M_\Phi^2}\right)}{M_\Sigma^2 - M_\Phi^2} - \frac{M_H^2 \log\left(\frac{M_\Sigma^2}{M_H^2}\right)}{M_\Sigma^2 - M_H^2} \right), \quad (2.62)$$

where M_H is mass of the SM Higgs.

Note that only Φ^0 and Φ^+ will contribute to the loop diagrams in Fig. 2.5. In deriving Eq. 2.62 we have assumed that these two states are degenerate with mass M_Φ .

In Fig. 2.6 we make a contour plot of the ratio $m_\nu^{loop}/m_\nu^{tree}$ in the $(M_\Phi - M_\Sigma)$ plane. From the plot it is clear that for smaller values of M_Φ and M_Σ , the dimension-7 contribution dominates over that coming from the dimension-5 term. This is the region relevant for our study and thus it suffices to take only the tree level contribution.

Chapter 3

Probing neutrino mass models at colliders

In the previous chapter, we have discussed various neutrino mass models which can have the scale of new physics at TeV and also allow a sizable production of particles with masses of TeV order.

In this chapter, we carry out a detailed study of collider signatures of three models: (i) the Babu-Nandi-Tavartkiladze-model (BNTM), (ii) the minimal linear seesaw model (MLSM) and (iii) the minimal Left-Right symmetric model (MLRSM). The basic features of the models are discussed in the previous chapter.

The main theme of this chapter is to examine the imprint of the seesaw mechanism at colliders. In this context, we mainly focus on the multilepton signatures at colliders which are hallmarks of the seesaw mechanism. The important signals are those comprising of light leptons (e, μ), as they can be found efficiently in the detectors. Leptonic SM processes are rare at hadron colliders and events with higher lepton multiplicity particularly so. Therefore, it is interesting to look for BSM signals with higher lepton multiplicity. Note that one of the channels in which the Higgs boson was discovered is the four-lepton channel $H \rightarrow ZZ^* \rightarrow 4\ell$ [107–109]. If neutrinos are Majorana particles, then there exist the possibility of same-sign-dilepton (SSDL) as was noticed in [110] in the context of LR symmetric models. In the context of TeV scale seesaw models this signal has been

studied, for instance, in Ref. [111–113]. SSDL are relatively background-free if the selection criteria are properly chosen. Experimental searches for SSDL, in particular constraining SUSY models are done in [114–117] and in the context of the LRSM in [74, 75]. If we have Higgs of higher charges in any model *e.g.* as in [93, 118] or R-parity violating supersymmetry [119], then same-sign-trilepton signal is also possible. Same-sign tri-lepton background from the SM is very tiny, and, therefore, this signal is important to look for BSM physics at the LHC. Same-sign tri-lepton, tri-lepton and four-lepton signals in the context of supersymmetric models are considered in Ref. [119–123]. Experimental searches for multilepton signals, in particular for supersymmetric models, are done by the CMS and the ATLAS collaborations [114, 124–129]. If the heavy neutrinos are Dirac particles then, their decays lead to the opposite-sign dilepton signal, and if the W -boson is allowed to decay leptonically then the signal is tri-lepton with missing energy due to the missing neutrino.

Another channel in which new physics can contribute is the decay of the Higgs boson to gamma gamma (2 photons). Since the photon has no mass, it does not couple to the Higgs boson directly. However, decay of the SM Higgs boson to diphoton can be modified by contributions of the BSM particles at the loop level. Particles which couple to the neutral Higgs boson and the photon, can contribute to the decay. Hence, only electrically charged particles can contribute as they couple to the photon. $H \rightarrow \gamma\gamma$ decay mode can be seen cleanly by the experiments, and it was one of the main Higgs discovery channels at the LHC [2, 3]. Initially $H \rightarrow \gamma\gamma$ decay branching ratio was away from the SM prediction. However, with more data there is a trend of converging towards the SM value. Initial experimental observations of the Higgs to diphoton decay normalized to the SM prediction, as pointed out by ATLAS [130] and CMS [131] were,

$$R_{\gamma\gamma} = 1.65 \pm 0.24(stat)_{-0.18}^{+0.25}(syst) \text{ (ATLAS)}, \quad (3.1)$$

$$R_{\gamma\gamma} = 0.78_{-0.26}^{+0.28} \text{ (CMS)}. \quad (3.2)$$

Recent observations for ATLAS [132] and CMS [133] are

$$R_{\gamma\gamma} = 1.17 \pm 0.27 \text{ (ATLAS)} , \quad (3.3)$$

$$R_{\gamma\gamma} = 1.14_{-0.23}^{+0.26} \text{ (CMS)} . \quad (3.4)$$

Thus, the central values are now closer to the SM value.

In this chapter, we have considered the s-channel production of the BSM particles, in which quarks from the two colliding protons produce them via s-channel propagator. In some of the cases, we have also considered Weak vector boson fusion (VBF) production of the particles. Weak VBF processes have been suggested quite some time ago in the context of Higgs searches [134–136]. They are characterized by the presence of two jets with large transverse momentum (p_T) in the forward region in opposite hemispheres along with other observables, like charged leptons. Interestingly LHC has a very rich “forward physics” program and for the necessary investigation there are dedicated detectors like LHCf [137] and(or) FP420 [138]. Due to uncertainties in the jet tagging, the efficiency is relatively low and, thus, the significance of these channels is rather suppressed. But nevertheless from the discovery perspective, many Beyond Standard Models can also be tested using forward jets. Such related studies are also important for dark matter searches through mono-jet plus missing energy [139–141].

The plan of the chapter is as follows. In the next section we discuss the various packages used for simulating signal and background events. For selecting multilepton events, we impose some selection criteria which suppress the SM background. These selection criteria are also discussed in the next section. Then we discuss the collider signatures of three specific models.

- ◇ In Section 3.2 we discuss the multilepton signature of Babu-Nandi-Tavartkiladze-model (BNTM) at the LHC and estimate the backgrounds from the SM. The result on the charged scalar contribution to $H \rightarrow \gamma\gamma$ channel is also presented. Then we summarize the study of the BNTM.

- ◇ In Section 3.3 we discuss the MLSM. In this analysis, first we discuss the LFV and the electroweak vacuum stability constraints. Then we study multilepton collider signatures of heavy neutrinos in this model for some benchmark points compatible with the constraints. In particular, we have looked for tri-lepton signature for both the cases of heavy neutrino production *i.e.* s-channel and VBF processes. Then we have calculated the significance of these signatures and summarized the study of this model.
- ◇ In the next section we discuss the minimal Left-Right symmetric model (MLRSM). After discussing the MLRSM briefly, we discuss the experimental and theoretical constraints on the masses of the new particles. Then we have discussed the allowed spectra for the charged Higgs bosons in the MLRSM that satisfy these constraints. In the next part, the collider signatures of charged scalars, when there is at least one doubly charged scalar is present, are discussed. In particular, tri-lepton and four-lepton signatures are studied. We have used dilepton invariant mass and lepton-lepton separation distributions for the same-sign dilepton (SSDL) and the opposite-sign dilepton (OSDL) to distinguish the origin of SSDL. We have also calculated the charged scalar contribution to the Higgs boson decay to diphoton. In addition, we study the four-lepton signature from the VBF production of a pair of doubly charged scalars at the LHC and future colliders. Then we summarize the study of the MLRSM.

3.1 Simulations and event selection

In this section, we give a general description of simulating events at colliders. First, model files are generated from packages like FeynRules. Then we implement model files in CalcHEP [142] or MadGraph [143]. Our signal and background processes, constructed out of parton level calculation of hard-scattering matrix elements, and relevant decay branching ratios are computed. To perform the full analysis, the “Les Houches Accord” (LHA) event file [144] generated through CalcHEP/MadGraph/ALPGEN is fed into PYTHIA [145]. PYTHIA

includes initial/final state radiations (ISR/FSR) from QED and QCD, parton showering, multiparton interactions and hadronization for a realistic estimate from simulation. For our analysis, we have used parton distribution function (PDF), CTEQ6L1 [146] from LHAPDF library [147]. We have chosen the default factorization (μ_F) and renormalization (μ_R) scales as set by PYTHIA unless otherwise mentioned.

Cuts used for the analysis	Values
Maximum pseudorapidity ($ \eta_\ell $) of a lepton	2.5
Minimum p_T of an isolated lepton	10 GeV
Detector efficiency for detecting electron (e^\pm)	0.7 (70%)
Detector efficiency for detecting muon (μ^\pm)	0.9 (90%)
Lepton-lepton separation ($\Delta R_{\ell\ell}$)	≥ 0.2
Lepton-photon separation ($\Delta R_{\ell\gamma}$)	≥ 0.2
Minimum hard p_T cuts on p_T -ordered leptons	(30,30,20,20,10,10) GeV
Missing transverse momentum	≥ 30 GeV (for $n\ell, SS3\ell$) < 30 GeV (for $FV4\ell$)
Lepton separated from reconstructed jet ($\Delta R_{\ell j}$)	≥ 0.4
Hadronic Activity around leptons $\frac{\sum p_{T,hadron}}{p_{T,\ell}}$	≤ 0.2
Electron energy smearing and muon p_T resolution	\checkmark
Z veto	$ m_{\ell\ell} - M_Z \geq 6\Gamma_Z$ GeV

Table 3.1: The cuts used to estimate SM backgrounds and signal events. For complete set of selection criteria, see the text.

The event selection criteria are described below [148–150]:

I. *Lepton Identification:*

- Electrons and muons are identified within the pseudorapidity $|\eta_\ell| \leq 2.5$.
- Each of the leptons is considered to have a minimum transverse momentum of 10 GeV, *i.e.* $p_{T,\ell} \geq 10$ GeV.

II. *Lepton Efficiency:*

- Detector efficiency for detecting an isolated electron (muon) is taken as 70% (90%).

III. *Lepton Isolation:*

- Two leptons are separately identified once they have a minimum separation of $\Delta R_{\ell\ell} \geq 0.2$, where $\Delta R_{\ell\ell} = \sqrt{\Delta\eta^2 + \Delta\phi^2}$ is the distance in pseudorapidity(η)-azimuth(ϕ) plane.
- Leptons are separated from photons if $\Delta R_{\ell\gamma} \geq 0.2$ with all the photons having $p_{T,\gamma} > 10$ GeV.
- A lepton is separately identified from all reconstructed *jets* with a minimum separation of $\Delta R_{\ell j} \geq 0.4$.
- Isolation cuts around the hard lepton(s) should control hadronic activity. However, cleaner identification of lepton requires hadronic activity $\frac{\sum p_{T,hadron}}{p_{T,\ell}} \leq 0.2$ around the lepton within the cone of size 0.2.

IV. *Hard Cuts:*

- *Hard p_T Cuts:* In a multilepton event, we demand that the first two hardest leptons should have a minimum transverse momentum of 30 GeV, while that for 3rd and 4th hardest leptons are 20 GeV each. Any additional lepton is identified with minimum transverse momentum of 10 GeV.
- *Missing Transverse Momentum:* We demand our multilepton events with minimum 30 GeV of missing transverse momentum $|\vec{P}_T|$ (except in the special cases of flavor violating four-lepton ($FV4\ell$) in the BNTM and the 4ℓ signal of the MLRSM). Total missing transverse momentum $\vec{P}_T = -\sum_{i=1}^{N_{obj}} \vec{P}_{T_i}$ is constructed from all reconstructed isolated objects (N_{obj}) such as leptons and *jets*.

Along with the above-mentioned selection criteria we have also implemented the followings in our analysis [148, 149] :

- The energy of electrons and p_T of muons (μ) are smeared according to the calorimeter resolutions.

- * *Electron Energy Smearing*: We consider the smearing of the electron energy E as follows:

$$\sigma(E)/E = \frac{a_1}{\sqrt{E}} \oplus a_2 \oplus \frac{a_3}{E},$$

where

$ \eta $	$a_1 \sqrt{\text{GeV}}$	a_2	a_3 (GeV)
< 1.5	0.030	0.005	0.200
> 1.5	0.055	0.005	0.600

- * *Muon p_T Resolution*: Muon p_T resolution is defined as

$$\sigma(p_T)/p_T = \begin{cases} b_1 & p_T \leq 100 \text{ GeV} \\ b_1 + b_2 \log(p_T/100), & p_T \geq 100 \text{ GeV}. \end{cases} \quad (3.5)$$

where,

$ \eta $	b_1	b_2
< 1.5	0.008	0.037
< 2.5 and > 1.5	0.020	0.050

- The *jets* are constructed using PYCELL, cone algorithm within PYTHIA. To find cluster, fixed detector grid of (100×72) assumed in (η, ϕ) plane with pseudo-rapidity $|\eta| < 2.5$. With minimum threshold for *jet* initiator p_T as 1.5 GeV, a cluster can be accepted as *jet* if minimum summed E_T is 20 GeV within cone size 0.7. To include energy resolution of detector, energy of each cell is also smeared.
- Z veto is implemented to reduce the SM background coming from the processes like $t\bar{t}(Z/\gamma^*)$, $W(Z/\gamma^*)$, $(Z/\gamma^*)(Z/\gamma^*)$. Opposite-sign but same-flavored lepton pair invariant mass $m_{\ell\ell}$ must be sufficiently away from Z mass, such that $|m_{\ell\ell} - M_Z| \geq 6\Gamma_Z$ GeV, where Γ_Z is the total decay width of the Z boson. However, signals remain mostly unaffected by this cut.

We have tabulated above-mentioned selection criteria in a compact form in Table 3.1. These cuts define the general framework for our numerical study. If

in a particular context we use different criteria, then that will be mentioned at the appropriate place.

3.2 Babu-Nandi-Tavartkiladze-model (BNTM)

This model provides an avenue to test the mechanism of neutrino mass generation at the LHC. The presence of the isospin 3/2 scalar multiplet Φ , especially the triply- and doubly-charged scalars can give rise to rich phenomenology at the LHC. Specifically, the cascade decays of these heavy charged scalars lead to multilepton final states. In this section, we discuss in detail the production and decay modes of these scalar fields and possible signals at the LHC.

The model has already been discussed in detail in the previous chapter. Here we focus on the collider phenomenology of the model.

3.2.1 Production and decay of isospin 3/2 Scalar

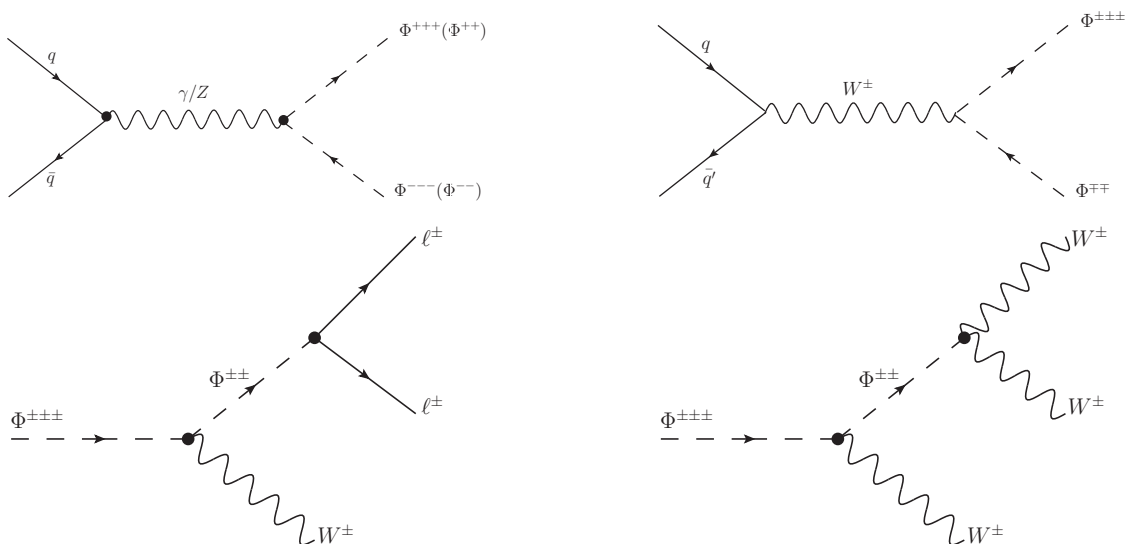


Figure 3.1: Representative diagrams for production and decay of doubly- and triply-charged scalars at hadron collider leading to multilepton (≥ 3) final states.

The heavy scalars are produced in pair through electroweak gauge bosons at

Large Hadron Collider through the following processes¹:

$$\begin{aligned}
 pp & \xrightarrow{Z/\gamma} \Phi^{\pm\pm\pm}\Phi^{\mp\mp\mp}, \Phi^{\pm\pm}\Phi^{\mp\mp}, \Phi^{\pm}\Phi^{\mp}; \\
 pp & \xrightarrow{W^{\pm}} \Phi^{\pm\pm\pm}\Phi^{\mp\mp}, \Phi^{\pm\pm}\Phi^{\mp}, \Phi^{\pm}\Phi^0.
 \end{aligned}
 \tag{3.6}$$

The parton level (lowest-order) representative diagrams contributing to these processes at the LHC are shown in the upper row of Fig. 3.1.

Fig. 3.2(a) shows the production cross sections of the charged scalars at the LHC for a center of mass energy $\sqrt{s} = 14$ TeV as a function of the scalar mass parameter M_{Φ^0} . We consider the triply- and doubly-charged scalars which are expected to give dominant contribution for the multilepton signals that we have studied. We have calculated our hard-scattering matrix elements for parton level processes by implementing the model in CalcHEP (version 3.2) [142].

The doubly charged scalar $\Phi^{\pm\pm}$ can dominantly decay into two W -bosons of the same charge. However, another dominant and, in fact, a remarkable decay channel can be realized from dimension-7 seesaw operator generating the neutrino mass. This effective vertex, discussed in Appendix A.4, is proportional to neutrino mass matrix elements ($m_{\nu_{ij}}$) and $\Phi^{\pm\pm}$ couples to lepton pair ($\ell_i\ell_j$) of same charge leading to lepton number violation. Since this vertex depends on the neutrino mass matrix elements, one expects relative differences in the signals for normal and inverted neutrino mass hierarchies.

Interplay of these two decay processes controls the significance of the observed lepton signal as we will demonstrate later. The triply-charged scalars $\Phi^{\pm\pm\pm}$ can decay into doubly charged scalars $\Phi^{\pm\pm}$ associated with W -boson apart from other 3-body modes which are suppressed. However, narrow mass difference between charged scalars as discussed in Section 2.7.3.1, typically produces off-shell $\Phi^{\pm\pm}$ which can decay further². The lower row of Fig. 3.1 demonstrates these decay modes of the triply-charged scalars. The final decay products (ℓW or WWW) are determined by the corresponding decay channels of the $\Phi^{\pm\pm}$. Decay branching

¹Note that $\Phi^0\Phi^0$ production is absent due to the lack of coupling between gauge bosons and pair of neutral scalars.

²At this point we note that a significant number of $\Phi^{\pm\pm}$ are produced off-shell and thus $M_{\Phi^{\pm\pm}}$ cannot be reconstructed from the same-sign-dilepton invariant mass.

ratios are calculated considering all the three charged leptons (e, μ, τ) and thus dominant decay modes are denoted by the symbol $\mathbb{1}$. On the other hand, ℓ stands for the two light charged leptons (e and μ) which only are considered in estimating the multilepton signals at the LHC. All necessary Feynman rules used in these calculations are listed in Appendix A.5.

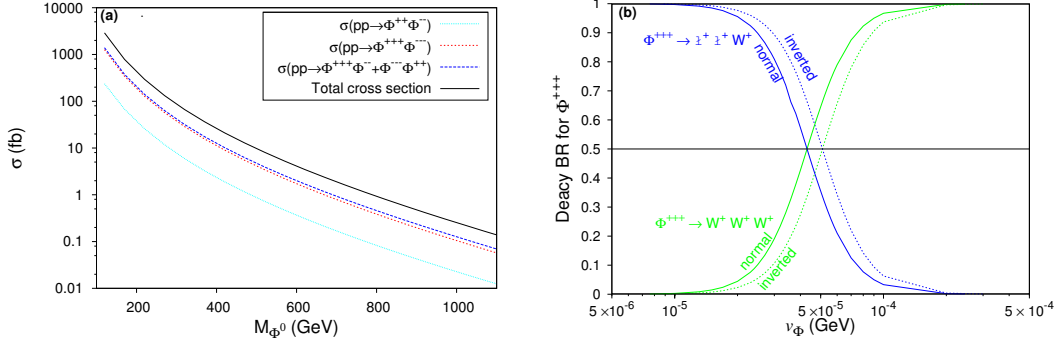


Figure 3.2: Figure (a): Production cross sections for the processes $pp \rightarrow \Phi^{+++}\Phi^{---}, \Phi^{++}\Phi^{--}, \Phi^{\pm\pm\pm}\Phi^{\mp\mp}$ at the LHC with $\sqrt{s}=14$ TeV and $\Delta M = -2.8$ GeV. Figure (b): Dependence of decay Branching Ratio (BR) of $\Phi^{\pm\pm\pm}$ on ν_Φ for IH and NH. Here $\mathbb{1}$ implies all three charged leptons (e, μ, τ).

Figure 3.2(b) demonstrates the decay Branching Ratios (BRs) of the triply-charged scalars in different modes for both neutrino mass hierarchies NH and IH. This plot is generated considering neutral scalar mass $M_{\Phi^0} = 400$ GeV together with mass difference between two successive scalars $\Delta M = (M_{\Phi^{\pm\pm\pm}} - M_{\Phi^{\pm\pm}}) = -2.8$ GeV³. This figure reflects how the interplay of the two decay channels of $\Phi^{\pm\pm}$, for different choices of ν_Φ , affects the BRs of $\Phi^{\pm\pm\pm}$. Note that the BRs of $\Phi^{\pm\pm\pm}$ closely follow that of $\Phi^{\pm\pm}$ excepting for an *offsetting factor due to off-shell phase-space* production in the decay of the former. From this figure three clear limits emerge:

- ◇ For small ν_Φ ($\lesssim 10^{-6}$ GeV), $\Phi^{\pm\pm\pm}$ mostly decays into $\mathbb{1}W$ with BR nearly equal to one for both NH and IH.
- ◇ On the other hand, in the larger ν_Φ region ($\gtrsim 10^{-4}$ GeV), $\Phi^{\pm\pm\pm}$ mostly de-

³Since members of Φ are allowed to have a small mass splitting, mass hierarchies among them, depending upon the *sign* of λ_4 , would have little impact on production and phenomenological signatures. So our choice of ΔM is representative by nature.

cays into $3W$ since large values of v_Φ suppress the lepton number violating effective coupling.

- ◇ For intermediate values of v_Φ , both channels can govern the decay. However, the exact values of the branching ratios depend on the neutrino mass hierarchies.

The above observations dictate the choice of the benchmark points in our study which are listed in Table 3.2. It can be noted that for lower values of M_Φ and intermediate ranges of $v_\Phi \sim \mathcal{O}(10^{-5} - 10^{-4})$ total decay width of charged scalar can be sufficiently low to show displaced vertex at the detector. This can lead to non-pointing multilepton signals, although we are not considering such scenarios in our analysis.

Neutrino hierarchy	Dominant $\Phi^{\pm\pm\pm}$ decay modes	Choice of v_Φ (GeV)
IH	HW	5×10^{-6}
	$\text{HW} - WWW$	5.1×10^{-5}
	WWW	0.5
NH	HW	5×10^{-6}
	$\text{HW} - WWW$	4.3×10^{-5}
	WWW	0.5

Table 3.2: Choice of parameter v_Φ for $M_{\Phi_0} = 400$ GeV and $\Delta M = -2.8$ GeV. Here H denotes all the three charged leptons (e, μ, τ).

3.2.1.1 Signatures of new physics

The pair productions and subsequent decays of the charged scalars followed by W^\pm decay lead to different leptonic final states. We have considered the following signatures of new physics:

- ◇ Multilepton events – 3ℓ , 4ℓ , 5ℓ and 6ℓ events,
- ◇ Same-sign-tri-lepton events ($\text{SS}3\ell$),
- ◇ LFV four-lepton events.

Here ℓ implies only the first two generations of charged leptons (e, μ). Specially important in this respect is the same-sign-tri-lepton signature which has very small background coming from the SM.

This model also accommodates spectacular lepton flavor violating decays of the charged scalars. These LFV signals can be originated from on-shell and/or off-shell leptonic decays of $\Phi^{\pm\pm}$. Of particular importance are the LFV four-lepton signal. In our study, we consider two kinds of signals $\ell_i^+ \ell_i^+ \ell_j^- \ell_j^-$ or $\ell_i^\pm \ell_j^\pm \ell_j^\mp \ell_j^\mp$ ($\ell_i \neq \ell_j = e, \mu$). The first one depends on diagonal terms of the light neutrino mass matrix, m_ν . The other final state is governed by both diagonal and off-diagonal elements of m_ν . These LFV signals are not accompanied by any missing neutrino, and therefore, are expected to be free from SM background.

3.2.1.2 Background estimation

processes	3ℓ (fb)	$\ell^+ \ell^+ \ell^-$ (fb)	$\ell^- \ell^- \ell^+$ (fb)	4ℓ (fb)	SS3 ℓ (fb)
$t\bar{t}$	18.973	9.522	9.451	–	–
$t\bar{t}(Z/\gamma^*)$	1.103	0.549	0.554	0.069	7.066×10^{-4}
$t\bar{t}W^\pm$	0.639	0.424	0.215	–	3.836×10^{-3}
$W^\pm(Z/\gamma^*)$	10.832	6.664	4.164	–	–
$(Z/\gamma^*)(Z/\gamma^*)$	1.175	0.594	0.581	0.047	–
$ttt\bar{t}$	–	–	–	–	1.327×10^{-4}
$t\bar{t}b\bar{b}$	–	–	–	–	$< 10^{-4}$
TOTAL	32.722	17.753	14.969	0.116	4.675×10^{-3}

Table 3.3: Dominant SM background contributions to the multilepton channels at the LHC with $\sqrt{S} = 14$ TeV after all the cuts discussed in Section 3.1. K-factor for $t\bar{t}$ is taken to be 2.2. Blank portions represent insignificant contributions compared to the leading processes in that channel. SM backgrounds for all other channels are expected to be negligible. Cross sections are in femtobarn (fb).

Using all the cuts discussed in the previous section, we have estimated the SM backgrounds for different significant processes tabulated in Table 3.3. We have used ALPGEN-2.14 [151] to generate events for the following SM processes: $t\bar{t}(Z/\gamma^*)$, $t\bar{t}W^\pm$, $t\bar{t}t\bar{t}$, $t\bar{t}b\bar{b}$, $W^\pm(Z/\gamma^*)$ (with 0 jet) at parton level. The ALPGEN output files are fed into PYTHIA to estimate the cross sections for these processes. The SM backgrounds that emerge from the processes $t\bar{t}$, and

$(Z/\gamma^*)(Z/\gamma^*)$ are estimated using PYTHIA. For $t\bar{t}$ process we have considered the K-factor to be 2.2 [152]. Similar kind of analysis are performed to estimate the SM backgrounds for same-sign-tri-lepton in [119], for tri-lepton in [120, 121] and for four-lepton in [121]. In passing we would like to mention that in our analysis neutral pions (π^0) are allowed to decay.⁴

3.2.1.3 Multilepton signatures

In this section, we present the results for 3ℓ , same-sign- 3ℓ , 4ℓ , LFV 4ℓ , 5ℓ , and 6ℓ events. Analysis is performed with a center of mass energy $\sqrt{s} = 14$ TeV at the LHC with an integrated luminosity of 100 fb^{-1} . The multilepton signal consists of charged leptons (e and/or μ) + X , accompanied by missing transverse momentum, where X can be associated jets. We compute the signal events for $M_{\Phi^0} = 400$ GeV, $\Delta M = -2.8$ GeV, and different choices of v_Φ , mentioned in Table 3.2. For each set of benchmark points, we present the results for both Inverted Hierarchy (Fig. 3.3) and Normal Hierarchy (Fig. 3.4).

Fig. 3.3(a) corresponds to $v_\Phi = 5 \times 10^{-6}$ GeV for which $\Phi \rightarrow \text{HW}$ branching ratio is nearly 100%. Fig. 3.3(b) corresponds to $v_\Phi = 5.1 \times 10^{-5}$ GeV for which $\Phi \rightarrow \text{HW}$ and $\Phi \rightarrow WWW$ branching ratios are $\sim 50\%$, while Fig. 3.3(c) corresponds to $v_\Phi = 0.5$ GeV for which $\Phi \rightarrow WWW$ branching ratio is $\sim 100\%$. The x-axis represents the specific n-lepton events ($n=3,4,5$, and 6) that have been considered. The y-axis depicts the number of events with that particular number of leptonic events. We show systematically the impact of different cuts in our analysis in Fig. 3.3. Each colored bar for a specific n-lepton signal shows the number of events after specific cuts.

In each plot the first column (blue) shows the number of events after lepton identification cut. The second column (green) is including the lepton efficiency cut. The red column at third position is after lepton isolation cut. Finally the fourth column (cyan) is after imposing hard p_T and missing transverse momentum cuts. In the fourth column only in tri-lepton events, the dark (black over

⁴We have noted that the neutral pion decay on/off affects the background estimation significantly due to the presence of the hadronic activity cut.

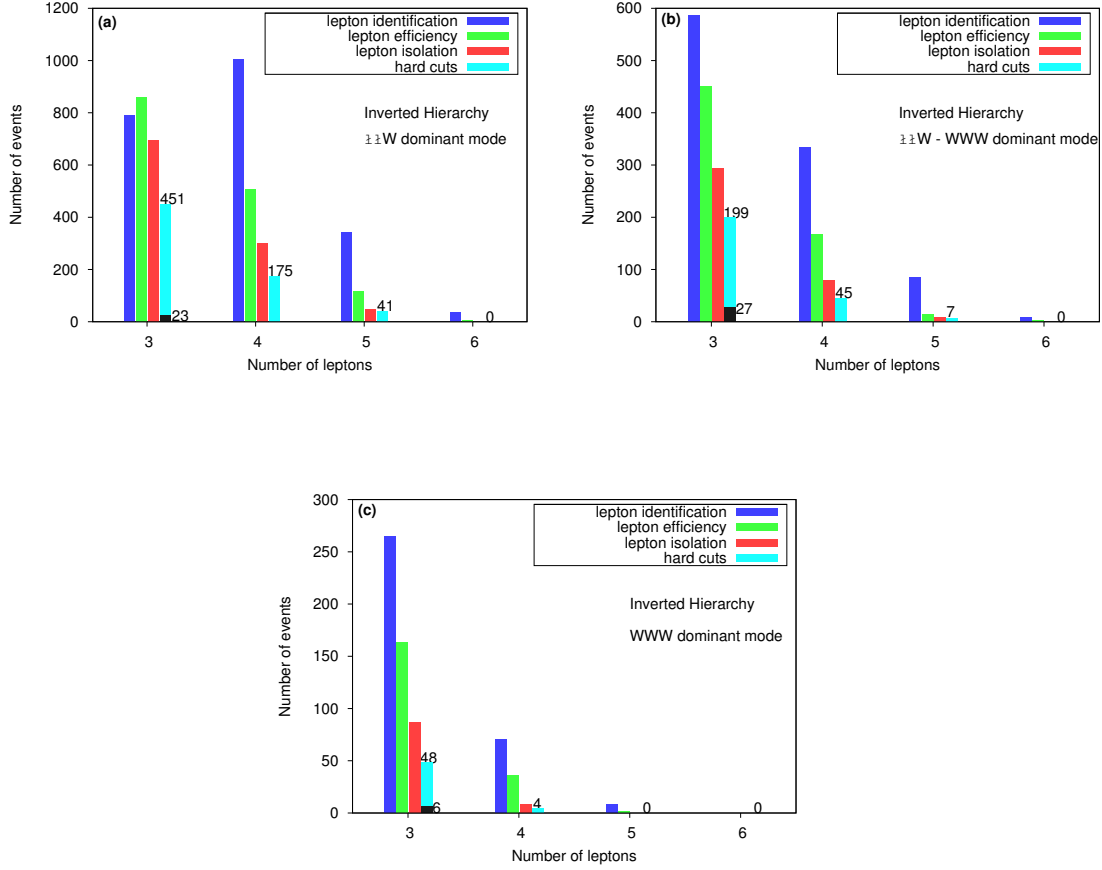


Figure 3.3: The colored histograms for a specific n -lepton signal show the number of events after implementing successive cuts in (a) hW , (b) $hW - WWW$ and (c) WWW dominant modes. The fourth column (cyan) represents the final multilepton signal events. In case of tri-lepton event the dark (black over cyan) shaded portion accounts for the same-sign-tri-lepton events. The final number of the respective multilepton events are also shown in the plots. The number of events are computed with $M_{\Phi^0} = 400$ GeV and $\Delta M = -2.8$ GeV for *Inverted Hierarchy* at the LHC-14 with an integrated luminosity of 100 fb^{-1} .

cyan) shaded bar represents the same-sign-tri-lepton events after implementing all the above-mentioned cuts.

From the plots, we find that no six-lepton event survives after we impose the cuts for all three cases of Fig. 3.3. There is no five-lepton event for the WWW dominant mode, but for the hW and $hW - WWW$ modes we get 41 and 7 events respectively. In general the number of events are more for the hW mode since the branching ratio is almost 100% for the chosen value of v_{Φ} . The effective leptonic BR of WWW dominant mode for $v_{\Phi} = 0.5$ GeV is very suppressed. Thus the number of events are suppressed. In our analysis, we include the possible

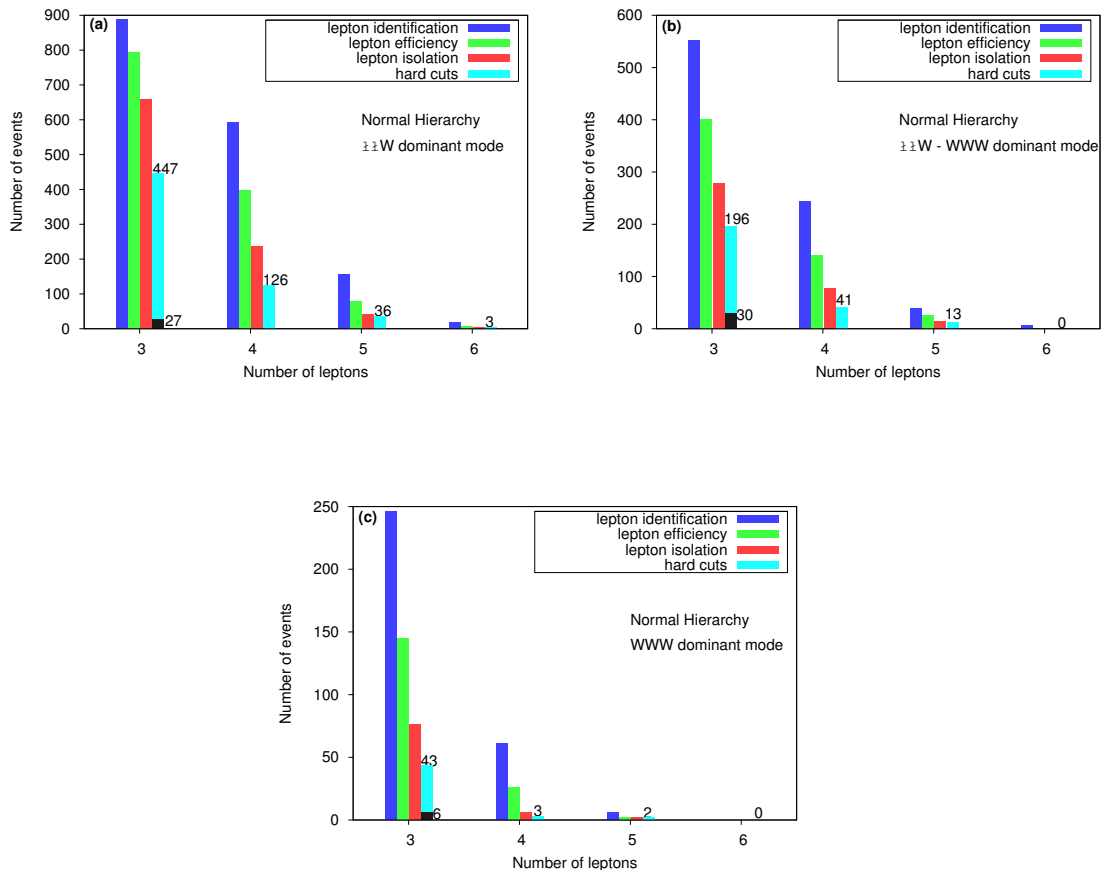


Figure 3.4: The colored histograms for a specific n -lepton signal show the number of events after implementing successive cuts in (a) $\mathbb{H}W$, (b) $\mathbb{H}W - WWW$ and (c) WWW dominant modes. The fourth column (cyan) represents the final multilepton signal events. In case of tri-lepton event the dark (black over cyan) shaded portion accounts for the same-sign-tri-lepton events. The final number of the respective multilepton events are also encoded in the plots. The number of events are computed with $M_{\Phi^0} = 400$ GeV and $\Delta M = -2.8$ GeV for *Normal Hierarchy* at the LHC-14 with integrated luminosity 100 fb^{-1} .

spillover from higher multiplicity events. This is noticeable for the tri-lepton events in the $\mathbb{H}W$ dominant mode (see Fig. 3.3(a)). We find 23 (27) $SS3\ell$ events in $\mathbb{H}W$ ($\mathbb{H}W - WWW$) dominant modes. For WWW mode there are only 6 $SS3\ell$ events, see Fig. 3.3(c).

In Fig. 3.4 we present the similar histograms corresponding to the multilepton signals for NH. There are 27, 30, 6 same-sign-tri-lepton events in $\mathbb{H}W$, $\mathbb{H}W - WWW$, and WWW dominant modes respectively. The general trend discussed in the context of Fig. 3.3 is reflected here. For both cases we find significant same-sign-tri-lepton, tri-lepton and four-lepton events over the SM background,

as noted from Table 3.3.

If we compare the total number of events for NH and IH for instance in the four-lepton channel then we see that they are not widely different. However, if one classifies these events in terms of lepton flavors then for NH and IH one gets a relatively different number of events in each category, as can be noticed from Table 3.4. The trend in the number of events can be explained to some extent from neutrino mixing. The current values of mixing angles imply that the heavy states have significant amount of both ν_e and ν_μ for IH. Thus, one would expect a somewhat similar number of events involving e and μ . This is reflected in Table 3.4. On the other hand, for NH the heaviest state has a relatively lower fraction of the ν_e component because of the smaller value of θ_{13} . So the number of electron events are less because the BRs are pushed in favor of more muonic events. This pattern is observed in all other multilepton channels where $\Phi\ell\ell$ vertex is involved. However, remember that combined results are an interplay of various factors, like e, μ identification efficiencies and energy resolutions.

4ℓ	$eeee$	$ee\mu\mu$	$e\mu\mu\mu$	$e\mu\mu\mu$	$\mu\mu\mu\mu$	Total events
IH	14	47	69	29	16	175
NH	1	1	23	40	61	126

Table 3.4: Neutrino mass hierarchy dependency in four-lepton signal in HW dominant region.

3.2.1.4 Lepton flavor violating signal

The multilepton events obtained in this model can be of mixed flavors and one can study the charged lepton flavor violation at the LHC. The interaction which is mainly responsible for this signal is the effective vertex, $\Phi^{\pm\pm}\ell_i^\mp\ell_j^\mp$, discussed in Appendix A.4. This is proportional to the light neutrino mass matrix elements $m_{\nu_{ij}}$, with $i, j = e, \mu$. Of special importance in this respect are the four-lepton signals. These are not accompanied by any neutrino in the final state and hence the flavor of all the final state leptons can be ascertained. Note that these type of signals originate from the inclusive pair productions of doubly-charged scalars. Based on the lepton flavors these signatures can be categorized into two classes:

i) $pp \rightarrow \ell_i^+ \ell_i^+ \ell_j^- \ell_j^- + X$, and ii) $pp \rightarrow \ell_i^\pm \ell_j^\pm \ell_j^\mp \ell_j^\mp + X$, with $\ell_i \neq \ell_j = e, \mu$. The former final state emerges when each of the $\Phi^{\pm\pm}$ decays into same flavors of charged leptons, but the latter arises if one of the $\Phi^{\pm\pm}$ decays into different flavors. Our parton level signals consist of four-leptons + X with no missing transverse momentum. Hence, we demand very small $|\vec{P}_T|$ (< 30 GeV) in event selection. We present the results for the LFV four-lepton signals in Table 3.5. For our study, we consider LFV signal in the $\text{h}W$ and $\text{h}W - WWW$ dominant regions. In the WWW dominant region since the decay of W 's leads to large missing energy coming from neutrinos, the lepton flavor violating nature of the final state cannot be determined. Hence, this region does not contribute to our signal.

From Table 3.5 we see that the numbers of events for NH and IH are different. This difference is more pronounced for the events of the first class which are the $ee\mu\mu$ type of events. In this case, the numbers of events are much less for NH because $(m_\nu)_{ee}^{NH} < (m_\nu)_{ee}^{IH}$. For the second class, there are two type of events – $eee\mu$ and $e\mu\mu\mu$. However, because of the higher detection efficiency of the muons the latter type of events give the dominant contribution. These are governed by the elements $(m_\nu)_{e\mu}$ and $(m_\nu)_{\mu\mu}$. For our choice of parameters, $(m_\nu)_{\mu\mu}^{NH} \approx (m_\nu)_{\mu\mu}^{IH}$ and $(m_\nu)_{e\mu}^{NH} > (m_\nu)_{e\mu}^{IH}$. Thus, we get more number of events for NH. In the $\text{h}W - WWW$ dominant region, the same trend can be observed though the number of events is significantly smaller since WWW channel does not contribute to this signal.

Dominant decay region	Hierarchy	# of events ($\ell_i^+ \ell_i^+ \ell_j^- \ell_j^- + X$)	# of events ($\ell_i^\pm \ell_j^\pm \ell_j^\mp \ell_j^\mp + X$)	Total
$\text{h}W$	IH	22	4	26
$\text{h}W$	NH	0	9	9
$\text{h}W - WWW$	IH	4	0	4
$\text{h}W - WWW$	NH	0	3	3

Table 3.5: Lepton flavor violating four-lepton signals at different dominant decay regions for normal and inverted hierarchies at the LHC. The signal events are computed using parameters $M_{\Phi^0} = 400$ GeV, $\Delta M = -2.8$ GeV, $|\vec{P}_T| < 30$ GeV.

3.2.2 New contributions to $H \rightarrow \gamma\gamma$

The charged scalars in this model couple to both, the neutral Higgs boson as well as the photon. Thus, they lead to added contributions to the Higgs to diphoton ($\gamma\gamma$) process. The dominant contribution comes from the diagram shown in Fig. 3.5. The relevant part of the Lagrangian reads as

$$\mathcal{L}_{H\gamma\gamma} = (y_3\Phi^{+++}\Phi^{---} + y_2\Phi^{++}\Phi^{--} + y_1\Phi^+\Phi^-)Hv, \quad (3.7)$$

where $y_3 = 2\lambda_3 - 3\lambda_4/2$, $y_2 = 2\lambda_3 - \lambda_4/2$, $y_1 = 2\lambda_3 + \lambda_4/2$.

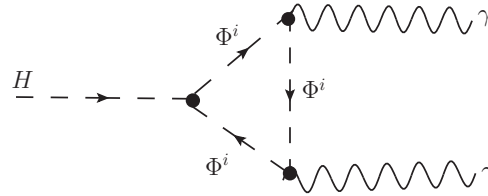


Figure 3.5: New diagrams that contribute in Higgs to diphoton decay through charged components of Φ . Here Φ^i represents singly, doubly and triply-charged scalars.

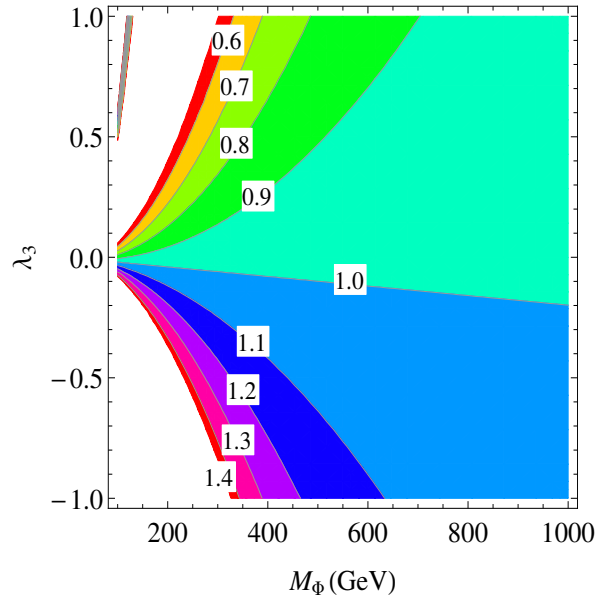


Figure 3.6: Iso-contour of $R_{\gamma\gamma}$ in the $M_\Phi - \lambda_3$ plane.

In Fig. 3.6 we plot the iso-contours of $R_{\gamma\gamma}$ in the $M_\Phi - \lambda_3$ plane, where $R_{\gamma\gamma}$ is the ratio of the partial decay widths of Higgs to diphoton for the new

model and that for the SM. To minimize the number of free parameters, we have varied λ_3 in the range $[-1, 1]$ and λ_4 is reconstructed from the following relation $\Delta M^2 = \frac{\lambda_4}{2}v^2$, with $\Delta M = -2.8$ GeV (see discussion in Section 3.2.1). We note that the Higgs to diphoton rate in this model can be larger (smaller) compared to the SM for $\lambda_3 < 0$ ($\lambda_3 > 0$) for values of M_{Φ^0} in the LHC-accessible range. Note that the multilepton signals that we consider do not depend on the parameter λ_3 . Since in the model under consideration the vector-like fermions are heavy their contribution to the diphoton decay rate is suppressed.

3.2.3 Summary: BNTM

Let us summarize our study of the BNTM. We consider a model which can generate neutrino masses through an effective dimension-7 operator. This requires the presence of an isospin 3/2 scalar and a pair of $Y = 2$ vector-like $SU(2)$ triplet fermions. The neutral fermion mass matrix is of the linear seesaw form and one can get light neutrinos of mass in the right ballpark even if the new particles are at $\mathcal{O}(\text{TeV})$ scale. We choose the scalar quadruplet to be of mass lower than TeV such that the charged scalars belonging to this can be pair produced at the LHC. Subsequent decays of these scalars to leptons or W-bosons and further decays of W-boson produce multilepton final states. We study the tri-lepton, same-sign tri-lepton, four-lepton, five-lepton and six-lepton signals in this model at the LHC at $\sqrt{s} = 14$ TeV with integrated luminosity $\int \mathcal{L} dt = 100 \text{ fb}^{-1}$. A noteworthy feature in this model is the presence of the effective vertex $\Phi^{\pm\pm}\ell^\mp\ell^\mp$ which facilitates the same-sign-tri-lepton events for which the SM background is not significant and hence they can herald new physics beyond SM. Further more since this vertex depends on the neutrino mass matrix elements, it induces a dependence on the neutrino mass hierarchy in the observed signal. We do a realistic simulation using CalcHEP and PYTHIA incorporating appropriate cuts. We also estimate the SM background using ALPGEN and PYTHIA. We choose the parameters of the model to cover the different dominant decay modes of the charged scalars. Among the events studied, the 6 lepton events do not survive the cuts for most of the benchmark points. For the other multilepton events,

significant excess over the SM background can be observed. Another hallmark of this model is the possibility of obtaining flavor violating four-lepton signal. We investigate this option in the context of the LHC and find significant number of events. We estimate the additional contribution to the $H \rightarrow \gamma\gamma$ rate in this model and delineate the parameter space in which this rate can deviate from the SM value.

3.3 Minimal Linear Seesaw Model (MLSM)

We now discuss collider phenomenology of the heavy neutrinos in the MLSM. The heavy neutrinos in this model are of Dirac type and the SSDL signal is suppressed⁵. In the context of this model we consider two possible production channels for the heavy neutrinos resulting in two different classes of signals. The first one of this is the s-channel process to produce heavy Dirac neutrinos associated with a lepton and finally giving the tri-lepton and missing energy signal. The second one is the production of heavy neutrinos through vector boson fusion (VBF) in which two electroweak vector bosons coming from two partons ‘fuse’ to produce the signal under consideration (tri-leptons) along with two highly forward jets. It becomes important in the context of hadron colliders since the tagging of forward jets allows us to reduce the background considerably. Also the lack of color exchange between these jets makes the central region free from the color activities and this is exploited by vetoing central jets; see [153] and references therein in the context of the Higgs search. This helps in minimizing the backgrounds further. For these reasons VBF remains an important channel to look for new physics [154–156] at hadron colliders.

In this chapter, we discuss vacuum meta-stability and LFV constraints in MLSM. For NH the most stringent constraint comes from LFV, whereas for IH case vacuum meta-stability constraint is more restrictive. This is because of cancellations occurring for IH for LFV processes [89]. The dependence of the bound on y_ν from meta-stability and LFV on the heavy neutrino mass has

⁵Due to the same reason heavy neutrino contribution towards $0\nu\beta\beta$ is suppressed [89].

Bound \ Parameter	Δ_{\odot}^2	Δ_{\oplus}^2	$\sin^2 \theta_{12}$	$\sin^2 \theta_{23}$	$\sin^2 \theta_{13}$	δ
	$[10^{-5} \text{eV}^2]$	$[10^{-5} \text{eV}^2]$				
3 σ range (NH)	7.12 – 8.20	2.31 – 2.74	0.27 – 0.37	0.36 – 0.68	0.017 – 0.033	0 – 2π
(IH)		2.21 – 2.64		0.37 – 0.67		
Used value (NH: Case - I)	7.15	2.73	0.27	0.36	0.033	0.0
Used value (NH: Case - II)	7.13	2.73	0.27	0.68	0.033	0.0
Used value (IH)	7.25	2.40	0.34	0.57	0.021	0.0

Table 3.6: Allowed 3σ ranges of oscillation parameters and benchmark values of these parameters used in our analysis to get the signal allowed by LFV and vacuum metastability. Case-I corresponds to the peak in Fig. 3.7(Left panel), while Case-II corresponds to a lower value of y_ν/M_N , for which $V_{\mu N}$ is maximum. The value of Majorana phase α is set at $3\pi/2$ ($3\pi/4$) for NH (IH) scenario.

been shown in [89]. The metastability bound on y_ν varies approximately in the range 0.4 - 0.5 for M_N varying in the range 100 - 1000 GeV. This bound is independent of the oscillation parameters. However, significant variation on the bound on y_ν from LFV constraint is possible within the allowed range of oscillation parameters, mostly due to unconstrained phases, δ and α . Details of the dependence can be followed from Fig. 3.7. For a particular M_N , the strength of the signal at LHC would depend on the value of y_ν . To maximize the signal we therefore choose the value of y_ν at the peak for NH case. However, for IH case the peak value is much above the vacuum metastability bound and therefore we choose maximum allowed value of y_ν satisfying the metastability bound. The corresponding parameter values are depicted in Table 3.6 for NH (case I) and IH. Note that, the above-mentioned cancellations within the terms, ensure the peak position corresponds to $\alpha + \delta = 3\pi/2$ ($3\pi/4$) for NH (IH), which is also evident in Fig. 3.7. We have chosen $\delta = 0$ in our analysis. For some other values of δ , the phase α has to be chosen so that one is at the peak. In Fig. 3.7 we also show the variation of this bound with respect to the θ_{23} mixing angle in lower octant (LO, $\theta_{23} < \pi/4$) and higher octant (HO, $\theta_{23} > \pi/4$). The y_ν value 0.4 (0.075) corresponds to IH (NH: Case-I) scenario for $M_N = 100$ GeV, which we will use in our analysis. These will be translated into the bounds on the mixing matrix elements, V_{IN} , depending on the heavy neutrino mass M_N . Since y_s is extremely small ($\mathcal{O}(10^{-10})$), Y_S (*cf.* Eq. 2.46) does not play any role in determining V_{IN} . The elements of the matrix V (*i.e.* V_{IN}) can be expressed in terms of U_{PMNS}

matrix, ρ and y_ν as follows:

$$\begin{aligned}
V_{eN_1} &= \frac{-i}{\sqrt{2}M_N} \frac{y_\nu v}{2} \left[\sqrt{1+\rho} (U_{PMNS})_{12}^* + i \sqrt{1-\rho} (U_{PMNS})_{11}^* \right] \\
&\simeq \frac{y_\nu v}{4M_N} \left[e^{i(\alpha+\delta)} (-2 + \sqrt{r}) r^{\frac{1}{4}} s_{12} - 2i s_{13} \right] + \mathcal{O} \left((\sqrt{r}, s_{13})^2 \right), \\
V_{\mu N_1} &= \frac{-i}{\sqrt{2}M_N} \frac{y_\nu v}{2} \left(\sqrt{1+\rho} (U_{PMNS})_{22}^* + i \sqrt{1-\rho} (U_{PMNS})_{21}^* \right) \\
&\simeq \frac{y_\nu v}{4M_N} \left[(-2 + \sqrt{r}) (e^{i\alpha} r^{\frac{1}{4}} c_{12} c_{23} + i s_{23}) + 2 e^{i(\alpha+\delta)} r^{\frac{1}{4}} s_{12} s_{23} s_{13} \right] \\
&\quad + \mathcal{O} \left((\sqrt{r}, s_{13})^2 \right). \tag{3.8}
\end{aligned}$$

The above expressions are for NH scenario and similar expressions can be computed for IH also. The element V_{eN_2} ($V_{\mu N_2}$) differs from V_{eN_1} ($V_{\mu N_1}$) by a phase factor. Note that in Table 3.6, we also consider a second set of oscillation parameters for NH (NH: Case II) corresponding to a lower value of y_ν of 0.056 with θ_{23} in the higher octant. This value is chosen such that $V_{\mu N}$ is maximum and muon signal may be larger, since muon has higher efficiency for detection.

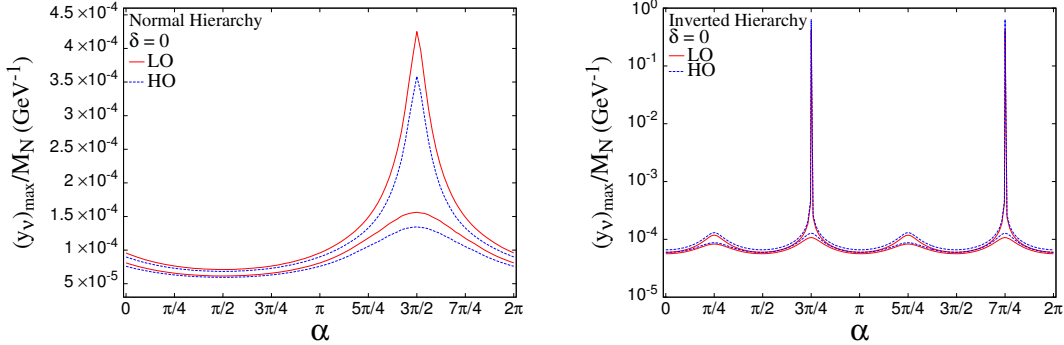


Figure 3.7: Bound on y_ν/M_N as a function of Majorana phase α , varying the oscillation parameters in the allowed 3σ range. Red-solid (Blue-dashed) curve corresponds to atmospheric angle (θ_{23}) residing in LO (HO) region. (Left plot) The plot is for NH scenario, where highest allowed value of y_ν/M_N lies in LO region. (Right plot) The same plot for IH scenario.

For phenomenological study, we have chosen three sets of benchmark points. To maximize the signal we choose the value of y_ν at the peak for NH case. However, for IH case the peak value is much above the vacuum metastability bound and, therefore, we choose maximum allowed value of y_ν satisfying the

metastability bound. Case-II for NH corresponds to a lower value of y_ν/M_N , for which $V_{\mu N}$ is maximum. The corresponding parameter values are depicted in Table 3.6 for NH (case I), NH (case II) and IH.

Heavy neutrinos can interact with the SM particles, via light-heavy mixing. To get some perspective on the degree of suppression in cross section coming from these (LFV and metastability) constraints we note down the corresponding V_{lN} values for $M_N = 100$ GeV : $V_{eN} = 1.95 \times 10^{-3}$, $V_{\mu N} = 2.93 \times 10^{-2}$ and $V_{\tau N} = 8.83 \times 10^{-2}$ for NH (Case-I) scenario, whereas, $V_{eN} = 1.43 \times 10^{-3}$, $V_{\mu N} = 4.14 \times 10^{-2}$ and $V_{\tau N} = 5.48 \times 10^{-2}$ for NH (Case-II) respectively. For IH these values are $V_{eN} = 0.48$, $V_{\mu N} = 4.15 \times 10^{-9}$ and $V_{\tau N} = 0.109$. Note that since our model is fully reconstructible and the only unknown parameter is y_ν which can be constrained from LFV and meta-stability bounds, we have definite predictions for the parameters V_{lN} and these values are different for NH and IH scenarios. Bounds on V_{lN} can also come from Electroweak Precision Data (EWPD) [157]. Our bounds for NH are consistent with these bounds. For IH we get a larger value for V_{eN} . However, it is to be noted that the EWPD bounds are obtained assuming mixing with a single charged lepton and can be evaded in the presence of cancellations or mixing with the other charged leptons [112].

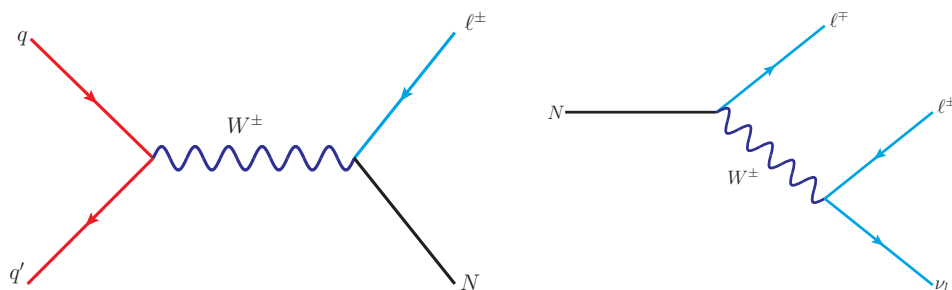


Figure 3.8: (Left plot) Leading order s-channel diagram for heavy neutrino production at hadron colliders, and (Right plot) representative diagram for one of the decay mode of the heavy neutrino. These two figures lead to tri-lepton + \cancel{E}_T signal considered in the analysis.

3.3.1 Phenomenology at the LHC

The dominant production channel of the heavy neutrinos at LHC is the s-channel process through virtual W-boson exchange. At the leading order the parton level process ($q\bar{q}' \rightarrow W^\pm \rightarrow \ell^\pm N$) is depicted in Fig. 3.8(left plot). The heavy neutrinos can also be produced through the VBF process where production of N is associated with two forward jets. Fig. 3.9 contains the representative parton level Feynman diagrams for VBF processes⁶.

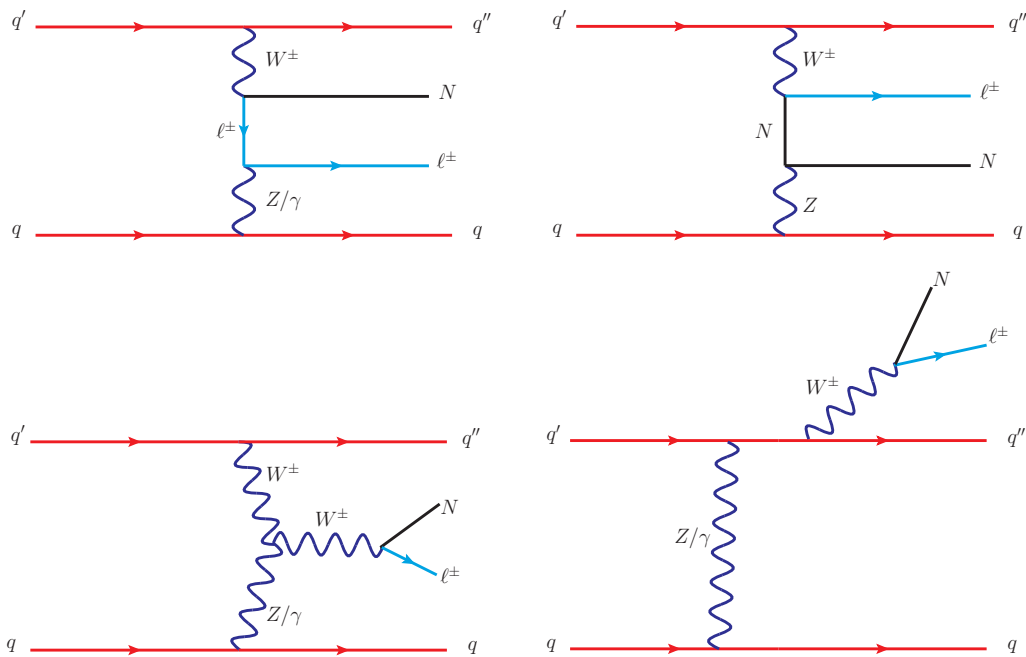


Figure 3.9: Representative parton level diagrams contributing to $N\ell jj$ production through vector boson fusion at hadron colliders. Mirror diagrams are not shown here and also the last diagram is one of the four diagrams with W^\pm emitting from each of the quark legs.

Estimated total production cross sections of these heavy Dirac neutrinos at the 14 TeV LHC in IH scenario are shown in Fig. 3.10 for both s -channel(solid-line) as well as VBF (dashed-line). For NH scenario, the s -channel production crosssections are shown in the same figure for two different cases (*cf.* Table 3.6),

⁶Note that there are some diagrams which are not truly VBF type, *i.e.* two gauge boson are not fused via t-channel (*e.g.* bottom right diagram in Fig. 3.9), but they can lead to the same final states. These diagrams are necessary for the requirements of gauge invariance and included both for BG [158, 159] and signal calculations.

Case-I (Red dot-dashed line) and Case-II (Black double dotted line). Basic cuts such as $p_{T\ell} > 20$ GeV and $|\eta_\ell| < 2.5$ are applied and y_ν values mentioned in the previous section are used. It is seen from the figure that although case II corresponds to a lower value of y_ν since $V_{\mu N}$ is larger, the production cross section is slightly larger. Since the VBF cross section is much lower we do not present the VBF cross section for the NH case. In these analyses, CTEQ6L1 [146] parton distribution functions have been used with the factorization scale set at the heavy neutrino mass M_N .

Heavy neutrinos N can decay into charged lepton or neutrino associated with gauge (or Higgs) boson as

$$N \rightarrow W^\pm l^\mp / Z\nu_l / H\nu_l, \quad \text{where } l \equiv e, \mu, \tau. \quad (3.9)$$

A representative diagram for decay of N ($N \rightarrow \ell^\mp W^\pm$) is shown in Fig. 3.8(right plot).

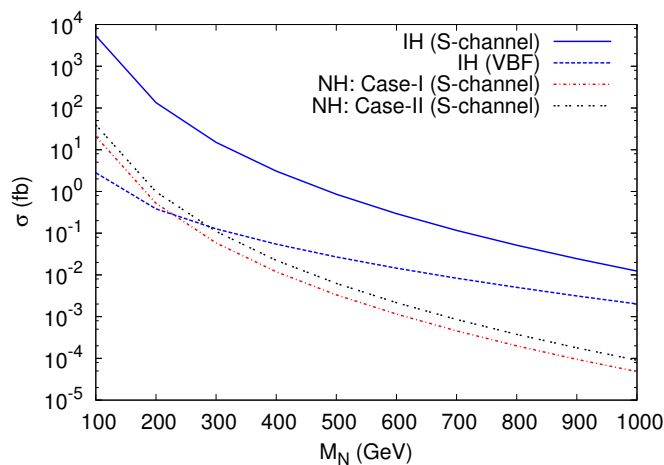


Figure 3.10: The total cross section is shown for production of heavy neutrino associated with light lepton ($pp \rightarrow N\ell$, where $\ell = e, \mu$) at the 14 TeV LHC through the leading order s-channel process, while dotted lines represent VBF production cross section.

In Fig. 3.11 we present the branching ratios for these decay channels as a function of heavy neutrino mass M_N both in the case of normal hierarchy (left) and inverted hierarchy (right). Total decay widths in each case are also demon-

strated with the solid line in each figure. Identifying that the charged lepton decay modes for heavy neutrino *i.e.* $N \rightarrow W^\pm l^\mp$ being the main channel for search at the hadron collider, we discuss the corresponding decay modes in detail for both scenarios. The figure clearly shows that for NH, Case-I⁷, heavy neutrinos mostly decay into tau lepton (τ) and W -boson. On the other hand, for IH, decay into the first generation lepton (e) possesses the maximum branching ratio. For NH, the decay to μ is low and decay to e is severely suppressed, while for IH, the decay to τ has a lower ratio and decay to μ is negligible. The W^\pm can have hadronic decay modes ($W^\pm \rightarrow jj$) or leptonic decay modes ($W^\pm \rightarrow l^\pm \nu$). The tri-lepton signal $pp \rightarrow l^\pm l^\mp l^\pm \nu$ comes from the later decay mode⁸.

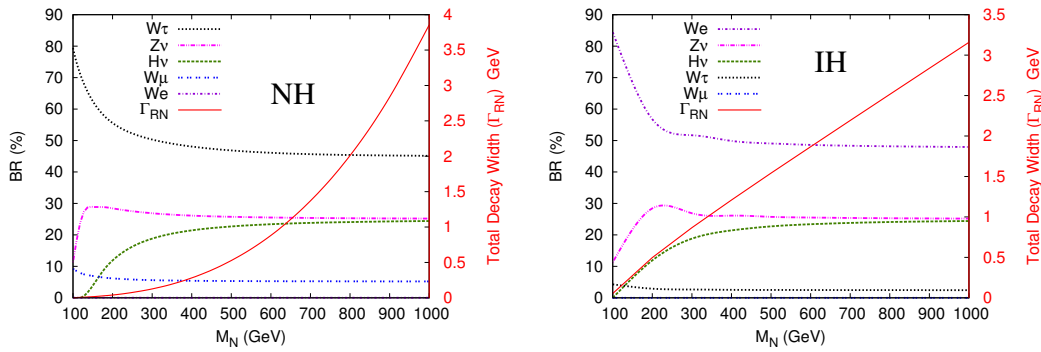


Figure 3.11: The decay branching ratios of the heavy neutrino (N) in different channels as a function of its mass in the case of the normal hierarchy, Case-I, (left) and inverted hierarchy (right). Total decay widths in each case are also demonstrated with the solid line in the same figure.

Other than charged lepton decay mode, N can also decay to Z boson or Higgs boson associated with neutrinos as listed in Eq. 3.9. The corresponding branching ratios are also shown in Fig. 3.11. Note that the branching ratio for

⁷For Case-II, although BRs to different channels likely to change, we do not show the corresponding plot as final production cross section for both the cases, after putting all the selection criteria, is very low for NH and beyond the reach of LHC at 14 TeV even with a luminosity of 3000 fb^{-1} .

⁸Evidently former decay mode leads to opposite-sign dileptons (OSDL), also suppressed by $|V_{lN}|^4$, but slightly larger compared to tri-lepton signal. However, significant irreducible backgrounds can come from $t\bar{t}$, VV (with $V = W, Z$), as well as $Z + Jets$ after vetoing dilepton invariant mass at Z -pole. Hence, we are not considering the OSDL as a signal. Estimate of these backgrounds for OSDL can be found in [160]. Note that their more specific selection criteria are not applicable for our present signal. Similarly, OSDL through VBF is suppressed by $|V_{lN}|^4$ and is beset with large background coming from WW , $\tau\tau$ and ZZ production at VBF[155].

$Z\nu$ is suppressed for lower values of the masses of the heavy neutrinos essentially because of W mass threshold. For the $H\nu$ decay mode, the Higgs mass threshold suppresses the decay rate for lower values of $M_N \sim 100$ GeV. However, as M_N increases these branching ratios increase to retain a $\sim 25\%$ level. Both these channels can contribute to the tri-lepton signal via leptonic decays and we have considered their contributions in our simulation. However, since we will apply Z -veto (to minimize the SM background), the contribution coming from $Z\nu$ decay mode will be suppressed after final event selection.

As lepton Yukawa is small, the $H\nu$ mode is also not going to contribute to our signal even for higher values of M_N .

3.3.2 Simulations and results

We have implemented the model in `FeynRules` [161] and generated the Feynman rules compatible with `MadGraph5` [143]. After generating Les Houches Event (LHE) [144] file from `MadGraph`, we have passed that to `PYTHIA6` [145] for showering and hadronization.

3.3.3 Selection criteria

To get enhancement in signal over background, in addition, we use the following selection criteria [118, 119] for VBF signal:

◇ VBF cuts [153, 162]:

- Central jet veto is also applied, in which we consider any jet with $E_{T3} > 20$ GeV and compute the rapidity with respect to the average of the two forward jets: $\eta_0 = \eta_3 - (\eta_1 + \eta_2)/2$. We veto the event if $|\eta_0| < 2$. Central jet veto is applied to suppress the QCD background substantially.
- Charged leptons need to fall in between the rapidities of two forward tagging jets *i.e.* $\eta_{j,min} < \eta_\ell < \eta_{j,max}$.
- p_T of jets: $p_{T_{j_1, j_2}} > 20$ GeV.

- Invariant mass of jets: $M_{j_1 j_2} > 600$ GeV.
- Pseudorapidity of jets: $\eta_{j_1} \cdot \eta_{j_2} < 0$ and $|\eta_{j_1} - \eta_{j_2}| > 4$. Demanding both the tagged jets in opposite hemisphere and a large rapidity separation among them significantly reduces the BG for VBF.

3.3.4 Background

3.3.4.1 For s-channel signal

To calculate the SM background we consider all channels that can produce or mimic the tri-lepton production with missing P_T . We closely follow Ref. [118, 163] where similar background analysis was done with the event selection criteria listed as above except the cuts related to the VBF. Events are generated using ALPGEN [151] for the processes coming from $t\bar{t}$, $t\bar{t}(Z/\gamma^*)$, $t\bar{t}W^\pm$, $W^\pm(Z/\gamma^*)$, $(Z/\gamma^*)(Z/\gamma^*)$ at the parton level and passed into PYTHIA. As expected $t\bar{t}$ and $W^\pm(Z/\gamma^*)$ contribute dominantly. These and other SM backgrounds are listed in Table 3.7. For each process, we classify the tri-lepton signals into four different flavor combinations and compute the cross section in each case along with the total contribution.

Process	Cross section (fb)				
	lll	eee	$ee\mu$	$e\mu\mu$	$\mu\mu\mu$
$t\bar{t}$	18.973	1.1383	7.0831	8.2214	2.5297
$W^\pm(Z/\gamma^*)$	10.832	0.0677	0.1311	5.9891	4.6440
$(Z/\gamma^*)(Z/\gamma^*)$	1.175	0.0734	0.0525	0.6400	0.4090
$t\bar{t}(Z/\gamma^*)$	1.103	0.0429	0.1329	0.4997	0.4275
$t\bar{t}W^\pm$	0.639	0.0328	0.2655	0.2424	0.0983
TOTAL	32.722	1.3552	7.6655	15.593	8.1086

Table 3.7: Dominant Standard Model background cross sections contributing to tri-lepton and missing transverse energy. These are calculated satisfying all the cuts (except VBF cuts) for the 14 TeV LHC. For each process we also classify the tri-lepton background into four different flavor combinations and present the cross section in each case along with the total contribution.

3.3.4.2 For VBF signal

Tri-lepton signal with missing P_T and two forward jets in VBF can be faked by different SM backgrounds. Processes like $t\bar{t}$ would produce b-jets and mostly effective in central region. Vetoing on jet activities in central region can eliminate most of the non-VBF type SM processes. However, most important irreducible background comes from $W^\pm Z$ and ZZ together with two extra forward jets once the gauge bosons decay leptonically. These processes can construct dominant SM background for the VBF production of $3\ell + \cancel{E}_T$ since they include the typical VBF topology and hence can easily pass the central jet veto criteria. These backgrounds are calculated⁹ using `MadGraph5` and `PYTHIA6`. In the Table 3.8 the dominant background cross sections after satisfying all the cuts including VBF cuts at 14 TeV LHC is tabulated. Like the case of s-channel backgrounds, for each process we also classify the tri-lepton signals into four different flavor combinations and compute the cross section in each case as well as the total contribution.

Process	Cross section (fb)				
	$\ell\ell\ell$	eee	$e\mu\mu$	$e\mu\mu$	$\mu\mu\mu$
$W^+ Z jj$	0.04068	0.00073	0.00105	0.02157	0.01734
$W^- Z jj$	0.01923	0.00038	0.00055	0.00994	0.00836
$ZZ jj$	0.00094	0.00002	0.00002	0.00066	0.00024
TOTAL	0.06085	0.00113	0.00162	0.03216	0.02594

Table 3.8: Dominant Standard Model background cross section contributing to tri-lepton and missing transverse energy associated with two forward jets. These are calculated satisfying all the cuts including VBF cuts for the 14 TeV LHC. Cross sections of four different flavor combinations, as well as the total cross section, are listed.

3.3.5 Signal

Earlier in Section. 3.3.1 we have presented the total heavy neutrino production cross sections for different light neutrino hierarchy with basic selection criteria. The cross section for NH scenario was found to be much lower than the IH scenario

⁹Next to leading order QCD corrections are available in [158, 159].

for s -channel. The branching ratios for decays of N to final states with μ and e are also very small for NH. Therefore, we will concentrate only on IH scenario henceforth. For this we consider both s -channel and VBF process. Although the VBF cross section for IH is lower or comparable to s -channel cross section for NH for lower values of M_N , the background for VBF processes are much smaller. Hence, we study this channel also for IH. In this section, we consider all leptonic decay modes of heavy neutrinos for a benchmark mass of M_N at 100 GeV with the cuts discussed in Section. 3.3.3.

3.3.5.1 Signal for s -channel

The signal coming from decay of heavy neutrinos

$$pp \rightarrow \ell^\pm N \rightarrow \ell^\pm(\ell^\mp W^\pm) \rightarrow \ell^\pm \ell^\mp \ell^\pm + \cancel{E}_T, \quad \text{where } \ell \equiv e, \mu.$$

Table 3.9 lists the final tri-lepton signal cross section through s -channel heavy neutrino production at 14 TeV LHC for the benchmark point $M_N = 100$ GeV incorporating all event selection criteria except VBF cuts as described earlier. The total contribution from the light leptons as well as the contributions from the four different flavor combinations are presented.

Hierarchy	Cross section (fb)				
	$\ell\ell\ell$	eee	$ee\mu$	$e\mu\mu$	$\mu\mu\mu$
IH	27.07	10.297	16.314	0.459	0.0

Table 3.9: Cross section for IH case. Final tri-lepton signal cross section through s -channel heavy neutrino production at the 14 TeV LHC for the benchmark point $M_N = 100$ GeV including all event selection cuts except VBF cuts. We classify the tri-lepton signals into four different flavor combinations and present the cross section in each case along with the total light lepton contribution.

As we can see from the Table 3.9 cross section in terms of flavors has the ordering: $ee\mu > eee > e\mu\mu > \mu\mu\mu$. We can understand this in the following way. There are total 8 possibilities which can produce $\ell\ell\ell$ events. There is only one way to produce $\mu\mu\mu$ and eee final states. However, there are three possible ways to get the $ee\mu$ channel depending on which one of ℓ_i 's in Fig. 3.8 is associated

with e and μ . Similarly for the $e\mu\mu$ final state also we get 3 possibilities. The amplitude for eee channel $\sim V_{eN}^4$; the $ee\mu$ channel goes as $\sim V_{eN}^2 + 2V_{eN}V_{\mu N}$; the $e\mu\mu$ channel goes as $\sim V_{\mu N}^2 + 2V_{eN}V_{\mu N}$ while the $\mu\mu\mu$ channel as $\sim V_{\mu N}^2$. Since $V_{eN} \gg V_{\mu N}$, the eee and $ee\mu$ cross sections are much larger whereas $\mu\mu\mu$ cross section is negligible. $ee\mu$ cross section is higher than the eee cross section because of higher muon efficiency in the detector, whereas the small $e\mu\mu$ cross section is due to a very tiny value of $V_{\mu N}$.

One can also compute the ratios of events with different flavor compositions in which some of the common systematic uncertainties can get canceled. For example $ee\mu/eee \sim \epsilon$ where ϵ denotes the relative efficiency of detection of muon over electron, $ee\mu/\mu\mu\mu \sim \epsilon V_{eN}^4/V_{\mu N}^4$; $eee/e\mu\mu \sim \epsilon^2 V_{eN}^4/V_{\mu N}^4$ etc. Since for a fixed y_ν , which in turn implies specific values for phases, the variation of the light-heavy mixing angles are not very much with oscillation parameters, these ratios vary within a very narrow range¹⁰ and hence can be used to test the model. Of course for different phase choices a different y_ν and hence different predictions can be obtained. However, a smaller value in y_ν would result in a lower event rate and hence it would be difficult to test at the LHC.

3.3.5.2 Signal for VBF

In this section, we present the results for the case where N is produced by VBF:

$$pp \rightarrow \ell^\pm N jj \rightarrow \ell^\pm (\ell^\mp W^\pm) jj \rightarrow \ell^\pm \ell^\mp \ell^\pm + \cancel{E}_T + jj (\text{forward jets}), \quad \text{where } \ell \equiv e, \mu.$$

In Table 3.10 we present the final tri-lepton signal cross sections through VBF production of heavy neutrinos at the 14 TeV LHC for the benchmark point $M_N = 100$ GeV, after including all cuts. Here we have only shown the case of inverted hierarchy and signal is found to be quite small. Although VBF backgrounds are small, the tiny production cross sections are insufficient for

¹⁰Note that, the allowed magnitude of mixings are as following: For a fixed value of y_ν ($= 0.4$), α ($= 3\pi/4$), δ ($= 0$) and M_N ($= 100$) GeV, the magnitude of $|V_{eN}|$ and $|V_{\mu N}|$ vary in a very small range for 3σ variation of oscillation parameters; $|V_{eN}| = 0.471 - 0.484$, $|V_{\mu N}| = 1.236 \times 10^{-4} - 1.272 \times 10^{-4}$. However, $|V_{\tau N}|$ varies little higher; $|V_{\tau N}| = 0.092 - 0.147$. Since we are considering modes involving only e and μ , the cross sections are likely to vary by a small amount for different set of oscillation parameters.

giving any signal with integrated luminosity of 300 fb^{-1} . Some indications from VBF can appear only at the HL-LHC (3000 fb^{-1}). However, 5σ significance can not be reached even for $M_N = 100 \text{ GeV}$.

Hierarchy	Cross section (fb)				
	lll	eee	$ee\mu$	$e\mu\mu$	$\mu\mu\mu$
IH	0.018068	7.09×10^{-3}	1.06×10^{-2}	4.06×10^{-4}	0.00

Table 3.10: Final tri-lepton signal through VBF production of heavy neutrino for the benchmark point $M_N = 100 \text{ GeV}$ at 14 TeV LHC for IH after all event selection cuts.

3.3.6 Discovery potential

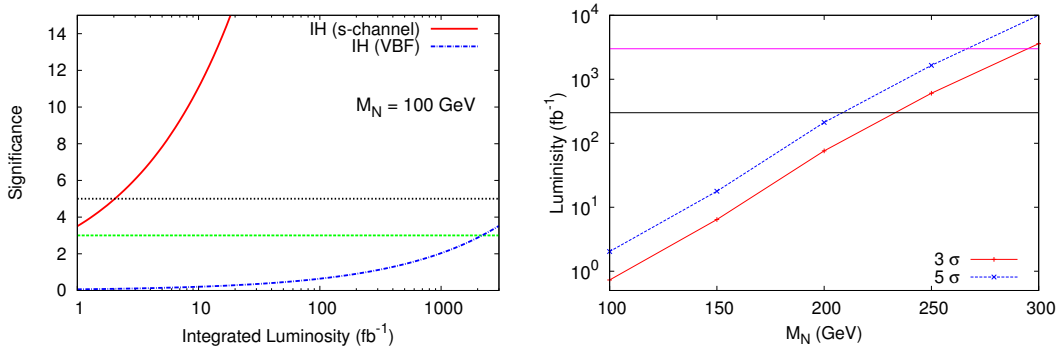


Figure 3.12: (Left) The variation of significance $S/\sqrt{S+B}$ for the s-channel production signal for benchmark point $M_N = 100 \text{ GeV}$ with the integrated luminosity available for the low luminosity option at 14 TeV LHC. Black-dotted (green-dashed) line parallel to the x-axis represents 5σ (3σ) significance. (Right) The lines for 3σ (red) and 5σ (blue) significance in terms of heavy neutrino mass and integrated luminosity. With 300 fb^{-1} luminosity at LHC14 the heavy neutrino mass in this model can be probed up to ~ 210 (230) GeV with $\sim 5\sigma$ (3σ) significance. For very high luminosity of 3000 fb^{-1} this can reach up to ~ 270 (295) GeV.

After numerical computation of all necessary signals and backgrounds, results are better represented in terms of significance, defined as $S/\sqrt{S+B}$, where $S(B) = \mathcal{L}\sigma_{S(B)}$, here \mathcal{L} being integrated luminosity available for the collider at certain machine energy and $\sigma_{S(B)}$ is the final cross section after all event selection, for given parameters like heavy neutrino mass and corresponding allowed couplings.

Fig. 3.12 (Left) demonstrates the expected significance coming from s-channel production of heavy Dirac neutrino of mass 100 GeV as a function of integrated luminosity at 14 TeV LHC. In the figure black-dotted (green-dashed) line shows 5σ (3σ) significance. From the figure it is clear that for the case of s-channel signal in the IH scenario, 3σ (5σ) significance can be achieved within the integrated luminosity ~ 0.73 (2.03) fb^{-1} . In the case of VBF channel, 3σ significance can be achieved with 2175 fb^{-1} luminosity, while 5σ significance is not achievable within 3000 fb^{-1} luminosity which is planned for the HL-LHC.

Fig. 3.12 (Right) shows the lines for 3σ (red) and 5σ (blue) significance in terms of heavy neutrino mass and integrated luminosity. With 300 fb^{-1} luminosity at LHC14 the heavy neutrino mass in this model can be probed up to ~ 210 (230) GeV with $\sim 5\sigma$ (3σ) significance. For very high luminosity of 3000 fb^{-1} this can reach up to ~ 270 (295) GeV. For VBF signal, since $M_N = 100$ GeV itself requires a very large integrated luminosity; higher values of M_N are not possible to explore.

3.3.7 Summary: MLSM

In this section, we have considered TeV scale minimal linear seesaw model which generates correct order of light neutrino masses and has sizable light-heavy mixing to produce heavy neutrinos at colliders like LHC. One of the important features of this model is that it can be fully reconstructible from oscillation data excepting an overall factor y_ν characterizing the Dirac Yukawa matrix. However, this parameter gets constrained by LFV and vacuum meta-stability bounds. The neutral fermion mass spectrum of this model consists of one massless, two light and two heavy neutrinos.

We have studied the collider phenomenology of TeV scale linear seesaw at 14 TeV LHC. The heavy neutrinos in this model can be dominantly produced through the s-channel. In a leading order calculation, subsequent decay of these leads to characteristic tri-lepton signal with missing p_T . We also consider the production of heavy neutrinos through the VBF process. The signal for this is tri-leptons with additional two forward jets which can be tagged. Both these

signals as well as SM backgrounds have been estimated with realistic simulations using MadGraph and PYTHIA.

We found that s-channel tri-lepton production process has potential to be discovered at the LHC for IH scenario. However, due to severe constraint on the light-heavy mixing coming from LFV in the case of NH scenario, both s-channel and VBF can not be probed at the 14 TeV LHC with proposed luminosity. For a benchmark point with a heavy neutrino mass $M_N = 100$ GeV, 3σ significance can be achieved with integrated luminosity of ~ 0.73 (2175) fb^{-1} for s-channel(VBF) signal in the IH scenario. 5σ significance can be reached for s-channel signal with an integrated luminosity of ~ 2 fb^{-1} , however, for VBF signal the required luminosity is ~ 6042 fb^{-1} , which is beyond the reach of projected luminosity at the LHC. Discovery reach in the tri-lepton channel can be achieved upto the heavy neutrino mass of ~ 210 (230) GeV with $\sim 5\sigma$ (3σ) significance at the low luminosity (300 fb^{-1}) option of 14 TeV LHC. In the high luminosity (3000 fb^{-1}) search, reach is upto ~ 270 (295) GeV, whereas VBF channel can only reach upto $\sim 3\sigma$ for M_N at 100 GeV. Our analysis uses values for the elements, V_{lN} of the light-heavy mixing matrix, which are consistent with the constraints coming from vacuum metastability and LFV. Any freedom of choosing larger values (*e.g.* $\sim \mathcal{O}(1)$) for these parameters can extend the discovery limit by a very significant amount. With the constraints used in this work, for V_{lN} , a detectable tri-lepton signal can only be obtained for the inverted hierarchical scenario with particular choices of phases leading to large y_ν . One can also compute the ratios of events with different flavor compositions which are proportional to the elements V_{lN} . They vary only within a narrow range with the 3σ variations of oscillation parameters and thus the model has very definite predictions for these ratios.

3.4 Collider Phenomenology of scalar fields within the Minimal Left-Right Symmetric Model (MLRSM)

The MLRSM is an example of gauge extension of the SM. The MLRSM enjoys the richness of containing several types of beyond-the-SM particles [69, 70] including heavy gauge bosons, heavy neutrinos, heavy charged and neutral scalars. In this section, we will discuss collider phenomenology of the charged scalars in the MLRSM.

After the Higgs boson discovery at the LHC[164, 165], there is presently large activity in searching for the scalar particles of any sort (neutral, charged) at the LHC. In particular, knowledge of the existence of doubly charged scalar bosons would be crucial for further directions in exploration of particle physics phenomena, for instance, their presence would strongly disfavor the minimal version of the supersymmetric Standard Model, MSSM [166–172]. There are two basic ways in which charged particles can be searched for. The first is indirect: looking for rare lepton flavor and number violating processes and precision measurements (deviations from the SM expectations). The second opportunity is provided by the accelerators where new particles can be produced directly at high energies, as in the LHC. There are already many analyses undertaken by the CMS and ATLAS collaborations regarding this kind of searches, and the present limits on masses of the charged scalars, along with the limits on other MLRSM particles, will be discussed in Section 3.4.1.

In this study we have considered Left-Right symmetric model based on the gauge group $SU(2)_L \otimes SU(2)_R \otimes U(1)_{B-L}$ [69] in its most restricted form, the so-called Minimal Left-Right Symmetric Model (MLRSM)¹¹, see section 2.6 for details of the model part. We choose to explore the most popular version of the model with Higgs representations – a bi-doublet Φ and two (left and right)

¹¹The main features of this model are equal $SU(2)$ left and right gauge couplings, $g_L = g_R$, and a scalar potential which contains a bidoublet and two triplet scalar multiplets, considered for the first time in [33], see also [71, 173].

triplets $\Delta_{L,R}$ [71, 173] We also assume that the vacuum expectation value of the left-handed triplet Δ_L vanishes, $\langle \Delta_L \rangle = 0$ and the CP symmetry can be violated by complex phases in the quark and lepton mixing matrices. Left and right gauge couplings are chosen to be equal, $g_L = g_R$. For reasons discussed in [174] and more extensively in [175], we consider diagonal neutrino mixings. It means that W_1 couples mainly to light neutrinos, while W_2 couples to the heavy ones. Z_1 and Z_2 turn out to couple to both of them [71, 176]. $W_L - W_R$ mixing is allowed and is very small, $\xi \leq 0.05$ [103], the most stringent bound being from astrophysics through the supernova explosion analysis [177]. In [178], energy constraints on such a model assuming $\kappa_2 = 0$, *i.e.*, $\xi = 0$ was considered, we do the same here. Moreover, in MLRSM $\tan 2\xi = -\frac{2\kappa_1\kappa_2}{v_R^2}$, which is really negligible for $v_R \geq 5$ TeV, as dictated by Eq. 3.10, where κ_1, κ_2 (v_R) are the vacuum expectation values of Φ (Δ_R).

It is worth to show how the situation looks like if we stick to the popular and to a large extent conservative version of the model (MLRSM), giving candle-like benchmark numbers for possible signals at the LHC. We should also be aware of the fact, that there are relations between model parameters in the Higgs, gauge and neutrino sectors [71, 178–180] and it needs further detailed studies. Also note that for estimation and discussion of observables which are able to measure final signals in the most efficient way, calculation of dominant tree level signals is sufficient at the moment.

In this section, we discuss [163, 178, 181] a dedicated analysis of the MLRSM [69, 70, 72] aiming at an exhaustive exploration of interesting BSM signals at present and future hadron colliders. From the experimental bound on the heavy gauge bosons and FCNC constraints, the parity breaking scale v_R of the right $SU(2)$ group in MLRSM must be already around $\mathcal{O}(5)$ TeV [77, 163, 178, 181, 182]. However, as we discussed in the previous section (refer [163, 181] for more details) in such models charged Higgs bosons can have masses at a much lower level of a few hundred GeV and that scenario is still consistent with experimental data. In this case it is imperative to cover all possible scenarios and their potential effects at the LHC should be analyzed carefully. Interestingly enough,

recent CMS study [74] can be interpreted in favor of right-handed currents.

In this section, we highlight the impact of the relatively light charged scalars in the phenomenology of the MLRSM. Then we note down the possible interesting processes within MLRSM. We study the production and decay modes of the charged scalars. We have provided some benchmark points where we have performed our simulations to make a realistic estimation of the signal events over the SM backgrounds. Our study is based on the reconstruction of the invariant masses of the final state leptons and their mutual separations from where we have shown how we can track the presence of doubly charged scalars. We also note down the impact of the charged scalars to the Higgs to diphoton decay rates. Subsequent part of this section is dedicated to study of multilepton signals via weak vector boson fusion (VBF) production of doubly charged scalar particles. Finally, we conclude the discussion on the collider phenomenology of the charged scalars in the MLRSM.

Before we go into the details of collider signatures of charged scalar particles in the MLRSM, let us discuss the constraints on particle masses from experiments as well as from theoretical considerations. We show that the theoretical considerations are also important, and we find that in the MLRSM some of the scalar masses are constrained from below. In particular, the lowest limit for the doubly charged scalar $H_1^{\pm\pm}$ mass is not much beyond the present limit given in Eq. 3.12 for many different model parameters.

3.4.1 Constraints in the MLRSM: experimental and theoretical

The searches at CMS and ATLAS have tightened up the limits on the masses of heavy gauge bosons. Let us mention that before the LHC era the fits for a charged gauge boson PDG reports $M_{W_2} > 715$ GeV [103, 180]. The new LHC analysis pushed the limits already much above 2 TeV [183–189]. All these searches provide robust bounds on the extra gauge bosons, for instance, the present limit for a charged heavy boson coming from the “golden” decay chain $W_R \rightarrow l_1 N_l \rightarrow l_1 l_2 j j$

is [188, 189]

$$M_{W_2} \geq 2.8 \text{ TeV}. \quad (3.10)$$

This limit (at 95 % Confidence Level (C.L.)) is for a genuine Left-Right symmetric model which we consider here (MLRSM) with $g_L = g_R$ and three degenerate heavy neutrinos and it is based on $\sqrt{s} = 8 \text{ TeV}$ data. Typically, limits for Z_2 mass are already beyond 2 TeV.

The combined LEP lower limit on the singly charged Higgs boson mass is about 90 GeV [190]. At the LHC, established limits for singly charged Higgs boson masses are

$$M_{H^\pm} = 80 \div 160 \text{ GeV}, \quad (3.11)$$

if $BR(t \rightarrow H^+b) < 5\%$ [191] and for the mass range $180 \text{ GeV} < M_{H^\pm} < 600 \text{ GeV}$, 95% confidence level upper limits are set on the production cross section of a charged Higgs boson in the range $0.017 - 0.9 \text{ pb}$, both with the assumption that $BR(H^+ \rightarrow \tau\nu) = 1$ [192].

For doubly charged Higgs bosons the analysis gives lower mass limits in a range

$$M_{H^{\pm\pm}} \geq 445 \text{ GeV (409 GeV) for CMS (ATLAS)}, \quad (3.12)$$

in the 100% branching fraction scenarios [193, 194].

The mass limit for heavy neutrinos is [195, 196]

$$M_{N_R} > 780 \text{ GeV}, \quad (3.13)$$

but it must be kept in mind that bounds on M_{N_R} and M_{W_2} are not independent from each other [188, 197]. Neutrinoless double beta decay allows for heavy neutrinos with relatively light masses, see *e.g.* [30, 33, 78, 198–201]. Detailed studies which take into account potential signals with $\sqrt{s} = 14 \text{ TeV}$ at the LHC

conclude that heavy gauge bosons and neutrinos can be found with up to 4 and 1 TeV, respectively, for typical LR scenarios [202, 203]. Such a relatively low (TeV) scale of the heavy sector is theoretically possible, even if GUT gauge unification is demanded, for a discussion, see *e.g.* [204, 205].

As we can see from Eq. 3.10, there are stringent limits on the heavy gauge boson masses, which imply that the scale in which the right $SU(2)$ gauge sector is broken is at $v_R > 5$ TeV. For such heavy gauge bosons most of the effects connected with them decouple in physical processes at collider physics. However, there is a potential avenue to go deeper and estimate more sensitive Higgs boson contributions. Of course, the effects coming from the scalar sector depend crucially also on their masses. Smaller the Higgs boson masses, larger effects are expected. The question is then: how small their masses can be by keeping the scale of v_R large?

3.4.2 Constraints from FCNC, SM Higgs boson mass, perturbativity

As we mentioned, all Higgs scalars are naturally of the order of v_R , in addition, neutral Higgs boson scalars A_1^0 and H_1^0 contribute to FCNC effects (see Appendix C) and must be large, above 10 TeV (see however [206] for alternative solutions). Let us see then if theoretically charged Higgs bosons can have masses below 1 TeV. In the model which we consider in this study we assume that the Higgs potential is given as in [71, 173], we will also use the same notation, for more details see Appendix B. For details on the parametrization of the Higgs scalar mass spectrum, see Appendix C. This model includes a number of parameters: $\mu_1, \mu_2, \mu_3, \rho_1, \rho_2, \rho_3, \rho_4, \alpha_1, \alpha_2, \alpha_3, \alpha_4, \lambda_1, \lambda_2, \lambda_3, \lambda_4$. The exact Higgs mass spectrum is calculated numerically. Minimization conditions are used to get values of dimensionful mass parameters μ_1, μ_2 and μ_3 which can be arbitrarily large, all other parameters are considered as free, but limited to the perturbative bound¹², $|\rho_i|, |\alpha_i|, |\lambda_i| < 10$. It is assumed that the lightest neutral Higgs particle

¹²We have taken this as 4π . A more precise determination of perturbative limits requires analysis of the Higgs potential with radiative corrections.

is the boson discovered by ATLAS and CMS collaborations. We have taken its mass to lie in the range

$$124.7 \text{ GeV} < M_{H_0^0} < 126.2 \text{ GeV}. \quad (3.14)$$

An example set of generated mass spectra of Higgs bosons for $v_R = 8 \text{ TeV}$ is presented in Fig. 3.13 (left figure). Mass spectra have been obtained by varying uniformly the Higgs potential parameters in a range $(-10,10)$. We have also taken into account the bounds on neutral Higgs bosons obtained from FCNC constraints assuming $m_{A_1^0}, m_{H_1^0} > 15 \text{ TeV}$ by fixing $\alpha_3 = 7.1$ (see Appendix C). The spectra which did not fulfill relation 3.14 were rejected. Altogether we have 6 neutral, 2 singly charged and 2 doubly charged Higgs boson particles in the MLRSM. The figure includes possible spectra of singly and doubly charged as well as neutral Higgs bosons. Some of them can be degenerate or nearly degenerate.

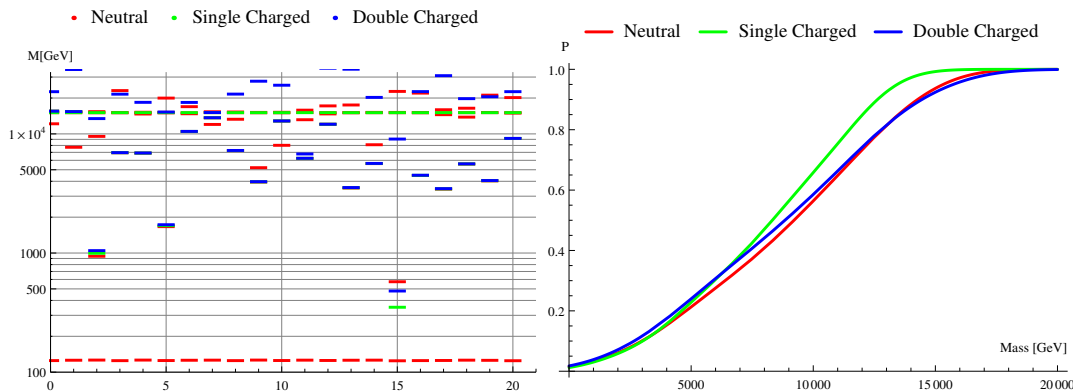


Figure 3.13: On left: an example of 20 Higgs mass spectra obtained by randomly chosen Higgs potential parameters. The constraint on the lowest neutral Higgs mass in Eq. 3.14 was imposed and the bounds coming from FCNC were taken into account. On right: cumulative distribution function P of the lowest mass of singly and doubly charged and next to lightest neutral scalars. For both figures, $v_R = 8 \text{ TeV}$.

This study shows that although the Higgs particles naturally tend to have masses of the order of the v_R scale, it is still possible to choose the potential

parameters such that some of the scalar particles can have masses much below 1 TeV (spectrum 15 in Fig. 3.13(Left)). To discuss the spectra more quantitatively, the cumulative distribution function P of the lowest masses of singly and doubly charged and next to lightest neutral scalar particles are plotted in the right part of Fig. 3.13, again for the same conditions as before and $v_R = 8$ TeV. These results show that for $v_R = 8$ TeV a fraction of the parameter space that gives lightest scalar masses below 1 TeV is at the level of 4%. It means that it is possible to generate the low mass spectra of Higgs boson masses in MLRSM keeping the scale of v_R large. However, what can not be seen on those plots is that in MLRSM not all four charged Higgs bosons can simultaneously be light. For instance, it is possible that H_1^\pm , $H_1^{\pm\pm}$ and $H_2^{\pm\pm}$ are light, for details, see Appendix C. The remaining charged scalar H_2^\pm is of the order of the v_R scale, so its effects at LHC is negligible, to make it lighter would require to go beyond MLRSM. However, for the sake of book keeping, we keep this particle in further discussion. If its mass at some points is assumed to be small¹³ (so we go beyond MLRSM), we denote it with a tilde, \tilde{H}_2^\pm . Its coupling is kept all the time as in MLRSM (why it can be so is discussed in Appendix C).

3.4.3 Scalar sector of the MLRSM and the lowest limit for the doubly charged scalar $H_1^{\pm\pm}$ mass

As we have discussed, charged scalars with masses at the level of a few hundred GeV can be realized in the MLRSM by allowing a percent-level tuning of the scalar potential parameters, compatible with both the large parity breaking scale v_R and severe bounds on neutral scalar masses ($M_{H_1^0, A_1^0}$) derived from flavor changing neutral currents (FCNC). This is non-trivial as both v_R and $M_{H_1^0, A_1^0}$ are at the level of a few TeV and all scalars apart from H_0^0 are naturally heavy, their leading mass terms are being proportional to v_R . Now, we look into further details and show that in fact the lowest bounds can be obtained for some of the scalar masses. The MLRSM scalar potential and its minimization followed by

¹³Note that, as we will see the cross section for production of H_2^\pm in associated with $H_2^{\pm\pm}$ is much smaller compared to that of $H_1^{\pm\pm}H_1^\mp$ production, even for $m_{H_2^\pm} < 1\text{TeV}$.

the diagonalization have been investigated in [173] and explicit relations between physical and unphysical scalar fields are given in [207]. For our purposes, we repeat here only a subset of formulas which we need for further discussion, they are valid as long as $\kappa_1 \ll v_R$, which is true as κ_1 and v_R are connected directly with masses of light and heavy charged gauge bosons, and $M_{W_1} \ll M_{W_2}$ [103, 163]

$$M_{H_0^0}^2 \simeq 2\kappa_1^2 \lambda_1, \quad (3.15)$$

$$M_{H_1^0}^2 \simeq \frac{1}{2} \alpha_3 v_R^2, \quad (3.16)$$

$$M_{A_1^0}^2 \simeq \frac{1}{2} \alpha_3 v_R^2 - 2\kappa_1^2 (2\lambda_2 - \lambda_3), \quad (3.17)$$

$$M_{H_3^0}^2 \simeq \frac{1}{2} v_R^2 (\rho_3 - 2\rho_1), \quad (3.18)$$

$$M_{H_1^{\pm\pm}}^2 \simeq \frac{1}{2} [v_R^2 (\rho_3 - 2\rho_1) + \alpha_3 \kappa_1^2], \quad (3.19)$$

$$M_{H_2^{\pm\pm}}^2 \simeq 2\rho_2 v_R^2 + \frac{1}{2} \alpha_3 \kappa_1^2. \quad (3.20)$$

As we can see, SM-like Higgs boson H_0^0 has a mass proportional to the vacuum expectation value κ_1 (\sim electroweak breaking scale, $M_{W_1} \sim \kappa_1$ [71]). Here, among the neutral scalars only A_1^0 and H_1^0 contribute to the FCNC interactions. To our knowledge, their effects have been discussed for the first time in the context of Left-Right models in [208], see also [77–79, 178, 209, 210] and Appendix C. In general their masses need to be at least of the order of 10 TeV, though some alternatives have also been considered in [206]. Also, the parity breaking scale v_R is already strongly constrained by a “golden” decay chain process $W_R \rightarrow l_1 N_l \rightarrow l_1 l_2 j j$ [188, 197], giving $M_{W_2} \geq 2.8$ TeV. This limit (at 95 % C.L.) is for a canonical Left-Right symmetric model which we consider here (MLRSM). There are also other model independent limits on the masses of gauge bosons ~ 4 TeV and we stay conservative while choosing this value that implies v_R is already bigger than 8 TeV. For more details and other possible scenarios see [163] and more recent by [211, 212].

Now, taking into account the above facts, for example with $M_{H_1^0, A_1^0} \geq 10$ TeV and $v_R \geq 8$ TeV, the scalar potential parameter α_3 can be determined, see Eq. 3.16. This parameter also enters into the relations of the masses of doubly

charged scalars, Eqs. 3.19 and 3.20. Thus the only remaining parameter on which $M_{H_1^{\pm\pm}}$ depends is $\delta\rho \equiv \rho_3 - 2\rho_1$.

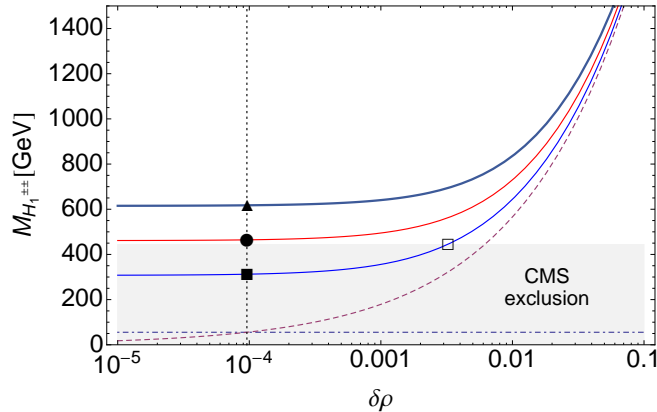


Figure 3.14: Dependence of the $H_1^{\pm\pm}$ mass on $\delta\rho \equiv \rho_3 - 2\rho_1$ for $v_R = 8$ TeV and various masses of flavor changing neutral Higgs scalars H_1^0 and A_1^0 . Points marked on the vertical dotted line by square, circle and triangle show minimal $M_{H_1^{\pm\pm}}$ corresponding to $M_{H_1^0, A_1^0} = 10, 15$ and 20 TeV, respectively (see Table 3.11). In the region left to the vertical dotted line, $M_{H_3^0}$ (dashed line) is smaller than 55.4 GeV (dash-dotted horizontal line). The horizontal grey strip represents the latest CMS exclusion limit on doubly charged Higgs boson mass. The mass spectrum represented by the filled square is obviously ruled out by the LHC. Hence, for $v_R = 8$ TeV and $M_{H_1^0, A_1^0} = 10$ TeV the minimal allowed value of $M_{H_1^{\pm\pm}}$ is 445 GeV (empty square) and one gets the following lower bound $\delta\rho \gtrsim 3 \cdot 10^{-3}$.

In Fig. 3.14 mass of $H_1^{\pm\pm}$ is given as a function of $\delta\rho$ for $v_R = 8$ TeV and different choices of $M_{H_1^0, A_1^0}$. Without loss of generality, it has been assumed that $M_{H_1^0} = M_{A_1^0}$, which implies that $2\lambda_2 = \lambda_3$, Eq. 3.17. Here, $\delta\rho$ starts from zero, as we aim at the minimal values of $M_{H_1^{\pm\pm}}$. For $\delta\rho = 0$, the only contribution to the $H_1^{\pm\pm}$ mass is connected with a second term in Eq. 3.19, however, the mass of H_3^0 also depends directly on $\delta\rho$, see Eq. 3.18. Thus it cannot be negative. Moreover, interpreting LEP II data related to $e^+e^- \rightarrow \gamma + \cancel{E}_T$, it is possible to find lower bound on $M_{H_3^0}$, which is about 55.4 GeV [213]. This leads to the minimal value for the mass of doubly charged scalar $H_1^{\pm\pm}$. It depends both on the minimal allowed values of $M_{H_3^0}$ and masses of the scalars H_1^0, A_1^0 that control FCNC. Let us note that for $v_R \sim 10$ TeV and small values of $\delta\rho$ (e.g. $\delta\rho \lesssim 5 \cdot 10^{-4}$), the dependence on $\delta\rho$ is rather weak and the mass of $H_1^{\pm\pm}$ is dominated by the term

$$\sqrt{\alpha_3 \kappa_1} / \sqrt{2} \approx 171 \sqrt{\alpha_3} \text{ GeV}.$$

$v_R = 8 \text{ TeV} (M_{W_2} = 3.76 \text{ TeV})$		
$M_{A_1^0, H_1^0} [\text{TeV}]$	α_3	$\min(M_{H_1^{\pm\pm}}) [\text{GeV}]$
10	3.13	312 (■)
15	7.03	465 (●)
20	12.5	617 (▲)
$v_R = 10 \text{ TeV} (M_{W_2} = 4.7 \text{ TeV})$		
$M_{A_1^0, H_1^0} [\text{TeV}]$	α_3	$\min(M_{H_1^{\pm\pm}}) [\text{GeV}]$
10	2.0	252
15	4.5	373
20	8.0	495
$v_R = 12 \text{ TeV} (M_{W_2} = 5.64 \text{ TeV})$		
$M_{A_1^0, H_1^0} [\text{TeV}]$	α_3	$\min(M_{H_1^{\pm\pm}}) [\text{GeV}]$
10	1.39	212
15	3.13	312
20	5.56	413

Table 3.11: Minimal masses of a doubly charged Higgs boson $H_1^{\pm\pm}$ as a function of the parity breaking scale v_R of the right sector of the model and the mass of neutral Higgs bosons $\{A_1^0, H_1^0\}$ which contribute to the FCNC effects. Corresponding masses of $H_2^{\pm\pm}$ are fixed by taking, in addition, $\rho_2 = \delta\rho/4$, which yields $M_{H_2^{\pm\pm}} = M_{H_1^{\pm\pm}}$. No LHC direct limits from Eq. 3.12 is applied. The symbols square, circle and triangle correspond to the points marked on Fig. 3.14.

As one can see from Fig. 3.14, for $M_{H_1^0, A_1^0} = 10 \text{ TeV}$ bounds from the LHC yield the following limit: $\delta\rho \gtrsim 3 \cdot 10^{-3}$. On the other hand, for bigger $M_{H_1^0, A_1^0}$ there are no restrictions on $\delta\rho$ from the LHC yet but the model itself predicts the minimal possible value of $M_{H_1^{\pm\pm}}$ masses.

It is worthwhile to note that taking into account experimental limits one can obtain the following bound on $M_{H_1^{\pm\pm}}$:

$$\sqrt{\min(M_{H_3^0}^2) + M_{H_1^0}^2 \kappa_1^2 / v_R^2} \approx \frac{2.41 \text{ TeV}^2}{v_R}. \quad (3.21)$$

The dashed line in Fig. 3.14 is for $M_{H_3^0}$. At $\delta\rho \approx 10^{-4}$, it crosses the horizontal line which corresponds to the lowest bound on the mass of H_3^0 . Hence, the region left to the vertical, dotted line is excluded due to the above-mentioned LEP constraints and minimal mass of $H_1^{\pm\pm}$ can be determined from the points at which solid lines intersect vertical, dotted line. Some precise values of $H_1^{\pm\pm}$

masses corresponding to such points are presented in the Table 3.11.

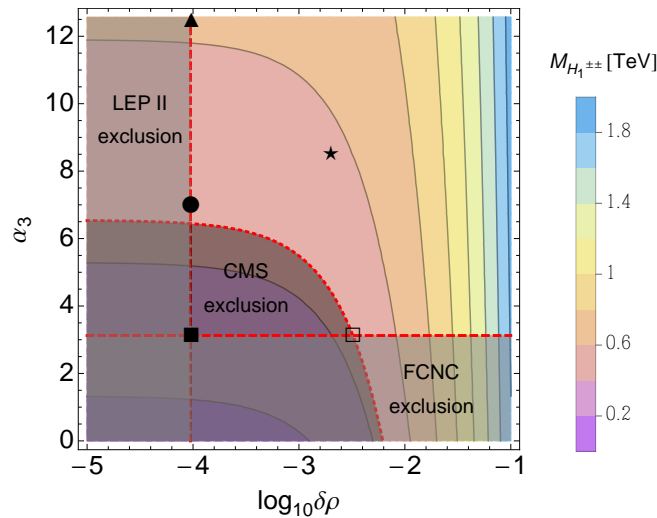


Figure 3.15: Dependence of the $H_1^{\pm\pm}$ mass (in TeV) on $\delta\rho$ and α_3 for $v_R = 8$ TeV. Solid lines divide the parameter space into colored regions in which mass of $H_1^{\pm\pm}$ is characterized according to the legend. Point marked by a \star corresponds to benchmark set of parameters in Eqs. 3.27-3.29. Shaded regions are excluded due to FCNC (under horizontal, dashed line), LEP (left to vertical dashed line) and CMS constraints (under curved dotted line). Squares, circle and triangle correspond to points marked in Fig. 3.14.

Let us remark that there is, in principle, no restriction from the scalar potential parameters on $M_{H_2^{\pm\pm}}$, as the parameter ρ_2 does not play any role to determine the masses of other remaining scalars, H_2^0, A_2^0, H_1^\pm and H_2^\pm . Thus this parameter is not constrained within the perturbative limit. Here, for example we have set $\rho_2 = \delta\rho/4$ in Table 3.11. Moreover, note that $\min(M_{H_1^{\pm\pm}})$ decreases with v_R , see Eq. 3.21.

It is clear that some of the $M_{H_1^{\pm\pm}}$ in Table 3.11 are already excluded by the LHC limits, Eq. 3.12. It means that the first constraints on scalar potential parameters can be derived from those experimental bounds, as already seen in Fig. 3.14 (point marked by empty square). To this end, it is worthwhile to examine the influence of α_3 on the masses of $H_1^{\pm\pm}$. Let us focus on $v_R = 8$ TeV case. When $\delta\rho$ is smaller than about 10^{-4} then the mass of the doubly charged scalar is dominated by the term $\sqrt{\alpha_3}\kappa_1/\sqrt{2}$. On the other hand, if $\delta\rho$ is bigger than 10^{-2} then its mass is mainly driven by $v_R\sqrt{\delta\rho/2}$. In Fig. 3.15, it is shown, how those masses depend on $\delta\rho$ and α_3 in the region of the parameter space

where both contributions to masses are important. In this plot, we have shaded the regions of the parameter space which are excluded either by FCNC (*i.e.* $M_{H_1^0, A_1^0} \gtrsim 10$ TeV) or LHC. Note that there is also the excluded region related to the lower bound on H_3^0 mass (left of the vertical dashed line). It is straightforward to do similar analysis for the dependence of $H_2^{\pm\pm}$ mass on α_3 and ρ_2 .

As an example, we present benchmark set of scalar masses which satisfy both FCNC and LHC constraints with light and degenerate masses of doubly charged scalars, assuming $v_R = 8$ TeV (all masses are given in GeV):

$$M_{H_0^0} = 125, \quad (3.22)$$

$$M_{H_1^0} = 16492, \quad M_{H_2^0} = 11314, \quad M_{H_3^0} = 253, \quad (3.23)$$

$$M_{A_1^0} = 16496, \quad M_{A_2^0} = 253, \quad (3.24)$$

$$M_{H_1^\pm} = 439, \quad M_{H_2^\pm} = 16496, \quad (3.25)$$

$$M_{H_1^{\pm\pm}} = 567, \quad M_{H_2^{\pm\pm}} = 567. \quad (3.26)$$

These masses are outcome of the following parameters of the scalar potential:

$$\rho_1 = 1.0, \quad \rho_2 = 5 \cdot 10^{-4}, \quad \rho_3 - 2\rho_1 = 2 \cdot 10^{-3}, \quad (3.27)$$

$$\lambda_1 = 0.13, \quad \lambda_2 = 0, \quad \lambda_3 = 1, \quad (3.28)$$

$$\alpha_3 = 8.5. \quad (3.29)$$

This scenario realizes mass spectrum with maximal number (three) of light charged scalars [163]. Of course, other setups are also possible. For example, increasing parity breaking scale to 20 TeV, setting $\alpha_3 \sim 0.5$, $\rho_1 \sim \rho_2 \gtrsim \alpha_3/4$ and tuning $\delta\rho \sim 10^{-3}$ give H_3^0 , A_2^0 , H_1^\pm and $H_1^{\pm\pm}$ masses $\sim v_R \sqrt{\delta\rho/2} \sim 450$ GeV, while the remaining scalars (beside H_0^0) have masses larger than $v_R \sqrt{\alpha_3/2} \sim 10$ TeV. The other option is to keep $v_R \sim 10$ TeV but also choose $\rho_2 \sim 10^{-3}$ and set $\delta\rho \sim \alpha_3 \sim 2$. As a result, only $H_2^{\pm\pm}$ is light, with mass ~ 500 GeV, while other scalars are heavier than 10 TeV.

Let us note that all these spectra are also in agreement with low-energy constraints, like the muon decay [174, 178, 179].

3.4.4 Constraints on α_3 and $\delta\rho$: adding vacuum stability condition

In the previous section we have worked with the scalar mass spectra which are compatible with unitarity of the potential parameters, large parity breaking scale v_R and severe bounds on neutral scalar masses ($M_{H_1^0}, M_{A_1^0}$) derived from Flavor Changing Neutral Current (FCNC) constraints. Here we further implement another necessary condition: vacuum stability of the scalar potential. It appears that even after taking into account all these constraints, the consistent scalar mass spectra can accommodate doubly charged Higgs boson masses in a region which can be explored by the LHC.

Analysis of the LHC data provides lower limits on doubly charged Higgs mass [214] depending on their leptonic decay branching fractions. In the scenario where $\text{BR}(H^{++} \rightarrow e^+e^+) = \text{BR}(H^{++} \rightarrow \mu^+\mu^+) \approx 0.5$ that limit is $M_{\text{LHC}} = M_{H^{\pm\pm}} \approx 450$ GeV, see Fig. 3.16 for details.

Limits on MLRSM potential parameters have been discussed lately in [181]. Similar to the earlier case we focus on α_3 and $\delta\rho = \rho_3 - 2\rho_1$ parameters, which are important for the scalar mass spectrum (all notations are as in [163, 181]). First, to suppress FCNC effects generated by H_1^0 and A_1^0 , we assume¹⁴ $M_{\text{FCNC}} = 10$ TeV. Because $M_{H_1^0, A_1^0} = \alpha_3 v_R^2/2$, this results in the following lower limit on α_3 :

$$\alpha_3 \geq \frac{2M_{\text{FCNC}}^2}{v_R^2}. \quad (3.30)$$

Taking into account that $M_{H_1^{\pm\pm}}^2 = (\delta\rho v_R^2 + \alpha_3 \kappa^2)/2$ one gets

$$\alpha_3 \geq \frac{1}{\kappa^2}(2M_{\text{LHC}}^2 - \delta\rho v_R^2), \quad (3.31)$$

where $\kappa = 246$ GeV is the electroweak symmetry breaking scale. Third constraint

¹⁴To our knowledge, their effects have been discussed for the first time in the context of Left-Right models in [208], see also [77, 78, 178, 209, 210] and recent [79]. In general, their masses need to be at least of the order of 10 TeV, though some alternatives have been also considered in [206].

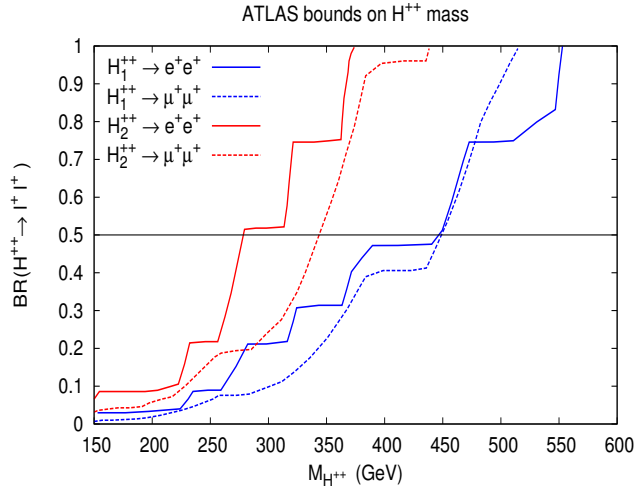


Figure 3.16: Exclusion limits on the masses of doubly charged scalars from ATLAS analysis, depending on their leptonic branching ratios. The lepton flavor violating modes are not shown here, as they are not concerned with the purpose of our analysis. This plot is based on Fig. 5 in [214].

originates from the *necessary condition* for the boundedness of the potential [215]:

$$\alpha_3 \leq \sqrt{8\lambda_1(4\pi - \delta\rho)} \quad (3.32)$$

The value of λ_1 is fixed by the lightest neutral Higgs boson mass as $M_{H_0^0} = 2\lambda_1\kappa^2$. As one can see these bounds suggested in Eqs. 3.30, 3.31 and 3.32 restrict a wide range of parameter space $(\alpha_3, \delta\rho)$ and rather allow a modest set of values.

Now, it is interesting and important to ask what is the maximum allowed mass splitting $\Delta M = M_{H_1^{\pm\pm}} - M_{H_1^\pm}$ that will be consistent with the bounds on $(\alpha_3, \delta\rho)$ derived above. Such queries cannot be unnoticed from phenomenological perspective because only for $\Delta M > M_{W_1}$, doubly charged Higgs can have following decay: $H_1^{\pm\pm} \rightarrow H_1^\pm W_1^\pm$. Thus, this has a massive impact on decay branching ratios of $H^{\pm\pm}$. It is straightforward to check that the biggest ΔM is reached for $\delta\rho$ saturating both inequalities in Eqs. 3.31 and 3.32 which imply

$$\frac{1}{\kappa^2}(2M_{\text{LHC}}^2 - \delta\rho v_R^2) = \sqrt{8\lambda_1(4\pi - \delta\rho)}. \quad (3.33)$$

The physical solution to this equation and corresponding maximal value of ΔM

is

$$\begin{aligned}\delta\rho &= \frac{2(M_{\text{LHC}}^2 - \sqrt{8\pi\lambda_1}\kappa^2)}{v_R^2}(1 + \dots), \\ \Delta M &= \Delta M_\infty(1 + \dots),\end{aligned}\tag{3.34}$$

where ‘...’ stands for corrections of the order of $\mathcal{O}(M_{\text{LHC}}^2/v_R^2, \kappa^2/v_R^2)$. One can check that ΔM depends on v_R very weakly and is nearly equal to the asymptotic value $\Delta M_\infty = \lim_{v_R \rightarrow \infty} \Delta M = M_{\text{LHC}} - \sqrt{M_{\text{LHC}}^2 - \sqrt{2\pi\lambda_1}\kappa^2} \approx 65.3 \text{ GeV}$, for $M_{\text{LHC}} = 450 \text{ GeV}$. As $\partial_{v_R} \Delta M > 0$, this implies that on-shell decay $H_1^{\pm\pm} \rightarrow H_1^\pm W_1^\pm$ is kinematically forbidden regardless of the scale v_R . Interestingly, we came to the same conclusion as in [216], but based on different kind of arguments. There is another consequence of the requirement that the scalar potential is bounded from below. Namely, one can show that, using Eqs. 3.30 and 3.32, in the allowed parameter space there is an upper limit on $H_1^{\pm\pm}$ mass:

$$M_{H_1^{\pm\pm}} \leq \frac{1}{2} \sqrt{8\pi v_R^2 - \frac{M_{\text{FCNC}}^4}{\lambda_1 v_R^2}}(1 + \dots) \approx 9.98 \text{ TeV},\tag{3.35}$$

where ‘...’ stands for the corrections of the order of $\mathcal{O}(\kappa^2/v_R^2)$. The maximal value of $M_{H_1^{\pm\pm}}$ is reached for $\delta\rho$ satisfying $\sqrt{8\lambda_1(4\pi - \delta\rho)} = 2M_{\text{FCNC}}^2/v_R^2$ and $\alpha_3 = 2M_{\text{FCNC}}^2/v_R^2$, which correspond to the intersection point of lines restricting regions defined by Eqs. 3.30 and 3.32. The situation is summarized in Fig. 3.17. Naturally, the minimal value of $H_1^{\pm\pm}$ mass in the discussed set up is M_{LHC} . For the sake of completeness, let us note that if there are no experimental limits on $M_{H_1^{\pm\pm}}$ and H_3^0 then the lowest possible mass of $H_1^{\pm\pm}$ consistent with the vacuum stability bound, Eq. 3.32 would be $\sqrt{2\sqrt{\pi}M_{H_3^0}v} \approx 330 \text{ GeV}$, which corresponds to $\delta\rho \rightarrow 0$ and $\alpha_3 \rightarrow \sqrt{32\pi\lambda_1}$. On the other hand, the MLRSM does not provide any relevant constraints on $H_2^{\pm\pm}$ mass¹⁵. In passing, we would like to mention that similar type of decay of $H_2^{\pm\pm}$ is kinematically forbidden as W_2^\pm and H_2^\pm are

¹⁵The only constraint which could arise is $M_{H_2^{\pm\pm}} < 2\sqrt{6\pi}v_R \approx 40 \text{ TeV}$ for $v_R = 8 \text{ TeV}$. It comes from the assumption that scalar potential parameter ρ_2 is in the perturbative regime $\rho_2 < 4\pi$.

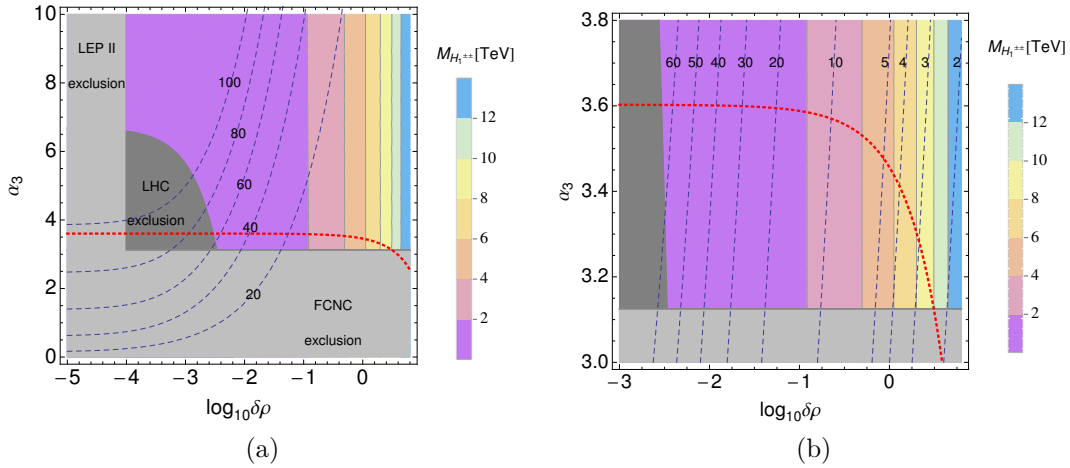


Figure 3.17: (*left panel*) Dependence of the $H_1^{\pm\pm}$ mass (in TeV) on $\delta\rho$ and α_3 for $v_R = 8$ TeV. The parameter space $(\delta\rho, \alpha_3)$ is divided into colored regions where mass of $H_1^{\pm\pm}$ is characterized according to the attached legend on-side legend strip. Shaded regions are excluded due to FCNC, LHC and LEP constraints - see Eqs. 3.30 and 3.31 and Refs. [181, 213] respectively. The parameter space above the red-dotted line is disfavored due to the unboundedness of the scalar potential - see Eq. 3.32. Blue, dashed lines represent sets of points $(\delta\rho, \alpha_3)$ for which mass splitting $(M_{H_1^{\pm\pm}} - M_{H_1^\pm})$ is 100, 80, 60, 40 and 20 GeV respectively. (*right panel*) Detailed view of the allowed part of parameter space with refined mass splitting lines.

much heavy, see the benchmarks in later section.

3.4.5 Multilepton signal from the charged scalars in MLRSM

In this study, we consider only the processes where charged Higgs particles can be produced directly as shown in the Table 3.12, first column. As we can see from the table, the cleanest signals are connected with doubly charged Higgs particles, that is why we focus particularly on them in this study. For some related discussions on doubly charged scalars, see *e.g.* [112, 182, 217–223].

For processes III-X important are charged Higgs boson decay modes. For doubly charged Higgs particles possible decay modes are

Primary production	Secondary production	Signal
I. $H_1^+ H_1^-$	$\ell^+ \ell^- \nu_L \nu_L$	$\ell^+ \ell^- \oplus MET$
–	$\ell^+ \ell^- N_R N_R$	depends on N_R decay modes
–	$\ell^+ \ell^- \nu_L N_R$	depends on N_R decay modes
II. $H_2^+ H_2^-$	$\ell^+ \ell^- \nu_L \nu_L$	$\ell^+ \ell^- \oplus MET$
–	$\ell^+ \ell^- N_R N_R$	depends on N_R decay modes
–	$\ell^+ \ell^- \nu_L N_R$	depends on N_R decay modes
III. $H_1^{++} H_1^{--}$	–	$\ell^+ \ell^+ \ell^- \ell^-$
–	$H_1^+ H_1^+ H_1^- H_1^-$	See I
–	$H_1^\pm H_1^\pm H_2^\mp H_2^\mp$	See I & II
–	$H_2^+ H_2^+ H_2^- H_2^-$	See II
–	$W_i^+ W_i^+ W_j^- W_j^-$	depends on W 's decay modes
IV. $H_2^{++} H_2^{--}$	–	$\ell^+ \ell^+ \ell^- \ell^-$
–	$H_2^+ H_2^+ H_2^- H_2^-$	See II
–	$H_1^\pm H_1^\pm H_2^\mp H_2^\mp$	See I & II
–	$H_1^+ H_1^+ H_1^- H_1^-$	See I
–	$W_i^+ W_i^+ W_j^- W_j^-$	depends on W 's decay modes
V. $H_1^{\pm\pm} H_1^\mp$	–	$\ell^\pm \ell^\pm \ell^\mp \nu_L$
VI. $H_2^{\pm\pm} H_2^\mp$	–	$\ell^\pm \ell^\pm \ell^\mp \nu_L$
VII. $H_1^\pm Z_i, H_1^\pm W_i$	–	See I & Z_i, W_i decay modes
VIII. $H_2^\pm Z_i, H_2^\pm W_i$	–	See II & Z_i, W_i decay modes
IX. $H_1^\pm \gamma$	–	See I
X. $H_2^\pm \gamma$	–	See II

Table 3.12: Phenomenologically interesting MLRSM processes at the LHC with primarily produced charged scalar particles and possible final signals. Here γ denotes a photon. ν_L are SM-like light neutrino states and N_R are heavy neutrino states dominated by right-handed weak neutrinos. From now on we will denote $N_R \equiv N$. Here ℓ represents light charged leptons e, μ .

$$\begin{aligned}
 \text{(i)} \quad & H_1^{\pm\pm} \rightarrow l^\pm l^\pm, \\
 \text{(ii)} \quad & H_1^{\pm\pm} \rightarrow H_1^\pm W_1^\pm; \\
 \text{(iii)} \quad & H_2^{\pm\pm} \rightarrow l^\pm l^\pm, \\
 \text{(iv)} \quad & H_2^{\pm\pm} \rightarrow H_2^\pm W_2^\pm; \\
 \text{(v)} \quad & H_2^{\pm\pm} \rightarrow W_2^\pm W_2^\pm; \\
 \text{(vi)} \quad & H_2^{\pm\pm} \rightarrow H_2^\pm W_1^\pm;
 \end{aligned} \tag{3.36}$$

where $l = e, \mu, \tau$.

Apart from the above decay modes, the other possibilities for the doubly

charged scalars can be

$$\begin{aligned} \text{(vii)} \quad & H_2^{\pm\pm} \rightarrow H_1^\pm H_1^\pm, \\ \text{(viii)} \quad & H_2^{\pm\pm} \rightarrow H_2^\pm H_2^\pm; \end{aligned} \tag{3.37}$$

when they are not degenerate with the singly charged ones. But for nearly or an exact degenerate case, the charged scalars dominantly decay through leptonic modes and here kinematics play a role too.

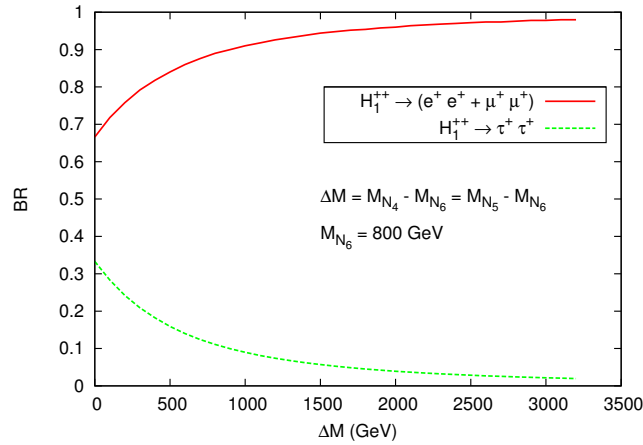


Figure 3.18: Branching ratios for the decay modes $(e^+e^+ + \mu^+\mu^+)$ and $\tau^+\tau^+$ of the doubly charged scalars as a function of ΔM , where $\Delta M = M_{N_4} - M_{N_6} = M_{N_5} - M_{N_6}$. We have kept fixed $M_{N_6} = 800$ GeV. Note that the BRs of both the doubly charged scalars (H_1^{++} and H_2^{++}) are the same in scenarios where $M_{W_2} \gg M_{H^{\pm\pm}}$ and $M_{H^{\pm\pm}} \simeq M_{H^\pm}$.

Fig. 3.18 shows a scenario in which pure leptonic decay modes can be realized. The crucial factor is the Yukawa coupling which depends (indirectly) on heavy right-handed neutrino mass. If heavy neutrino masses are degenerate then democratic scenario is understood where all leptonic channels are the same (*i.e.* $\text{BR}(H^{\pm\pm} \rightarrow e^\pm e^\pm) \simeq 33\%$).

Typically, as can be seen from Fig. 3.18, for right-handed neutrino masses to be 1 TeV, 1 TeV and 800 GeV for N_4, N_5, N_6 respectively, the branching ratios are the following

$$\begin{aligned} \text{BR}(H_{1/2}^{\pm\pm} \rightarrow e^\pm e^\pm) &= 37.9\%, \\ \text{BR}(H_{1/2}^{\pm\pm} \rightarrow \mu^\pm \mu^\pm) &= 37.9\%, \\ \text{BR}(H_{1/2}^{\pm\pm} \rightarrow \tau^\pm \tau^\pm) &= 24.2\%. \end{aligned} \tag{3.38}$$

If the first two generations neutrinos (N_4, N_5) have masses above ~ 4 TeV, τ decay mode is practically irrelevant. From the discussion it is also clear, that *one of the decay modes can dominate if only one of the right-handed neutrino masses is much bigger than remaining two heavy neutrino states*. Limits in Eq. 3.12 assume 100% leptonic decays, in our case, taking into account Fig. 3.18, Eq. 3.38 and results given in [193, 194], mass limits are much weaker, at about 300 GeV, see *e.g.* Fig. 3 in [194].

For decays of singly charged H_1^\pm scalars situation is analogical as for doubly charged scalars (possible decay modes to neutral H_1^0 and A_1^0 scalars are negligible for $M_{H_1^0}, M_{A_1^0} \gg M_{H_1^\pm}$, as dictated by FCNC constraints).

\tilde{H}_2^\pm decays hadronically, namely, for $100 \text{ GeV} < M_{\tilde{H}_2^\pm} < 200 \text{ GeV}$

$$\begin{aligned} \text{BR}(\tilde{H}_2^+ \rightarrow c\bar{s}) &= 95\%, \\ \text{BR}(\tilde{H}_2^+ \rightarrow c\bar{d}) &= 5\%, \end{aligned} \tag{3.39}$$

and $\text{BR}(\tilde{H}_2^+ \rightarrow t\bar{b}) \sim 100\%$ for $M_{\tilde{H}_2^\pm} > 200 \text{ GeV}$.

3.4.5.1 Primary production of heavy charged Higgs bosons at the LHC

Below different processes involving solely charged scalar productions are classified. In analysis which follow $v_R = 8000 \text{ GeV}$ to respect with a large excess the present exclusion limits on W_2^\pm , and Z_2 masses. SM-Higgs like mass is set to 125 GeV, masses of neutral scalar particles are set at a very high limit (~ 10 TeV). In this way, as already discussed, scenarios are realized with relatively light (hundreds of GeV) charged Higgs bosons while remaining non-standard particles within MLRSM are much heavier. All cross sections given in this section are without any kinematic cuts, those will be considered with final signals and distributions in Section 3.4.7.

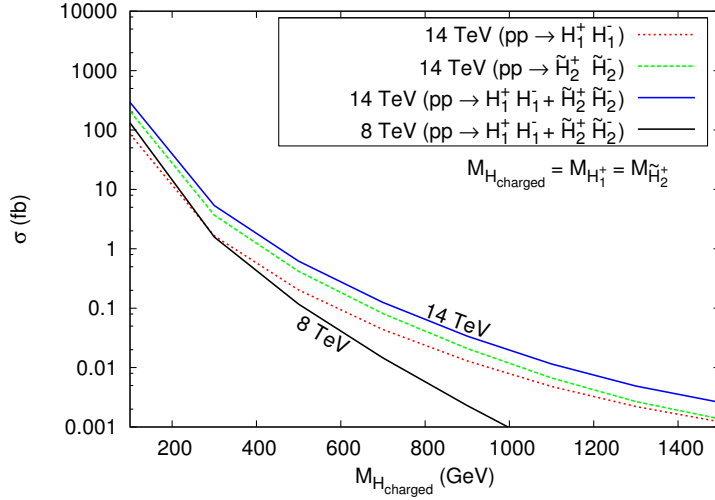


Figure 3.19: Production cross sections for $pp \rightarrow H_1^+ H_1^-$ and $pp \rightarrow \tilde{H}_2^+ \tilde{H}_2^-$ processes without imposing kinematic cuts.

3.4.5.2 $pp \rightarrow H_1^+ H_1^-$ and $pp \rightarrow H_2^+ H_2^-$

The cross section for singly charged scalar pair production as a function of their mass is given in Fig. 3.19. This process is dominated by s-channel γ, Z_1 and t-channel quark exchange diagrams. Contributions coming from s-channel H_0^0, Z_2 and H_1^0 bosons are negligible for considered MLRSM parameters. For singly charged scalar mass of 400 GeV, the cross sections are (as discussed in Section 2, H_2^\pm Higgs boson is assumed to be light and we denote it here with a tilde, for $M_{H_2^\pm} \gg 1$ TeV the considered cross section is negligible, $\sigma(pp \rightarrow \tilde{H}_2^\pm \tilde{H}_2^\mp) \simeq 0$)

$$\sigma(pp \rightarrow H_1^\pm H_1^\mp) = 0.12 \text{ (0.52) fb}, \quad (3.40)$$

$$\sigma(pp \rightarrow \tilde{H}_2^\pm \tilde{H}_2^\mp) = 0.27 \text{ (1.12) fb}, \quad (3.41)$$

while for singly charged scalar mass equals to 600 GeV are

$$\sigma(pp \rightarrow H_1^\pm H_1^\mp) = 0.01 \text{ (0.09) fb}, \quad (3.42)$$

$$\sigma(pp \rightarrow \tilde{H}_2^\pm \tilde{H}_2^\mp) = 0.03 \text{ (0.18) fb}, \quad (3.43)$$

with $\sqrt{s} = 8$ (14) TeV.

Increasing center of mass energy from $\sqrt{s} = 8$ TeV to $\sqrt{s} = 14$ TeV the cross sections grow by factors $\sim 4 \div 7$, depending on masses of charged Higgs bosons. In general cross sections fall down below 0.1 fb for masses of charged scalars above approximately 730 (420) GeV for $\sqrt{s} = 14$ (8) TeV.

3.4.5.3 $pp \rightarrow H_1^{++}H_1^{--}$ and $pp \rightarrow H_2^{++}H_2^{--}$

The dominant contribution to these processes is via neutral s-channel current, *i.e.*, via Z_1 and γ . Contributions coming from s-channel H_0^0, Z_2 and H_1^0 are negligible for considered MLRSM parameters.

To explore the phenomenological aspects of the doubly charged scalars in the MLRSM model we consider two scenarios. *Scenario I* when the doubly charged scalars are degenerate in mass, *i.e.*, $M_{H_1^{\pm\pm}} = M_{H_2^{\pm\pm}}$. This scenario is motivated by analysis of the Higgs potential. In *Scenario II* masses are different, *i.e.*, $M_{H_1^{\pm\pm}} \neq M_{H_2^{\pm\pm}}$.

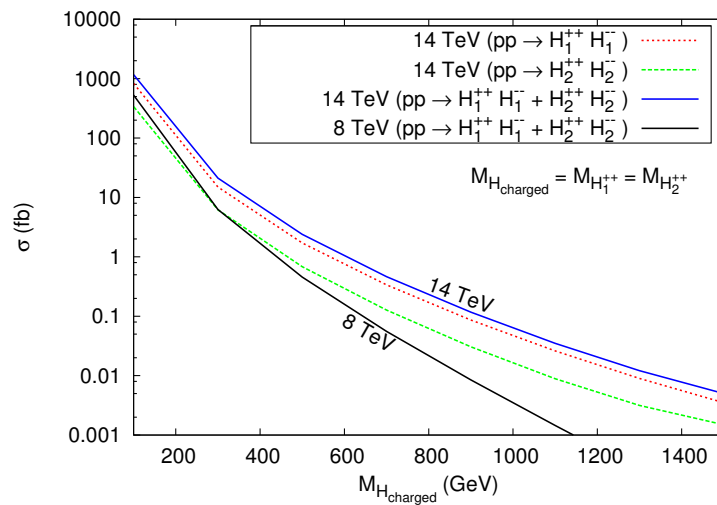


Figure 3.20: Scenario I. Cross sections for $pp \rightarrow H_1^{++}H_1^{--}$ and $pp \rightarrow H_2^{++}H_2^{--}$ processes without imposing kinematic cuts.

Scenario I, degenerate mass spectrum

In our analysis we set our benchmark point with both of the doubly charged scalars at the same mass $M_{H_1^{++}} = M_{H_2^{++}} = 400$ GeV. In this case, the cross

section at the LHC without imposing any cut at $\sqrt{s} = 8$ (14) TeV is

$$\sigma(pp \rightarrow (H_1^{++}H_1^{--} + H_2^{++}H_2^{--}) \rightarrow \ell_i^+\ell_i^+\ell_j^-\ell_j^-) = 1.44 \text{ (6.06) fb}, \quad (3.44)$$

The contributions to the cross sections from two possible channels are noted for $\sqrt{s} = 8$ (14) TeV as

$$\sigma(pp \rightarrow H_1^{++}H_1^{--}) = 1.09 \text{ (4.58) fb}, \quad (3.45)$$

$$\sigma(pp \rightarrow H_2^{++}H_2^{--}) = 0.45 \text{ (1.86) fb}, \quad (3.46)$$

where $\ell_{i,j} = e, \mu$.

For $M_{H_1^{++}} = M_{H_2^{++}} = 600$ GeV it is

$$\sigma(pp \rightarrow (H_1^{++}H_1^{--} + H_2^{++}H_2^{--}) \rightarrow \ell_i^+\ell_i^+\ell_j^-\ell_j^-) = 0.14 \text{ (0.95) fb}, \quad (3.47)$$

for $\sqrt{s} = 8$ (14) TeV. The contributions to the cross sections from individual channels for $\sqrt{s} = 8$ (14) TeV are as following:

$$\sigma(pp \rightarrow H_1^{++}H_1^{--}) = 0.11 \text{ (0.73) fb}, \quad (3.48)$$

$$\sigma(pp \rightarrow H_2^{++}H_2^{--}) = 0.04 \text{ (0.28) fb}. \quad (3.49)$$

The cross sections for pair productions of doubly charged scalars at the LHC with 14 and 8 TeV are given in Fig. 3.20. From the figure we can see that cross sections fall very rapidly as the masses of the doubly charged scalars increase. Also, the production cross section for $H_1^{\pm\pm}$ is much larger than that for $H_2^{\pm\pm}$ as shown in the figure. The cross section at $\sqrt{s} = 14$ (8) TeV for scalar masses above 920(640) GeV is ≤ 0.1 fb.

Scenario II, non-degenerate mass spectrum

Here we choose another set of benchmark points where the doubly charged scalars are non-degenerate. The cross section for the same process with $M_{H_1^{\pm\pm}} = 400$

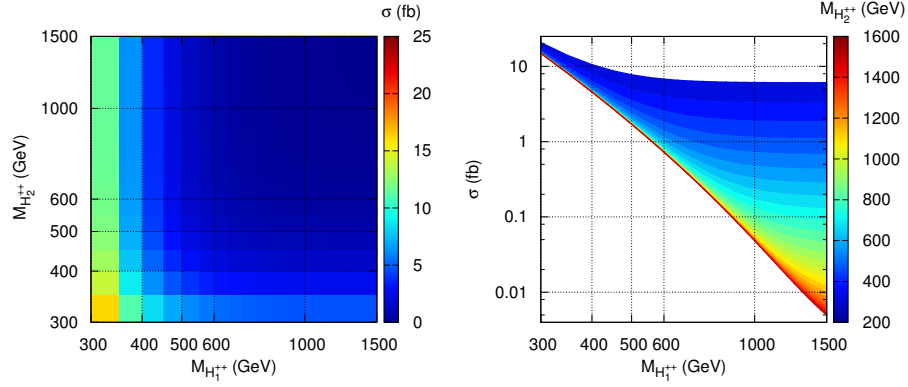


Figure 3.21: Scenario II. Contour plots for the $pp \rightarrow (H_1^{++}H_1^{--} + H_2^{++}H_2^{--})$ cross section. $\sqrt{s} = 14$ TeV, no kinematic cuts imposed.

GeV and $M_{H_2^{\pm\pm}} = 500$ GeV at $\sqrt{s} = 14$ TeV is

$$\sigma(pp \rightarrow (H_1^{++}H_1^{--} + H_2^{++}H_2^{--}) \rightarrow \ell_i^+\ell_i^+\ell_j^-\ell_j^-) = 4.95 \text{ fb.} \quad (3.50)$$

The contributions to the cross sections from individual channels are given as:

$$\sigma(pp \rightarrow H_1^{++}H_1^{--}) = 1.09 \text{ (4.58) fb,} \quad (3.51)$$

$$\sigma(pp \rightarrow H_2^{++}H_2^{--}) = 0.13 \text{ (0.69) fb,} \quad (3.52)$$

for $\sqrt{s} = 8$ (14) TeV.

Contour plots for the $pp \rightarrow (H_1^{++}H_1^{--} + H_2^{++}H_2^{--})$ cross section as a function of doubly charged scalar masses is shown in Fig. 3.21 (left). On the right plot of Fig. 3.21 different projections are used where X and Y axes are for $M_{H_1^{++}}$ and the cross section, respectively, whereas $M_{H_2^{++}}$ is projected as a contour. As can be seen from these figures, cross sections at the level of 1 fb can be obtained for doubly charged scalar masses up to approximately 600 GeV.

3.4.5.4 $pp \rightarrow H_1^{\pm\pm}H_1^\mp$ and $pp \rightarrow H_2^{\pm\pm}H_2^\mp$

The production of a doubly charged scalar in association with a singly charged scalar goes through the charged s-channel interaction where $W_{1,2}^\pm$ gauge bosons

are exchanged. Diagrams with s-channel exchanged singly charged scalar H_2^\pm is negligible (its coupling to W_1 is proportional to v_L which is zero). As W_2^\pm is very heavy, the dominant contribution originates from the process via W_1^\pm .

For this state we consider a different set of benchmark points, we set $v_R = 8$ TeV and the following charged scalar masses: $M_{H_1^{\pm\pm}} = 483$ GeV, $M_{H_2^{\pm\pm}} = 527$ GeV, $M_{H_1^\pm} = 355$ GeV, $M_{H_2^\pm} = 15066$ GeV. The choice is for the following Higgs potential parameters (for the mass formulas, see the Appendix): $\rho_1 = 0.2397, \rho_2 = 0.0005, \rho_3 = 0.48, \lambda_1 = 0.13, \lambda_2 = -0.87, \lambda_3 = -5.17, \alpha_3 = 7.09$. This example shows that a wide spectrum of charged scalar masses can be easily obtained, still keeping reasonable small potential parameters (important for higher order perturbation analysis). To reduce τ channel decays, the masses for the heavy right-handed neutrinos are set at 4 TeV for the first two generations and 800 GeV for the third generation, see Fig. 3.18. The cross section for the process before any kinematic cuts with a center of mass energy $\sqrt{s} = 8(14)$ TeV at the LHC is

$$\sigma\left(pp \rightarrow (H_1^{\pm\pm}H_1^\mp + H_2^{\pm\pm}H_2^\mp) \rightarrow \ell\ell\nu_\ell\right) = 1.44 (6.05) \text{ fb.} \quad (3.53)$$

The contributions to the cross sections from individual channels are noted as:

$$\sigma(pp \rightarrow H_1^{\pm\pm}H_1^\mp) = 1.48 (6.24) \text{ fb,} \quad (3.54)$$

$$\sigma(pp \rightarrow H_2^{\pm\pm}H_2^\mp) \sim 0 (0) \text{ fb,} \quad (3.55)$$

with $\sqrt{s} = 8 (14)$ TeV.

For the model consistency (*i.e.* chosen potential parameters), the second singly charged scalar has been chosen with very high mass $M_{H_2^\pm} = 15066$ GeV. Even if it has low mass (~ 400 GeV) then also the cross section for the processes $pp \rightarrow H_2^{\pm\pm}H_2^\mp$ is very low compared to $pp \rightarrow H_1^{\pm\pm}H_1^\mp$, as $H_2^{\pm\pm}H_2^\mp W_1^\mp$ coupling is proportional to $\sin\xi$ and $H_2^{\pm\pm}H_2^\mp W_2^\mp$ coupling is proportional to $\cos\xi$. On the other hand, $H_1^{\pm\pm}H_1^\mp W_1^\mp$ coupling is proportional to $\cos\xi$ and $H_1^{\pm\pm}H_1^\mp W_2^\mp$ coupling is proportional to $\sin\xi$. In both the cases, W_2^\pm mediated processes are much less dominant than the W_1^\pm mediated processes. But as the charged

gauge boson mixing angle ξ is neglected, the $H_2^{\pm\pm}H_2^\mp W_1^\mp$ vertex is much more suppressed compared to $H_1^{\pm\pm}H_1^\mp W_1^\mp$.

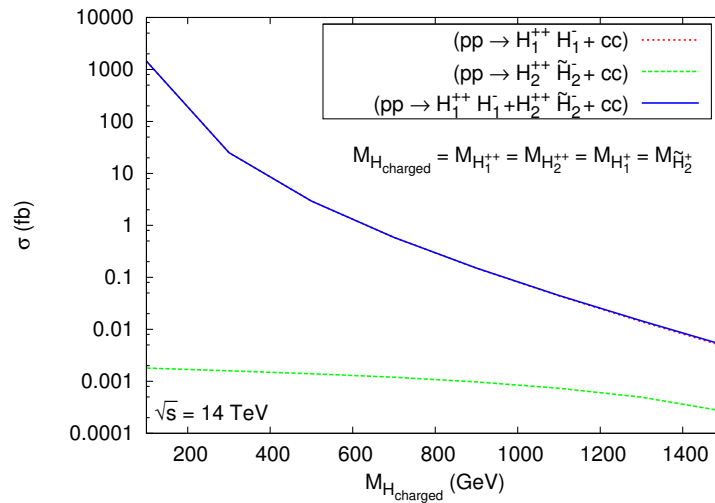


Figure 3.22: Production cross sections for $pp \rightarrow H_1^{++}H_1^-$ and $pp \rightarrow H_2^{++}\tilde{H}_2^-$ processes at $\sqrt{s} = 14$ TeV and no kinematic cuts are imposed. Mass of H_2^\pm is allowed to be small and denoted with a tilde.

It appears that in MLRSM mixed processes, $pp \rightarrow H_1^{++}H_2^-$ and $pp \rightarrow H_2^{++}H_1^-$, vanishes as $v_L = 0$. In Fig. 3.22 the total cross section for two considered processes are given. The mass of H_2^\pm is allowed to be small and because, as discussed before, this is not natural in the MLRSM, its contribution is denoted with a tilde. Anyway, its contribution (keeping a form of its couplings as dictated by MLRSM) is negligible. Final comparison of cross sections of different processes discussed in Sections 3.4.5.2, 3.4.5.3 and 3.4.5.4 is given in Fig. 3.23. We can see that the largest cross sections are for a pair production of singly with doubly charged scalars, and the cross sections for production of doubly charged scalar pair is slightly lower, while the smallest cross section is for pair production of singly charged scalars. Contributions from processes where H_2^\pm is involved are negligible or at most much smaller than corresponding results where H_1^\pm is involved. Keeping in mind the status of the SM background (analyses for our purposes in Section 3.4.8) we look for multilepton signals for three or more leptons. Thus, we focus in the following sections on the processes which involve primary production of at least one doubly charged scalar.

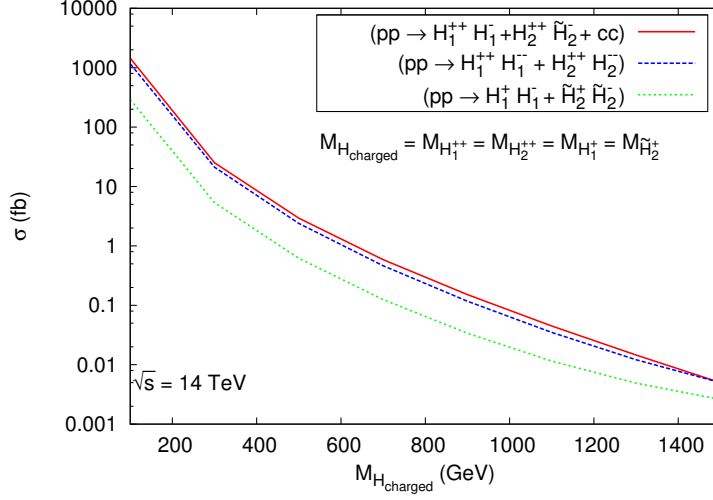


Figure 3.23: Summary of various MLRSM LHC production cross sections considered in the study is shown with charged scalars at $\sqrt{s} = 14$ TeV and without kinematic cuts. We have taken degenerate mass $M_{H_{charged}}$ for $M_{H_1^{++}}$, $M_{H_2^{++}}$, $M_{H_1^+}$ and $M_{H_2^+}$.

3.4.6 Primary production of a heavy Higgs and gauge bosons

3.4.6.1 $pp \rightarrow W_{1/2}^\mp H_{1/2}^\pm$, $pp \rightarrow Z_{1/2} H_{1/2}^\pm$ and $pp \rightarrow \gamma H_{1/2}^\pm$

In our scenarios the production cross sections for these processes are very small and can be ignored. This is because the W_2/Z_2 propagator diagrams are suppressed as they are as heavy as few TeV. For the other light propagators the scalar-gauge boson-gauge boson vertices are proportional to $\sin\xi$ and/or v_L , which are zero here.

3.4.7 Simulations and results for final lepton signals

In this study we are interested in tri- and four-lepton signal events. To enhance such signals, suitable kinematic cuts are applied in order to decrease the SM backgrounds.

3.4.7.1 Events selection criteria

The detailed simulation criteria mentioned in the initial part of the section, are used in our study.

3.4.7.2 Signal events for doubly charged Higgs particles in MLRSM

Doubly charged scalars decay mainly to either a pair of same-sign charged leptons or charged gauge bosons depending on the choice of parameters. As already discussed, we have chosen the parameter space in such a way that the doubly charged scalars decay to charged leptons with almost 100% branching ratio.

This decay is lepton number violating and can also be possibly lepton flavor violating. In our scenarios we assume no lepton flavor violation as the Yukawa couplings are considered to be flavor diagonal. Thus, the four-lepton final state contains two pairs of same-sign and same-flavored charged leptons where each pair has opposite charges to each other. As there is no neutrino (missing energy) or jet involved it is easy to reconstruct the momentum of the final state particles. We have reconstructed invariant masses¹⁶ for same-sign dileptons (SSDL) and opposite-sign dileptons (OSDL). As the doubly charged scalars are the parents of the dilepton pairs, the invariant masses of the SSDL are expected to give a clean peak around the mass of the doubly charged scalar, which is not necessarily a case for OSDL.

3.4.7.3 $pp \rightarrow H_1^{++} H_1^{--}$ and $pp \rightarrow H_2^{++} H_2^{--}$

Scenario I, degenerate doubly charged mass spectrum

As calculated in Section II, Eq. 3.44, if $M_{H_1^{++}} = M_{H_2^{++}} = 400$ GeV, the cross section at the LHC with a center of mass energy $\sqrt{s} = 14$ TeV is $\sigma(pp \rightarrow (H_1^{++} H_1^{--} + H_2^{++} H_2^{--}) \rightarrow \ell_i^+ \ell_i^+ \ell_j^- \ell_j^-) = 6.06$ fb, where $\ell_{i,j} = e, \mu$. After implementing all the cuts, as described in Section 3.4.7.1, the four-lepton events with no missing energy can be estimated. Each pair of SSDL originates from dif-

¹⁶The invariant mass for a lepton pair is defined as $m_{\ell_1 \ell_2} = \sqrt{(E_1 + E_2)^2 - (\vec{P}_1 + \vec{P}_2)^2}$, where E_i and \vec{P}_i are the energy and three-momentum of ℓ_i , respectively.

ferent doubly charged scalars. We have plotted the reconstructed invariant mass distributions for both SSDL and OSDL in Fig. 3.24 with anticipated integrated luminosity $L = 300 \text{ fb}^{-1}$. As both the doubly charged scalars are degenerate the invariant mass peaks occur at around 400 GeV. *This clean reconstruction of the invariant mass is indeed possible even in the hadronic environment and can be a smoking gun feature indicating the presence of doubly charged scalars.*

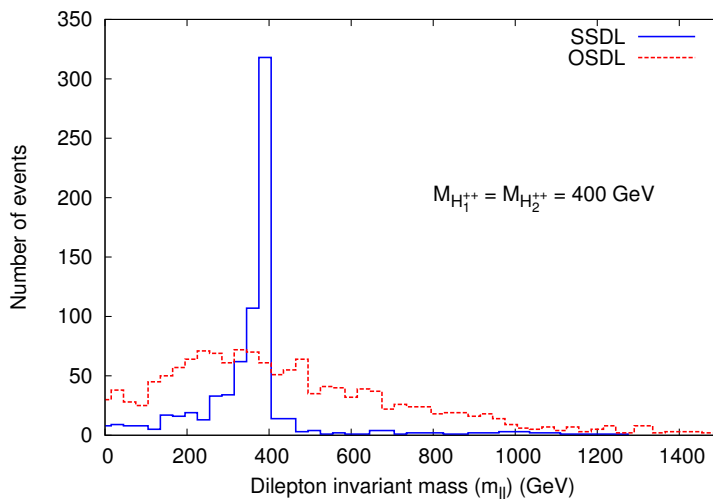


Figure 3.24: Invariant mass for SSDL and OSDL for $(pp \rightarrow H_{1,2}^{++} H_{1,2}^{--} \rightarrow 4l)$ with $M_{H_1^{++}} = M_{H_2^{++}} = 400 \text{ GeV}$ for $\sqrt{s} = 14 \text{ TeV}$ and $L = 300 \text{ fb}^{-1}$. As the doubly charged scalars are degenerate in mass both the invariant mass peaks occur at the same place and, thus, cannot be distinguished.

We have computed this process also with a center of mass energy 8 TeV. In this case we find that the cross section, with $\sqrt{s} = 8 \text{ TeV}$ at the LHC, is 1.06 fb, about 6 times smaller than for $\sqrt{s} = 14 \text{ TeV}$. If we take present integrated luminosity to be 25 fb^{-1} , then the total number of the events even before all the cuts, is statistically insignificant to analyze this particular process at the LHC after implementing all the selection criteria. Thus to observe this four-lepton signal for this scenario needs more data in future.

To select the doubly charged scalar signal properly and in an independent way, there is another interesting variable which can be used for determination of

signals as suggested in [222]

$$\Delta R_{\ell_1 \ell_2} = \sqrt{(\eta_1 - \eta_2)^2 + (\phi_1 - \phi_2)^2}, \quad (3.56)$$

where η_i and ϕ_i denote pseudorapidity and azimuth of ℓ_i , respectively. $\Delta R_{\ell\ell}$ is the separation between two light charged leptons (ℓ) in azimuth-pseudorapidity plane. Its physical importance is that in the detector if $\Delta R_{\ell\ell}$ is smaller than the specified value then one can not distinguish whether the deposited energy is really by one or two leptons. So, one chooses only events for which leptons are well separated. *We expect that the leptons originated from a single doubly charged scalar will be less separated than the leptons coming from different charged scalars.* In the processes that we have considered the doubly charged scalars decay mainly into pairs of same flavored same-sign leptons. Thus, in the case of opposite-sign dilepton pairs, each of them are coming from different doubly charged scalars and, therefore, must be well separated. We have plotted the $\Delta R_{\ell\ell}$ distribution to address this feature. It is pretty clear from Fig. 3.25 that the distribution peaks at smaller $\Delta R_{\ell\ell}$ for same-sign lepton pairs while that for the oppositely charged lepton pairs peaks at a larger value of $\Delta R_{\ell\ell}$, as expected. This implies that most of the leptons in the SSDL pairs are less separated than the leptons which belong to the OSDL pairs.

Scenario II, non-degenerate doubly charged mass spectrum

Here we choose another set of benchmark points where the doubly charged scalars are non-degenerate. In Section II, Eq. 3.50, the cross section at $\sqrt{s} = 14$ TeV has been calculated for the same process with $M_{H_1^{\pm\pm}} = 400$ GeV and $M_{H_2^{\pm\pm}} = 500$ GeV, $\sigma = 4.95$ fb. As $M_{H_2^{\pm\pm}} > M_{H_1^{\pm\pm}}$, the production cross section for $H_1^{\pm\pm}$ is much larger than that for $H_2^{\pm\pm}$. *Thus, the four-lepton events will be generated mostly from the leptonic decays of the $H_1^{\pm\pm}$ pair than $H_2^{\pm\pm}$ decays.* This statement is very distinctively clear from the invariant mass distributions of the same-sign dileptons, as shown in Fig. 3.26. Maximum number of same dilepton events are with an invariant mass peak around $M_{H_1^{\pm\pm}} = 400$ GeV and that around

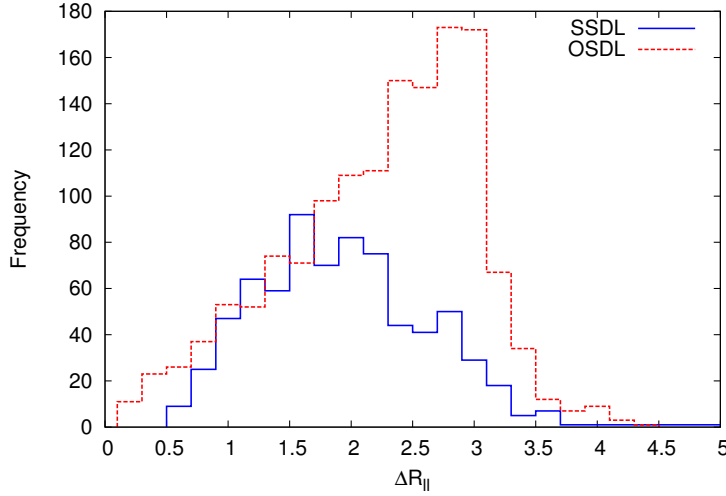


Figure 3.25: Lepton - lepton separations for the same-sign lepton pairs ($\Delta R_{\ell\pm\ell\pm}$) and opposite-sign lepton pairs ($\Delta R_{\ell\pm\ell\mp}$) for ($pp \rightarrow H_{1,2}^{++} H_{1,2}^{--} \rightarrow 4l$) within the degenerate scenario with $M_{H_1^{++}} = M_{H_2^{++}} = 400$ GeV for $\sqrt{s} = 14$ TeV and $L = 300 \text{ fb}^{-1}$.

$M_{H_2^{\pm\pm}} = 500$ GeV is much smaller, as expected.

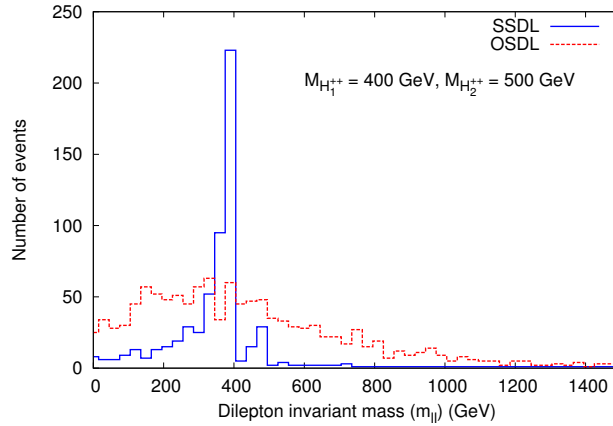


Figure 3.26: Invariant mass for SSDL and OSDL signals in the ($pp \rightarrow H_{1,2}^{++} H_{1,2}^{--} \rightarrow 4l$) process in the non-degenerate mass scenario with $M_{H_1^{\pm\pm}} = 400$ GeV and $M_{H_2^{\pm\pm}} = 500$ GeV for $\sqrt{s} = 14$ TeV and $L = 300 \text{ fb}^{-1}$.

We also performed the $\Delta R_{\ell\ell}$ distribution for the same benchmark point. The results shown in Fig. 3.27 are as our expectation, as explained before.

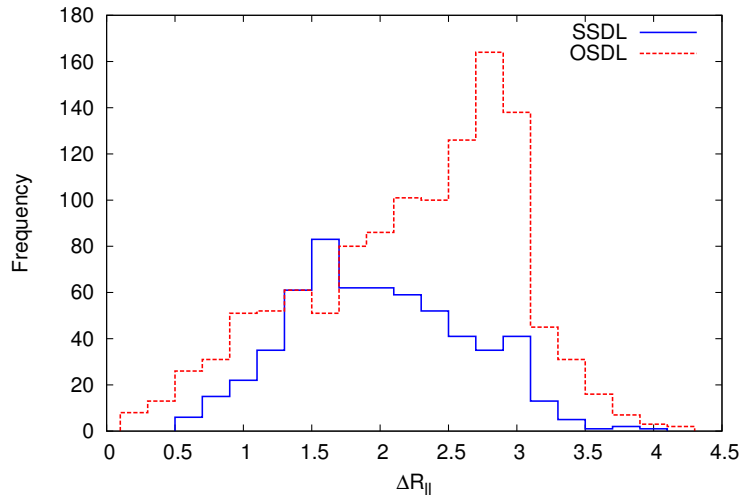


Figure 3.27: Lepton - lepton separations for same-sign lepton pairs ($\Delta R_{\ell^\pm \ell^\pm}$) and opposite-sign lepton pairs ($\Delta R_{\ell^\pm \ell^\mp}$) in the ($pp \rightarrow H_{1,2}^{++} H_{1,2}^{--} \rightarrow 4l$) process for non-degenerate mass scenario having $M_{H_1^\pm} = 400$ GeV and $M_{H_2^\pm} = 500$ GeV with $\sqrt{s} = 14$ TeV and $L = 300$ fb $^{-1}$.

3.4.7.4 $pp \rightarrow H_1^{\pm\pm} H_1^\mp$ and $pp \rightarrow H_2^{\pm\pm} H_2^\mp$

These processes lead to the tri-lepton events with missing p_T , see Table 3.12. For chosen MLRSM parameters, Eq. 3.53, the cross section for the process $pp \rightarrow (H_1^{\pm\pm} H_1^\mp + H_2^{\pm\pm} H_2^\mp) \rightarrow \ell \ell \ell \nu_\ell$, before cuts, with a center of mass energy $\sqrt{s} = 14$ TeV is $\sigma = 6.05$ fb. The tri-lepton events can be classified into two categories: either $\ell^+ \ell^+ \ell^-$ or $\ell^- \ell^- \ell^+$. The first and second types of signals are originated from W_1^+ and W_1^- mediated processes, respectively. Thus, it is indeed possible to estimate the charge asymmetry, defined as the ratio of the number of events of $\ell^+ \ell^+ \ell^-$ type to the number of events of $\ell^- \ell^- \ell^+$ type at the LHC. This is very similar to the forward-backward asymmetry at Tevatron. This charge asymmetry depends on the Parton Distribution Functions (PDF) and, thus, is a special feature of the LHC. We have estimated this ratio (R_\pm^+) with the above choices of charged scalar masses with $\sqrt{s} = 14$ TeV and integrated luminosity 300 fb $^{-1}$.

We find 554 tri-lepton signal events after all the cuts and that leads to

$$R_-^+ = \frac{\# \text{ of events for } \ell^+\ell^+\ell^-}{\# \text{ of events for } \ell^-\ell^-\ell^+} = \frac{396}{158} \simeq 2.51. \quad (3.57)$$

In SM the corresponding value calculated for the main processes given in the next section in Table 3.13 is $(R_-^+)_{SM} = \frac{17.751}{14.962} = 1.186$. This value is slightly different from the calculated values in [224] where higher order corrections are taken into account and the specific kinematic cuts are different. Nevertheless, MLRSM value given in Eq. 3.57 differs substantially from its SM counterpart to signify its presence.

As discussed in Section II, the $H_2^{\pm\pm}H_2^\mp W_1^\mp$ vertex is much more suppressed as compared to $H_1^{\pm\pm}H_1^\mp W_1^\mp$. Thus, in this case most of the tri-lepton events are originated from $pp \rightarrow H_1^{\pm\pm}H_1^\mp$ process. This is clearly visible from the invariant mass distributions. Here we have plotted the same and opposite-sign dilepton invariant mass distributions, see Fig. 3.28. As discussed earlier, *in the opposite-sign lepton pairs two leptons have different origin, thus, their invariant mass distribution is continuous while the same-sign dilepton invariant mass distributions always peak around the mass of the doubly charged scalars.*

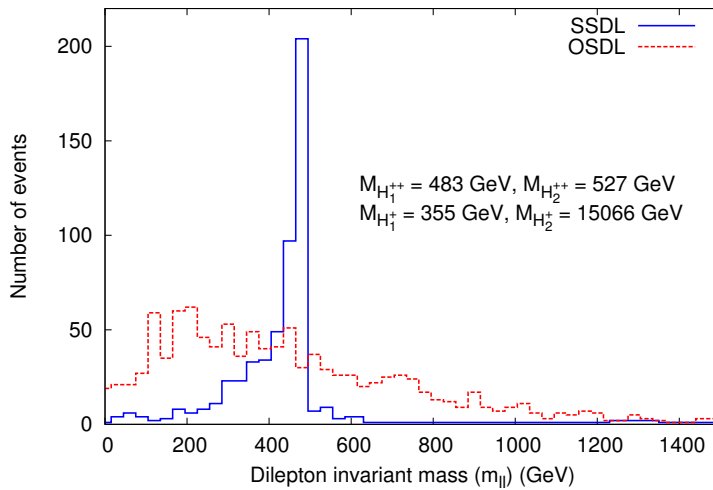


Figure 3.28: Invariant mass plots for SSDL and OSDL for the signals $\ell^\pm\ell^\pm\ell^\mp +$ missing p_T , at the LHC with $\sqrt{s} = 14$ TeV and integrated luminosity 300 fb^{-1} .

From Fig. 3.28, it is distinctly seen that the significant amount of same-sign dilepton pairs peaks at $M_{H_1^{\pm\pm}} = 483$ GeV rather than $M_{H_2^{\pm\pm}} = 527$ GeV. This implies that the dominant contribution to these tri-lepton events are generated through $pp \rightarrow H_1^{\pm\pm} H_1^\mp$ process (*cf.* Fig. 3.22) and the further leptonic decays of the charged scalars.

In Fig. 3.29, separations between leptons are plotted. As can be seen from this figure the SSDL separations peak at a lower value of $\Delta R_{\ell\ell}$, while OSDL separations peak at a larger value of $\Delta R_{\ell\ell}$. This is because same-sign lepton pairs have the origin from the same mother, while opposite-sign lepton pairs have both the leptons from different mothers.

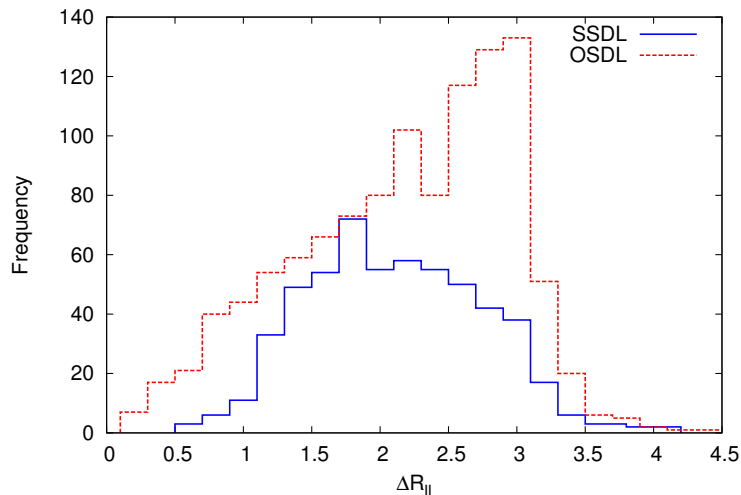


Figure 3.29: Lepton-lepton separation plot for same-sign leptons ($\Delta R_{\ell\pm\ell\pm}$) and opposite-sign leptons ($\Delta R_{\ell\pm\ell\mp}$) in the process ($pp \rightarrow (H_1^{\pm\pm} H_1^\mp + H_2^{\pm\pm} H_2^\mp) \rightarrow 3\ell$). Here $\sqrt{s} = 14$ TeV and integrated luminosity 300 fb^{-1} at the LHC.

For $\sqrt{s} = 8$ TeV and the same benchmark point the production cross section $\sigma(pp \rightarrow (H_1^{\pm\pm} H_1^\mp + H_2^{\pm\pm} H_2^\mp) \rightarrow \ell\ell\nu_\ell) = 1.44 \text{ fb}$ is about four times smaller than for $\sqrt{s} = 14$ TeV, Eq. 3.53. With an integrated luminosity 25 fb^{-1} at $\sqrt{s} = 8$ TeV and 300 fb^{-1} at $\sqrt{s} = 14$ TeV, total number of events is about 50 times smaller in the former case, so the difference is substantial.

Distributions presented so far show that it is possible to extract clear signals for doubly charged scalars at the LHC. However, for signal identification crucial

is how large the SM background effects are and the significance too.

3.4.8 Background estimation and significance of signals

Kinematic cuts are used which have been investigated and established for the first time in [225]. The cuts are optimized in a way such that we can reduce the SM background and enhance the signal events¹⁷. Standard Model background cross sections for tri- and four-lepton signals are given in Table 3.13. In this table we have also separately computed the backgrounds for $\ell^+\ell^+\ell^-$ and $\ell^-\ell^-\ell^+$.

processes	3 ℓ (fb)	$\ell^+\ell^+\ell^-$ (fb)	$\ell^-\ell^-\ell^+$ (fb)	4 ℓ (fb)
$t\bar{t}$	18.973	9.522	9.451	–
$t\bar{t}(Z/\gamma^*)$	1.103	0.549	0.552	0.0816
$t\bar{t}W^\pm$	0.639	0.422	0.214	–
$W^\pm(Z/\gamma^*)$	10.832	6.664	4.164	–
$(Z/\gamma^*)(Z/\gamma^*)$	1.175	0.594	0.581	0.0362
TOTAL	32.722	17.751	14.962	0.1178

Table 3.13: Dominant Standard Model background contributions (in fb) for tri- and four-lepton signals at the LHC with $\sqrt{s} = 14$ TeV after obeying suitable selection criteria defined in the text. The $t\bar{t}$ cross section is presented here after the inclusion of k-factor. While computing the SM contributions to 4 ℓ final state, no missing p_T cut has been applied.

In principle, the tri-lepton contributions can come also from $H_1^{++}H_1^{--}$ and $H_2^{++}H_2^{--}$ involved processes if during simulations one of the four-leptons does not satisfy the cuts. But in our case, this contribution is negligible due to the extra missing energy cut applied as one of the gate pass for the tri-lepton events. Thus, all the productions together are considered and all the intermediate particles are allowed to decay. After passing through the cuts, tri-lepton and four-lepton events are counted.

In Table 3.14 we present the total background and signal events for 25 and

¹⁷In our analysis, while computing the tri-lepton events (signal and background), the p_T of the third hardest lepton needs to be greater than 20 GeV, and also a missing p_T cut (> 30 GeV) must be satisfied, see Section 3.4.7.1. Thus, the tri-lepton background for process like $t\bar{t}$ where one of the lepton is coming from semi-leptonic decays of B 's is reduced. Here the hadronic activity cut also reduces the hadronic activity around the selected leptons and plays a crucial role in this case. All these cuts reduce the efficiency of misidentification of b-jets as leptons. In our case, this is less than 0.05%.

Luminosity	Background 3 ℓ events	Signal 3 ℓ events	Background 4 ℓ events	Signal 4 ℓ events	
				scenario I	scenario II
25 fb $^{-1}$	797.5	46.2	2.9	(i) 30 (ii) 4.4	24.8
300 fb $^{-1}$	9569.7	554	34.8	(i) 360 (ii) 53	298

Table 3.14: Number of background and signal events at 25 fb $^{-1}$ and 300 fb $^{-1}$ as an anticipated integrated luminosity at next 14 TeV run of LHC. The tri-lepton signal is computed for following charged scalar masses: $M_{H_1^{\pm\pm}} = 483$ GeV, $M_{H_2^{\pm\pm}} = 527$ GeV, $M_{H_1^\pm} = 355$ GeV, $M_{H_2^\pm} = 15066$ GeV. Scenario I reflects degeneracy of doubly charged scalar masses with (i) $M_{H_1^{\pm\pm}} = M_{H_2^{\pm\pm}} = 400$ GeV and (ii) $M_{H_1^{\pm\pm}} = M_{H_2^{\pm\pm}} = 600$ GeV, while Scenario II realises their non-degenerate spectrum, namely $M_{H_1^{\pm\pm}} = 400$ and $M_{H_2^{\pm\pm}} = 500$ GeV. Here we have used the same kinematical cuts as applied while estimating the SM background events. We have not implemented other extra cuts, like invariant mass ($m_{\ell\ell}$) and lepton separation ($\Delta R_{\ell\ell}$) to estimate the signal and background events in this table.

300 fb $^{-1}$ integrated luminosities. It is clear that four-lepton signals are well beyond the SM background. The tri-lepton signal is also very prominent over the background (what matters is the signal excess over the background fluctuations). To see it properly, in Table 3.15 the significance of different signals is shown.

Assuming the significance at the level of 5 as a comfortable discovery limit, we can see that LHC, in the next run will be sensitive to masses of doubly charged Higgs bosons belonging to MLRSM up to approximately 600 GeV.

We have focused here on doubly charged Higgs bosons, aiming at their small masses, but we can see that they are entangled by the scalar potential parameters, and some singly charged and neutral scalars are relatively light.

Fig. 3.30 gives an estimation of cross sections for the pair production of doubly charged Higgs bosons at LHC for the center of mass energies at present (8 TeV), forthcoming run (13–14 TeV) and in the further perspective (100 TeV). For the simplicity, we assume that masses of $H_1^{\pm\pm}$ and $H_2^{\pm\pm}$ are degenerate *i.e.* $\delta\rho = 4\rho_2$. Limits on the doubly charged Higgs boson $H_1^{\pm\pm}$ masses from recent LHC data have been taken into account, and exclusion limits are explicitly given in Fig. 3.30.

Here, the cross section for the process $pp \rightarrow (H_1^{\pm\pm} H_1^{\mp\mp} \oplus H_2^{\pm\pm} H_2^{\mp\mp}) \rightarrow 4\ell$ for

Significance	3 ℓ events	4 ℓ events	
		scenario I	scenario II
S/\sqrt{B}	5.66	(i) NA (ii) NA	NA
$S/\sqrt{S+B}$	5.51	(i) 18.11 (ii) 5.65	16.34

Table 3.15: The significance of the signals given in Table 3.14 is computed using two definitions of significance: (i) S/\sqrt{B} , and (ii) $S/\sqrt{S+B}$, where S and B are the total number of signal and background events for 300 fb^{-1} integrated luminosity, respectively. The parameters are the same as given in Table 3.14. Here ‘NA’ implies that S/\sqrt{B} can not be used as the definition of significance in these cases as $S \ll B$ is not justified.

different center of mass energies $\sqrt{s} = 8, 14$ and 100 TeV at the LHC with only basic cut (lepton $p_T > 10 \text{ GeV}$) is shown in Fig. 3.30 for different set of doubly charged scalar masses. We have also implemented the detailed event selection criteria¹⁸, as given in [118, 163] to compute the SM background for this final state coming from $t\bar{t}(Z/\gamma^*), (Z/\gamma^*)(Z/\gamma^*)$. Using the same set of cuts the signal event cross section is estimated for doubly charged scalar masses [450-900] GeV. We have pointed out four benchmark points for the following masses of doubly charged scalars: 450, 600, 700 and 900 GeV. The corresponding significances¹⁹ of the signal for integrated luminosity 300 fb^{-1} are 13.8, 5.7, 3.3 and 1.0 respectively. Thus, at the LHC with $\sqrt{s} = 14 \text{ TeV}$ center of mass energy and 300 fb^{-1} luminosity up to 600 GeV mass of the doubly charged scalars can be probed with significance ≥ 5 . Finally, it is worthwhile to note that due to kinematics for $\sqrt{s} = 100 \text{ TeV}$ discussed cross section does not change significantly when mass of doubly charged scalars increases.

¹⁸These event selection criteria are implemented in PYTHIA. They include lepton transverse momentum (p_T), pseudorapidity cuts, smearing of leptons, lepton-lepton (photon, jet) separation, hadronic activity, missing p_T and Z-veto.

¹⁹Significance of the signal is conveniently measured by the ratio $S/\sqrt{S+B}$, where S and B are the total number of signal and background events respectively.

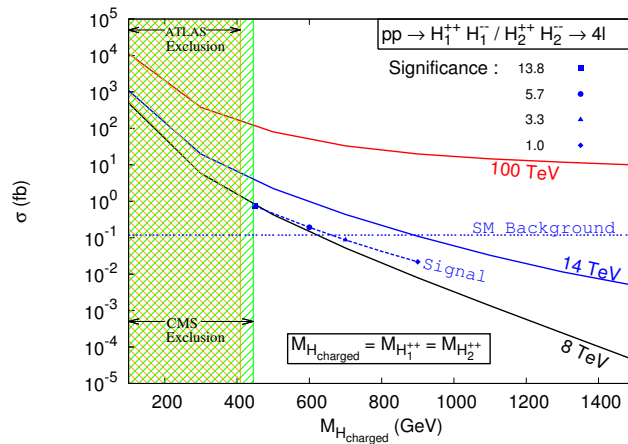


Figure 3.30: Cross section σ for the pair production of doubly charged scalars $H_i^{\pm\pm}$ decaying to four-leptons for $\sqrt{s} = 8, 14$ and 100 TeV at the LHC (solid lines) without the detailed selection cuts (see the text for details). The dotted-blue horizontal line is the estimation for the SM background for 4ℓ final state with $\sqrt{s} = 14$ TeV incorporating the detailed event selection criteria. Also the cross section for the process $pp \rightarrow H_1^{++} H_1^{-} / H_2^{++} H_2^{-} \rightarrow 4\ell$ with $\sqrt{s} = 14$ TeV after implementing the same full selection cuts is depicted by the dashed-blue line for doubly charged scalar mass range $[450-900]$ GeV. The four patches on the “Signal” line denote the significance of the signal. It is assumed that $\delta\rho = 4\rho_2$, what results in $M_{H_1^{\pm\pm}} = M_{H_2^{\pm\pm}}$, see Eqs. (3.69)-(3.72).

3.4.9 MLRSM charged Higgs bosons contribution to $H_0^0 \rightarrow$

$\gamma\gamma$

In LR symmetric model there are (singly-, doubly-) charged scalars and charged gauge boson (W_2^\pm) which couple to photons and hence they can contribute to $H_0^0 \rightarrow \gamma\gamma$ channel where H_0^0 is the SM-like neutral Higgs taken to be 125 GeV. Since W_2^\pm are heavy, their contributions are suppressed compared to charged scalars, so we look for charged scalar contributions. They contribute to the channel via a loop shown in Fig. 3.31.

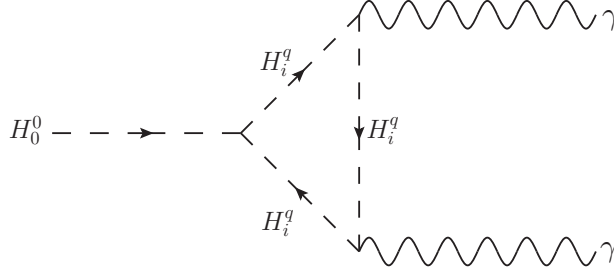


Figure 3.31: Charged scalar contribution to the $H_0^0 \rightarrow \gamma\gamma$ channel at the LHC. In the loop there are three contributions coming from the charged scalars $H_i^q \equiv H_1^{\pm\pm}, H_2^{\pm\pm}, H_1^{\pm}$. In MLRSM H_2^{\pm} is very heavy and its contribution is negligible.

Following [226–228] we can write the enhancement factor for this channel, which is nothing but a ratio of partial decay width in the new model to that in the SM

$$R_{\gamma\gamma} = \left| 1 + \sum_{S=H_{1,2}^{\pm\pm}, H_1^{\pm}} Q_S^2 \frac{c_S}{2} \frac{k_+^2}{M_S^2} \frac{A_0(\tau_S)}{A_1(\tau_{W_1}) + N_c Q_t^2 A_{1/2}(\tau_t)} \right|^2. \quad (3.58)$$

In the above equation Q_S is electric charge of charged scalars in unit of e , M_S is a mass of scalars. N_c is color factor which is 1 for color singlet scalars and $\tau_i = 4m_i^2/m_{H_0^0}^2$ ($i = W_1, t, S$). c_S are the coupling of the Higgs boson with the charged scalars and $k_+ = \sqrt{k_1^2 + k_2^2}$ where k_1, k_2 are the vacuum expectation values of the bi-doublet. The expressions for c_S are as follows

$$c_{H_0^0 H_1^+ H_1^-} = - \left[\frac{2\alpha_1 k_+^2 + 8\alpha_2 k_1 k_2 + \alpha_3 (k_+^2)}{2k_+^2} \right], \quad (3.59)$$

$$c_{H_0^0 H_1^{++} H_1^{--}} = - \left[\frac{\alpha_1 k_+^2 + k_1 (4\alpha_2 k_2 + \alpha_3 k_1)}{k_+^2} \right], \quad (3.60)$$

$$c_{H_0^0 H_2^{++} H_2^{--}} = - \left[\frac{\alpha_1 k_+^2 + k_1 (4\alpha_2 k_2 + \alpha_3 k_1)}{k_+^2} \right]. \quad (3.61)$$

Here the parameters that are involved in the above Eqs. 3.59-3.61, are contained in the scalar potential and following the convention as suggested in [71].

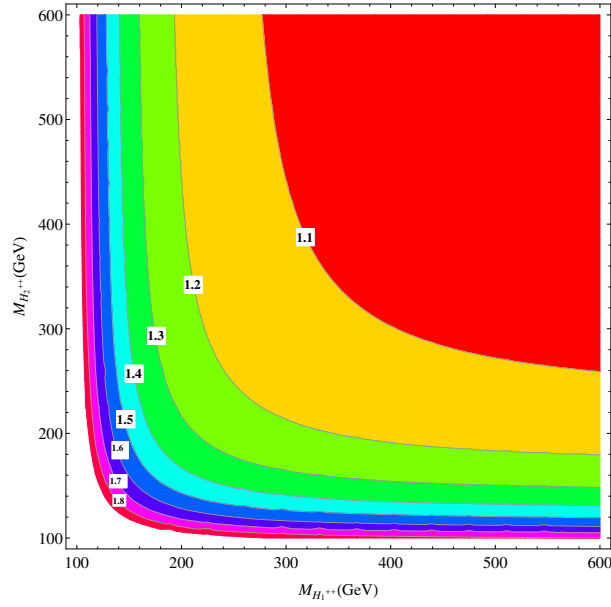


Figure 3.32: $R_{\gamma\gamma}$ with the variation of charged scalar masses.

$A_{1/2}$, A_1 and A_0 are loop functions for fermions, vector bosons and scalars respectively, given as

$$A_{1/2}(x) = 2x^2[x^{-1} + (x^{-1} - 1)f(x^{-1})], \quad (3.62)$$

$$A_1(x) = -x^2[2x^{-2} + 3x^{-1} + 3(2x^{-1} - 1)f(x^{-1})], \quad (3.63)$$

$$A_0(x) = -x^2[x^{-1} - f(x^{-1})]. \quad (3.64)$$

For the SM-like Higgs mass below threshold, *i.e.*, $m_{H_0^0} < 2m_{loop}$ (m_{loop} is a mass of a particle in the loop) $f(x) = \arcsin^2(\sqrt{x})$.

In Fig. 3.32 we present a contour plot to show the contributions from the charged scalars to $R_{\gamma\gamma}$. We have assumed $M_{H_1^{++}} = M_{H_1^+}$ to reduce the number of free parameters.

Experimental observations of the Higgs to diphoton decay normalized to the

SM prediction, as pointed out by ATLAS and CMS is given as in [130], [131]:

$$R_{\gamma\gamma} = 1.65 \pm 0.24(stat)_{-0.18}^{+0.25}(syst) \text{ (ATLAS)}, \quad (3.65)$$

$$R_{\gamma\gamma} = 0.78_{-0.26}^{+0.28} \text{ (CMS)}. \quad (3.66)$$

Recent observations for ATLAS [132] and CMS [133] are

$$R_{\gamma\gamma} = 1.17 \pm 0.27 \text{ (ATLAS)}, \quad (3.67)$$

$$R_{\gamma\gamma} = 1.14_{-0.23}^{+0.26} \text{ (CMS)}. \quad (3.68)$$

As errors are still very large, it is too early to make any conclusive remarks on these results, especially that tendency seems to be that the anomaly systematically approaches 1. However, MLRSM can accommodate wide range of $R_{\gamma\gamma}$ values by the charged Higgs boson effects, for related discussions, see *e.g.* in [229].

3.4.10 MLRSM VBF signal

In the previous part, we have focused on searches for the multilepton signals associated with any number of jets, *i.e.*, there was no jet veto. Here, the analysis of possible VBF-type signals with four-leptons and two jets using suitable VBF cuts are discussed.

We have used our version of the Left-Right symmetric model implemented in FeynRules (v2.0.31) [161, 230]. The general signal and background analyses for multilepton and tagged forward jets are performed using ALPGEN (v2.14) [151], Madgraph (v2.2.2) [143] and PYTHIA (v6.421)[145].

3.4.10.1 Possible processes which identify doubly charged Higgs through VBF in the MLRSM

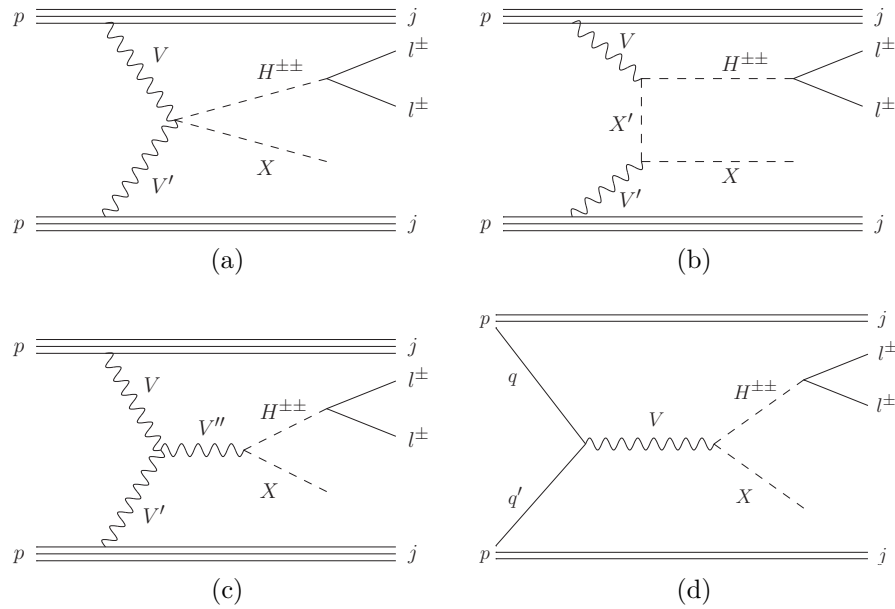


Figure 3.33: Basic processes which lead to $H^{\pm\pm}$ pair production. In the first three diagrams $H^{\pm\pm}$ is produced through fusion of two vector bosons V and V' . Each of them can be W^\pm , Z^0 or γ . The second product of the fusion, scalar X , is $H^{\pm\pm}$, H^\pm or H^0 depending on the configuration of colliding vector bosons. Analogously, scalar X' and vector boson V'' can be identified once V and V' are specified. In the last diagram $H^{\pm\pm}$ is produced through collision of two quarks q and q' in the Drell-Yan process. The second product of the decay, scalar X , can be identified as $H^{\pm\pm}$, H^\pm or H^0 once V is specified. The signals generated with the diagram (d) are usual tri-lepton and four-lepton signals, which we considered in the previous part.

There are many interesting channels in which doubly charged Higgs particles can be produced in the MLRSM. In hadron collider, productions of doubly charged Higgs particles crucially depend on their couplings with vector bosons. These charged scalars ($H^{\pm\pm}$) are produced either through neutral and charged currents or fusion processes. Representative classes of diagrams which contribute to $H^{\pm\pm}$ productions associated with two jets are given in Fig. 3.33.

If $X = H^{\pm\pm}$ in Fig. 3.33 then doubly charged Higgs particles are produced in pairs. Assuming further that $H^{\pm\pm}$ decays predominantly into leptons, a signal of four-leptons associated with two forward jets in the final state is:

$pp \rightarrow H_{1/2}^{\pm\pm} H_{1/2}^{\mp\mp} jj \rightarrow \ell^\pm \ell^\pm \ell^\mp \ell^\mp jj$. In a Drell-Yan case also (diagram (d) in Fig. 3.33), if $X = H^{\pm\pm}$, four-leptons plus two jets signal is possible, though its contribution is suppressed once the VBF cuts are activated.

We should also mention that vector boson fusion diagrams interfere substantially with Bremsstrahlung-like (or Drell-Yan) processes [231].

Here, we focus on the pair production of doubly charged scalars associated with two forward jets. As mentioned already this signature can be promising since LHC has dedicated search channels for tagged forward jets. VBF processes with doubly charged Higgs bosons have been considered lately in [216] with the main focus on tri-lepton signals with missing energy. In [216] there is also an interesting discussion on scalar self-energy corrections to W_L^\pm and $\Delta\rho_{EW}$ parameter. It has been argued that there exists severe constraints on the charged scalar mass splitting. We need to consider complete calculations including renormalization. We recall a series of papers on the 1-loop corrections to the muon decay in MLRSM, starting with qualitative results [179, 232] and finishing with quantitative analysis [174]. The upshot of all these analyses, important for our present discussion, is that there is a strong fine-tuning between contributions to $\Delta\rho_{EW}$ from different classes of non-standard particles: Higgs and additional gauge *bosons* and heavy neutrinos (*fermions*). By their nature, cancellations among bosonic and fermionic type of diagrams are present, and a change of mass spectrum of Higgs bosons can be compensated by different choices of v_R scale (gauge bosons) and masses of heavy neutrinos. These analyses in context of the LHC have been considered in details in [178].

3.4.10.2 Predictions for $pp \rightarrow H_{1/2}^{\pm\pm} H_{1/2}^{\mp\mp} jj \rightarrow \ell^\pm \ell^\pm \ell^\mp \ell^\mp jj$ in the MLRSM

Before we discuss our simulated results, selection criteria should be defined, which are crucial for extracting proper signals and reducing the SM background. For selecting leptons we use the same criteria as defined in Section 3.1. The Parton Distribution Function (PDF) for proton is defined by CTEQ6L1 [146]. After satisfying the selection criteria, additional cuts are applied to identify the forward jets. The detail of these VBF cuts are depicted in Table 3.16.

Cuts	$p_{T_{j_1}}, p_{T_{j_2}}$	$ \eta_{j_1} - \eta_{j_2} $	$m_{j_1 j_2}$	$\eta_{j_1} * \eta_{j_2}$
VBF	≥ 50	> 4	500	< 0

Table 3.16: Selection criteria for the forward jets. The two highest p_T jets $p_{T_{j_1}}, p_{T_{j_2}}$ are chosen as the VBF forward jets.

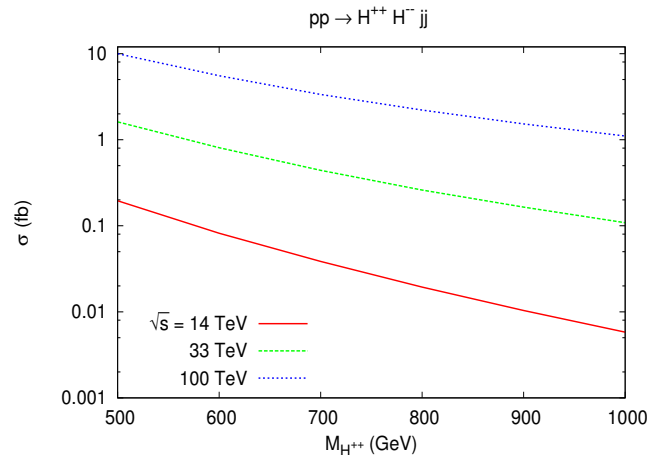


Figure 3.34: Dependence of cross sections (σ) with the masses of doubly charged scalars for the process $pp \rightarrow H^{++} H^{-} jj$ for different center of mass energies: 14 TeV (red-solid), 33 TeV (green-dashed), and 100 TeV (blue-dotted) respectively.

Taking care of the constraints on potential parameters discussed in Section 3.4.4, in Fig. 3.34 results are presented for the doubly charged Higgs production process with two jets as a function of their mass. While computing the MLRSM mass spectrum, we have set $v_R = 8$ TeV (which leads to $M_{W_2} = 3.76$ TeV). The analyses are performed for LHC with 14 TeV collision energy considering high luminosity HL-LHC option [233] as well as for future scenarios such as HE-LHC with a center of mass energy 33 TeV [233, 234] or 100 TeV FCC-hh facility [235–238]. The cross section for this process has been computed with a large p_{T_j} and VBF cuts as defined in Table 3.16

As an example of representative Higgs mass spectrum (bench mark) used in calculations, assuming degenerate doubly charged Higgs masses $M_{H_1^{\pm\pm}} = M_{H_2^{\pm\pm}} = 500$ [1000] GeV where masses of remaining scalar particles compati-

ble with results of section 3.4.4 can be chosen as (in GeV):

$$M_{H_0^0} = 125 [125],, M_{H_1^0} = 10431 [10431], \quad (3.69)$$

$$M_{H_2^0} = 27011 [27011], M_{H_3^0} = 384 [947], \quad (3.70)$$

$$M_{A_1^0} = 10437 [10437], M_{A_2^0} = 384 [947], \quad (3.71)$$

$$M_{H_1^\pm} = 446 [974], M_{H_2^\pm} = 10433 [10433]. \quad (3.72)$$

This spectrum is obtained with the following set of potential parameters ($v_R = 8 \text{ TeV}$):

$$\lambda_1 = 0.129 [0.129], \lambda_2 = 0 [0], \quad (3.73)$$

$$\lambda_3 = 1 [1] \lambda_4 = 0 [0], \quad (3.74)$$

$$\alpha_1 = 0 [0], \alpha_2 = 0 [0], \alpha_3 = 3.4 [3.4], \quad (3.75)$$

$$\rho_1 = 5.7 [5.7], \rho_2 = 0.00115 [0.00701], \quad (3.76)$$

$$\rho_3 = 11.405 [11.428]. \quad (3.77)$$

The cross sections for the following process at the parton level with minimal imposed cuts are given as:

$$\begin{aligned} & \sigma(pp \rightarrow H_{1/2}^{\pm\pm} H_{1/2}^{\mp\mp} jj \rightarrow \ell^\pm \ell^\pm \ell^\mp \ell^\mp jj) \\ & = \begin{cases} 4.04 [0.12] \times 10^{-2} \text{ fb} & \text{for } \sqrt{s} = 14 \text{ TeV}, \\ 45.30 [3.36] \times 10^{-2} \text{ fb} & \text{for } \sqrt{s} = 33 \text{ TeV}, \\ 282.80 [31.76] \times 10^{-2} \text{ fb} & \text{for } \sqrt{s} = 100 \text{ TeV}, \end{cases} \end{aligned} \quad (3.78)$$

where $\ell = e, \mu$. These minimal cuts are *e.g.* minimum p_T cut for leptons and jets such that they are identified as observable in the detector and do not contribute to missing energy.

The result in Eq. 3.78 is further processed using the VBF cuts

$$\begin{aligned} & \sigma(pp \rightarrow H_{1/2}^{\pm\pm} H_{1/2}^{\mp\mp} jj \rightarrow \ell^\pm \ell^\pm \ell^\mp \ell^\mp jj) \\ & = \begin{cases} 0.54 [0.01] \times 10^{-2} \text{ fb} & \text{for } \sqrt{s} = 14 \text{ TeV}, \\ 6.21 [0.40] \times 10^{-2} \text{ fb} & \text{for } \sqrt{s} = 33 \text{ TeV}, \\ 37.01 [3.54] \times 10^{-2} \text{ fb} & \text{for } \sqrt{s} = 100 \text{ TeV}. \end{cases} \end{aligned} \quad (3.79)$$

For the sake of completeness let us display contributions from two intermediate channels with the default cuts in Madgraph (MG):

$$\begin{aligned} & \sigma(pp \rightarrow H_1^{\pm\pm} H_1^{\mp\mp} jj) \\ & = \begin{cases} 11.16 [0.39] \times 10^{-2} \text{ fb} & \text{for } \sqrt{s} = 14 \text{ TeV}, \\ 90.87 [7.05] \times 10^{-2} \text{ fb} & \text{for } \sqrt{s} = 33 \text{ TeV}, \\ 599.70 [73.28] \times 10^{-2} \text{ fb} & \text{for } \sqrt{s} = 100 \text{ TeV}, \end{cases} \end{aligned} \quad (3.80)$$

and

$$\begin{aligned} & \sigma(pp \rightarrow H_2^{\pm\pm} H_2^{\mp\mp} jj) \\ & = \begin{cases} 8.35 [0.19] \times 10^{-2} \text{ fb} & \text{for } \sqrt{s} = 14 \text{ TeV}, \\ 71.20 [3.81] \times 10^{-2} \text{ fb} & \text{for } \sqrt{s} = 33 \text{ TeV}, \\ 401.40 [37.43] \times 10^{-2} \text{ fb} & \text{for } \sqrt{s} = 100 \text{ TeV}. \end{cases} \end{aligned} \quad (3.81)$$

As one can see the cross sections in Eqs. 3.80 and 3.81 are larger than these given in Eq. 3.78. The reason for this is while computing the cross section for leptonic final state, *i.e.*, Eq. 3.78, all the selection cuts are incorporated and that reduces the cross section by a large amount.

Some technical details related to computing method are in order here. At the MG level one can control gluon contributions using option `QCD=0`. The cross section for $pp \rightarrow H_{1,2}^{\pm\pm} H_{1,2}^{\mp\mp} jj$ with switched off gluons turns out to be about 5 times smaller than that for with gluons. Hence, QCD contributions to that signal are really important. However, in both cases distributions of rapidity (y) of jets are quite different. For gluons the rapidity distributions for jets are peaked around $y = 0$ which implies that jets are emitted mostly perpendicular

to the beam. For VBF rapidity distributions are peaked around $|y| \sim 3$ and $|y_1 - y_2| \sim 5$, *i.e.*, there are two back-to-back jets emitted along the beam. Hence, setting $\text{QCD}=0$ allows us to preselect processes which are consistent with VBF cuts. Effectively it shortens computing time²⁰.

Let us comment on the $H^{\pm\pm}$ decay scenario used in calculations. It is assumed that $H^{\pm\pm}$ dominantly decay into pairs of the same-sign and same-flavored charged leptons (for all possibilities within MLRSM, see [163]). In other words, it is assumed that Yukawa coupling matrix of doubly charged scalar $H_2^{\pm\pm}$ with charged leptons is diagonal. Assuming no mixed leptonic decay modes ($e\mu$), *i.e.*, no lepton flavor violation, the coupling of doubly charged scalar $H_2^{\pm\pm}$ with charged leptons in MLRSM is proportional to the heavy neutrino mass of the corresponding lepton generation. Thus, the $ee, \mu\mu$ decay modes will be larger as compared to the $\tau\tau$ case if the first and second generations of right-handed neutrinos are more massive than the third generation one. This point has been clarified and shown numerically in Fig. 2.5 in Ref. [163]. In the present analysis the masses of the first two generations of right-handed neutrinos are taken to be 3 TeV and mass of the third one is at the level of 800 GeV. As $v_R = 8$ TeV, the Yukawa couplings are within the perturbative limit. If the $\tau\tau$ decay mode would be larger, predictions given here should be rescaled properly using corresponding branching ratios (for instance, in the democratic three generation case, branching ratio for the ee and $\mu\mu$ channels would be decreased by about 15%, each).

The SM background at the LHC for the signal $4\ell + 2$ jets is accounted from the process $pp \rightarrow ZZ(\gamma\gamma, Z\gamma)jj \rightarrow \ell^+\ell^-\ell^+\ell^-jj$. We have noted that after implementation of the selection cuts the dominant background comes from $pp \rightarrow ZZjj \rightarrow \ell^+\ell^-\ell^+\ell^-jj$ process.

For $\sqrt{s} = 14, 33, 100$ TeV pp collisions, the SM background is given in Table 3.17 both at the parton level and after hadronization and passing through implemented cuts.

We can see that the background is suppressed very effectively. The results in

²⁰Typical run times for generating 5×10^4 events of $pp \rightarrow H_{1/2}^{\pm\pm}H_{1/2}^{\mp\mp}jj$ and $pp \rightarrow H_{1/2}^{\pm\pm}H_{1/2}^{\mp\mp}jj \rightarrow \ell^{\pm}\ell^{\pm}\ell^{\mp}\ell^{\mp}jj$ with $\text{QCD}=0$ are, respectively, about 3 h and 54 h on 8 core 3.4 GHz CPU.

Process: $ZZjj$ with \sqrt{s} in TeV	Cross section [fb] at parton level in Madgraph	Cross section [fb] after showering, and hadronization in PYTHIA
14	0.115	0.003
33	1.109	0.008
100	4.794	0.038

Table 3.17: Standard Model cross section in fb for $\ell^+\ell^-\ell^+\ell^-jj$ final state and $\sqrt{s} = 14, 33, 100$ TeV LHC. The cuts are suitably applied, see section 3.4.10.2, to compute the SM background at parton level and after incorporating showering and hadronization in PYTHIA.

Table 3.17 are obtained in the leading order, electroweak corrections can change the results not more than 10% [239] which can change the significance of signals at the level of about one percent at most.

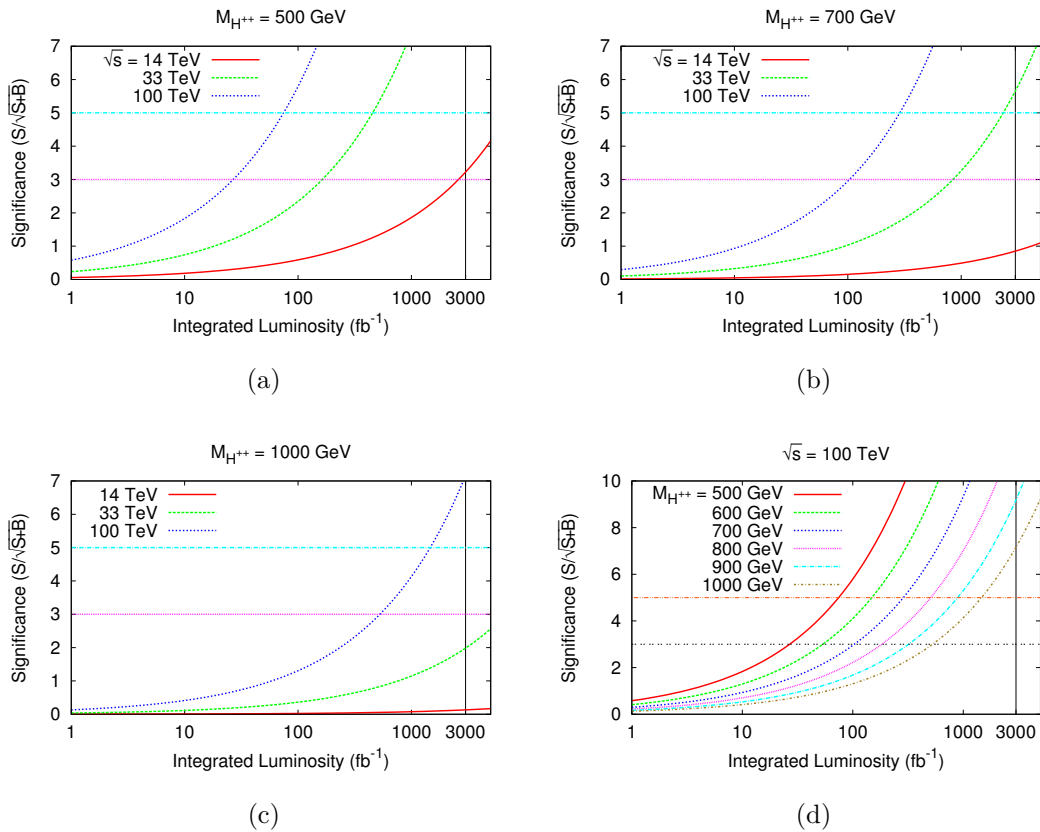


Figure 3.35: Variations of significance of *signal* with integrated luminosities for different energies of pp colliders and various doubly charged Higgs boson masses.

Finally, to judge the strength of the MLRSM signals we decided to show

the dependence of the significance of the result as a function of the integrated luminosity. As can be seen in Fig. 3.35 (left-top), a comfortable value of the significance at the level of 5 can be reached for $M_{H^{\pm\pm}} = 500$ GeV in pp collisions with

- ◇ $\sqrt{s} = 100$ TeV and with 100 fb^{-1} integrated luminosity;
- ◇ $\sqrt{s} = 33$ TeV and with 700 fb^{-1} integrated luminosity.

No signal at this significance level (~ 5) can be reached with $\sqrt{s} = 14$ TeV pp collisions, even if the integrated luminosity is around 3000 fb^{-1} .

In Fig. 3.35 (right-top) we can see that doubly charged Higgs bosons with masses up to $M_{H^{\pm\pm}} = 700$ GeV with significance at the level of 5 can be probed for both center of mass energy 33 and 100 TeV with integrated luminosities around 3000 and 300 fb^{-1} respectively. In Fig. 3.35 (left-bottom) it is evident that 1 TeV doubly charged scalar can be probed with significance of 5 only with 100 TeV collider with luminosity at least 1000 fb^{-1} . The Fig. 3.35 (right-bottom) summarizes the situation for the FCC-hh collider option for three different set of masses of doubly charged scalars: 500, 600, 700, 800, 900 and 1000 GeV. This figure also shows that significance at the level of 7 can be reached for $M_{H^{\pm\pm}} = 1$ TeV and $\sqrt{s} = 100$ TeV with integrated luminosities around 3000 fb^{-1} . We can see that the 100 TeV collider opens up very wide range of Higgs boson masses which can be explored.

3.5 Summary: MLRSM

Here we have concentrated on studies connected with discovery potential of the charged Higgs bosons within the canonical MLRSM which is already phenomenologically rich enough and worth separate investigations. Though different low energy data and the LHC exclusion plots already constrain masses of the heavy gauge bosons W_2 and Z_2 very much, the charged scalars can still be relatively light. It has been shown which of the singly and doubly charged Higgs bosons can be light, in agreement with FCNC limits on the neutral Higgs boson particles, as

both the charged and the neutral scalar sectors are connected through the Higgs potential parameters. We found that in the MLRSM not all four charged Higgs bosons can simultaneously be light. For instance, it is possible that H_1^\pm , $H_1^{\pm\pm}$ and $H_2^{\pm\pm}$ are light. The remaining charged scalar H_2^\pm is of the order of the v_R scale, so its effects at the LHC is negligible. To make it lighter would require one to go beyond the MLRSM.

Though there are many free parameters in the Higgs sector, present experimental limits on masses of doubly charged Higgs bosons already put first constraints on some of these parameters. In our analysis we obtained a lower limit on the charged scalar mass $M_{H_1^{\pm\pm}}$ consistent with LEP, LHC and FCNC bounds. The other doubly charged scalar $H_2^{\pm\pm}$ is theoretically not constrained from below in the discussed model and it can be tuned to any desirable value, in agreement with experimental data. The lowest limit on $M_{H_1^{\pm\pm}}$ is important, as we know that production cross section for $H_1^{\pm\pm}$ is much bigger than that of $H_2^{\pm\pm}$ [163]. Here, we have also pinned down the parameters that play important roles while determining the individual masses of the charged scalars and their respective splittings. Cross sections for the pair productions of doubly charged scalars followed by their leptonic decays have been discussed together with the estimation of the SM background at 14 TeV center of mass energy. and that will draw the upper limit on the masses of the doubly charged scalars that can be possibly probed at the LHC.

We have analysed four-lepton and tri-lepton signal from the s-channel pair production of charged scalars, $pp \rightarrow H_{1/2}^{++} H_{1/2}^{--}$ and $pp \rightarrow H_{1/2}^{\pm\pm} H_{1/2}^{\mp\mp}$, respectively. The charged scalars can be produced at the LHC with non-negligible cross sections. However, their production cross sections decrease rapidly with their masses, that is why we have undertaken here more detailed and systematic studies including the production and decays of charged scalars. We have concentrated on the single and pair production of doubly charged scalars. We have chosen the benchmark points in such a way that signals connected with doubly charged scalars can dominate over non-standard signals coming from both heavy gauge and neutral Higgs bosons. As a rule of thumb, for all considered processes

with doubly charged scalars cross sections are about 1 fb for their masses in the vicinity of $400 \div 500$ GeV, which is about the present lowest limit on their masses. If planned integrated luminosity in the next LHC run at $\sqrt{s} = 14$ TeV is about 10 times larger than present values, clear signals with four-leptons without missing energy and tri-lepton signals can be detected. It will be an indication for doubly charged scalar effects. These multilepton final states possess very small SM background. We have shown that MLRSM model can give such signals for doubly charged masses up to approximately 600 GeV. In our analysis, we have used the dilepton invariant mass and lepton-lepton separation distributions. We also estimate the amount of charge asymmetry in signal as well as background events, and show that this might be a smoking gun feature for future discovery. The same and opposite-sign charged lepton signals have been analyzed using proper kinematic cuts and the clear impact of doubly charged scalars are noted carefully.

In the Left-Right symmetric models charged gauge bosons are very heavy and they do not contribute significantly to the Higgs to diphoton process. However, the relatively light charged scalars can contribute easily. We have incorporated the impact of the light charged scalars in this process and estimated the strength of this contribution over the SM one.

The LHC still has a room for discovery of Left-Right gauge symmetry signals through MLRSM doubly charged Higgs bosons with s-channel production as long as long as their masses will be below 1 TeV range ($m_{H_{1/2}^{\pm\pm}} \leq 600$ GeV).

We have also looked for four-lepton signature from production and decays of pair of doubly charged Higgs bosons through vector boson fusion within MLRSM framework, $pp \rightarrow H_{1/2}^{++} H_{1/2}^{--} jj$. To do so we have evaluated suitable benchmark points for masses of Higgs bosons, which are in agreement with several constraints coming from FCNC, mass of the SM like Higgs, vacuum stability, LEP II and recent ATLAS searches on doubly charged scalars. There are strong relations among masses of doubly, singly and neutral scalars which forbid us to choose their individual values freely, leaving us with suitable benchmarks that we have used in this study. We have further noted and shown that the splitting between the

doubly ($H_1^{\pm\pm}$) and singly (H_1^\pm) charged scalars is less than M_{W_1} , irrespective of the $SU(2)_R$ breaking scale. Thus, the on-shell decay $H_1^{\pm\pm} \rightarrow H_1^\pm W_1^\pm$ is protected and the decay branching ratio of the doubly charged scalar $H_1^{\pm\pm}$ is affected.

After settling these issues regarding the spectrum we have computed the signal cross section for the process $pp \rightarrow H_{1/2}^{\pm\pm} H_{1/2}^{\mp\mp} jj \rightarrow \ell^\pm \ell^\pm \ell^\mp \ell^\mp jj$ using realistic cuts. The necessary SM background for this final state is also evaluated. It has been shown that 14TeV LHC even with high integrated luminosity will not be sensitive to the VBF-like signals $H_{1/2}^{\pm\pm} H_{1/2}^{\mp\mp} jj$, even with relatively light doubly charged Higgs bosons (say, ~ 500 GeV). We have shown much better perspective exists for the future FCC colliders with a center of mass energies 33 and (or) 100 TeV.

In passing we would like to mention that we have used the VBF cuts as adopted in [216]. We have compared the ATLAS and CMS (tight & loose) suggested cuts which are not very different from significance point of view. For further improved predictions, in future the analysis including NLO corrections should be undertaken. For instance it is known that electroweak corrections to VBF signals are within 10% level [239] and might have a mild impact on significance computed at leading order.

To summarize the chapter, we have done detailed analysis of various multilepton signatures and corresponding backgrounds from the SM. The analysis has been done for three models: the BNTM, the MLRSM and the MLSM. In all these models there is potential for signals to be discovered at the next run of the LHC.

Chapter 4

Phenomenological implications of neutrino mass models

The Left-Right symmetric theories lead to new effects or give additional contributions to various new physics observables at both energy and intensity frontiers, which can be tested in current and future experiments, if the scale of parity restoration is in the few TeV range. In particular, a TeV-scale Minimal Left-Right Symmetric Model (MLRSM) leads to the spectacular lepton number violating process of same-sign dilepton plus two jets at the LHC [110, 178, 202, 203, 240–242], as well as potentially large contributions to its low-energy analog, namely, neutrinoless double beta decay [30, 81, 198, 200, 201, 243–250]. In addition, there are a plethora of lepton flavor violating (LFV) processes, such as $\mu \rightarrow e\gamma$, $\mu \rightarrow 3e$, $\mu \rightarrow e$ conversion in nuclei, which can get sizable contributions from the right-handed sector [81, 198, 200, 240, 245, 246, 250–254].

In this chapter, we focus on the scalar triplet contribution to the low-energy LNV and LFV processes within a TeV-scale MLRSM framework. It is known that for triplet masses much larger than the RH neutrino and gauge boson masses, the triplet contributions to these processes are sub-dominant [198, 200, 245]. However, since the direct experimental searches for these triplets at the LHC still allow for the possibility of triplet masses $\gtrsim 500$ GeV [214] and the current lower limits on the RH gauge boson masses are in the few TeV range [183–189], it is worthwhile analyzing the possible scenarios where the triplet masses

are comparable to or slightly higher than the RH neutrino or RH gauge boson masses in the theory. In such cases, we find that the triplet contribution to $0\nu\beta\beta$ and LFV processes can indeed be sizable, and in most cases, is already ruled out by existing experimental constraints or can be probed in future experiments.

The framework for the MLRSM is discussed in Section 2.6. We have done our analysis for two interesting limits:

(i) Type-I dominance, where the VEV of Δ_L can be set to zero and the first term on the r.h.s. of Eq. 2.33 vanishes, so that the light neutrino mass matrix is governed by the usual type-I seesaw contribution [30]:

$$m_\nu \simeq -m_D M_R^{-1} m_D^\top. \quad (4.1)$$

In this case, the light-heavy neutrino mixing $V_{\ell N} \simeq m_D M_R^{-1}$ may or may not give large contributions to the low-energy processes, depending on the textures of m_D and M_R to satisfy the neutrino oscillation data [81]. In our case this mixing is small. Since our focus is on the triplet contribution, we will assume for simplicity that m_D is proportional to the identity matrix [200]. In this case, Eq. 4.1 suggests that $m_\nu \propto M_R^{-1}$ and the same PMNS mixing matrix U which diagonalizes m_ν also diagonalizes M_R^{-1} . This implies M_R is diagonalized by U^* , since U is assumed to be unitary. Moreover, the ratios of the RH neutrino mass eigenvalues (M_i) are related to the corresponding mass eigenvalues in the light neutrino sector (m_i), which are experimentally constrained for a given mass hierarchy. Thus, the only free parameter in the RH neutrino sector is the overall mass scale, which we will fix by specifying the heaviest neutrino mass eigenvalue, to be denoted hereafter by M_N . More explicitly, for normal hierarchy (NH) of light neutrino masses, we have $M_N = M_1$, and therefore, $M_2 = (m_1/m_2)M_N$ and $M_3 = (m_1/m_3)M_N$. Similarly, for inverted hierarchy (IH), we have $M_N = M_3$, and therefore, $M_1 = (m_3/m_1)M_N$ and $M_2 = (m_3/m_2)M_N$ [200].

(ii) Type II dominance, when the Dirac mass term m_D is negligible, so that the

light neutrino mass matrix is solely governed by the Higgs triplet contribution:

$$m_\nu \simeq m_L. \quad (4.2)$$

In this case, the light-heavy neutrino mixing $V_{\ell N}$ is necessarily small and does not play any role in the LNV and LFV observables. Moreover, if parity (or charge conjugation) is taken to be the discrete L-R symmetry at the TeV-scale, this implies $f_L = f_R$ (or $f_L = f_R^*$). Hence, Eq. 4.2 suggests that $m_\nu \propto M_R$, *i.e.*, the same PMNS mixing matrix U diagonalizes both LH and RH neutrino sectors. In this case, for NH, we have $M_N = M_3$, and therefore, $M_1 = (m_1/m_3)M_N$ and $M_2 = (m_2/m_3)M_N$, whereas for IH, we have $M_N = M_2$, and therefore, $M_1 = (m_1/m_2)M_N$ and $M_3 = (m_3/m_2)M_N$ [198].

In the following, we will be mostly interested in the masses of the doubly-charged scalars, and for simplicity, we will assume them to be equal in the LH and RH sectors. For convenience, we further define the parameter

$$\frac{1}{M_\Delta^2} = \frac{1}{m_{\delta_L^{\pm\pm}}^2} + \frac{1}{m_{\delta_R^{\pm\pm}}^2}, \quad (4.3)$$

and express our results for fixed values of the ratio of the heaviest neutrino mass M_N to M_Δ : $r \equiv M_N/M_\Delta$.

4.1 Lepton flavor violation

In the SM, the LFV decay rates are suppressed by the light neutrino masses, and hence, are well below the current experimental limits [49, 50] and even the distant-future sensitivities [51–53]. On the other hand, in the MLRSM, several new contributions appear due to the additional RH current interactions, which could lead to sizable LFV rates for a TeV-scale ν_R . For example, the $\mu \rightarrow e\gamma$ process receives new contributions from both the scalar and gauge sectors, which can be classified into three categories, namely, those involving purely LH currents (LL), purely RH currents (RR) and mixed LH-RH currents (LR), as shown in

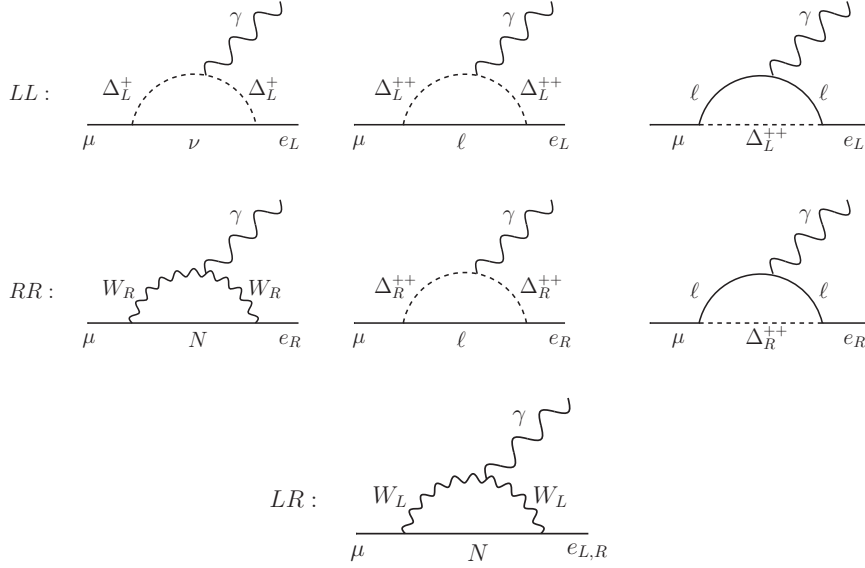
Figure 4.1: Feynman diagrams for $\mu \rightarrow e\gamma$ in the MLRSM.

Fig. 4.1. The corresponding branching ratio is given by [245]

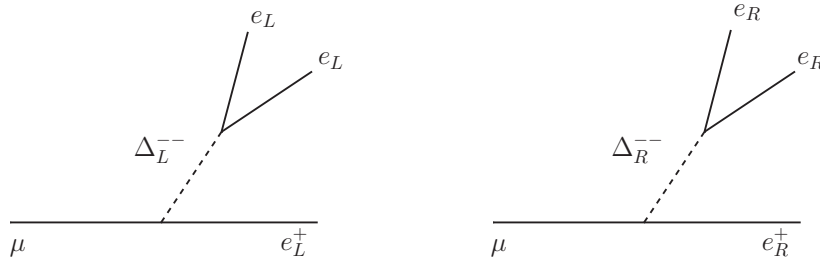
$$\text{BR}(\mu \rightarrow e\gamma) = \frac{3\alpha_{\text{em}}}{2\pi} (|G_L^\gamma|^2 + |G_R^\gamma|^2), \quad (4.4)$$

where $\alpha_{\text{em}} \equiv e^2/4\pi$ is the electromagnetic coupling constant, and the form factors G_L^γ and G_R^γ are given by

$$G_L^\gamma = \sum_{i=1}^3 \left(V_{\mu i} V_{ei}^* |\xi|^2 |G_1^\gamma(a_i) - S_{\mu i}^* V_{ei}^* \xi e^{-i\alpha} G_2^\gamma(a_i) \frac{M_i}{m_\mu} + V_{\mu i} V_{ei}^* \left[\frac{m_{W_L}^2}{m_{W_R}^2} G_1^\gamma(b_i) + \frac{2b_i}{3} \frac{m_{W_L}^2}{m_{\delta_R^{++}}^2} \right] \right), \quad (4.5)$$

$$G_R^\gamma = \sum_{i=1}^3 \left(S_{\mu i}^* S_{ei} G_1^\gamma(a_i) - V_{\mu i} S_{ei} \xi e^{i\alpha} G_2^\gamma(a_i) \frac{M_i}{m_\mu} + V_{\mu i} V_{ei}^* b_i \left[\frac{2}{3} \frac{m_{W_L}^2}{m_{\delta_L^{++}}^2} + \frac{1}{12} \frac{m_{W_L}^2}{m_{\delta_L^+}^2} \right] \right), \quad (4.6)$$

with $a_i \equiv \left(\frac{M_i}{m_{W_L}}\right)^2$, $b_i \equiv \left(\frac{M_i}{m_{W_R}}\right)^2$, M_i being the eigenvalues of the RH neutrino mass matrix and V is the RH neutrino mixing matrix which is related to the PMNS mixing matrix in our case, and S is the light-heavy neutrino mixing matrix which can be neglected for the choice of our parameters. Similarly, we can drop

Figure 4.2: Feynman diagrams for $\mu \rightarrow 3e$ in the MLRSM.

the terms depending on the $W_L - W_R$ mixing parameter ξ which is experimentally constrained to be $\lesssim 10^{-3}$ [1]. The loop functions $G_{1,2}^\gamma(a)$ are given as

$$G_1^\gamma(a) = -\frac{2a^3 + 5a^2 - a}{4(1-a)^3} - \frac{3a^3}{2(1-a)^4} \ln a, \quad (4.7)$$

$$G_2^\gamma(a) = \frac{a^2 - 11a + 4}{2(1-a)^2} - \frac{3a^2}{(1-a)^3} \ln a. \quad (4.8)$$

For the LFV process $\mu \rightarrow 3e$, the Higgs triplets Δ_L and Δ_R contribute to the leading order, as shown in Fig. 4.2, thereby making the branching ratio of this process potentially large [254, 255]:

$$\text{BR}(\mu \rightarrow 3e) = \frac{1}{8} |h_{\mu e} h_{ee}^*|^2 \left(\frac{m_{W_L}^4}{m_{\delta_L^{++}}^4} + \frac{m_{W_L}^4}{m_{\delta_R^{++}}^4} \right), \quad (4.9)$$

where $h_{\alpha\beta} \equiv \sum_{i=1}^3 V_{\alpha i} V_{\beta i} M_i / m_{W_R}$. Note that there is also an one-loop induced contribution in the Type-I dominance [256], which is however suppressed by the loop factors as well as by the light-heavy neutrino mixing, and hence, we can safely ignore it, as compared to the tree-level contribution given by Eq. 4.9. In Ref. [198], it has been pointed out that the current experimental constraint on $\text{BR}(\mu \rightarrow 3e) \leq 1.0 \times 10^{-12}$ [50] requires that in Eq. 4.9, the triplet scalar masses must be at least 10 times the heaviest RH neutrino mass scale in the theory, *i.e.*, the ratio $r \lesssim 0.1$, thereby making the Higgs triplet contribution to $\mu \rightarrow e\gamma$ and $0\nu\beta\beta$ negligible. We show that while this is true in general, there can also be cancellations due to the variations of the CP phases in the PMNS mixing matrix in which cases, this is not strictly required, *i.e.*, the $\mu \rightarrow 3e$ rate can in

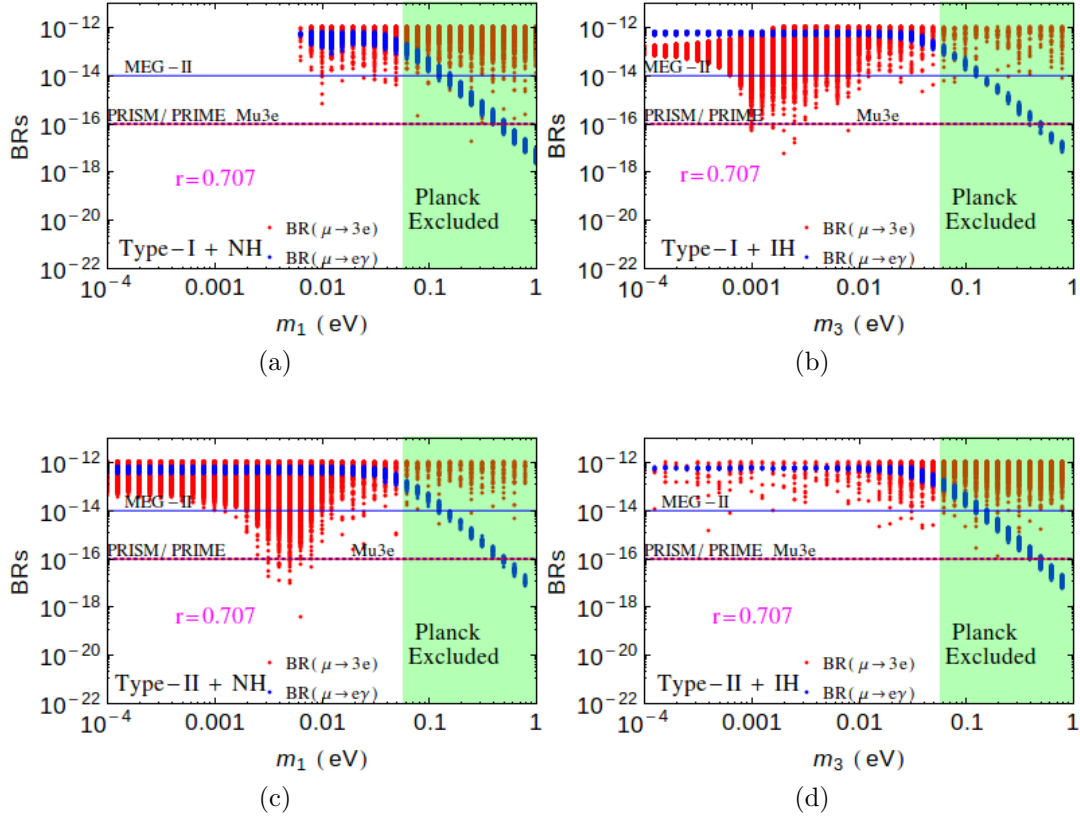


Figure 4.3: The predicted branching ratios of $\mu \rightarrow e\gamma$ (blue points) and $\mu \rightarrow 3e$ (red points) processes (when for a given light neutrino mass, current experimental bounds on the branching ratios of both are simultaneously satisfied) as a function of the lightest neutrino mass for NH (left panels) and IH (right panels) in Type-I (top panels) and Type-II (bottom panels) dominance. The ratio of the heaviest neutrino mass and the Higgs triplet mass has been set to $r = 0.707$. The green shaded region is disfavored at 95% C.L. from Planck data. The blue solid horizontal line is for MEG-II sensitivity, while PRISM/PRIME and Mu3e will have sensitivities up to the blue dotted and red solid horizontal lines respectively.

principle be compatible with the experimental constraint even for larger values of r . In these interesting scenarios, the Higgs triplet contribution to other LFV and $0\nu\beta\beta$ processes can become sizable, and hence, must be included in the analysis. This is illustrated below with three representative values of r (moderate, small and large). We show that r values as large as $\mathcal{O}(1)$ are still allowed by current experimental constraints, giving rise to interesting effects in low-energy LNV and LFV observables.

4.1.1 Moderate value of r

We first consider the scenario with $r = 0.707$. For illustration, we set the RH gauge boson mass $m_{W_R} = 3.5$ TeV, largest heavy neutrino mass $M_N = 500$ GeV and the Higgs triplet masses $m_{\delta_R^{++}} = m_{\delta_L^{++}} = M_{\delta_L^+} = 1$ TeV, which are consistent with the direct experimental constraints from the LHC. Using these parameters and Eqs. 4.4 and 4.9, we compute the $\mu \rightarrow e\gamma$ and $\mu \rightarrow 3e$ branching ratios, respectively, as a function of the lightest neutrino mass. We take into account the 3σ variation of the oscillation parameters as given by a recent global fit [19], as well as the variation of the Dirac CP phase δ between $[0, 2\pi]$ and Majorana phases $\alpha_{1,2}$ between $[0, \pi]$. We demand that our predicted LFV branching ratios should satisfy the current limits: $\text{BR}(\mu \rightarrow e\gamma) < 5.7 \times 10^{-13}$ from MEG [49] and $\text{BR}(\mu \rightarrow 3e) < 1.0 \times 10^{-12}$ from SINDRUM [50] experiments. Our results are shown in Fig. 4.3 by the blue ($\mu \rightarrow e\gamma$) and red ($\mu \rightarrow 3e$) scattered points for NH (left panels) and IH (right panels) in Type-I (top panels) and Type-II (bottom panels) dominance. We find that for the type-I, NH case, the predicted LFV branching ratios of $\mu \rightarrow e\gamma$ and $\mu \rightarrow 3e$ are allowed by the present experimental constraints, only if the lightest neutrino mass $m_1 \geq 0.01$ eV. For all other cases, lower values of $m_1(m_3)$ are allowed. A part of this parameter space with quasi-degenerate neutrinos is disfavored by the most stringent limit on the sum of light neutrino masses $\Sigma_i m_i < 0.17$ eV at 95% C.L from Planck data [25], as shown by the green shaded region in Fig. 4.3. From Fig. 4.3, we conclude that for moderate values of M_N/M_Δ , the predicted LFV branching ratios for both Type-I and Type-II dominance are within the reach of future experiments, such as MEG-II [51], PRISM/PRIME [52] and Mu3e [53], as shown by the blue and red horizontal lines in Fig. 4.3.

To better understand the dependence of the branching ratio on the lightest neutrino mass, we consider only the best-fit values of the oscillation parameters, as depicted in Fig. 4.4, where we show the individual contributions G_L^γ , G_R^γ (*cf.* Eqs. 4.5 and 4.6) to the branching ratio of $\mu \rightarrow e\gamma$, as well as the total contribution, for two different CP violating phases. For the line labeled

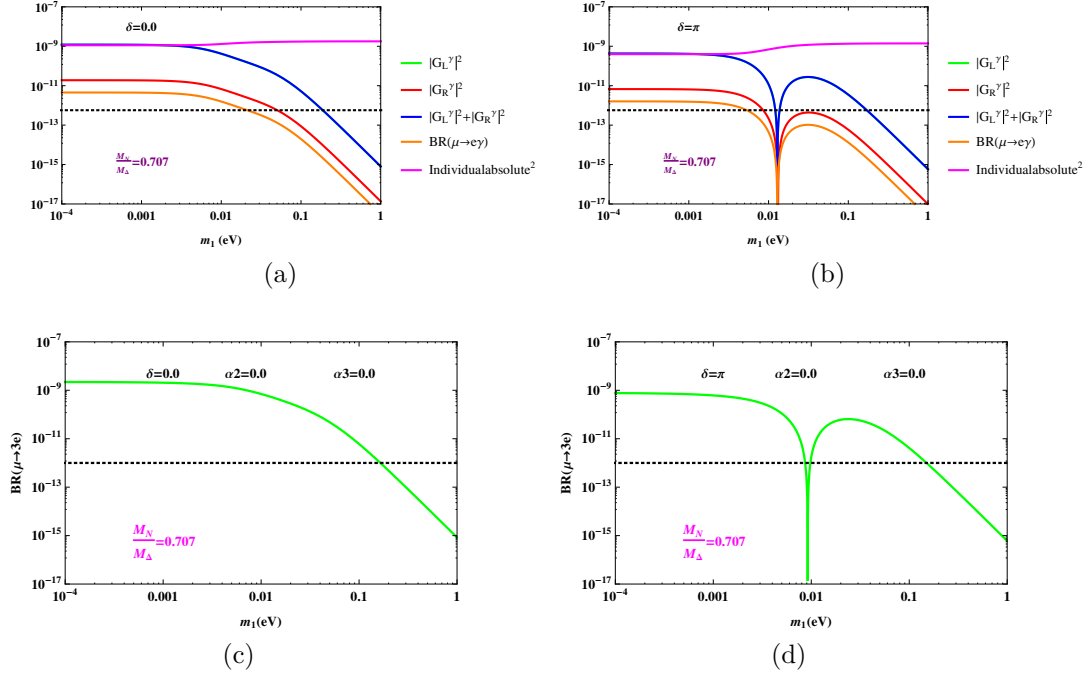


Figure 4.4: *Upper panels:* Variation of G_L^γ , G_R^γ and the total branching ratio of $\mu \rightarrow e\gamma$ process as a function of the light neutrino mass for $\delta = 0$ (left) and π (right). *Lower panels:* Variation of the branching ratio of $\mu \rightarrow 3e$ as a function of the lightest neutrino mass for $\delta = 0$ (left) and π (right). Here we have chosen $\alpha_2 = 0$, $\alpha_3 = 0$, $M_N/M_\Delta = 0.707$, Type-I dominance and NH case.

as $(\text{individual absolute})^2$, we have summed over the absolute-square of the individual contributions inside G_L^γ , G_R^γ , thereby neglecting the possibility of any interference. However, the interference terms are important for the total contribution to the branching ratio $\mu \rightarrow e\gamma$. The phase variation induces suppression in the branching ratio due to cancellation between different contributions. We highlight this particular feature with suitable choices of the CP phases $\delta = 0$ and π in Fig. 4.4 (upper panels). From Figs. 4.4a and Fig. 4.4b, it is evident that while the $(\text{individual absolute})^2$ increases with the lightest neutrino mass, the contributions G_L^γ , G_R^γ as well as the total $\text{BR}(\mu \rightarrow e\gamma)$ decrease for quasi-degenerate light neutrino masses. This happens due to the cancellation between three comparable heavy neutrino contributions. Similar feature is visible for $\mu \rightarrow 3e$ process, as depicted in Fig. 4.4c. From Fig. 4.4 (right panels), it is evident that for the Dirac CP phase $\delta = \pi$, there is an additional suppression in the branching ratios of $\mu \rightarrow e\gamma$ and $\mu \rightarrow 3e$ near $m_1 \sim 0.01$ eV due to exact

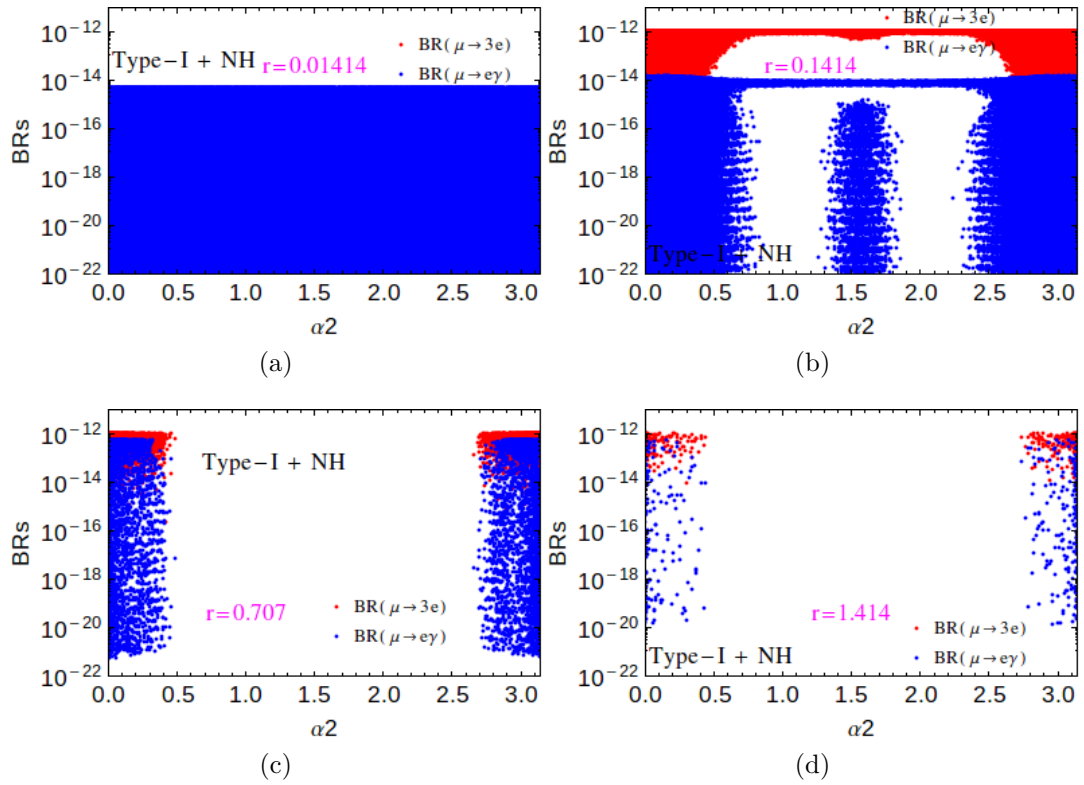


Figure 4.5: The predicted branching ratios of $\mu \rightarrow e\gamma$ (blue points) and $\mu \rightarrow 3e$ (red points) processes, when experimental bounds on the branching ratios of both are simultaneously satisfied, as a function of the Majorana phase α_2 for Type-I and NH case.

cancellation between the different terms.

In Fig. 4.5 we show the constraints on the Majorana phase α_2 that can be obtained from LFV bounds for the Type-I, NH case for different values of the ratio r . The oscillation parameters are varied as before and m_1 is varied in the range 10^{-4} eV to 1 eV. The figures show that for $r = 0.01414$, corresponding to $M_\Delta = 50$ TeV, there are no constraints from LFV processes as for such a heavy mass, the triplet is effectively decoupled. As the value of r increases the allowed values of α_2 start getting restricted from LFV constraints and the preferred values for α_2 are seen to cluster around 0 and π . For $r = 1.414$ the LFV constraints are stronger and the density of the points are lesser.

4.1.2 Smaller value of r

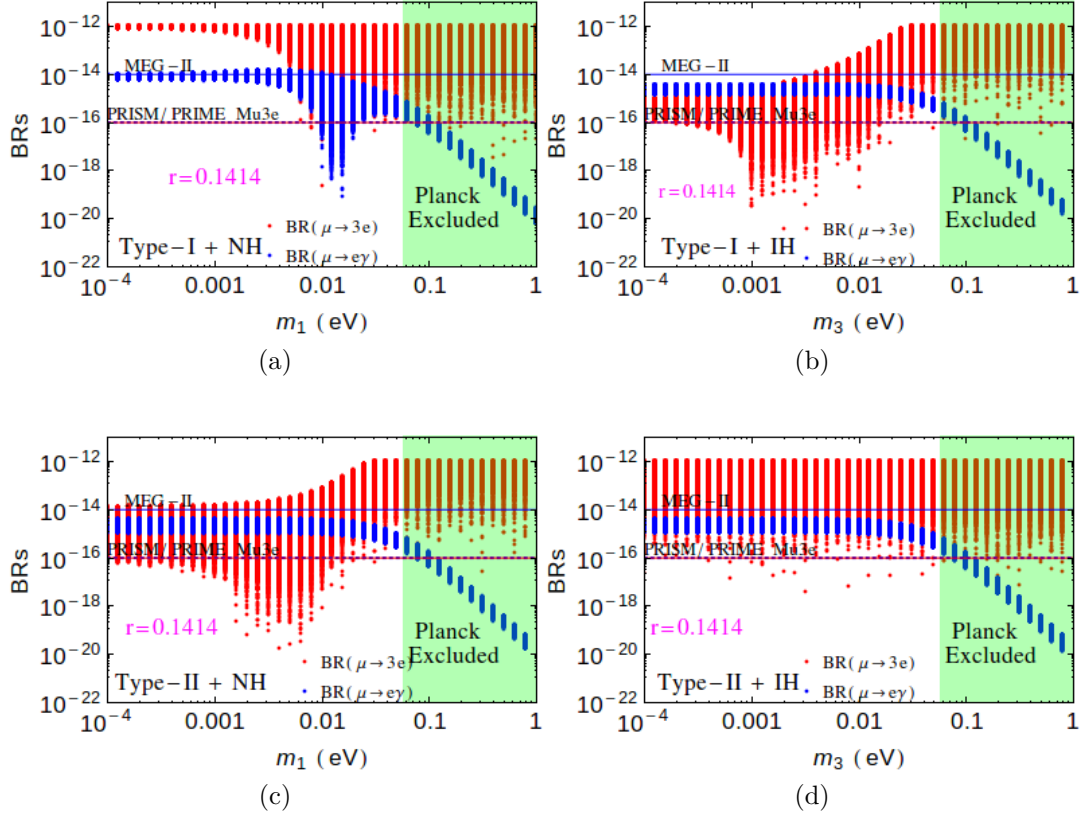


Figure 4.6: The predicted branching ratios of $\mu \rightarrow e\gamma$ (blue points) and $\mu \rightarrow 3e$ (red points) processes as a function of the lightest neutrino mass for NH (left panels) and IH (right panels) in Type-I (top panels) and Type-II (bottom panels) dominance. The ratio of the heaviest neutrino mass and the Higgs triplet mass has been set to $r = 0.1414$. The green shaded region is disfavored at 95% C.L. from Planck data. The blue solid horizontal line is for MEG-II sensitivity, while PRISM/PRIME and Mu3e will have sensitivities up to the blue dotted and red solid horizontal lines respectively.

Next we consider the case where $M_N = 500$ GeV and $m_{\delta_R^{++}} = m_{\delta_L^{++}} = 5$ TeV, leading to $r = 0.1414$. For such a heavy Higgs triplet, we expect its contribution to LFV processes to be relatively smaller, thereby allowing more MLRSM parameter space for hierarchical neutrinos. This is indeed the case, as shown in Fig. 4.6. A few comments are in order: (i) For the process $\mu \rightarrow e\gamma$, the predicted branching ratio is beyond the reach of MEG-II upgrade [51] excepting for Type-I dominance and NH, where hierarchical m_1 ($\lesssim 0.01$ eV) may just be within the

reach. However, for the process $\mu \rightarrow 3e$, the predicted branching ratios are within the experimental reach of Mu3e [53]. (ii) For the scenarios shown in Figs. 4.6 (a), (b) and (c), an additional suppression occurs due to phase cancellation in the branching ratio of $\mu \rightarrow 3e$ for $m_{\text{lightest}} \sim 10^{-3} - 10^{-2}$ eV, thereby making part of the allowed parameter space beyond the reach of the Mu3e sensitivity. However, the Type-II dominance IH cases is not affected by such phase-cancellation (*cf.* Fig. 4.6 (d)) and hence, can be tested more easily in future.

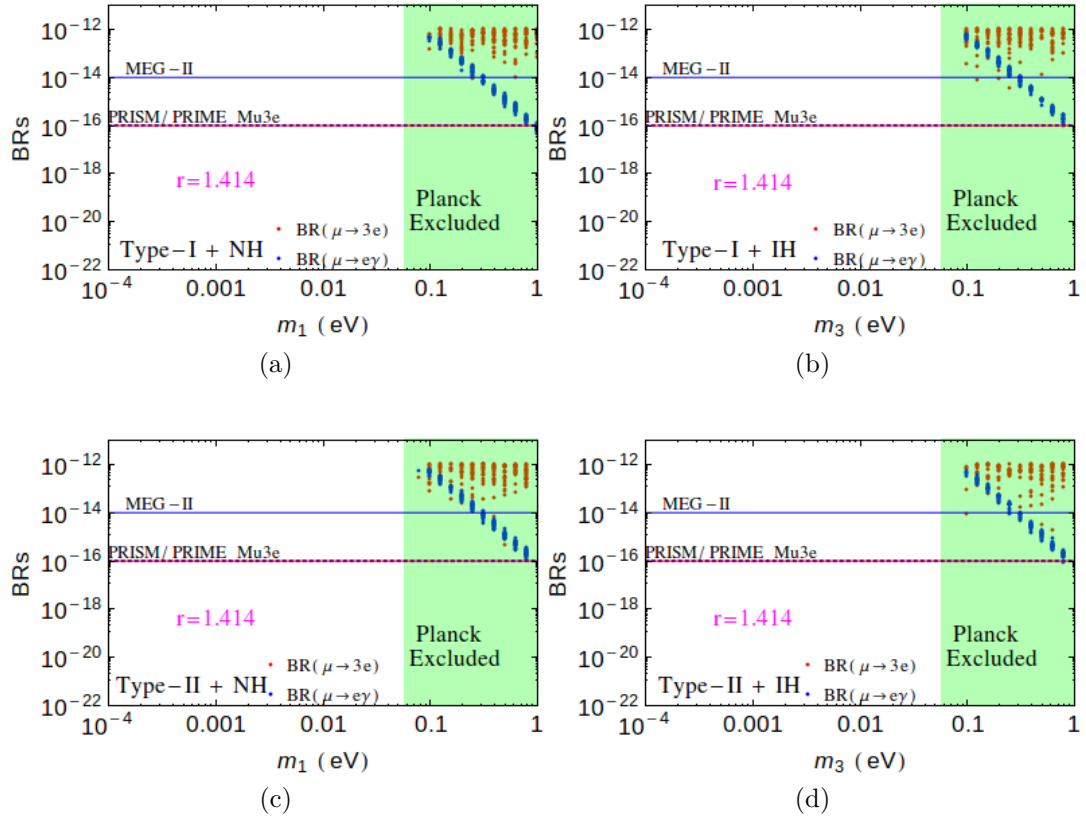


Figure 4.7: The predicted branching ratios of $\mu \rightarrow e\gamma$ (blue points) and $\mu \rightarrow 3e$ (red points) processes as a function of the lightest neutrino mass for NH (left panels) and IH (right panels) in Type-I (top panels) and Type-II (bottom panels) dominance. The ratio of the heaviest neutrino mass and the Higgs triplet mass has been set to $r = 1.414$. The green shaded region is disfavored at 95% C.L. from Planck data. The blue solid horizontal line is for MEG-II sensitivity, while PRISM/PRIME and Mu3e will have sensitivities up to the blue dotted and red solid horizontal lines respectively.

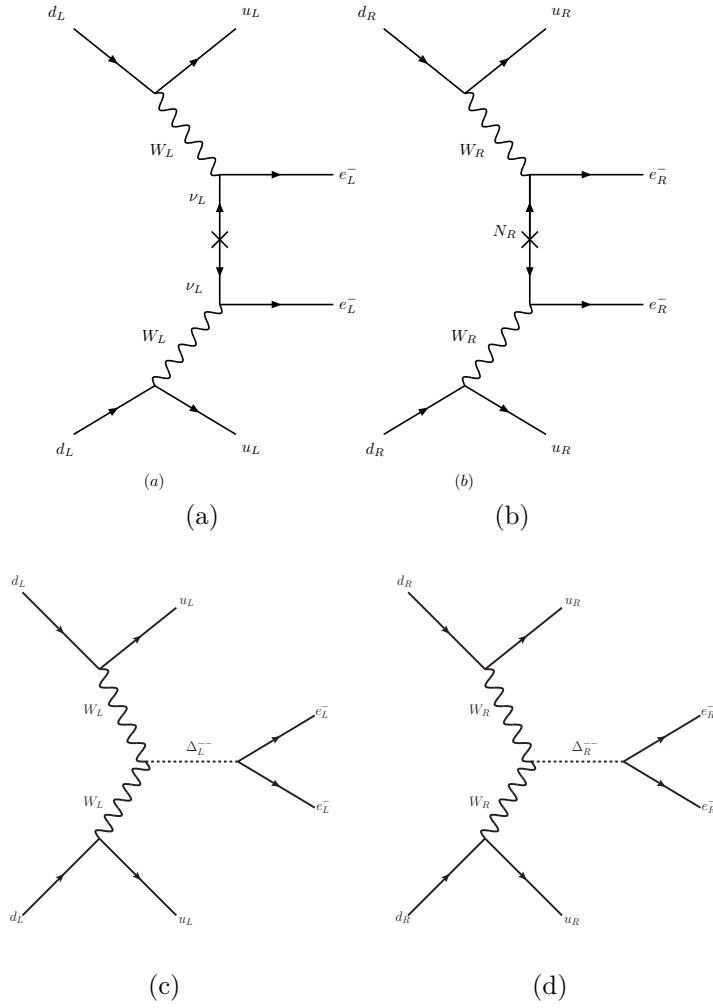


Figure 4.8: The dominant LH and RH current contributions to the $0\nu\beta\beta$ process in our model.

4.1.3 Larger value of r

In Fig. 4.7, we show the prediction for the other interesting regime, *i.e.*, lighter Higgs triplet and heavier RH neutrinos. We consider $M_N = 500$ GeV and $m_{\delta_R^{++}} = m_{\delta_L^{++}} = 500$ GeV, so that $r = 1.414$. In this case, the predicted LFV rates will be much larger than the previous two cases, due to a large triplet contribution. Hence, this scenario is heavily constrained from present experimental constraints. It is evident from Fig. 4.7 that the predicted branching ratios are in agreement with the experimental LFV rates, only for quasi-degenerate mass regime, which is already disfavored by the cosmological constraints from Planck.

4.2 Neutrinoless double beta decay

In a TeV-scale MLRSM, there are several new contributions to the LNV process of $0\nu\beta\beta$ [30, 81, 198, 200, 201, 243–250, 257], due to the presence of RH currents and Higgs triplets.

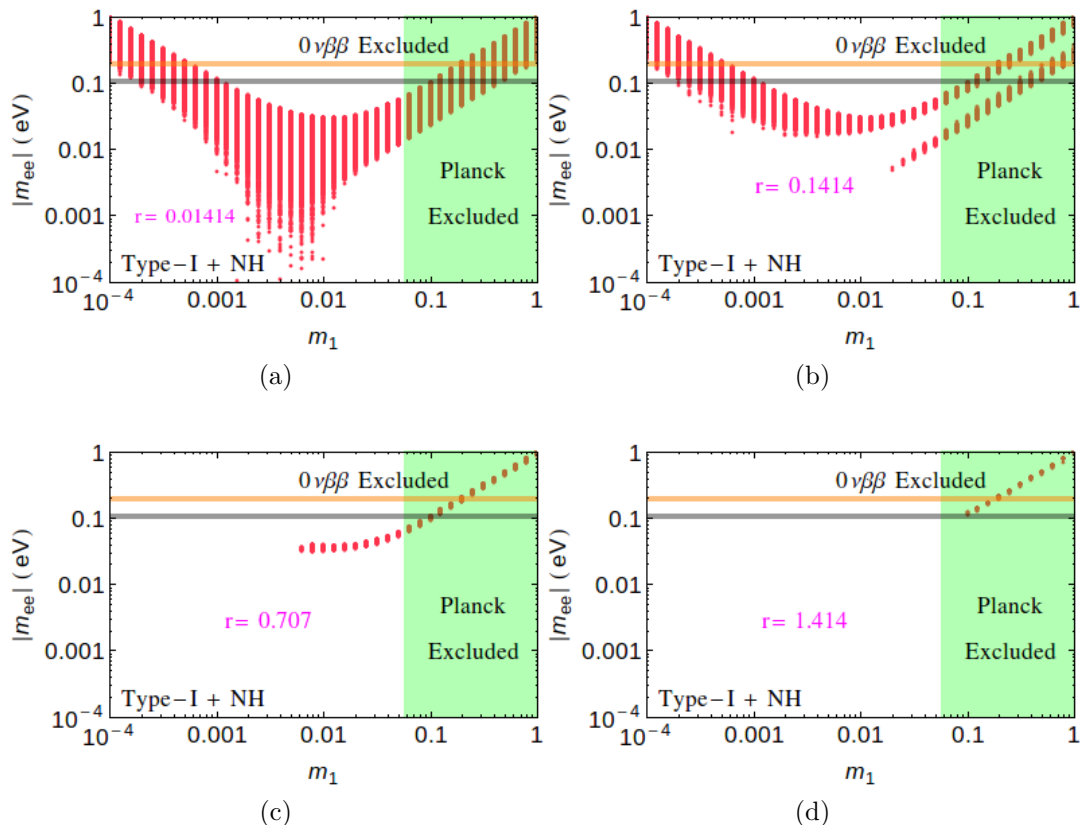


Figure 4.9: The variation of the effective neutrino mass as a function of the lightest neutrino mass for Type-I dominance with NH. The different panels correspond to different values of r . The green shaded area is disfavored at 95% C.L. by Planck. The orange band corresponds to the range of $|m_{ee}| = 0.18 - 0.22$ eV, the region above which is excluded at 90% C.L. by the combined limit from GERDA [258]. The black band corresponds to the future limit ($|m_{ee}| = 0.098 - 0.12$ eV) from Gerda-II.

As discussed in the previous section, the present bounds from $\mu \rightarrow e\gamma$ and $\mu \rightarrow 3e$ still allow the heavy neutrino to Higgs triplet masses as large as $\mathcal{O}(1)$. So the Higgs triplet contribution to $0\nu\beta\beta$ can in principle be sizable and should not be neglected. In our subsequent discussion of $0\nu\beta\beta$, we therefore take into account the Higgs triplet contribution from Δ_R . The contribution from the other

Higgs triplet Δ_L is suppressed by the light neutrino mass. Also we assume the mixing between the LH and RH sectors to be small, so that their contributions to $0\nu\beta\beta$ can be neglected.

Thus, in our case, the half life of $0\nu\beta\beta$ only includes purely LH and RH contributions:

$$\frac{1}{T_{1/2}^{0\nu}} = G_{01}^{0\nu} \left(\left| \mathcal{M}_{\nu}^{0\nu} \eta_{\nu} \right|^2 + \left| \mathcal{M}_{N}^{0\nu} \eta_R \right|^2 \right), \quad (4.10)$$

where $G_{01}^{0\nu}$ is the phase space factor and $\mathcal{M}_{\nu,N}^{0\nu}$ are the relevant nuclear matrix elements (NMEs) for light and heavy neutrino contributions, respectively. The particle physics parameters η_{ν} and η_R correspond to the LH and RH amplitudes, respectively (*cf.* Fig 4.8):

$$\eta_{\nu} = \frac{1}{m_e} \sum_i U_{ei}^2 m_i, \quad \eta_R = m_p \left(\frac{m_{WL}}{m_{WR}} \right)^4 \left(\sum_i \frac{V_{ei}^{*2}}{M_i} + \sum_i \frac{V_{ei}^{*2} M_i}{m_{\delta_R^{++}}^2} \right), \quad (4.11)$$

where m_e and m_p are the masses of electron and proton, respectively. The corresponding effective neutrino mass is given by

$$m_{ee} = U_{ei}^2 m_i + \langle p^2 \rangle \left(\frac{m_{WL}}{m_{WR}} \right)^4 \left(\sum_i \frac{V_{ei}^{*2}}{M_i} + \sum_i \frac{V_{ei}^{*2} M_i}{m_{\delta_R^{++}}^2} \right), \quad (4.12)$$

where $\langle p^2 \rangle = (198)^2 \text{ MeV}^2 ((185)^2 \text{ MeV}^2)$ for $M_{WR} = 3500 \text{ GeV}$ (2000 GeV). Note that the value of $\langle p^2 \rangle$ refer to Ge^{76} nuclei for which we have done our analysis.

In Fig. 4.9, we show the effective mass m_{ee} versus the lightest neutrino mass m_1 for Type-I dominance with NH and for different values of the ratio r . In obtaining the effective mass we have used only those values of parameters that are consistent with the experimental limits of $\mu \rightarrow e\gamma$ and $\mu \rightarrow 3e$ processes. Thus these plots are inclusive of LFV constraints.

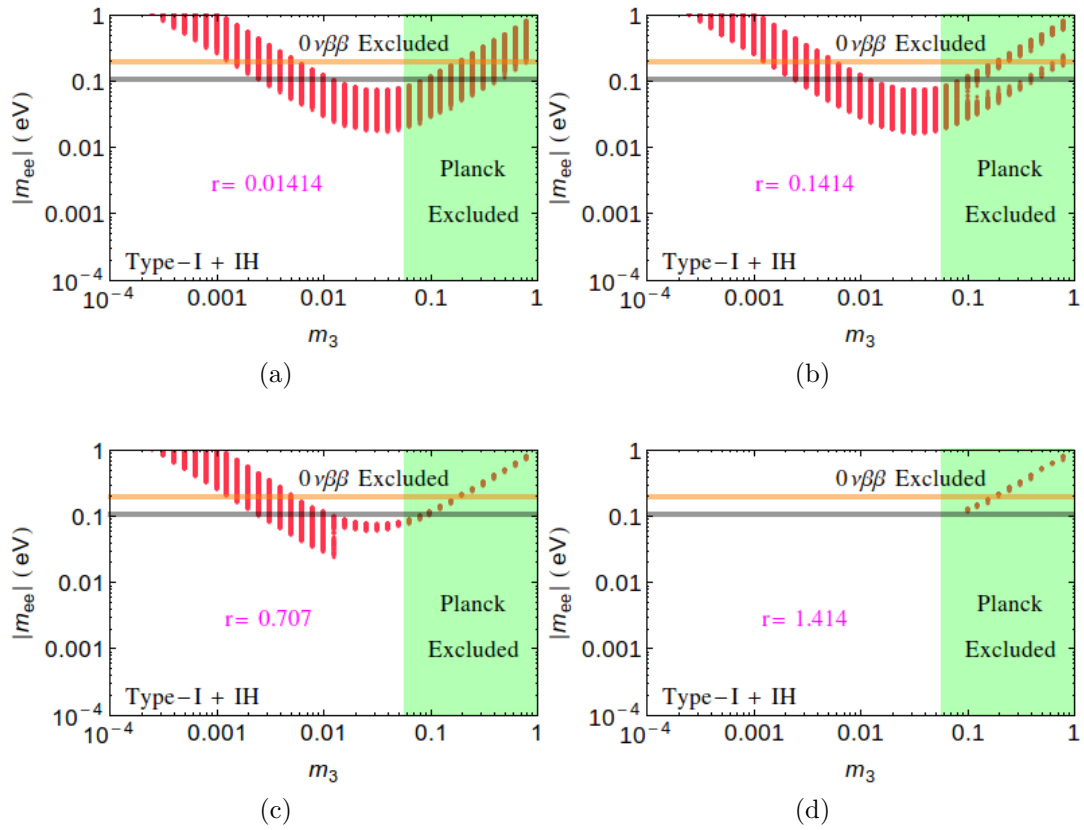


Figure 4.10: The variation of the effective mass as a function of the lightest neutrino mass for Type-I dominance and IH. The different panels correspond to different values of r . The green shaded area is disfavored at 95% C.L. by Planck. The orange band corresponds to the range of $|m_{ee}| = 0.18 - 0.22$ eV, the region above which is excluded at 90% C.L. by the combined limit from GERDA [258]. The black band corresponds to the future limit ($|m_{ee}| = 0.098 - 0.12$ eV) from Gerda-II.

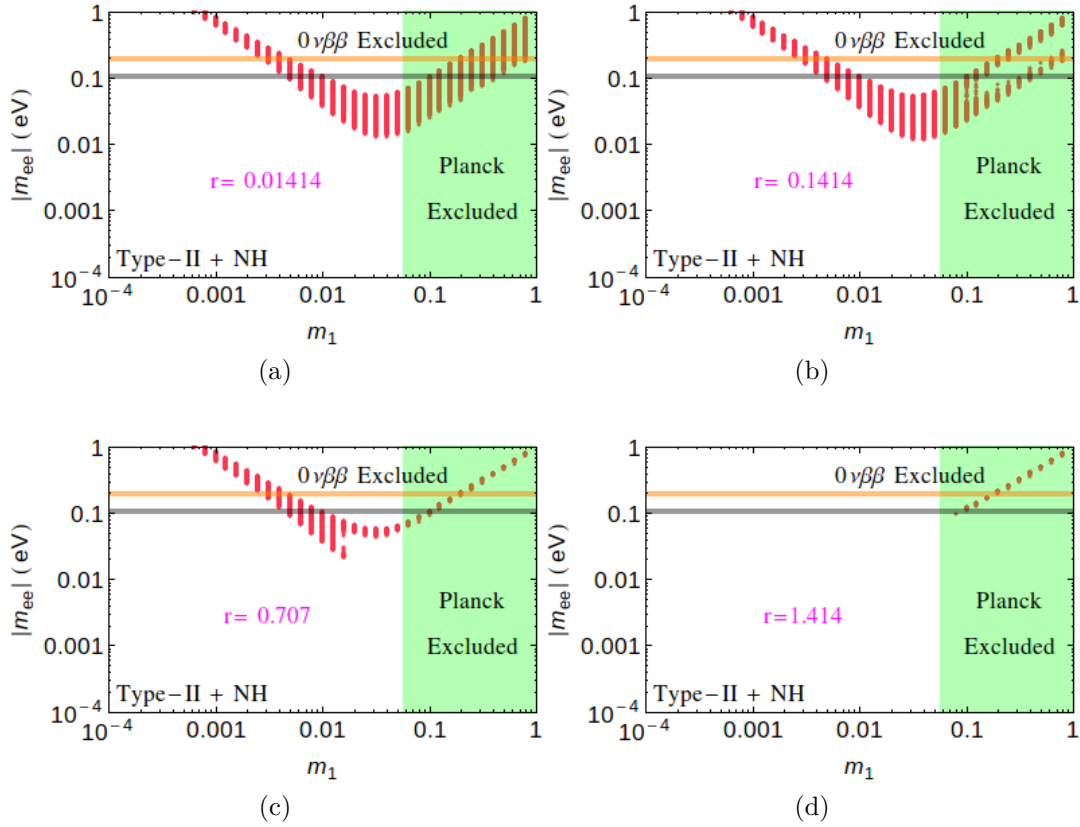


Figure 4.11: The variation of the effective mass as a function of the light neutrino mass for Type-II dominance and NH. The orange band corresponds to the range of $|m_{ee}| = 0.18 - 0.22$ eV, the region above which is excluded at 90% C.L. by the combined limit from GERDA [258]. The black band corresponds to the future limit ($|m_{ee}| = 0.098 - 0.12$ eV) from Gerda-II.

Fig. 4.9a is for $r = 0.01414$ ($M_N = 500$ GeV, $M_\Delta = 50$ TeV). For such a high value of M_Δ , it is almost decoupled and there are no constraints from the LFV processes. Thus the m_{ee} plot for $0\nu\beta\beta$ is the same as that obtained in [200] without including the triplet contribution. Note that the width of the plot in this case is due to the variation over the mixing angles and phases. Note that for this case although there are no constraints from LFV, current $0\nu\beta\beta$ bounds disfavor lower (fully hierarchical) and higher (QD) values of m_1 . The later are also disfavored from Planck data.

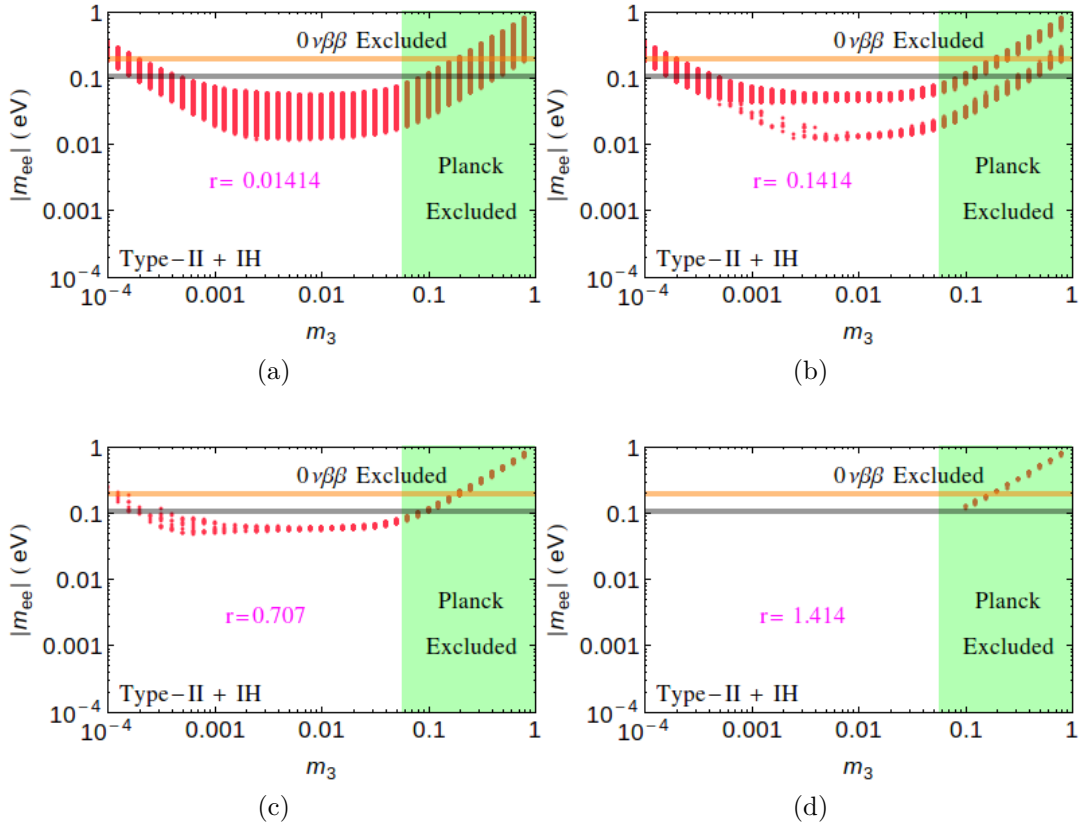


Figure 4.12: The variation of the effective mass as a function of the lightest neutrino mass for Type-II dominance and IH. The different panels correspond to different values of r . The green shaded area is disfavored at 95% C.L. by Planck. The orange band corresponds to the range of $|m_{ee}| = 0.18 - 0.22$ eV, the region above which is excluded at 90% C.L. by the combined limit from GERDA [258]. The black band corresponds to the future limit ($|m_{ee}| = 0.098 - 0.12$ eV) from Gerda-II.

As we got to a higher value of $r = 0.1414$ ($M_N = 500$ GeV, $M_\Delta = 5000$ GeV) and a lower value of M_Δ in Fig. 4.9b the whole range of m_1 is seen to be allowed from the current LFV constraints (see Fig. 4.6). However, there are constraints on the Majorana phase α_2 as has been shown in Fig. 4.5 of Section 4.1. This rules out a part of the parameter space and very low values of m_{ee} are not obtained. The shape of the curve for m_{ee} can be attributed to the constraints on the phases from LFV bounds. We have checked that if LFV constraints are not included then the figure for m_{ee} replicates the one for $r = 0.01414$.

For smaller Higgs triplet masses that lead to larger value of r , such as, $r = 0.707$ and 1.414 , the hierarchical mass range $m_1 \leq 0.01$ eV is ruled out and

the experimentally allowed region is the quasi-degenerate region (see the first panel corresponding to type-I NH in Fig. 4.3 and Fig. 4.7) The impact of the LFV constraints on the prediction for $0\nu\beta\beta$ is clearly visible from Fig. 4.9c and Fig. 4.9d, where mostly for quasi-degenerate light neutrino masses, the effective mass is in agreement with the LFV constraints. Note that the QD region is already disfavoured by the Planck data and the value of the effective mass in this region is also beyond the current experimental limit and hence is excluded. For $r=0.707$ a small window for m_1 ($\sim 0.005 - 0.05$ eV) still exists which is consistent with all the current constraints. However this region is beyond the reach of the future Ge experiments.

Similarly, in Figs. 4.10, 4.11 and 4.12, we show the effective mass versus lightest neutrino mass for the case of Type-I dominance with IH, Type-II dominance with NH and IH, respectively. For these cases again the $r = 0.01414$ gives m_{ee} as is obtained without the inclusion of the triplet effect. Also note that for these plots the cancellation region with very low value of m_{ee} is not obtained. From the figures, it is evident that a large $r = 1.414$ is highly constrained, whereas a moderate value of r is more favorable and some regions exist which can further be tested in next generation $0\nu\beta\beta$ experiments, such as GERDA-II [259], along with the future LFV experiments. The exclusion of certain regions of parameter space specially for higher values of the lowest mass is due to the constraint on the phase α_2 from LFV processes.

4.3 Diboson excess, LFV and $0\nu\beta\beta$

A number of recent resonance searches with the $\sqrt{s} = 8$ TeV LHC data have observed excess events around an invariant mass of 2 TeV, the most notable one being a 3.4σ local excess in the ATLAS search [260–262] for a heavy resonance decaying into a pair of SM gauge bosons VV (with $V = W, Z$), followed by the hadronic decay of the diboson system.

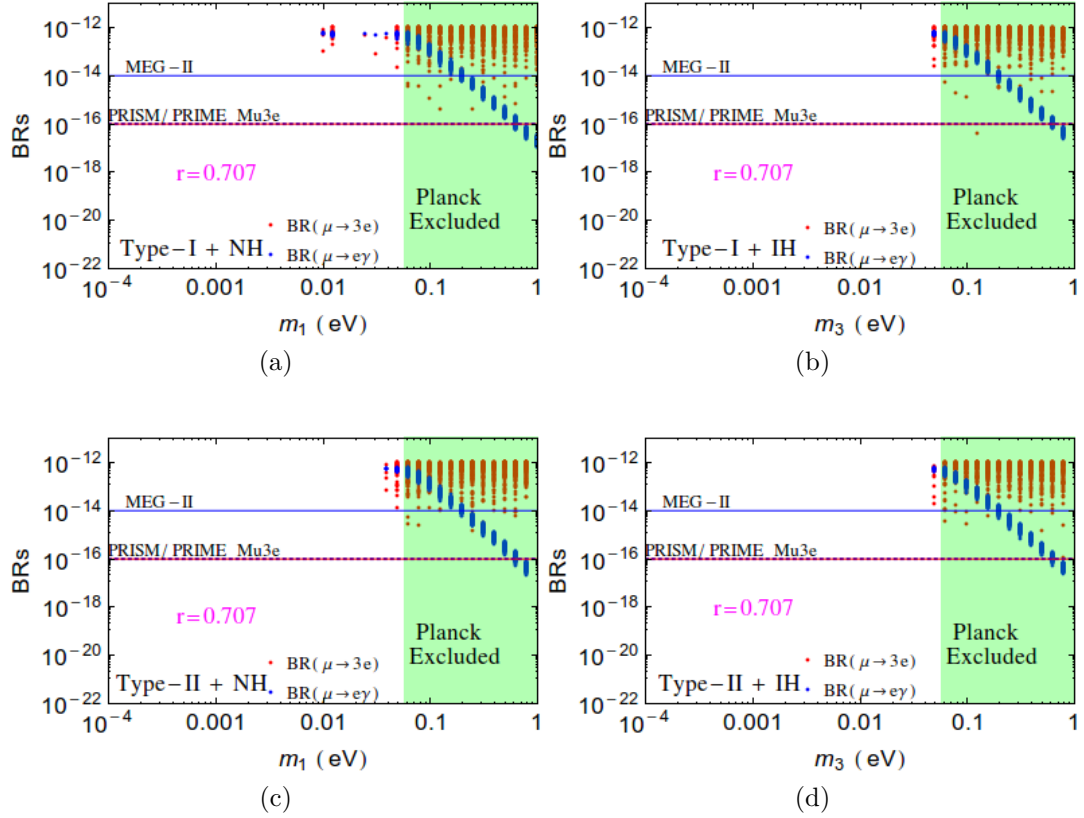


Figure 4.13: The branching ratio of $\mu \rightarrow e\gamma$ and $\mu \rightarrow 3e$ vs light neutrino mass, for the right-handed gauge boson mass $M_{W_R} = 2$ TeV and $\frac{M_N}{M_\Delta} = 0.707$. The different panels correspond to: (a) Type-I dominant NH (b) Type-I dominant IH (c) Type-II dominant NH (d) Type-II dominant IH.

The corresponding CMS search also reports a mild excess around the same invariant mass [263, 264]. This diboson excess can be explained by a TeV-scale MLRSM for the RH gauge boson mass $m_{W_R} = 2$ TeV and the corresponding gauge coupling $g_R = 0.5$ [265–271]. In this section, we study the implications of the diboson excess on the predictions of LFV and $0\nu\beta\beta$ (see also [250]). For the gauge couplings $g_R \neq g_L$, the LFV process $\mu \rightarrow e\gamma$, $\mu \rightarrow 3e$ will be as follows:

$$\text{BR}(\mu \rightarrow e\gamma) = \frac{3\alpha_{\text{em}}}{2\pi} (|G_L^\gamma|^2 + |G_R^\gamma|^2), \quad (4.13)$$

where the factors G_L^γ and G_R^γ are given by,

$$G_L^\gamma \sim \left(\frac{g_R}{g_L}\right)^2 \sum_{i=1}^3 V_{L\mu i} V_{L e i}^* \left[\left(\frac{m_{W_L}}{m_{W_R}}\right)^2 G_1^\gamma(b_i) + \frac{2b_i}{3} \frac{m_{W_L}^2}{m_{\delta_R^{++}}^2} \right], \quad (4.14)$$

$$G_R^\gamma \sim \left(\frac{g_R}{g_L}\right)^2 \sum_{i=1}^3 V_{L\mu i} V_{L e i}^* b_i \left[\frac{2}{3} \left(\frac{m_{W_L}}{m_{\delta_L^{++}}}\right)^2 G_1^\gamma(b_i) + \frac{1}{12} \frac{m_{W_L}^2}{m_{H_1^+}^2} \right]. \quad (4.15)$$

The effective mass of $0\nu\beta\beta$ will be of the following form:

$$m_{ee} = U_{ei}^2 m_i + \left(\frac{g_R}{g_L}\right)^4 \langle p^2 \rangle \left(\frac{M_{W_L}}{M_{W_R}}\right)^4 \left(\sum_i \frac{V_{ei}^{*2}}{M_i} + \sum_i \frac{V_{ei}^{*2} M_i}{M_{\delta_R^{++}}^2} \right). \quad (4.16)$$

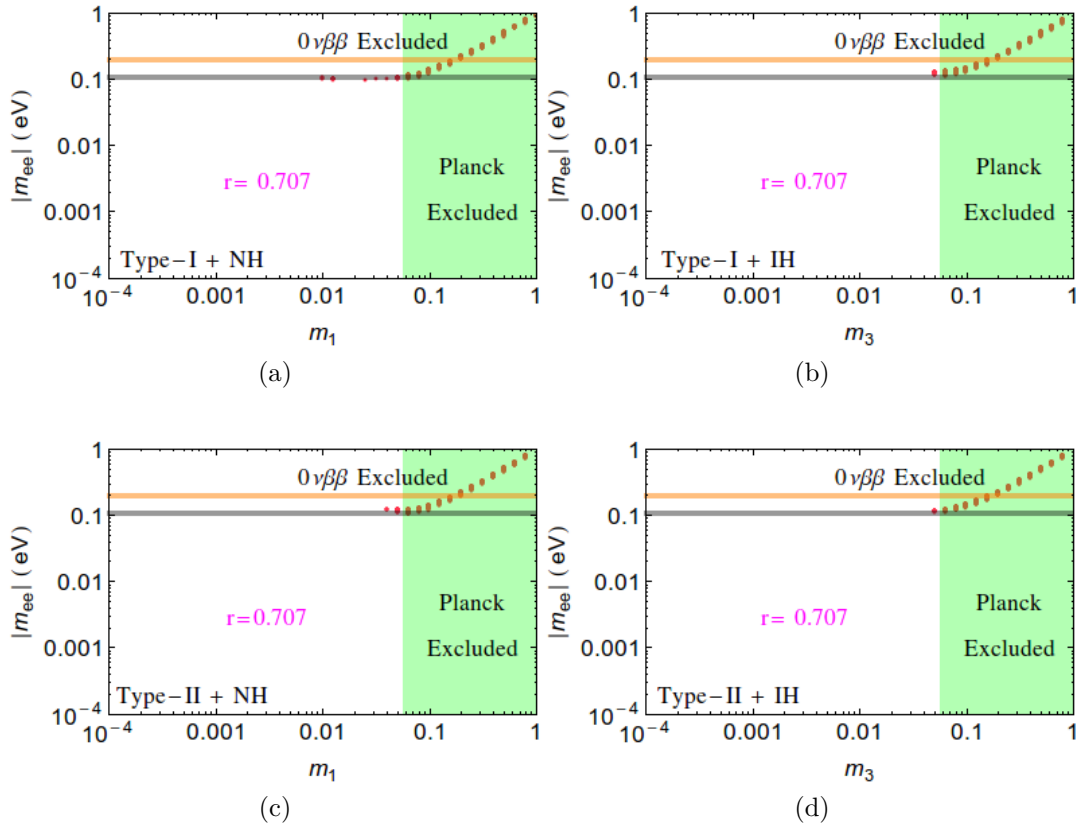


Figure 4.14: The effective mass m_{ee} vs light neutrino mass, for the right-handed gauge boson mass $M_{W_R} = 2$ TeV and $\frac{M_N}{M_\Delta} = 0.707$. The different panels correspond to: (a) Type-I dominant NH (b) Type-I dominant IH (c) Type-II dominant NH (d) Type-II dominant IH. The orange band corresponds to the range of $|m_{ee}| = 0.18 - 0.22$ eV, the region above which is excluded at 90% C.L. by the combined limit from GERDA [258]. The black band corresponds to the future limit ($|m_{ee}| = 0.098 - 0.12$ eV) from Gerda-II.

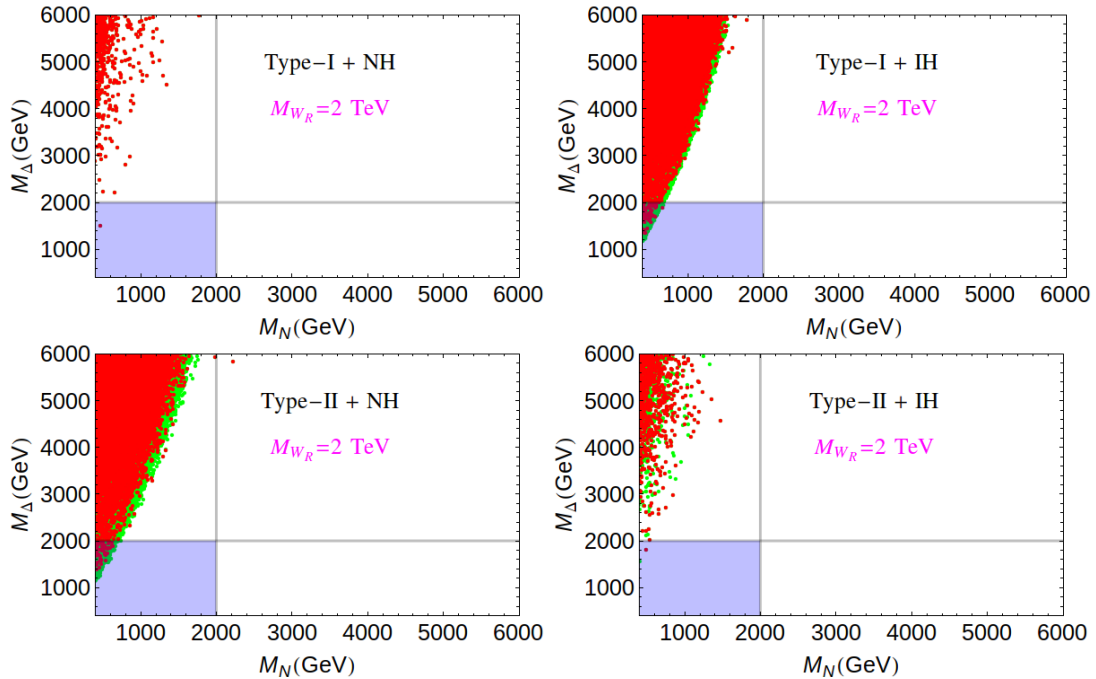


Figure 4.15: The allowed region in the M_N vs M_Δ plane that is experimentally allowed by LFV processes, as well as $0\nu\beta\beta$. The green points are after satisfying the LFV constraints, while the red points also satisfy the current upper bound on effective mass $m_{ee} < 0.18$ eV. It is evident, that for $M_{W_R} = 2$ TeV and $g_R = 0.5$, the lighter Higgs triplet and heaviest neutrino masses, such as, 500 GeV is ruled out by the experimental constraints.

In Figs. 4.13 and 4.14, we show the branching ratios of $\mu \rightarrow e\gamma$, $\mu \rightarrow 3e$ processes and the effective mass m_{ee} for the right-handed gauge boson mass $M_{W_R} = 2$ TeV. Comparing Fig. 4.13 with Fig. 4.3 of $M_{W_R} = 3.5$ TeV, it is evident that even moderate value of $r = 0.707$ is severely constrained. This is also reflected in Fig. 4.14 from $0\nu\beta\beta$ limits. Finally in Fig. 4.15, we show the allowed region in the M_N vs M_Δ plane that is experimentally allowed by LFV processes, as well as $0\nu\beta\beta$. It is evident, that for $M_{W_R} = 2$ TeV and $g_R = 0.5$, the lighter Higgs triplet and heaviest neutrino masses, such as, 500 GeV is ruled out by the experimental constraints. The blue shaded regions correspond to the natural case with M_N and $M_\Delta \lesssim 2$ TeV. In the figures the green points are after satisfying the LFV constraints, while the red points also satisfy the current upper bound on effective mass $m_{ee} < 0.18$ eV.

4.4 Summary

To summarize this chapter, we have studied the correlated constraints from LFV and $0\nu\beta\beta$ for a TeV scale MLRSM including the contribution of the Higgs triplet (Δ_R). Earlier this contribution was neglected assuming LFV constraints to be satisfied only if the ratio of the heaviest right handed neutrino mass to the triplet mass: $\frac{M_N}{M_\Delta} = r < 0.1$. We show that for lower values of M_Δ (allowed by the current constraints), such that $r \lesssim \mathcal{O}(1)$, it is possible to get allowed parameter regions consistent with the LFV limits. We perform our investigation in the Type-I and Type-II seesaw dominance limits for both NH and IH. We fix the mass of the heaviest sterile neutrino $M_N = 500$ GeV and vary the triplet mass to get various values of the quantity r . For a moderate value of $r = 0.707$, lower values of m_1 are disfavoured for only the type-I, NH case from LFV constraints. Constraints are also obtained on the phase α_2 restricting it near 0 and π . For $r = 1.414$, LFV data puts strong constraints on the light neutrino mass and only quasi-degenerate region remains consistent with LFV constraints. However, this region is disfavoured by Planck experiment as well as current experiments on $0\nu\beta\beta$. For a smaller $r = 0.1414$ the constraints from LFV are not very strong. We also give the predictions for m_{ee} for all the cases including the constraints from LFV. In general as r is enhanced, because of the LFV constraints, less and less regions are allowed for m_{ee} in all the cases. For lower values of $r = 0.1414, 0.707$, the current limits of $0\nu\beta\beta$ disfavours some regions for smaller values of the lowest mass as well as the QD regions which are in any case disfavoured by the Planck data. The LFV constraints on the Majorana phase α_2 play a non-trivial role in ruling out parts of parameter spaces. Finally, we also study the allowed parameter space for $M_{W_R} = 2$ TeV and $g_R = 0.5$ which is motivated by the recent indication of a diboson excess by the ATLAS experiment. This scenario is heavily constrained even for a moderate value of $r = 0.707$.

Chapter 5

Conclusion and future prospects

Neutrinos are massless in the SM but oscillation experiments have established that they have mass. The mechanism of neutrino mass generation remains a profound puzzle in particle physics. One of the unique features for neutrinos as compared to the other fermions is the possibility of having a Majorana mass term, which violates lepton number by 2 units. Since the masses of neutrinos are much smaller as compared to their charged counterparts questions arise as to whether the mechanism of neutrino mass generation is different and can be connected to the Majorana nature of the neutrinos. A natural way to generate small neutrino masses is provided by the seesaw models which require neutrinos to be Majorana particles. The outstanding performance of the world's largest collider, the LHC, has generated a lot of interest to search for signatures of models that can generate neutrino masses, at colliders. For this the scale of new physics should be $\sim \text{TeV}$.

In this thesis we have examined the possibility of probing neutrino mass models at colliders. Thus our prime interest is the TeV scale models which also allow for a sizable production of the BSM particles. We have studied three scenarios (i) the Babu-Nandi-Tavartkiladze-model (BNTM), in which neutrino mass is generated by a higher dimensional operator ($d = 7$) at tree level, and by a dimension-5 operator at one loop level. The smallness of the neutrino masses is partially attributed to the small lepton number violating coupling, along with the suppression from higher dimensionality and the loop factor; (ii) the minimal

linear seesaw model (MLSM), in which, smallness of neutrino mass is assured by a tiny lepton number violating parameter; (iii) the minimal Left-Right symmetric model (MLRSM), which is a model with an extended gauge sector. In case of the MLRSM, even though the light-heavy mixing is small there can be interesting consequences at the collider as well as for LFV and $0\nu\beta\beta$ processes due to the presence of right-handed currents at the TeV scale.

The LHC has discovered the Higgs boson and looks forward to discover/get a hint of new physics in its future runs. The multilepton signatures are regarded as an important window to look for BSM physics at the LHC. As the multiplicity of charged leptons ($\ell = e, \mu$) increases, the SM backgrounds decrease. We have analyzed the multilepton signatures in the above three models. In the BNTM and the MLRSM, the multilepton signatures originate from the charged scalars, while in the MLSM the decays of heavy neutrinos lead to the multilepton signals. We have discussed the production and decays of the BSM particles *i.e.*, the charged scalars and the heavy neutrinos. In the MLSM and the MLRSM, we have considered the standard s-channel and for some cases VBF productions of the heavy neutrinos and the charged scalars. For our numerical study, various packages like CalcHEP, ALPGEN, MadGraph, PYTHIA are used.

BNTM is an example model in which neutrino masses are generated by higher dimensional operators. Neutrino masses are generated through an effective dimension-7 operator at the tree level and through a dimension-5 operator at the one loop level. This model is an extension of the SM with an isospin 3/2 scalar and a pair of vector-like $SU(2)_L$ triplet fermions with hypercharge 2. We have studied the multilepton signatures originating from the charged scalars in this model. We chose the scalar quadruplet to be of mass lower than TeV such that the charged scalars belonging to this can be pair produced at the LHC. Subsequent decays of these scalars to leptons or W -bosons and further decays of W -boson produce multilepton final states. We have analysed the tri-lepton, same-sign tri-lepton, four-lepton, five-lepton and six-lepton signals in this model at the LHC at $\sqrt{s} = 14$ TeV with an integrated luminosity $\int \mathcal{L} dt = 100 \text{ fb}^{-1}$. The important signatures of this model are the same-sign-tri-lepton, five-lepton

and six-lepton signals which have almost nil background from the SM.

A noteworthy feature in this model is the presence of the effective vertex $\Phi^{\pm\pm}\ell^{\mp}\ell^{\mp}$ which facilitates the same-sign-tri-lepton events for which the SM background is not significant and hence they can herald new physics beyond the SM. Moreover, since this vertex depends on the neutrino mass matrix elements, it induces a dependence on the neutrino mass hierarchy in the observed signal. The signatures are studied for both NH and IH. We choose the parameters of the model to cover the different dominant decay modes of the charged scalars. Among the events studied, the 6 lepton events do not survive the cuts for most of the benchmark points. For the other multilepton events significant excess over the SM background can be observed. Another hallmark of this model is the possibility of obtaining flavor violating four-lepton signal. We have investigated this option in the context of the LHC and found significant number of events. We have also estimated the additional contribution due to the presence of the new particles, to the $H \rightarrow \gamma\gamma$ rate in this model. In conclusion we find that, this model is phenomenologically rich, can generate small neutrino mass consistent with data and can also be probed at the LHC through the multilepton signatures.

The MLSM is an extension of the SM by two heavy gauge singlets with opposite lepton numbers. The model consists of one massless, two light Majorana and two heavy Dirac neutrinos. This model is fully reconstructible from the oscillation data, except an overall coupling. This coupling is constrained by the LFV and stability of the electroweak vacuum [89]. We have studied the collider phenomenology of heavy neutrinos in the MLSM at the LHC with 14 TeV center of mass energy. In particular the tri-lepton signals with missing energy, in both the cases of heavy neutrino productions- s-channel and VBF, have been considered. This model can have significance at the LHC for particular combinations of the Majorana phases, otherwise the model can not give significant signals of the heavy neutrinos at the LHC. We found that the s-channel tri-lepton production process have potential to be discovered at the LHC for IH scenario. However due to severe constraint on the light-heavy mixing coming from LFV in the case of NH scenario, both s-channel and VBF productions can not be probed at the

14 TeV LHC with proposed luminosity. For a benchmark point with a heavy neutrino mass $M_N = 100$ GeV, 3σ significance can be achieved with integrated luminosity of ~ 0.73 (2175) fb^{-1} for s -channel (VBF) signal in the IH scenario. 5σ significance can be reached for s -channel signal with a integrated luminosity of ~ 2 fb^{-1} , however for VBF signal the required luminosity is ~ 6042 fb^{-1} , which is beyond the reach of projected luminosity at the LHC. Discovery reach in the tri-lepton channel can be achieved up to the heavy neutrino mass of ~ 210 (230) GeV with $\sim 5\sigma$ (3σ) significance at the low luminosity (300 fb^{-1}) option of 14 TeV LHC. In the high luminosity (3000 fb^{-1}) search, reach is up to ~ 270 (295) GeV, whereas, VBF channel can only reach up to $\sim 3\sigma$ for M_N at 100 GeV.

The MLRSM is a gauge extension of the SM with the gauge group $SU(2)_L \otimes SU(2)_R \otimes U(1)_{B-L}$. The scalar sector consists of two Higgs triplets and a bi-doublet. The MLRSM restores the parity symmetry beyond some higher scale, the parity breaking scale, and explain the chiral asymmetry of the SM once the parity symmetry is broken spontaneously. It leads naturally to seesaw mechanism which has been a paradigm for understanding small neutrino mass. If the scale of the Left-Right symmetry breaking is low (\sim TeV), one would directly see its signatures at colliders. Other processes like $0\nu\beta\beta$, LFV can also get contributions from the particles having low mass scale.

We have noted down the bounds on the masses of the BSM particles in the MLRSM. Different low energy and collider data have already pushed the masses of the heavy gauge bosons in the MLRSM beyond 1 TeV, but the masses of the charged scalars can be lower. Even after considering FCNC constraint which requires some of the neutral scalars to be beyond 10 TeV, the SM Higgs mass constraint and the constraints on the masses of the particles from the LHC, some of the charged scalar can be light. From the constraints coming from FCNC and mass of the SM-like Higgs, we found that three of the charged scalars $H_1^{\pm\pm}$, $H_2^{\pm\pm}$ and H_1^{\pm} can be simultaneously light, but the fourth one, H_2^{\pm} , can not be light. From theoretical considerations we also found a lowest limit on the masses of the doubly charged scalar, $M_{H_1^{\pm\pm}}$, while the other doubly charged scalar, $H_2^{\pm\pm}$, is not constrained from below. The lowest limit on $M_{H_1^{\pm\pm}}$ is important, as the

production of $H_1^{\pm\pm}$ is much bigger than that of $H_2^{\pm\pm}$ [163].

We have concentrated on studies connected with discovery potential of the charged Higgs bosons within canonical MLRSM which is already phenomenologically rich. They can be produced at the LHC with non-negligible cross sections. However, their production cross sections decrease rapidly with their masses, that is why we have undertaken here more detailed and systematic studies including the production and decays of charged scalars. We have focused on the single and pair production of doubly charged scalars. We have chosen the benchmark points in such a way that signals connected with doubly charged scalars can dominate over non-standard signals coming from both heavy gauge and neutral Higgs bosons. We have analyzed the four-lepton and tri-lepton signals at the LHC. If planned integrated luminosity in the next LHC run at $\sqrt{s} = 14$ TeV is about 10 times larger than the present value ($\sim 30 \text{ fb}^{-1}$), clear signals with four-leptons without missing energy and tri-lepton signals can be detected. This will be an indication of doubly charged scalars. These multi lepton final states possess very small SM background. We have shown that the MLRSM can give such signals for doubly charged masses up to approximately 600 GeV. In our analysis we have used the dilepton invariant mass and lepton-lepton separation distributions. We also estimate the amount of charge asymmetry in signal as well as background events, and show that this might be a smoking gun feature for future discovery. The same- and opposite-sign charged lepton signals have been analyzed using proper kinematic cuts and the clear impact of doubly charged scalars are noted carefully. In the MLRSM the charged gauge bosons are heavy ($\gtrsim 3\text{TeV}$), but the charged scalars can contribute to $H \rightarrow \gamma\gamma$ branching ratio. This contribution has been calculated.

We have also considered production and decays of pair of doubly charged Higgs bosons through vector boson fusion within MLRSM framework. To do so we have evaluated suitable benchmark points for masses of Higgs bosons, which are in agreement with several constraints coming from FCNC, vacuum stability, LEP II and recent ATLAS searches on doubly charged scalars. We have further noted and shown that the splitting between the doubly ($H_1^{\pm\pm}$) and singly (H_1^\pm)

charged scalars is less than M_{W_1} , irrespective of the $SU(2)_R$ breaking scale. Thus the on-shell decay $H_1^{\pm\pm} \rightarrow H_1^\pm W_1^\pm$ is protected and the decay branching ratio of the doubly charged scalar $H_1^{\pm\pm}$ is affected.

We have computed the signal cross section for the process $pp \rightarrow H_{1/2}^{\pm\pm} H_{1/2}^{\mp\mp} jj \rightarrow \ell^\pm \ell^\pm \ell^\mp \ell^\mp jj$ using realistic cuts. The necessary SM background for this final state is also evaluated. It has been shown that the 14 TeV LHC even with high integrated luminosity will not be sensitive to the VBF-like signals $H_{1/2}^{\pm\pm} H_{1/2}^{\mp\mp} jj$, even with relatively light doubly charged Higgs bosons (~ 500 GeV). However, we have shown that much better perspective exists for the future FCC colliders with center of mass energies 33 and (or) 100 TeV.

Indeed, we are in a very exciting moment and the next LHC run should be decisive if our scenario with relatively light charged Higgs bosons can be realized. The 14 TeV LHC still has a room for discovery of Left-Right gauge symmetry signals through s-channel production of the MLRSM doubly charged Higgs bosons as long as their masses are below 1 TeV range ($m_{H_{1/2}^{\pm\pm}} \leq 600$ GeV). In the case of VBF production of doubly charged scalars, 14 TeV LHC will not be sensitive even for $m_{H^{\pm\pm}} \sim 500$ GeV, however, 100 TeV FCC-hh collider can give significant signals for ~ 1 TeV.

Using examples of the MLRSM (and the BNTM) we have shown that we are slowly approaching to the era at the LHC physics where details of the elusive Higgs sectors can be analyzed.

We have also studied phenomenological consequences other than the colliders, in the context of the MLRSM in Chapter 4. In the TeV scale MLRSM, there can be additional contributions to LFV processes as well as $0\nu\beta\beta$, which can arise from the diagrams involving a right-handed gauge boson W_R together with the heavy Majorana neutrinos N_R , or Higgs triplet states Δ_R . In this chapter, we discussed in detail the possible interplay between different contributions. We have done our analysis for Type-I and Type-II dominant seesaw mechanism. For lower masses of the Higgs triplets, which is in agreement with the present experimental limits, its contribution can significantly enhance the branching ratio of $\mu \rightarrow e\gamma$ and $\mu \rightarrow 3e$, thereby disfavoring such scenarios. The natural suppression

in the branching ratios occur, when the light as well as the heavy neutrinos are quasi-degenerate among themselves. The predicted branching ratio can be explored in next generation LFV and $0\nu\beta\beta$ experiments for moderate to large ratio of M_N/M_Δ . We have also studied the implication of the recent diboson excess by ATLAS on LFV processes and $0\nu\beta\beta$. With the right-handed gauge boson mass $M_{W_R} = 2$ TeV, as required to explain the diboson excess, even moderate values of M_N/M_Δ are severely constrained by the present $0\nu\beta\beta$ and LFV limits.

To summarize, we have studied the collider signatures of three specific TeV scale models in this thesis and for one of the models studied the impact for LFV and neutrinoless double beta decay. The hallmark of all the models that we have considered is the multilepton signatures. However, the mechanism of neutrino mass generation as well as the particle content are different in the three different models. The minimal model is the MLSM which can be constrained from LFV and vacuum stability, however since heavy neutrinos are of Dirac nature neutrinoless double beta due to the additional neutrinos are suppressed. The signature that we have studied in this case is the tri-lepton signal with mixed charged leptons. On the other hand in the BNTM, although the neutrino mass matrix has the same form as that in the MLSM, the presence of the triply charged Higgs scalar gives rise to the same-sign-tri-lepton signature due to the lepton number violating vertex. We have assumed the additional fermion sector in this model to be beyond the reach of the colliders. Such studies have been performed in Ref. [118]. LFV in the context of this model has also been studied in [96]. A correlated study of LFV and collider signals in this model can also be interesting. There are also models with higher dimensional operators with $d > 7$ with higher dimensional representations of additional scalars and fermions. There are further scopes of similar studies in the context of some of these models. The MLRSM offers very interesting phenomenology due to the right-handed sector at TeV scale. Several interesting things can still be done in the context of these models. This includes more detailed comparison studies including also lepton spin correlations and their angular distributions with other non-standard models where doubly charged scalars exist. Such studies have been performed in the

context of the type-II seesaw model in [272]). One can also do studies of dedicated distributions for processes involving doubly charged Higgs bosons with both jets and missing energy; In the MLRSM, VBF-like signals connected with $H_2^{\pm\pm}$ scalar production (which is a part of the right-handed triplet) is comparable with the $H_1^{\pm\pm}$ scalar production, see Eqs. (3.80) and (3.81). Thus the cross section for signal events are larger compared to that for Type-II seesaw scenario with same masses for triplet scalars. This may be an avenue to disentangle between MLRSM and SM with additional triplet, *e.g.* Higgs Triplet Model [182, 273, 274], though detailed analyses are needed to make more precise statement.

As a general conclusion of the thesis, we have looked for signatures of neutrino mass generation mechanisms at colliders and at other low energy experiments. Only after analyzing carefully the experiment data from different sectors, one can find out which of the models studied in this thesis, if any, is the right description of nature.

Appendix A

Feynman rules in the BNTM

A.1 Quadruplet scalar kinetic term

The quadruplet scalar kinetic term in Eq. 2.50 reads as:

$$\mathcal{L} = (D^\mu \Phi)^\dagger (D_\mu \Phi). \quad (\text{A.1})$$

The Feynman rules for the interaction of the Φ field with gauge bosons can be obtained from the covariant derivative

$$D_\mu \Phi = \left(\partial_\mu - ig\vec{T} \cdot \vec{W}_\mu - ig' \frac{Y}{2} B_\mu \right) \Phi. \quad (\text{A.2})$$

Since the Φ belongs to the isospin-3/2 representation of $SU(2)$, the generators T_a can be expressed as,

$$T_1 = \begin{pmatrix} 0 & \sqrt{3}/2 & 0 & 0 \\ \sqrt{3}/2 & 0 & 1 & 0 \\ 0 & 1 & 0 & \sqrt{3}/2 \\ 0 & 0 & \sqrt{3}/2 & 0 \end{pmatrix}, \quad T_2 = \begin{pmatrix} 0 & -i\sqrt{3}/2 & 0 & 0 \\ i\sqrt{3}/2 & 0 & -i & 0 \\ 0 & i & 0 & -i\sqrt{3}/2 \\ 0 & 0 & i\sqrt{3}/2 & 0 \end{pmatrix},$$

$$T_3 = \text{diag}(3/2, 1/2, -1/2, -3/2). \quad (\text{A.3})$$

A.2 Yukawa interactions of fermion triplets

The Yukawa Lagrangian for the Σ field is given as:

$$\mathcal{L}_Y = Y_i \overline{l_{iL}^C} H^b \Sigma_{L a' b} \epsilon^{aa'} + Y_i' \overline{\Sigma_R}^{ab} \Phi_{abc} l_{iL c'} \epsilon^{cc'} + h.c., \quad (\text{A.4})$$

where a, b etc. are $SU(2)$ indices.

The components of $\Sigma_{L,R}$ are:

$$\Sigma_{11} = \Sigma^{++}, \Sigma_{12} = \frac{1}{\sqrt{2}} \Sigma^+, \Sigma_{22} = \Sigma^0.$$

The components of quadruplet scalar field Φ are:

$$\begin{aligned} \Phi_{111} &= \Phi^{+++}, & \Phi_{112} &= \frac{1}{\sqrt{3}} \Phi^{++}, \\ \Phi_{122} &= \frac{1}{\sqrt{3}} \Phi^+, & \Phi_{222} &= \Phi^0. \end{aligned} \quad (\text{A.5})$$

In the form of component fields the terms in Eq. A.4 can be written as:

$$\overline{l_{iL}^C} H^* \Sigma_L = \overline{\nu_{iL}^C} H^- \frac{1}{\sqrt{2}} \Sigma_L^+ + \overline{\nu_{iL}^C} H^0 \Sigma_L^0 - \overline{l_{iL}^- C} H^- \Sigma_L^{++} - \overline{l_{iL}^- C} H^0 \frac{1}{\sqrt{2}} \Sigma_L^+ \quad (\text{A.6})$$

$$\begin{aligned} \overline{\Sigma_R}^{ab} \Phi_{abc} l_{iL c'} \epsilon^{cc'} &= \overline{\Sigma_R}^{++} \Phi^{+++} l_{iL}^- + 2 \frac{1}{\sqrt{2}} \overline{\Sigma_R}^+ \frac{1}{\sqrt{3}} \Phi^{++} l_{iL}^- - 2 \frac{1}{\sqrt{2}} \overline{\Sigma_R}^+ \frac{1}{\sqrt{3}} \Phi^+ \nu_{iL} \\ &\quad - \overline{\Sigma_R}^{++} \frac{1}{\sqrt{3}} \Phi^{++} \nu_{iL} - \overline{\Sigma_R}^0 \Phi^0 \nu_{iL} + \overline{\Sigma_R}^0 \frac{1}{\sqrt{3}} \Phi^+ l_{iL}^-. \end{aligned} \quad (\text{A.7})$$

A.3 Neutrino mass through dimension-7 effective vertex

In this sub-section we discuss the tree level diagram which gives rise to the dimension-7 effective operator, see Fig. A.1.

The tree level diagram can be evaluated in the small momentum transfer

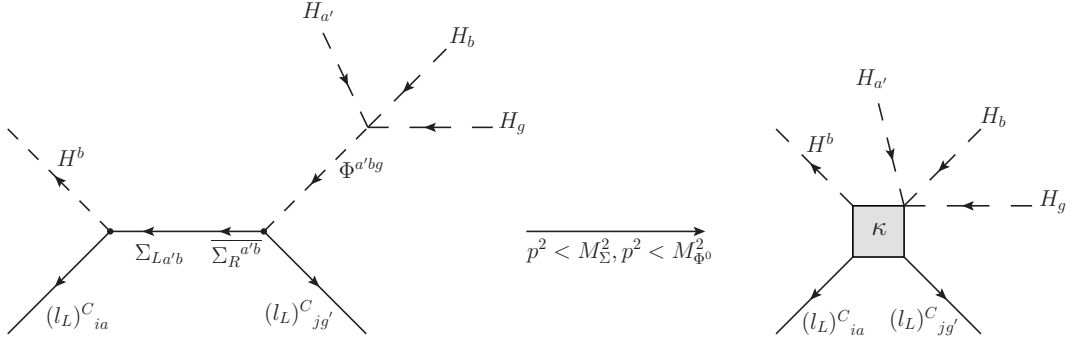


Figure A.1: The tree-level diagram for the generation of the dimension-7 effective vertex is shown on the left-hand side. The right-hand figure shows the effective vertex in the low energy approximation.

limit as,

$$\begin{aligned}
M_{ij} &= P_L(Y_i Y'_j) \frac{1}{\not{p} - M_\Sigma} \frac{1}{p^2 - M_{\Phi^0}^2} \lambda_5 \varepsilon_{aa'} \varepsilon_{gg'} P_L + \quad i \leftrightarrow j \\
&\xrightarrow{p^2 < M_\Sigma^2, p^2 < M_{\Phi^0}^2} (Y_i Y'_j) \frac{1}{M_\Sigma} \frac{1}{M_{\Phi^0}^2} \lambda_5 \varepsilon_{aa'} \varepsilon_{gg'} P_L + \quad i \leftrightarrow j. \quad (\text{A.8})
\end{aligned}$$

The diagram on the right-side can be evaluated as,

$$\mathcal{L}_\kappa = \kappa_{ij} \left(\overline{l_L^i} \sigma^\alpha \varepsilon H \right) \left(H^T \sigma^\alpha \varepsilon l_L^j \right) (H^\dagger H) + \text{h.c.}, \quad (\text{A.9})$$

$$= -\kappa_{ij} \left(\overline{l_{L a}^i} H_{a'} l_{L g'}^j H^b H_b H_g \right) \varepsilon_{aa'} \varepsilon_{gg'} + \text{h.c.}, \quad (\text{A.10})$$

which leads to

$$M_{ij} = -\kappa_{ij} \varepsilon_{aa'} \varepsilon_{gg'} P_L. \quad (\text{A.11})$$

Tree level matching then gives,

$$\kappa_{ij} = -\frac{(Y_i Y'_j + Y'_i Y_j) \lambda_5}{M_\Sigma M_{\Phi^0}^2}. \quad (\text{A.12})$$

Therefore, the neutrino mass after symmetry breaking is

$$m_{\nu_{ij}} = -\frac{(Y_i Y'_j + Y'_i Y_j) \lambda_5}{M_\Sigma M_{\Phi^0}^2} v^4. \quad (\text{A.13})$$

A.4 Lepton flavor violating effective vertex

There is an interesting lepton number violating vertex which arises in this model from the diagram in Fig. A.2.

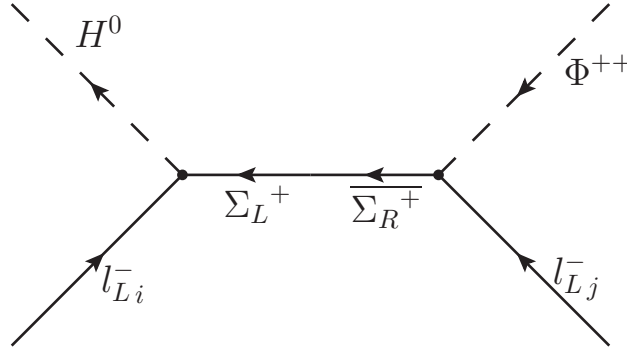


Figure A.2: Effective vertex of $\Phi^{++}l_i^-l_j^-$ coupling.

In the limit of small momentum transfer, integrating out the heavy fields Σ , this diagram gives rise to an effective $\Phi^{++}l_i^-l_j^-$ vertex, which after the H^0 field gets VEV gives $\frac{m\nu_{ij}}{2\sqrt{3}v_\Phi}$. The singly charged and neutral scalar (Φ^\pm, Φ^0) can also have similar effective vertex and can decay to a lepton and a neutrino or two neutrinos.

A.5 Feynman rules

In this section we tabulate the Feynman rules required in the calculation, involving the additional particles in the model – namely the the isospin 3/2 scalar and the vector-like triplet fermions. We also tabulate the Feynman rule corresponding to the dimension-7 effective operator obtained by integrating out the triplet fermions and the isospin 3/2 scalars. The arrows on the fermion lines indicate the direction of the lepton number flow.

◇ Feynman rules relevant for production and detection of Φ

The interactions from the expansion of Eq. A.1 give rise to the following vertices used in our calculations. The last one comes from the diagram

discussed in Appendix A.4 and depends on the effective neutrino mass.

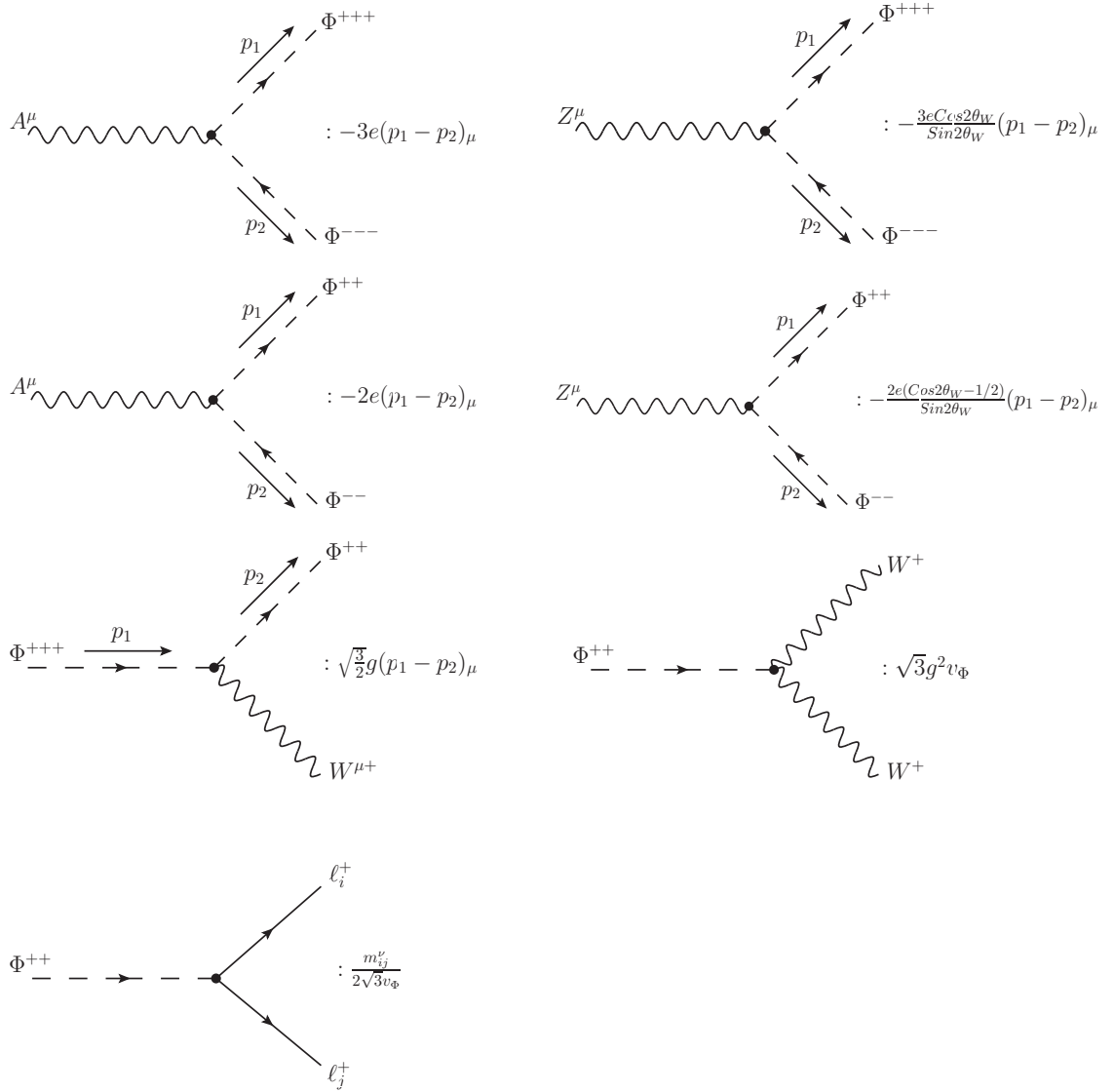


Figure A.3: Feynman rules for the production and decays of charged scalars.

◇ **The Feynman rules for the Yukawa interactions of Σ**

The Yukawa Interactions of Σ are calculated in Section A.2. The vertex factors are extracted from Eq. A.4.

◇ **The Feynman rules for effective vertex κ**

The effective vertex κ is derived in Eqs. A.11, A.12.

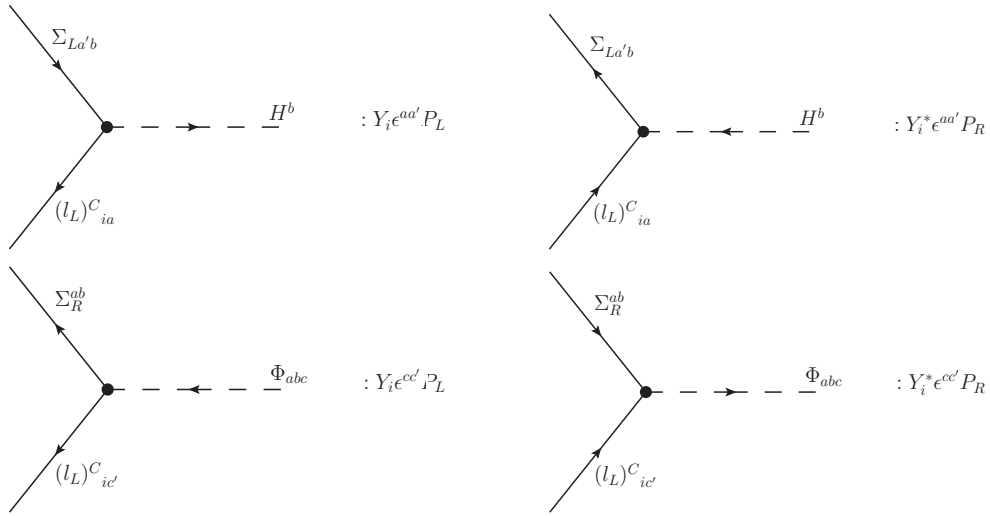


Figure A.4: Feynman rules for Yukawas in the Lagrangian.

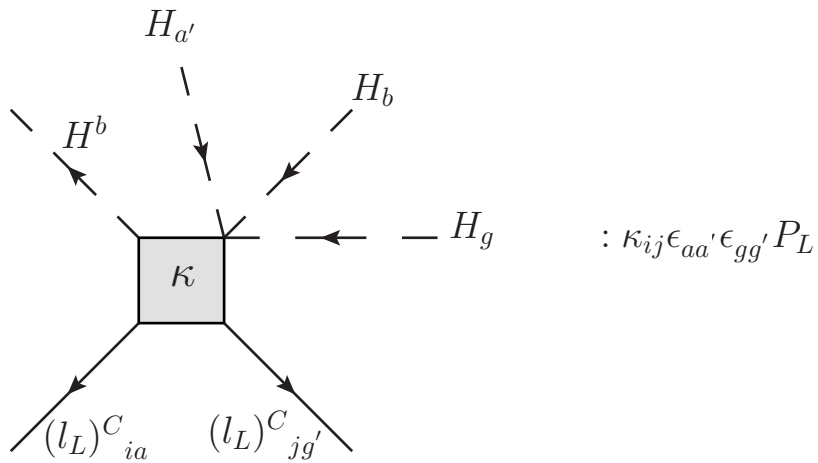


Figure A.5: Feynman rules for the effective vertices.

Appendix B

Potential in the MLRSM

B.1 Scalar potential of the MLRSM

In this section we write the most general Higgs potential of the MLRSM. It was discussed elaborately in Ref. [\[275\]](#), and is given as,

$$\begin{aligned}
\mathcal{L}_{Higgs} = & -\mu_1^2 Tr[\Phi^\dagger \Phi] - \mu_2^2 (Tr[\tilde{\Phi} \Phi^\dagger] + Tr[\tilde{\Phi}^\dagger \Phi]) \\
& -\mu_3^2 (Tr[\Delta_L \Delta_L^\dagger] + Tr[\Delta_R \Delta_R^\dagger]) \\
& +\lambda_1 Tr[\Phi \Phi^\dagger]^2 + \lambda_2 (Tr[\tilde{\Phi} \Phi^\dagger]^2 + Tr[\tilde{\Phi}^\dagger \Phi]^2) + \lambda_3 (Tr[\tilde{\Phi} \Phi^\dagger] Tr[\tilde{\Phi}^\dagger \Phi]) \\
& +\lambda_4 (Tr[\Phi \Phi^\dagger] (Tr[\tilde{\Phi} \Phi^\dagger] + Tr[\tilde{\Phi}^\dagger \Phi])) \\
& +\rho_1 (Tr[\Delta_L \Delta_L^\dagger]^2 + Tr[\Delta_R \Delta_R^\dagger]^2) \\
& +\rho_2 (Tr[\Delta_L \Delta_L] Tr[\Delta_L^\dagger \Delta_L^\dagger] + Tr[\Delta_R \Delta_R] Tr[\Delta_R^\dagger \Delta_R^\dagger]) \\
& +\rho_3 (Tr[\Delta_L \Delta_L^\dagger] Tr[\Delta_R \Delta_R^\dagger]) \\
& +\rho_4 (Tr[\Delta_L \Delta_L] Tr[\Delta_R^\dagger \Delta_R^\dagger] + Tr[\Delta_R \Delta_R] Tr[\Delta_L^\dagger \Delta_L^\dagger]) \\
& +\alpha_1 (Tr[\Phi \Phi^\dagger] (Tr[\Delta_L \Delta_L^\dagger] + Tr[\Delta_R \Delta_R^\dagger])) \\
& +\alpha_2 (Tr[\Phi \tilde{\Phi}^\dagger] Tr[\Delta_R \Delta_R^\dagger] + Tr[\tilde{\Phi} \Phi^\dagger] Tr[\Delta_L \Delta_L^\dagger]) \\
& +\alpha_2^* (Tr[\Phi^\dagger \tilde{\Phi}] Tr[\Delta_R \Delta_R^\dagger] + Tr[\tilde{\Phi}^\dagger \Phi] Tr[\Delta_L \Delta_L^\dagger]) \\
& +\alpha_3 (Tr[\Phi \Phi^\dagger \Delta_L \Delta_L^\dagger] + Tr[\Phi^\dagger \Phi \Delta_R \Delta_R^\dagger]) \\
& +\beta_1 (Tr[\Phi \Delta_R \Phi^\dagger \Delta_L^\dagger] + Tr[\Phi^\dagger \Delta_L \Phi \Delta_R^\dagger]) \\
& +\beta_2 (Tr[\tilde{\Phi} \Delta_R \Phi^\dagger \Delta_L^\dagger] + Tr[\tilde{\Phi}^\dagger \Delta_L \Phi \Delta_R^\dagger]) \\
& +\beta_3 (Tr[\Phi \Delta_R \tilde{\Phi}^\dagger \Delta_L^\dagger] + Tr[\Phi^\dagger \Delta_L \tilde{\Phi} \Delta_R^\dagger]). \tag{B.1}
\end{aligned}$$

The potential is invariant under the symmetry $\Delta_L \leftrightarrow \Delta_R, \Phi \leftrightarrow \Phi^\dagger$. To avoid the fine tuning problem the β terms (Eq. A2 in [275]) are made to vanish, $\beta_i = 0$ ($i=1,2,3$). This implies that $v_L = 0$. The α_2 parameter is assumed to be real, therefore there is no explicit CP violation in the Higgs potential and the spontaneous CP symmetry breaking also does not appear as vacuum expectation values are real.

Appendix C

FCNC in the MLRSM

C.1 Reconciling FCNC effects and large v_R with relatively light charged Higgs mass spectrum within MLRSM

A scan of potential parameters based on the numerical diagonalization and minimization of the complete MLRSM Higgs potential within our own implementation of the FeynRules package [161] has been performed. This leads to the Fig. 3.13. Here, just for illustration, we discuss it in a simplified form based on approximations discussed in [207]. In MLRSM there is one neutral SM-like Higgs boson having mass proportional to the vacuum expectation value (VEV) κ_1 (\sim electroweak breaking scale). The other Higgs bosons are much heavier. A natural mass scale for them is driven by v_R which decides about the $SU(2)_R \otimes U(1)_{B-L}$ breaking scale. As discussed in the main text, we assume large v_R (~ 8 TeV), to be consistent with the experimental constraints.

The minimization and diagonalization of the MLRSM Higgs potential have been investigated in [173] and explicit correlations among physical and unphysical scalar fields are given in [207]. For the sake of completeness, here we have depicted them along with their mass relations considering $\kappa_2 = 0$:

◇ masses

$$M_{H_0^0}^2 \simeq 2\kappa_1^2 \lambda_1, \quad (C.1)$$

$$M_{H_1^0}^2 \simeq \frac{1}{2} \alpha_3 v_R^2, \quad (C.2)$$

$$M_{H_2^0}^2 \simeq 2\rho_1 v_R^2, \quad M_{H_3^0}^2 \simeq \frac{1}{2} v_R^2 (\rho_3 - 2\rho_1), \quad (C.3)$$

$$M_{A_1^0}^2 \simeq \frac{1}{2} \alpha_3 v_R^2 - 2\kappa_1^2 (2\lambda_2 - \lambda_3), \quad (C.4)$$

$$M_{A_2^0}^2 \simeq \frac{1}{2} v_R^2 (\rho_3 - 2\rho_1), \quad (C.5)$$

$$M_{H_1^\pm}^2 \simeq \frac{1}{2} v_R^2 (\rho_3 - 2\rho_1) + \frac{1}{4} \alpha_3 \kappa_1^2, \quad M_{H_2^\pm}^2 \simeq \frac{1}{2} \alpha_3 \left[v_R^2 + \frac{1}{2} \kappa_1^2 \right], \quad (C.6)$$

$$M_{H_1^{\pm\pm}}^2 \simeq \frac{1}{2} \left[v_R^2 (\rho_3 - 2\rho_1) + \alpha_3 \kappa_1^2 \right], \quad M_{H_2^{\pm\pm}}^2 \simeq 2\rho_2 v_R^2 + \frac{1}{2} \alpha_3 \kappa_1^2. \quad (C.7)$$

◇ Unphysical fields in terms of the physical fields¹ (“G” stands for Goldstone modes)

$$\phi_1^0 \simeq \frac{1}{\sqrt{2}} [H_0^0 + i\tilde{G}_1^0], \quad (C.8)$$

$$\phi_2^0 \simeq \frac{1}{\sqrt{2}} [H_1^0 - iA_1^0], \quad (C.9)$$

$$\delta_R^0 = \frac{1}{\sqrt{2}} (H_2^0 + iG_2^0), \quad \delta_L^0 = \frac{1}{\sqrt{2}} (H_3^0 + iA_2^0), \quad (C.10)$$

$$\delta_L^\pm = H_1^\pm, \quad \delta_R^\pm \simeq G_R^\pm, \quad (C.11)$$

$$\phi_1^\pm \simeq H_2^\pm, \quad \phi_2^\pm \simeq G_L^\pm, \quad (C.12)$$

$$\delta_L^{\pm\pm} = H_1^{\pm\pm}, \quad \delta_R^{\pm\pm} = H_2^{\pm\pm}. \quad (C.13)$$

As masses of quarks are non-degenerate, FCNC effects appear through the A_0 part of the following Lagrangian [71]

$$\begin{aligned} L_{quark-Higgs}(u, d) = & - \bar{U} \left[P_L \left(M_{diag}^u B_0^* + U^{CKM} M_{diag}^d U^{CKM\dagger} A_0 \right) \right. \\ & \left. + P_R \left(M_{diag}^u B_0 + U^{CKM} M_{diag}^d U^{CKM\dagger} A_0^* \right) \right] U, \end{aligned} \quad (C.14)$$

¹In [163] we wrongly assigned $H_1^{\pm\pm}$ with right triplet and $H_2^{\pm\pm}$ with left triplet in Eq. A.13. We would like to thank Juan Carlos Vasquez for drawing our attention to this fact as he considered also this process in [276].

where A_0 is a linear combination of neutral physical Higgs and Goldstone fields connected with a bi-doublet Φ [173], and taking into account Eq. C.9, we finally have

$$A_0 = \sqrt{2} (\kappa_1 \phi_2^0) = (H_1^0 - iA_1^0). \quad (\text{C.15})$$

To suppress the effects connected with these fields [78, 178, 208–210], their masses need to be at least ~ 10 TeV. In our analysis we have kept them to be ~ 15 TeV:

$$m_{H_1^0}, m_{A_1^0} > 15 \text{ TeV}. \quad (\text{C.16})$$

It can be easily shown that for the masses of Higgs bosons, as in Eqs. C.2–C.7, we can find parameters of the MLRSM Higgs potential within the perturbative limit, and simultaneously satisfy the light charged Higgs bosons and Eq. C.16. This can be achieved even after keeping three charged Higgs bosons $H_1^{\pm\pm}, H_2^{\pm\pm}, H_1^\pm$ relatively light. For instance, with $v_R = 8$ TeV and $\kappa_1 = 246$ GeV we find the scalar spectrum (in GeV)

$$M_{H_0^0} = 125, \quad (\text{C.17})$$

$$M_{H_1^0} = 15062, \quad M_{H_2^0} = 11313, \quad M_{H_3^0} = 505, \quad (\text{C.18})$$

$$M_{A_1^0} = 15066, \quad (\text{C.19})$$

$$M_{A_2^0} = 505, \quad (\text{C.20})$$

$$M_{H_1^\pm} = 602, \quad M_{H_2^\pm} = 15066, \quad (\text{C.21})$$

$$M_{H_1^{\pm\pm}} = 685, \quad M_{H_2^{\pm\pm}} = 463, \quad (\text{C.22})$$

where

$$\rho_1 = 1, \quad \rho_2 = 0, \quad \rho_3 = 2.008, \quad (\text{C.23})$$

$$\lambda_1 = 0.13, \quad \lambda_2 = 0, \quad \lambda_3 = 1, \quad (\text{C.24})$$

$$\alpha_3 = 7.09. \quad (\text{C.25})$$

We can see that the remaining fourth charged Higgs boson H_2^\pm in MLRSM is naturally very heavy. To make it light, one needs to go beyond MLRSM and incorporate new terms in the scalar potential which would affect MLRSM Higgs boson masses².

²Let us imagine that an additional intermediate energy scale is introduced connected with VEV of an additional $SU(2)_L$ and $SU(2)_R$ singlet scalar field (such scalars give for instance heavy neutrino Majorana mass terms but they decouple from other low energy phenomenological effects). If this scalar couple to the MLRSM right handed triplet fields, it would modify Eqs.C.6-C.7 but because of its large VEV, mixing of MLRSM Higgs scalars with this state would be negligible, so the effective couplings of MLRSM Higgs bosons, including H_2^\pm , would stay the same.

Bibliography

- [1] K. Olive *et al.* (Particle Data Group), [Chin.Phys.](#) **C38**, 090001 (2014).
- [2] G. Aad *et al.* (ATLAS Collaboration), [Phys.Lett.](#) **B716**, 1 (2012), [arXiv:1207.7214 \[hep-ex\]](#).
- [3] S. Chatrchyan *et al.* (CMS Collaboration), [Phys.Lett.](#) **B716**, 30 (2012), [arXiv:1207.7235 \[hep-ex\]](#).
- [4] T. Lee and C.-N. Yang, [Phys.Rev.](#) **104**, 254 (1956).
- [5] C. Wu, E. Ambler, R. Hayward, D. Hoppes, and R. Hudson, [Phys.Rev.](#) **105**, 1413 (1957).
- [6] P. W. Anderson, [Phys. Rev.](#) **130**, 439 (1963).
- [7] F. Englert and R. Brout, [Phys. Rev. Lett.](#) **13**, 321 (1964).
- [8] P. W. Higgs, [Phys. Rev. Lett.](#) **13**, 508 (1964).
- [9] G. S. Guralnik, C. R. Hagen, and T. W. B. Kibble, [Phys. Rev. Lett.](#) **13**, 585 (1964).
- [10] P. W. Higgs, [Phys. Rev.](#) **145**, 1156 (1966).
- [11] E. Fermi, [Z.Phys.](#) **88**, 161 (1934).
- [12] M. Goldhaber, L. Grodzins, and A. Sunyar, [Phys.Rev.](#) **109**, 1015 (1958).
- [13] F. Reines and C. Cowan, [Phys.Rev.](#) **92**, 830 (1953).
- [14] F. Reines and C. L. Cowan, [Nature](#) **178**, 446 (1956).

- [15] F. Reines and C. Cowan, *Phys.Rev.* **113**, 273 (1959).
- [16] G. Danby, J. Gaillard, K. A. Goulianos, L. Lederman, N. B. Mistry, *et al.*, *Phys.Rev.Lett.* **9**, 36 (1962).
- [17] K. Kodama *et al.* (DONUT), *Phys.Lett.* **B504**, 218 (2001), [arXiv:hep-ex/0012035 \[hep-ex\]](#).
- [18] S. Bilenky, *Eur.Phys.J.* **H38**, 345 (2013), [arXiv:1210.3065 \[hep-ph\]](#).
- [19] D. Forero, M. Tortola, and J. Valle(2014), [arXiv:1405.7540 \[hep-ph\]](#).
- [20] S. Goswami, *Proceedings, 9th International Conference on Particles, strings and cosmology (PASCOS 2003)*, *Pramana* **62**, 241 (2004), [arXiv:hep-ph/0307224 \[hep-ph\]](#).
- [21] V. N. Aseev *et al.* (Troitsk), *Phys. Rev.* **D84**, 112003 (2011), [arXiv:1108.5034 \[hep-ex\]](#).
- [22] C. Kraus *et al.*, *Eur. Phys. J.* **C40**, 447 (2005), [arXiv:hep-ex/0412056 \[hep-ex\]](#).
- [23] R. H. Robertson (KATRIN)(2013), [arXiv:1307.5486 \[physics.ins-det\]](#).
- [24] R. G. H. Robertson, in *Neutrino Oscillation Workshop (NOW 2014) Conca Specchiulla, Otranto, Lecce, Italy, September 7-14, 2014* (2015) , <http://inspirehep.net/record/1342446/files/arXiv:1502.00144.pdf>, [arXiv:1502.00144 \[nucl-ex\]](#).
- [25] P. A. R. Ade *et al.* (Planck)(2015), [arXiv:1502.01589 \[astro-ph.CO\]](#).
- [26] P. Minkowski, *Phys.Lett.* **B67**, 421 (1977).
- [27] T. Yanagida, *Conf.Proc.* **C7902131**, 95 (1979).
- [28] M. Gell-Mann, P. Ramond, and R. Slansky, *Conf.Proc.* **C790927**, 315 (1979).
- [29] S. Glashow, *NATO Adv.Study Inst.Ser.B Phys.* **59**, 687 (1980).

- [30] R. N. Mohapatra and G. Senjanovic, [Phys.Rev.Lett.](#) **44**, 912 (1980).
- [31] M. Magg and C. Wetterich, [Phys.Lett.](#) **B94**, 61 (1980).
- [32] G. Lazarides, Q. Shafi, and C. Wetterich, [Nucl.Phys.](#) **B181**, 287 (1981).
- [33] R. N. Mohapatra and G. Senjanovic, [Phys.Rev.](#) **D23**, 165 (1981).
- [34] J. Schechter and J. Valle, [Phys.Rev.](#) **D25**, 774 (1982).
- [35] R. Foot, H. Lew, X. He, and G. C. Joshi, [Z.Phys.](#) **C44**, 441 (1989).
- [36] L. Evans and P. Bryant, [JINST](#) **3**, S08001 (2008).
- [37] (1984), LEP Design Report: Vol.2. The LEP Main Ring, CERN-LEP-84-01.
- [38] G. Aad *et al.* (ATLAS), [JINST](#) **3**, S08003 (2008).
- [39] O. Adriani *et al.* (LHCf), [JINST](#) **3**, S08006 (2008).
- [40] S. Chatrchyan *et al.* (CMS), [JINST](#) **3**, S08004 (2008).
- [41] G. Anelli *et al.* (TOTEM), [JINST](#) **3**, S08007 (2008).
- [42] A. A. Alves, Jr. *et al.* (LHCb), [JINST](#) **3**, S08005 (2008).
- [43] J. Pinfold *et al.* (MoEDAL)(2009).
- [44] K. Aamodt *et al.* (ALICE), [JINST](#) **3**, S08002 (2008).
- [45] M. Moe, [Ann. Rev. Nucl. Part. Sci.](#) **64**, 247 (2014).
- [46] S. R. Elliott, A. A. Hahn, and M. K. Moe, [Phys. Rev. Lett.](#) **59**, 2020 (1987).
- [47] A. Meroni, S. T. Petcov, and F. Simkovic, [JHEP](#) **02**, 025 (2013), [arXiv:1212.1331 \[hep-ph\]](#).
- [48] A. de Gouvea and P. Vogel, [Prog.Part.Nucl.Phys.](#) **71**, 75 (2013), [arXiv:1303.4097 \[hep-ph\]](#).

- [49] J. Adam *et al.* (MEG Collaboration), *Phys.Rev.Lett.* **110**, 201801 (2013), [arXiv:1303.0754 \[hep-ex\]](#).
- [50] U. Bellgardt *et al.* (SINDRUM), *Nucl. Phys.* **B299**, 1 (1988).
- [51] A. M. Baldini *et al.*(2013), [arXiv:1301.7225 \[physics.ins-det\]](#).
- [52] Y. Kuno, *NuFact04*, *Nucl. Phys. Proc. Suppl.* **149**, 376 (2005).
- [53] A. Blondel *et al.*(2013), [arXiv:1301.6113 \[physics.ins-det\]](#).
- [54] J. Casas, V. Di Clemente, A. Ibarra, and M. Quiros, *Phys.Rev.* **D62**, 053005 (2000), [arXiv:hep-ph/9904295 \[hep-ph\]](#).
- [55] I. Gogoladze, N. Okada, and Q. Shafi, *Phys.Lett.* **B668**, 121 (2008), [arXiv:0805.2129 \[hep-ph\]](#).
- [56] M. Shaposhnikov and C. Wetterich, *Phys.Lett.* **B683**, 196 (2010), [arXiv:0912.0208 \[hep-th\]](#).
- [57] M. Holthausen, K. S. Lim, and M. Lindner, *JHEP* **1202**, 037 (2012), [arXiv:1112.2415 \[hep-ph\]](#).
- [58] N. Cabibbo, L. Maiani, G. Parisi, and R. Petronzio, *Nucl.Phys.* **B158**, 295 (1979).
- [59] C. Ford, D. Jones, P. Stephenson, and M. Einhorn, *Nucl.Phys.* **B395**, 17 (1993), [arXiv:hep-lat/9210033 \[hep-lat\]](#).
- [60] W. Grimus and L. Lavoura, *JHEP* **0011**, 042 (2000), [arXiv:hep-ph/0008179 \[hep-ph\]](#).
- [61] S. Weinberg, *Phys.Rev.Lett.* **43**, 1566 (1979).
- [62] J. Schechter and J. Valle, *Phys.Rev.* **D22**, 2227 (1980).
- [63] E. Ma and D. Roy, *Nucl.Phys.* **B644**, 290 (2002), [arXiv:hep-ph/0206150 \[hep-ph\]](#).

- [64] B. Bajc and G. Senjanovic, [JHEP 0708](#), 014 (2007), [arXiv:hep-ph/0612029 \[hep-ph\]](#).
- [65] D. Binosi and L. Theussl, [Comput.Phys.Commun.](#) **161**, 76 (2004), [arXiv:hep-ph/0309015 \[hep-ph\]](#).
- [66] E. J. Chun and S. K. Kang, [Phys.Rev.](#) **D63**, 097902 (2001), [arXiv:hep-ph/0001296 \[hep-ph\]](#).
- [67] T. Hambye and G. Senjanovic, [Phys.Lett.](#) **B582**, 73 (2004), [arXiv:hep-ph/0307237 \[hep-ph\]](#).
- [68] E. Ma and U. Sarkar, [Phys.Rev.Lett.](#) **80**, 5716 (1998), [arXiv:hep-ph/9802445 \[hep-ph\]](#).
- [69] R. Mohapatra and J. C. Pati, [Phys.Rev.](#) **D11**, 2558 (1975).
- [70] G. Senjanovic and R. N. Mohapatra, [Phys.Rev.](#) **D12**, 1502 (1975).
- [71] P. Duka, J. Gluza, and M. Zralek, [Annals Phys.](#) **280**, 336 (2000), [arXiv:hep-ph/9910279 \[hep-ph\]](#).
- [72] R. N. Mohapatra, [UNIFICATION AND SUPERSYMMETRY. THE FRONTIERS OF QUARK - LEPTON PHYSICS](#) (Springer, Berlin, 1986) ISBN 978-1-4757-1930-7, 978-1-4757-1928-4.
- [73] U. Sarkar, *Particle and astroparticle physics*, Series in high energy physics, cosmology, and gravitation (Taylor & Francis, New York, USA, 2008) ISBN 9781584889311, "<http://www.crcpress.com/product/isbn/9781584889311>".
- [74] V. Khachatryan *et al.* (CMS)(2014), [arXiv:1407.3683 \[hep-ex\]](#).
- [75] G. Aad *et al.* (ATLAS), [JHEP 07](#), 162 (2015), [arXiv:1506.06020 \[hep-ex\]](#).
- [76] G. Beall, M. Bander, and A. Soni, *11th International Symposium on Lepton and Photon Interactions at High Energies Ithaca, New York, August 4-9, 1983*, [Phys. Rev. Lett.](#) **48**, 848 (1982).

- [77] Y. Zhang, H. An, X. Ji, and R. N. Mohapatra, *Nucl. Phys.* **B802**, 247 (2008), [arXiv:0712.4218 \[hep-ph\]](#).
- [78] A. Maiezza, M. Nemevsek, F. Nesti, and G. Senjanovic, *Phys.Rev.* **D82**, 055022 (2010), [arXiv:1005.5160 \[hep-ph\]](#).
- [79] S. Bertolini, A. Maiezza, and F. Nesti, *Phys.Rev.* **D89**, 095028 (2014), [arXiv:1403.7112 \[hep-ph\]](#).
- [80] A. Zee, *Phys.Lett.* **B161**, 141 (1985).
- [81] P. Bhupal Dev, S. Goswami, and M. Mitra, *Phys. Rev.* **D91**, 113004 (2015), [arXiv:1405.1399 \[hep-ph\]](#).
- [82] M.-C. Chen and J. Huang, *Mod.Phys.Lett.* **A26**, 1147 (2011), [arXiv:1105.3188 \[hep-ph\]](#).
- [83] G. 't Hooft, C. Itzykson, A. Jaffe, H. Lehmann, P. K. Mitter, I. M. Singer, and R. Stora, *NATO Sci. Ser. B* **59**, pp.1 (1980).
- [84] P.-H. Gu and U. Sarkar, *Phys.Lett.* **B694**, 226 (2010), [arXiv:1007.2323 \[hep-ph\]](#).
- [85] H. Zhang and S. Zhou, *Phys.Lett.* **B685**, 297 (2010), [arXiv:0912.2661 \[hep-ph\]](#).
- [86] M. Hirsch, S. Morisi, and J. Valle, *Phys.Lett.* **B679**, 454 (2009), [arXiv:0905.3056 \[hep-ph\]](#).
- [87] F. Bazzocchi, *Phys.Rev.* **D83**, 093009 (2011), [arXiv:1011.6299 \[hep-ph\]](#).
- [88] M. Gavela, T. Hambye, D. Hernandez, and P. Hernandez, *JHEP* **0909**, 038 (2009), [arXiv:0906.1461 \[hep-ph\]](#).
- [89] S. Khan, S. Goswami, and S. Roy, *Phys.Rev.* **D89**, 073021 (2014), [arXiv:1212.3694 \[hep-ph\]](#).
- [90] M. Malinsky, T. Ohlsson, Z.-z. Xing, and H. Zhang, *Phys.Lett.* **B679**, 242 (2009), [arXiv:0905.2889 \[hep-ph\]](#).

- [91] S. Khan, *Nucl.Phys.* **B864**, 38 (2012), [arXiv:1203.5043 \[hep-ph\]](#).
- [92] I. Gogoladze, N. Okada, and Q. Shafi, *Phys.Lett.* **B672**, 235 (2009), [arXiv:0809.0703 \[hep-ph\]](#).
- [93] K. Babu, S. Nandi, and Z. Tavartkiladze, *Phys.Rev.* **D80**, 071702 (2009), [arXiv:0905.2710 \[hep-ph\]](#).
- [94] F. Bonnet, D. Hernandez, T. Ota, and W. Winter, *JHEP* **0910**, 076 (2009), [arXiv:0907.3143 \[hep-ph\]](#).
- [95] S. Kanemura and T. Ota, *Phys.Lett.* **B694**, 233 (2010), [arXiv:1009.3845 \[hep-ph\]](#).
- [96] Y. Liao, G.-Z. Ning, and L. Ren, *Phys.Rev.* **D82**, 113003 (2010), [arXiv:1008.0117 \[hep-ph\]](#).
- [97] I. Picek and B. Radovicic, *Phys.Lett.* **B687**, 338 (2010), [arXiv:0911.1374 \[hep-ph\]](#).
- [98] Y. Liao, *JHEP* **1106**, 098 (2011), [arXiv:1011.3633 \[hep-ph\]](#).
- [99] K. Kumericki, I. Picek, and B. Radovicic, *Phys.Rev.* **D86**, 013006 (2012), [arXiv:1204.6599 \[hep-ph\]](#).
- [100] K. L. McDonald, *JHEP* **1307**, 020 (2013), [arXiv:1303.4573 \[hep-ph\]](#).
- [101] B. Ren, K. Tsumura, and X.-G. He, *Phys.Rev.* **D84**, 073004 (2011), [arXiv:1107.5879 \[hep-ph\]](#).
- [102] C.-K. Chua and S. S. Law, *Phys.Rev.* **D83**, 055010 (2011), [arXiv:1011.4730 \[hep-ph\]](#).
- [103] J. Beringer *et al.* (Particle Data Group), *Phys.Rev.* **D86**, 010001 (2012).
- [104] M. Cirelli, N. Fornengo, and A. Strumia, *Nucl.Phys.* **B753**, 178 (2006), [arXiv:hep-ph/0512090 \[hep-ph\]](#).
- [105] M. Einhorn, D. Jones, and M. Veltman, *Nucl.Phys.* **B191**, 146 (1981).

- [106] J. Chakraborty, *Phys.Lett.* **B690**, 382 (2010), [arXiv:1005.1377](https://arxiv.org/abs/1005.1377) [hep-ph].
- [107] A. Salvucci, *The Higgs Boson in the $H \rightarrow ZZ^{(*)} \rightarrow 4l$ decay channel with the ATLAS detector at the LHC*, Ph.D. thesis, Nijmegen U. (2014-04-09), <http://inspirehep.net/record/1339840/files/CERN-THESIS-2014-132.pdf>.
- [108] L. Finco (CMS), *Proceedings, 26th Conference on High Energy Physics (IFAE 2014)*, *Nuovo Cim.* **C038**, 5 (2015), [arXiv:1409.2646](https://arxiv.org/abs/1409.2646) [hep-ex].
- [109] G. Aad *et al.* (ATLAS), *Phys. Rev.* **D91**, 012006 (2015), [arXiv:1408.5191](https://arxiv.org/abs/1408.5191) [hep-ex].
- [110] W.-Y. Keung and G. Senjanovic, *Phys.Rev.Lett.* **50**, 1427 (1983).
- [111] A. Ali, A. V. Borisov, and N. B. Zamorin, *Eur. Phys. J.* **C21**, 123 (2001), [arXiv:hep-ph/0104123](https://arxiv.org/abs/hep-ph/0104123) [hep-ph].
- [112] F. del Aguila and J. Aguilar-Saavedra, *Nucl.Phys.* **B813**, 22 (2009), [arXiv:0808.2468](https://arxiv.org/abs/0808.2468) [hep-ph].
- [113] S. K. Majee and N. Sahu, *Phys. Rev.* **D82**, 053007 (2010), [arXiv:1004.0841](https://arxiv.org/abs/1004.0841) [hep-ph].
- [114] S. Chatrchyan *et al.* (CMS), *Phys. Rev. Lett.* **109**, 071803 (2012), [arXiv:1205.6615](https://arxiv.org/abs/1205.6615) [hep-ex].
- [115] S. Chatrchyan *et al.* (CMS), *JHEP* **01**, 163 (2014), [Erratum: *JHEP*01,014(2015)], [arXiv:1311.6736](https://arxiv.org/abs/1311.6736).
- [116] O. Ducu (ATLAS), *Proceedings, 2nd International Conference on New Frontiers in Physics (ICNFP 2013)*, *EPJ Web Conf.* **71**, 00043 (2014).
- [117] L. Muniz, *Search for new physics in same-sign dilepton events in the CMS detector at the Large Hadron Collider*, Ph.D. thesis, Florida U. (2014), http://inspirehep.net/record/1340411/files/Muniz_Thesis_2014.pdf.

- [118] G. Bambhaniya, J. Chakraborty, S. Goswami, and P. Konar, *Phys.Rev.* **D88**, 075006 (2013), [arXiv:1305.2795 \[hep-ph\]](#).
- [119] B. Mukhopadhyaya and S. Mukhopadhyay, *Phys.Rev.* **D82**, 031501 (2010), [arXiv:1005.3051 \[hep-ph\]](#).
- [120] S. Mukhopadhyay and B. Mukhopadhyaya, *Phys.Rev.* **D84**, 095001 (2011), [arXiv:1108.4921 \[hep-ph\]](#).
- [121] S. Mondal, S. Biswas, P. Ghosh, and S. Roy, *JHEP* **1205**, 134 (2012), [arXiv:1201.1556 \[hep-ph\]](#).
- [122] J. D'Hondt, K. De Causmaecker, B. Fuks, A. Mariotti, K. Mawatari, C. Petersson, and D. Redigolo, *Phys. Lett.* **B731**, 7 (2014), [arXiv:1310.0018 \[hep-ph\]](#).
- [123] P. Bandyopadhyay, K. Huitu, and A. S. Keceli, *JHEP* **05**, 026 (2015), [arXiv:1412.7359 \[hep-ph\]](#).
- [124] S. Chatrchyan *et al.* (CMS), *Phys. Lett.* **B704**, 411 (2013), [arXiv:1106.0933 \[hep-ex\]](#).
- [125] S. Chatrchyan *et al.* (CMS), *JHEP* **06**, 169 (2012), [arXiv:1204.5341 \[hep-ex\]](#).
- [126] G. Aad *et al.* (ATLAS), *Phys. Lett.* **B718**, 841 (2013), [arXiv:1208.3144 \[hep-ex\]](#).
- [127] *A search for anomalous production of events with three or more leptons using 19.5/fb of $\sqrt{s}=8$ TeV LHC data*, Tech. Rep. CMS-PAS-SUS-13-002 (CERN, Geneva, 2013) <https://cds.cern.ch/record/1599719>.
- [128] *Search for supersymmetry in events with four or more leptons in 21 fb^{-1} of pp collisions at $\sqrt{s} = 8$ TeV with the ATLAS detector*, Tech. Rep. ATLAS-CONF-2013-036 (CERN, Geneva, 2013) <https://cds.cern.ch/record/1532429>.

- [129] *Search for RPV SUSY in the four-lepton final state*, Tech. Rep. CMS-PAS-SUS-13-010 (CERN, Geneva, 2013) <https://cds.cern.ch/record/1550552>.
- [130] *Measurements of the properties of the Higgs-like boson in the two photon decay channel with the ATLAS detector using 25 fb⁻¹ of proton-proton collision data*, Tech. Rep. ATLAS-CONF-2013-012 (CERN, Geneva, 2013) <https://cds.cern.ch/record/1523698>.
- [131] *Updated measurements of the Higgs boson at 125 GeV in the two photon decay channel*, Tech. Rep. CMS-PAS-HIG-13-001 (CERN, Geneva, 2013) <https://cds.cern.ch/record/1530524>.
- [132] G. Aad *et al.* (ATLAS), *Phys. Rev.* **D90**, 112015 (2014), [arXiv:1408.7084](https://arxiv.org/abs/1408.7084) [hep-ex].
- [133] V. Khachatryan *et al.* (CMS), *Eur. Phys. J.* **C74**, 3076 (2014), [arXiv:1407.0558](https://arxiv.org/abs/1407.0558) [hep-ex].
- [134] R. N. Cahn and S. Dawson, *Phys. Lett.* **B136**, 196 (1984), [Erratum: *Phys. Lett.* **B138**, 464 (1984)].
- [135] D. L. Rainwater and D. Zeppenfeld, *JHEP* **12**, 005 (1997), [arXiv:hep-ph/9712271](https://arxiv.org/abs/hep-ph/9712271) [hep-ph].
- [136] D. L. Rainwater, D. Zeppenfeld, and K. Hagiwara, *Phys.Rev.* **D59**, 014037 (1998), [arXiv:hep-ph/9808468](https://arxiv.org/abs/hep-ph/9808468) [hep-ph].
- [137] K. Kawade, O. Adriani, L. Bonechi, M. Bongi, G. Castellini, *et al.*, *JINST* **9**, P03016 (2014), [arXiv:1312.5950](https://arxiv.org/abs/1312.5950) [physics.ins-det].
- [138] M. Albrow *et al.* (FP420 R and D), *JINST* **4**, T10001 (2009), [arXiv:0806.0302](https://arxiv.org/abs/0806.0302) [hep-ex].
- [139] P. J. Fox, R. Harnik, J. Kopp, and Y. Tsai, *Phys.Rev.* **D85**, 056011 (2012), [arXiv:1109.4398](https://arxiv.org/abs/1109.4398) [hep-ph].

- [140] *Search for New Phenomena in Monojet plus Missing Transverse Momentum Final States using 10fb-1 of pp Collisions at $\sqrt{s}=8$ TeV with the ATLAS detector at the LHC*, Tech. Rep. ATLAS-CONF-2012-147 (CERN, Geneva, 2012) <https://cds.cern.ch/record/1493486>.
- [141] V. Khachatryan *et al.* (CMS)(2014), [arXiv:1408.3583](https://arxiv.org/abs/1408.3583) [hep-ex].
- [142] A. Pukhov(2004), [arXiv:hep-ph/0412191](https://arxiv.org/abs/hep-ph/0412191) [hep-ph].
- [143] J. Alwall, M. Herquet, F. Maltoni, O. Mattelaer, and T. Stelzer, *JHEP* **1106**, 128 (2011), [arXiv:1106.0522](https://arxiv.org/abs/1106.0522) [hep-ph].
- [144] J. Alwall, A. Ballestrero, P. Bartalini, S. Belov, E. Boos, *et al.*, *Comput.Phys.Commun.* **176**, 300 (2007), [arXiv:hep-ph/0609017](https://arxiv.org/abs/hep-ph/0609017) [hep-ph].
- [145] T. Sjostrand, S. Mrenna, and P. Z. Skands, *JHEP* **0605**, 026 (2006), [arXiv:hep-ph/0603175](https://arxiv.org/abs/hep-ph/0603175) [hep-ph].
- [146] J. Pumplin, D. Stump, J. Huston, H. Lai, P. M. Nadolsky, *et al.*, *JHEP* **0207**, 012 (2002), [arXiv:hep-ph/0201195](https://arxiv.org/abs/hep-ph/0201195) [hep-ph].
- [147] M. Whalley, D. Bourilkov, and R. Group(2005), [arXiv:hep-ph/0508110](https://arxiv.org/abs/hep-ph/0508110) [hep-ph].
- [148] S. Mukhopadhyay, *New physics with low missing energy: identification and discrimination at the LHC*, Ph.D. thesis, HRI, Allahabad, http://www.hri.res.in/~libweb/theses/softcopy/thesd_satyanarayan_mukhopadhyay.pdf.
- [149] G. Aad *et al.* (ATLAS)(2009), [arXiv:0901.0512](https://arxiv.org/abs/0901.0512) [hep-ex].
- [150] G. L. Bayatian *et al.* (CMS), *J. Phys.* **G34**, 995 (2007).
- [151] M. L. Mangano, M. Moretti, F. Piccinini, R. Pittau, and A. D. Polosa, *JHEP* **0307**, 001 (2003), [arXiv:hep-ph/0206293](https://arxiv.org/abs/hep-ph/0206293) [hep-ph].
- [152] M. Cacciari, S. Frixione, M. L. Mangano, P. Nason, and G. Ridolfi, *JHEP* **0809**, 127 (2008), [arXiv:0804.2800](https://arxiv.org/abs/0804.2800) [hep-ph].

- [153] D. L. Rainwater(1999), [arXiv:hep-ph/9908378 \[hep-ph\]](#).
- [154] A. Datta, P. Konar, and B. Mukhopadhyaya, *Phys.Rev.Lett.* **88**, 181802 (2002), [arXiv:hep-ph/0111012 \[hep-ph\]](#).
- [155] D. Choudhury, A. Datta, K. Huitu, P. Konar, S. Moretti, *et al.*, *Phys.Rev.* **D68**, 075007 (2003), [arXiv:hep-ph/0304192 \[hep-ph\]](#).
- [156] G.-C. Cho, K. Hagiwara, J. Kanzaki, T. Plehn, D. Rainwater, *et al.*, *Phys.Rev.* **D73**, 054002 (2006), [arXiv:hep-ph/0601063 \[hep-ph\]](#).
- [157] J. de Blas, *Proceedings, 1st Large Hadron Collider Physics Conference (LHCP 2013)*, *EPJ Web Conf.* **60**, 19008 (2013), [arXiv:1307.6173 \[hep-ph\]](#).
- [158] G. Bozzi, B. Jager, C. Oleari, and D. Zeppenfeld, *Phys.Rev.* **D75**, 073004 (2007), [arXiv:hep-ph/0701105 \[hep-ph\]](#).
- [159] B. Jager, C. Oleari, and D. Zeppenfeld, *Phys. Rev.* **D73**, 113006 (2006), [arXiv:hep-ph/0604200 \[hep-ph\]](#).
- [160] J. Eckel, M. J. Ramsey-Musolf, W. Shepherd, and S. Su, *JHEP* **11**, 117 (2014), [arXiv:1408.2841 \[hep-ph\]](#).
- [161] N. D. Christensen and C. Duhr, *Comput.Phys.Commun.* **180**, 1614 (2009), [arXiv:0806.4194 \[hep-ph\]](#).
- [162] E. Yazgan, J. Damgov, N. Akchurin, V. Genchev, D. Green, *et al.*, *Eur.Phys.J.* **C53**, 329 (2008), [arXiv:0706.1898 \[hep-ex\]](#).
- [163] G. Bambhaniya, J. Chakraborty, J. Gluza, M. Kordiaczyńska, and R. Szafron, *JHEP* **05**, 033 (2014), [arXiv:1311.4144 \[hep-ph\]](#).
- [164] G. Aad *et al.* (ATLAS), *Phys. Lett.* **B716**, 1 (2012), [arXiv:1207.7214 \[hep-ex\]](#).
- [165] S. Chatrchyan *et al.* (CMS), *Phys. Lett.* **B716**, 30 (2012), [arXiv:1207.7235 \[hep-ex\]](#).

- [166] H. Baer, V. Barger, and A. Mustafayev, *Phys. Rev.* **D85**, 075010 (2012), [arXiv:1112.3017 \[hep-ph\]](#).
- [167] S. Heinemeyer, O. Stal, and G. Weiglein, *Phys. Lett.* **B710**, 201 (2014), [arXiv:1112.3026 \[hep-ph\]](#).
- [168] A. Arbey, M. Battaglia, A. Djouadi, F. Mahmoudi, and J. Quevillon, *Phys. Lett.* **B708**, 162 (2012), [arXiv:1112.3028 \[hep-ph\]](#).
- [169] P. Draper, P. Meade, M. Reece, and D. Shih, *Phys. Rev.* **D85**, 095007 (2012), [arXiv:1112.3068 \[hep-ph\]](#).
- [170] A. Arbey, M. Battaglia, and F. Mahmoudi, *Eur. Phys. J.* **C72**, 1906 (2012), [arXiv:1112.3032 \[hep-ph\]](#).
- [171] F. Brummer, S. Kraml, and S. Kulkarni, *JHEP* **08**, 089 (2012), [arXiv:1204.5977 \[hep-ph\]](#).
- [172] M. M. Nojiri, G. Polesello, and D. R. Tovey, *JHEP* **03**, 063 (2006), [arXiv:hep-ph/0512204 \[hep-ph\]](#).
- [173] J. Gunion, J. Grifols, A. Mendez, B. Kayser, and F. I. Olness, *Phys.Rev.* **D40**, 1546 (1989).
- [174] M. Czakon, J. Gluza, and J. Hejczyk, *Nucl.Phys.* **B642**, 157 (2002), [arXiv:hep-ph/0205303 \[hep-ph\]](#).
- [175] J. Gluza, *Acta Phys.Polon.* **B33**, 1735 (2002), [arXiv:hep-ph/0201002 \[hep-ph\]](#).
- [176] J. Gluza and M. Zralek, *Phys.Rev.* **D48**, 5093 (1993).
- [177] R. N. Mohapatra and S. Nussinov, *Phys.Rev.* **D39**, 1378 (1989).
- [178] J. Chakraborty, J. Gluza, R. Sevillano, and R. Szafron, *JHEP* **1207**, 038 (2012), [arXiv:1204.0736 \[hep-ph\]](#).
- [179] M. Czakon, M. Zralek, and J. Gluza, *Nucl.Phys.* **B573**, 57 (2000), [arXiv:hep-ph/9906356 \[hep-ph\]](#).

- [180] M. Czakon, J. Gluza, and M. Zralek, *Phys.Lett.* **B458**, 355 (1999), [arXiv:hep-ph/9904216](https://arxiv.org/abs/hep-ph/9904216) [hep-ph].
- [181] G. Bambhaniya, J. Chakraborty, J. Gluza, T. Jeliński, and M. Kordiaczynska, *Phys. Rev.* **D90**, 095003 (2014), [arXiv:1408.0774](https://arxiv.org/abs/1408.0774) [hep-ph].
- [182] A. Melfo, M. Nemevsek, F. Nesti, G. Senjanovic, and Y. Zhang, *Phys.Rev.* **D85**, 055018 (2012), [arXiv:1108.4416](https://arxiv.org/abs/1108.4416) [hep-ph].
- [183] *Search for Narrow Resonances using the Dijet Mass Spectrum with 19.6fb⁻¹ of pp Collisions at sqrt(s)=8 TeV*, Tech. Rep. CMS-PAS-EXO-12-059 (CERN, Geneva, 2013) <https://cds.cern.ch/record/1519066>.
- [184] *Search for Resonances in the Dilepton Mass Distribution in pp Collisions at sqrt(s) = 8 TeV*, Tech. Rep. CMS-PAS-EXO-12-061 (CERN, Geneva, 2013) <https://cds.cern.ch/record/1519132>.
- [185] *Search for New Phenomena in the Dijet Mass Distribution updated using 13.0 fb⁻¹ of pp Collisions at sqrt(s) = 8 TeV collected by the ATLAS Detector*, Tech. Rep. ATLAS-CONF-2012-148 (CERN, Geneva, 2012) <https://cds.cern.ch/record/1493487>.
- [186] *Search for W' → t b̄ in proton-proton collisions at a centre-of-mass energy of sqrt(s) = 8 TeV with the ATLAS detector*, Tech. Rep. ATLAS-CONF-2013-050 (CERN, Geneva, 2013) <https://cds.cern.ch/record/1547566>.
- [187] *Search for high-mass dilepton resonances in 20 fb⁻¹ of pp collisions at sqrt(s) = 8 TeV with the ATLAS experiment*, Tech. Rep. ATLAS-CONF-2013-017 (CERN, Geneva, 2013) <https://cds.cern.ch/record/1525524>.
- [188] *Search for a heavy neutrino and right-handed W of the left-right symmetric model in pp collisions at 8 TeV*, Tech. Rep. CMS-PAS-EXO-12-017 (CERN, Geneva, 2012) <https://cds.cern.ch/record/1460445>.
- [189] C. O. U. Vuosalo (CMS Collaboration), *Searches for new physics with leptons and/or jets at CMS*, Tech. Rep. CMS-CR-2013-155 (CERN, Geneva,

- 2013) comments: 6 pages, 5 figures, presented at the XXI International Workshop on Deep-Inelastic Scattering and Related Subjects, April 2013, Marseille, France, <https://cds.cern.ch/record/1558322>.
- [190] in *Lepton and photon interactions at high energies. Proceedings, 20th International Symposium, LP 2001, Rome, Italy, July 23-28, 2001* (2001) [arXiv:hep-ex/0107031](https://arxiv.org/abs/hep-ex/0107031) [hep-ex], <http://weblib.cern.ch/abstract?CERN-L3-NOTE-2689>.
- [191] S. Chatrchyan *et al.* (CMS), *JHEP* **1207**, 143 (2012), [arXiv:1205.5736](https://arxiv.org/abs/1205.5736) [hep-ex].
- [192] *Search for charged Higgs bosons in the τ +jets final state with pp collision data recorded at $\sqrt{s} = 8$ TeV with the ATLAS experiment*, Tech. Rep. ATLAS-CONF-2013-090 (CERN, Geneva, 2013) <https://cds.cern.ch/record/1595533>.
- [193] *Inclusive search for doubly charged Higgs in leptonic final states with the 2011 data at 7 TeV*, Tech. Rep. CMS-PAS-HIG-12-005 (CERN, Geneva, 2012) <https://cds.cern.ch/record/1430020>.
- [194] G. Aad *et al.* (ATLAS), *Eur.Phys.J.* **C72**, 2244 (2012), [arXiv:1210.5070](https://arxiv.org/abs/1210.5070) [hep-ex].
- [195] S. Chatrchyan *et al.* (CMS), *Phys.Rev.Lett.* **109**, 261802 (2012), [arXiv:1210.2402](https://arxiv.org/abs/1210.2402) [hep-ex].
- [196] G. Aad *et al.* (ATLAS), *Eur. Phys. J.* **C72**, 2241 (2012), [arXiv:1209.4446](https://arxiv.org/abs/1209.4446) [hep-ex].
- [197] C. Vuosalo (CMS), *Proceedings, 21st International Workshop on Deep-Inelastic Scattering and Related Subjects (DIS 2013)*, PoS **DIS2013**, 122 (2013), [arXiv:1307.2168](https://arxiv.org/abs/1307.2168).
- [198] V. Tello, M. Nemevsek, F. Nesti, G. Senjanovic, and F. Vissani, *Phys.Rev.Lett.* **106**, 151801 (2011), [arXiv:1011.3522](https://arxiv.org/abs/1011.3522) [hep-ph].

- [199] M. Nemevsek, F. Nesti, G. Senjanovic, and V. Tello(2011), [arXiv:1112.3061](#) [hep-ph].
- [200] J. Chakrabortty, H. Z. Devi, S. Goswami, and S. Patra, *JHEP* **1208**, 008 (2012), [arXiv:1204.2527](#) [hep-ph].
- [201] P. Bhupal Dev, S. Goswami, M. Mitra, and W. Rodejohann(2013), [arXiv:1305.0056](#) [hep-ph].
- [202] M. Nemevsek, F. Nesti, G. Senjanovic, and Y. Zhang, *Phys.Rev.* **D83**, 115014 (2011), [arXiv:1103.1627](#) [hep-ph].
- [203] A. Ferrari, J. Collot, M.-L. Andrieux, B. Belhorma, P. de Saintignon, *et al.*, *Phys.Rev.* **D62**, 013001 (2000).
- [204] N. Shaban and W. J. Stirling, *Phys.Lett.* **B291**, 281 (1992).
- [205] J. Chakrabortty and A. Raychaudhuri, *Phys.Rev.* **D81**, 055004 (2010), [arXiv:0909.3905](#) [hep-ph].
- [206] D. Guadagnoli and R. N. Mohapatra, *Phys.Lett.* **B694**, 386 (2011), [arXiv:1008.1074](#) [hep-ph].
- [207] J. Gluza and M. Zralek, *Phys.Rev.* **D51**, 4695 (1995), [arXiv:hep-ph/9409225](#) [hep-ph].
- [208] G. Ecker, W. Grimus, and H. Neufeld, *Phys.Lett.* **B127**, 365 (1983).
- [209] R. N. Mohapatra, G. Senjanovic, and M. D. Tran, *Phys.Rev.* **D28**, 546 (1983).
- [210] M. Pospelov, *Phys.Rev.* **D56**, 259 (1997), [arXiv:hep-ph/9611422](#) [hep-ph].
- [211] F. F. Deppisch, T. E. Gonzalo, S. Patra, N. Sahu, and U. Sarkar, *Phys. Rev.* **D90**, 053014 (2014), [arXiv:1407.5384](#) [hep-ph].
- [212] M. Heikinheimo, M. Raidal, and C. Spethmann, *Eur. Phys. J.* **C74**, 3107 (2014), [arXiv:1407.6908](#) [hep-ph].

- [213] A. Datta and A. Raychaudhuri, *Phys.Rev.* **D62**, 055002 (2000), [arXiv:hep-ph/9905421 \[hep-ph\]](#).
- [214] G. Aad *et al.* (ATLAS)(2014), [arXiv:1412.0237 \[hep-ex\]](#).
- [215] J. Chakrabortty, P. Konar, and T. Mondal, *Phys.Rev.* **D89**, 095008 (2014), [arXiv:1311.5666 \[hep-ph\]](#).
- [216] B. Dutta, R. Eusebi, Y. Gao, T. Ghosh, and T. Kamon, *Phys.Rev.* **D90**, 055015 (2014), [arXiv:1404.0685 \[hep-ph\]](#).
- [217] K. Huitu, J. Maalampi, A. Pietila, and M. Raidal, *Nucl.Phys.* **B487**, 27 (1997), [arXiv:hep-ph/9606311 \[hep-ph\]](#).
- [218] M. L. Swartz, *Phys. Rev. D* **40**, 1521 (Sep 1989), <http://link.aps.org/doi/10.1103/PhysRevD.40.1521>.
- [219] T. G. Rizzo, *Phys.Rev.* **D25**, 1355 (1982).
- [220] J. Maalampi and N. Romanenko, *Phys.Lett.* **B532**, 202 (2002), [arXiv:hep-ph/0201196 \[hep-ph\]](#).
- [221] F. del Aguila, M. Chala, A. Santamaria, and J. Wudka, *Phys.Lett.* **B725**, 310 (2013), [arXiv:1305.3904 \[hep-ph\]](#).
- [222] K. Babu, A. Patra, and S. K. Rai(2013), doi:\bibinfo{doi}{10.1103/PhysRevD.88.055006}, [arXiv:1306.2066 \[hep-ph\]](#).
- [223] F. del Aguila and M. Chala(2013), [arXiv:1311.1510 \[hep-ph\]](#).
- [224] C.-H. Kom and W. J. Stirling, *Eur.Phys.J.* **C69**, 67 (2010), [arXiv:1004.3404 \[hep-ph\]](#).
- [225] G. Bambhaniya, J. Chakrabortty, S. Goswami, and P. Konar(2013), [arXiv:1305.2795 \[hep-ph\]](#).
- [226] R. Martinez, M. A. Perez, and J. J. Toscano, *Phys. Rev. D* **40**, 1722 (Sep 1989), <http://link.aps.org/doi/10.1103/PhysRevD.40.1722>.

- [227] I. Picek and B. Radovic, *Phys.Lett.* **B719**, 404 (2013), [arXiv:1210.6449](#) [hep-ph].
- [228] M. Carena, I. Low, and C. E. Wagner, *JHEP* **1208**, 060 (2012), [arXiv:1206.1082](#) [hep-ph].
- [229] P. Bhupal Dev, D. K. Ghosh, N. Okada, and I. Saha, *JHEP* **1303**, 150 (2013), [arXiv:1301.3453](#).
- [230] C. Degrande, C. Duhr, B. Fuks, D. Grellscheid, O. Mattelaer, *et al.*, *Comput.Phys.Commun.* **183**, 1201 (2012), [arXiv:1108.2040](#) [hep-ph].
- [231] A. Massironi (CMS)(2014), [arXiv:1409.2990](#) [hep-ex].
- [232] M. Czakon, J. Gluza, F. Jegerlehner, and M. Zralek, *Eur.Phys.J.* **C13**, 275 (2000), [arXiv:hep-ph/9909242](#) [hep-ph].
- [233] W. Barletta, M. Battaglia, M. Klute, M. Mangano, S. Prestemon, *et al.*(2013), [arXiv:1310.0290](#) [physics.acc-ph].
- [234] R. Assmann, L. Rossi, F. Zimmermann, O. Dominguez Sanchez, G. de Rijk, J. M. Jimenez, R. Bailey, O. Brüning, L. Tavian, E. Todesco, *et al.*, *First thoughts on a higher-energy LHC*, Tech. Rep. (2010) report No. CERN-ATS-2010-177, CERN, 2010.
- [235] Future Circular Colilder, <http://cern.ch/fcc>.
- [236] fCC on CERN Document Server, <http://cds.cern.ch/collection/FutureCircularColliderDocuments?ln=en>.
- [237] J. Gutleber, M. Benedikt, and F. Zimmermann, *Study Brief February 2015*, Tech. Rep. CERN-ACC-2015-027 (CERN, Geneva, 2015) <http://cds.cern.ch/record/1994232>.
- [238] fCC Week 2015, <http://indico.cern.ch/event/340703/>.
- [239] S. Catani, L. Cieri, G. Ferrera, D. de Florian, and M. Grazzini, *Phys.Rev.Lett.* **103**, 082001 (2009), [arXiv:0903.2120](#) [hep-ph].

- [240] S. Das, F. Deppisch, O. Kittel, and J. Valle, *Phys.Rev.* **D86**, 055006 (2012), [arXiv:1206.0256 \[hep-ph\]](#).
- [241] J. A. Aguilar-Saavedra and F. R. Joaquim, *Phys. Rev.* **D86**, 073005 (2012), [arXiv:1207.4193 \[hep-ph\]](#).
- [242] C.-Y. Chen, P. S. B. Dev, and R. N. Mohapatra, *Phys. Rev.* **D88**, 033014 (2013), [arXiv:1306.2342 \[hep-ph\]](#).
- [243] R. N. Mohapatra and J. D. Vergados, *Phys. Rev. Lett.* **47**, 1713 (1981).
- [244] M. Hirsch, H. V. Klapdor-Kleingrothaus, and O. Panella, *Phys. Lett.* **B374**, 7 (1996), [arXiv:hep-ph/9602306 \[hep-ph\]](#).
- [245] J. Barry and W. Rodejohann, *JHEP* **09**, 153 (2013), [arXiv:1303.6324 \[hep-ph\]](#).
- [246] P. S. B. Dev, C.-H. Lee, and R. Mohapatra(2013), [arXiv:1309.0774 \[hep-ph\]](#).
- [247] W.-C. Huang and J. Lopez-Pavon, *Eur. Phys. J.* **C74**, 2853 (2014), [arXiv:1310.0265 \[hep-ph\]](#).
- [248] D. Borah and A. Dasgupta(2015), [arXiv:1509.01800 \[hep-ph\]](#).
- [249] S.-F. Ge, M. Lindner, and S. Patra, *JHEP* **10**, 077 (2015), [arXiv:1508.07286 \[hep-ph\]](#).
- [250] R. L. Awasthi, P. S. B. Dev, and M. Mitra(2015), [arXiv:1509.05387 \[hep-ph\]](#).
- [251] Riazuddin, R. E. Marshak, and R. N. Mohapatra, *Phys. Rev.* **D24**, 1310 (1981).
- [252] P. B. Pal, *Nucl. Phys.* **B227**, 237 (1983).
- [253] R. N. Mohapatra, *Phys. Rev.* **D46**, 2990 (1992).

- [254] V. Cirigliano, A. Kurylov, M. J. Ramsey-Musolf, and P. Vogel, *Phys. Rev. D* **70**, 075007 (2004), [arXiv:hep-ph/0404233 \[hep-ph\]](#).
- [255] V. Cirigliano, A. Kurylov, M. J. Ramsey-Musolf, and P. Vogel, *Phys. Rev. Lett.* **93**, 231802 (2004), [arXiv:hep-ph/0406199 \[hep-ph\]](#).
- [256] A. Ilakovac and A. Pilaftsis, *Nucl.Phys.* **B437**, 491 (1995), [arXiv:hep-ph/9403398 \[hep-ph\]](#).
- [257] C. E. Picciotto and M. S. Zahir, *Phys. Rev.* **D26**, 2320 (1982).
- [258] M. Agostini *et al.* (GERDA), *Phys. Rev. Lett.* **111**, 122503 (2013), [arXiv:1307.4720 \[nucl-ex\]](#).
- [259] B. Majorovits (GERDA), *Proceedings, 5th Topical Workshop on Low Radioactivity Techniques (LRT 2015)*, *AIP Conf. Proc.* **1672**, 110003 (2015), [arXiv:1506.00415 \[hep-ex\]](#).
- [260] G. Aad *et al.* (ATLAS)(2015), [arXiv:1506.00962 \[hep-ex\]](#).
- [261] G. Aad *et al.* (ATLAS), *Eur. Phys. J.* **C75**, 69 (2015), [arXiv:1409.6190 \[hep-ex\]](#).
- [262] G. Aad *et al.* (ATLAS), *Eur. Phys. J.* **C75**, 209 (2015), [Erratum: *Eur. Phys. J.*C75,370(2015)], [arXiv:1503.04677 \[hep-ex\]](#).
- [263] V. Khachatryan *et al.* (CMS), *JHEP* **08**, 173 (2014), [arXiv:1405.1994 \[hep-ex\]](#).
- [264] V. Khachatryan *et al.* (CMS), *JHEP* **08**, 174 (2014), [arXiv:1405.3447 \[hep-ex\]](#).
- [265] J. Hisano, N. Nagata, and Y. Omura, *Phys. Rev.* **D92**, 055001 (2015), [arXiv:1506.03931 \[hep-ph\]](#).
- [266] K. Cheung, W.-Y. Keung, P.-Y. Tseng, and T.-C. Yuan(2015), doi:\bibinfo{doi}{10.1016/j.physletb.2015.10.029}, [arXiv:1506.06064 \[hep-ph\]](#).

- [267] B. A. Dobrescu and Z. Liu(2015), [arXiv:1506.06736 \[hep-ph\]](#).
- [268] Y. Gao, T. Ghosh, K. Sinha, and J.-H. Yu, *Phys. Rev.* **D92**, 055030 (2015), [arXiv:1506.07511 \[hep-ph\]](#).
- [269] J. Brehmer, J. Hewett, J. Kopp, T. Rizzo, and J. Tattersall, *JHEP* **10**, 182 (2015), [arXiv:1507.00013 \[hep-ph\]](#).
- [270] P. S. B. Dev and R. N. Mohapatra, *Phys. Rev. Lett.* **115**, 181803 (2015), [arXiv:1508.02277 \[hep-ph\]](#).
- [271] F. F. Deppisch, L. Graf, S. Kulkarni, S. Patra, W. Rodejohann, N. Sahu, and U. Sarkar(2015), [arXiv:1508.05940 \[hep-ph\]](#).
- [272] A. Akeroyd and S. Moretti, *Phys.Rev.* **D86**, 035015 (2012), [arXiv:1206.0535 \[hep-ph\]](#).
- [273] Z. Kang, J. Li, T. Li, Y. Liu, and G.-Z. Ning(2014), [arXiv:1404.5207 \[hep-ph\]](#).
- [274] S. Kanemura, M. Kikuchi, K. Yagyu, and H. Yokoya, *Phys.Rev.* **D90**, 115018 (2014), [arXiv:1407.6547 \[hep-ph\]](#).
- [275] N. G. Deshpande, J. F. Gunion, B. Kayser, and F. I. Olness, *Phys. Rev.* **D44**, 837 (1991).
- [276] J. C. Vasquez(2014), [arXiv:1411.5824 \[hep-ph\]](#).

Publications attached with the thesis

1. “*Left-Right Symmetry and the Charged Higgs Bosons at the LHC*”
Gulab Bambhaniya, J. Chakraborty, J. Gluza, M. Kordiaczyńska and R. Szafron, JHEP **1405**, 033 (2014) [arXiv:1311.4144 [hep-ph]].
2. “*Looking for hints of a reconstructible seesaw model at the Large Hadron Collider*”
Gulab Bambhaniya, S. Goswami, S. Khan, P. Konar and T. Mondal, Phys. Rev. D **91**, no. 7, 075007 (2015) arXiv:1410.5687 [hep-ph].

RECEIVED: November 26, 2013

REVISED: February 19, 2014

ACCEPTED: April 10, 2014

PUBLISHED: May 8, 2014

Left-right symmetry and the charged Higgs bosons at the LHC

G. Bambhaniya,^a J. Chakraborty,^b J. Gluza,^c M. Kordiaczyńska^c and R. Szafron^d

^a*Theoretical Physics Division, Physical Research Laboratory,
Navarangpura, Ahmedabad – 380009, India*

^b*Department of Physics, Indian Institute of Technology,
Kanpur – 208016, India*

^c*Institute of Physics, University of Silesia,
Uniwersytecka 4, PL-40-007 Katowice, Poland*

^d*Department of Physics, University of Alberta,
Edmonton, AB T6G 2E1, Canada*

E-mail: gulab@prl.res.in, joydeep@iitk.ac.in, gluza@us.edu.pl,
mkordiaczynska@us.edu.pl, szafron@ualberta.ca

ABSTRACT: The charged Higgs boson sector of the Minimal Manifest Left-Right Symmetric model (MLRSM) is investigated in the context of LHC discovery search for new physics beyond Standard Model. We discuss and summarise the main processes within MLRSM where heavy charged Higgs bosons can be produced at the LHC. We explore the scenarios where the amplified signals due to relatively light charged scalars dominate against heavy neutral Z_2 and charged gauge W_2 as well as heavy neutral Higgs bosons signals which are dumped due to large vacuum expectation value v_R of the right-handed scalar triplet. Consistency with FCNC effects implies masses of two neutral Higgs bosons A_1^0, H_1^0 to be at least of 10 TeV order, which in turn implies that in MLRSM only three of four charged Higgs bosons, namely $H_{1,2}^{\pm\pm}$ and H_1^\pm , can be simultaneously light. In particular, production processes with one and two doubly charged Higgs bosons are considered. We further incorporate the decays of those scalars leading to multi lepton signals at the LHC. Branching ratios for heavy neutrino N_R , W_2 and Z_2 decay into charged Higgs bosons are calculated. These effects are substantial enough and cannot be neglected. The tri- and four-lepton final states for different benchmark points are analysed. Kinematic cuts are chosen in order to strength the leptonic signals and decrease the Standard Model (SM) background. The results are presented using di-lepton invariant mass and lepton-lepton separation distributions for the same sign (SSDL) and opposite sign (OSDL) di-leptons as well as the charge asymmetry are also discussed. We have found that for considered MLRSM processes tri-lepton and four-lepton signals are most important for their detection when compared to the SM background. Both of the signals can be detected at 14 TeV collisions at the LHC with integrated luminosity at the level of 300 fb^{-1} with doubly charged Higgs bosons up to approximately 600 GeV. Finally, possible extra contribution of the charged MLRSM scalar particles to the measured Higgs to di-photon ($H_0^0 \rightarrow \gamma\gamma$) decay is computed and pointed out.

KEYWORDS: Beyond Standard Model, Higgs Physics, GUT, Standard Model

ARXIV EPRINT: [1311.4144](https://arxiv.org/abs/1311.4144)

Contents

1	Introduction	1
2	MLRSM processes with charged Higgs boson particles at the LHC	3
2.1	Primary production of heavy charged Higgs bosons at the LHC	9
2.1.1	$pp \rightarrow H_1^+ H_1^-$ and $pp \rightarrow H_2^+ H_2^-$	9
2.1.2	$pp \rightarrow H_1^{++} H_1^{--}$ and $pp \rightarrow H_2^{++} H_2^{--}$	10
2.1.3	$pp \rightarrow H_1^{\pm\pm} H_1^\mp$ and $pp \rightarrow H_2^{\pm\pm} H_2^\mp$	12
2.2	Primary production of a heavy Higgs and gauge bosons	14
2.2.1	$pp \rightarrow W_{1/2}^\mp H_{1/2}^\pm$, $pp \rightarrow Z_{1/2} H_{1/2}^\pm$ and $pp \rightarrow \gamma H_{1/2}^\pm$	14
3	Simulations and results for final lepton signals	14
3.1	Events selection criteria	14
3.2	Signal events for doubly charged Higgs particles in MLRSM	15
3.2.1	$pp \rightarrow H_1^{++} H_1^{--}$ and $pp \rightarrow H_2^{++} H_2^{--}$	16
3.2.2	$pp \rightarrow H_1^{\pm\pm} H_1^\mp$ and $pp \rightarrow H_2^{\pm\pm} H_2^\mp$	19
3.3	Background estimation and significance of signals	20
4	MLRSM charged Higgs bosons contribution to $H_0^0 \rightarrow \gamma\gamma$	21
5	Conclusions and outlook	24
A	Reconciling FCNC effects and large v_R with relatively light charged Higgs mass spectrum within MLRSM	26

1 Introduction

The LHC machine is working incredibly well shifting up the discovery limits for all the non-standard masses. For the same reason it is also true for the non-standard couplings and their possible values are shrinking more and more. Good examples are parameters connected with Left-Right (LR) symmetric models. These models enjoy richness of several types of beyond-the-SM particles [1, 2]. No wonder that these models are interesting for theoretical and phenomenological studies, for some recent works see [3–9] and explored also by the LHC collaborations.

The searches at CMS and ATLAS have tightened up the limits on the masses of heavy gauge bosons. Let us mention that before the LHC era the fits to low energy charged and neutral currents were quite modest, e.g. for a charged gauge boson PDG reports $M_{W_2} > 715 \text{ GeV}$ [10, 11]. The new LHC analysis pushed the limits already much above 2 TeV [12–18]. All these searches provide robust bounds on the extra gauge bosons, for

instance, the present limit for a charged heavy boson coming from the “golden” decay chain $W_R \rightarrow l_1 N_l \rightarrow l_1 l_2 j j$ is [17, 18]

$$M_{W_2} \geq 2.8 \text{ TeV}. \tag{1.1}$$

This limit (at 95% C.L.) is for a genuine left-right symmetric model which we consider here (MLRSM) with $g_L = g_R$ and three degenerate generations of heavy neutrinos and it is based on $\sqrt{s} = 8 \text{ TeV}$ data. Typically, also limits for Z_2 mass are already beyond 2 TeV.

The combined LEP lower limit on the singly charged Higgs boson mass is about 90 GeV [19]. At the LHC, established limits for singly charged Higgs boson masses are

$$M_{H^\pm} = 80 \div 160 \text{ GeV}, \tag{1.2}$$

if $\text{BR}(t \rightarrow H^+ b) < 5\%$ [20] and for higher masses than 160 GeV, see the limits in [21].

For doubly charged Higgs bosons the analysis gives lower mass limits in a range

$$M_{H^{\pm\pm}} \geq 445 \text{ GeV} \text{ (409 GeV)} \quad \text{for CMS (ATLAS)}, \tag{1.3}$$

in the 100% branching fraction scenarios [22, 23].

The mass limit for heavy neutrinos is [24, 25]

$$M_{N_R} > 780 \text{ GeV}, \tag{1.4}$$

but it must be kept in mind that bounds on M_{N_R} and M_{W_2} are not independent from each other [17, 18]. Neutrinoless double beta decay allows for heavy neutrinos with relatively light masses, see e.g. [26–32]. Detailed studies which take into account potential signals with $\sqrt{s} = 14 \text{ TeV}$ at the LHC conclude that heavy gauge bosons and neutrinos can be found with up to 4 and 1 TeV, respectively, for typical LR scenarios [3, 4]. Such a relatively low (TeV) scale of the heavy sector is theoretically possible, even if GUT gauge unification is demanded, for a discussion, see e.g. [33, 34].

In this paper we consider Left-Right symmetric model based on the $SU(2)_L \otimes SU(2)_R \otimes U(1)_{B-L}$ gauge group [1] in its most restricted form, so-called Minimal Left-Right Symmetric Model (MLRSM). We choose to explore the most popular version of the model with Higgs representations — a bi-doublet Φ and two (left and right) triplets $\Delta_{L,R}$ [35, 36]. We also assume that the vacuum expectation value of the left-handed triplet Δ_L vanishes, $\langle \Delta_L \rangle = 0$ and the CP symmetry can be violated by complex phases in the quark and lepton mixing matrices. Left and right gauge couplings are chosen to be equal, $g_L = g_R$. For reasons discussed in [37] and more extensively in [38], we discuss see-saw diagonal light-heavy neutrino mixings. It means that W_1 couples mainly to light neutrinos, while W_2 couples to the heavy ones. Z_1 and Z_2 turn out to couple to both of them [36, 39]. $W_L - W_R$ mixing is allowed and is very small, $\xi \leq 0.05$ [10], the most stringent data comes from astrophysics through the supernova explosion analysis [40]. In our last paper we considered low energy constraints on such a model assuming $\kappa_2 = 0$, i.e., $\xi = 0$ [7], we do the same here. Moreover, in MLRSM $\tan 2\xi = -\frac{2\kappa_1\kappa_2}{v_R^2}$, which is really negligible for $v_R \geq 5 \text{ TeV}$, as dictated by eq. (1.1), where $\kappa_1, \kappa_2(v_R)$ are the vacuum expectation values of $\Phi(\Delta_R)$.

We think that it is worth to show how the situation looks like if we stick to the popular and to a large extent conservative version of the model (MLRSM), giving candle-like benchmark numbers for possible signals at the LHC. We should also be aware of the fact, that there are relations between model parameters in the Higgs, gauge and neutrino sectors [7, 11, 36, 41] and it needs further detailed studies. For estimation and discussion of observables which are able to measure final signals in the most efficient way, calculation of dominant tree level signals is sufficient at the moment. Production processes are calculated and relevant diagrams are singled out using CalcHEP [42]. For general analysis, multi lepton codes ALPGEN [43], PYTHIA [44], Madgraph [45] are used. Feynman rules are generated with our version of the package using FeynRules [46, 47]. The backgrounds for multi lepton signals (3 and 4 leptons) are estimated using ALPGEN-PYTHIA.

In this paper we have grabbed the impact of the relatively light charged scalars in the phenomenology of Left-Right symmetric model. We first discuss how the decay branching ratios of W_2 , Z_2 , and N_R are affected by the presence of these light charged scalars. Then we note down the possible interesting processes within MLRSM. We study the production and decay modes of the charged scalars. We have provided some benchmark points where we have performed our simulations to make a realistic estimation of the signal events over the SM backgrounds. Our study is based on the reconstruction of the invariant masses of the final state leptons and their mutual separations from where we have shown how we can track the presence of doubly charged scalars. We also note down the impact of the charged scalars in the Higgs to di-photon decay rates. Then we conclude and give an outlook.

2 MLRSM processes with charged Higgs boson particles at the LHC

There are already severe limits on the heavy gauge boson masses, eq. (1.1), which infer that scale in which the right SU(2) gauge sector is broken at $v_R > 5$ TeV (for approximate relations between gauge boson masses and v_R , see for example eq. (2.4) in [7]). This is already an interesting situation as for such heavy gauge bosons most of the effects connected with them decouple in physical processes at collider physics. Then there is a potential room to go deeper and estimate more sensitive Higgs boson contributions. Of course, the effects coming from the scalar sector depend crucially also on their masses. Smaller the Higgs boson masses, larger effects are expected. The question is then: how small their masses can be by keeping the right scale v_R large? In the paper we assume light charged scalar masses up to 600 GeV, this choice of masses will be justified when production cross sections are considered.

The point is that all Higgs scalars are naturally of the order of v_R , in addition, neutral Higgs boson scalars A_1^0 and H_1^0 contribute to FCNC effects (see the appendix) and must be large, above 10 TeV (see however [48] for alternative solutions). Let us see then if theoretically charged Higgs bosons can have masses below 1 TeV. In the model which we consider in this paper we assume that the Higgs potential is given as in [35, 36], we will also use the same notation, for details on the parametrisation of the Higgs scalar mass spectrum, see the appendix. This model includes a number of parameters: $\mu_1, \mu_2, \mu_3, \rho_1, \rho_2, \rho_3, \rho_4, \alpha_1, \alpha_2, \alpha_3, \alpha_4, \lambda_1, \lambda_2, \lambda_3, \lambda_4$. The exact Higgs mass spectrum is calculated numerically.

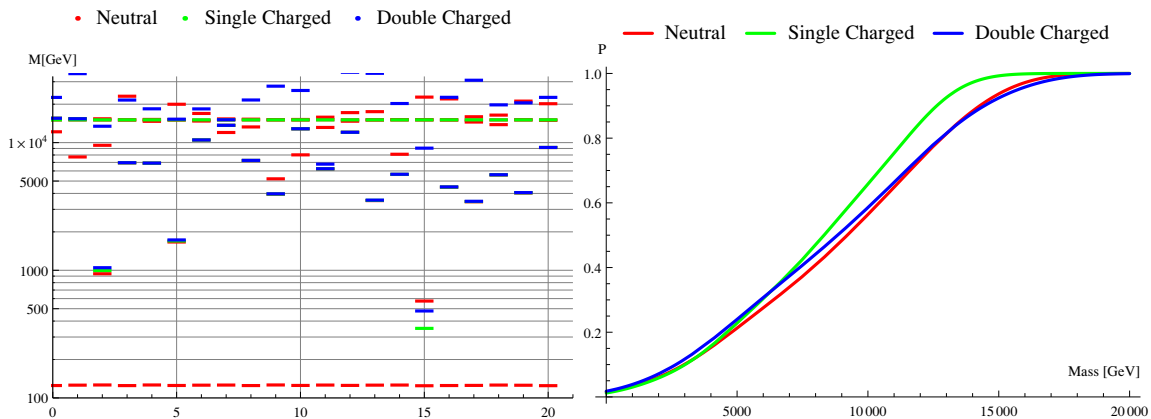


Figure 1. *On left:* an example of 20 Higgs mass spectra obtained by randomly chosen Higgs potential parameters. The constrain on the lowest neutral Higgs mass eq. (2.1) was imposed and the bounds coming from FCNC were taken into account. *On right:* cumulative distribution function P of the lowest mass of singly and doubly charged and next to lightest neutral scalars. For both figures, $v_R = 8$ TeV.

Minimisation conditions are used to get values of dimensionful mass parameters μ_1, μ_2 and μ_3 which can be arbitrarily large, all other parameters are considered as free, but limited to the perturbative bound,¹ $|\rho_i|, |\alpha_i|, |\lambda_i| < 10$. It is assumed that the lightest neutral Higgs particle is the boson discovered by ATLAS and CMS collaborations. We have taken its mass to lie in the range

$$124.7 \text{ GeV} < M_{H_0^0} < 126.2 \text{ GeV}. \tag{2.1}$$

An example set of generated mass spectra of Higgs bosons for $v_R = 8$ TeV is presented in figure 1 (left figure). Mass spectra have been obtained by varying uniformly the Higgs potential parameters in a range $(-10, 10)$. We have also taken into account the bounds on neutral Higgs bosons obtained from FCNC constrains assuming $m_{A_1^0}, m_{H_1^0} > 15$ TeV by fixing $\alpha_3 = 7.1$ (see appendix A). The spectra which did not fulfill relation (2.1) were rejected. Altogether we have 6 neutral, 2 singly charged and 2 doubly charged Higgs boson particles in the MLRSM. The figure includes possible spectra of singly and doubly charged as well as neutral Higgs bosons. Some of them can be degenerated or nearly degenerated.

This study shows that although the Higgs particles naturally tend to have masses of the order of the v_R scale, it is still possible to choose the potential parameters such that some of the scalar particles can have masses much below 1 TeV (spectrum 15). To discuss spectra more quantitatively, the cumulative distribution function P of the lowest masses of singly and doubly charged and next to lightest neutral scalar particles are plotted on right figure 1, again for the same conditions as before and $v_R = 8$ TeV. These results show that for $v_R = 8$ TeV a fraction of the parameter space that gives lightest scalar masses below 1 TeV is at the level of 4%. It means that it is possible to generate the low mass spectra of Higgs boson masses in MLRSM keeping large v_R scale. However, what can not be seen

¹Which is equal to 4π , otherwise proper analysis of the Higgs potential with radiative corrections to determine perturbative regions would be needed.

Primary production	Secondary production	Signal
I. $H_1^+ H_1^-$	$\ell^+ \ell^- \nu_L \nu_L$	$\ell^+ \ell^- \oplus MET$
–	$\ell^+ \ell^- N_R N_R$	depends on N_R decay modes
–	$\ell^+ \ell^- \nu_L N_R$	depends on N_R decay modes
II. $H_2^+ H_2^-$	$\ell^+ \ell^- \nu_L \nu_L$	$\ell^+ \ell^- \oplus MET$
–	$\ell^+ \ell^- N_R N_R$	depends on N_R decay modes
–	$\ell^+ \ell^- \nu_L N_R$	depends on N_R decay modes
III. $H_1^{++} H_1^{--}$	–	$\ell^+ \ell^+ \ell^- \ell^-$
–	$H_1^+ H_1^+ H_1^- H_1^-$	See I
–	$H_1^\pm H_1^\pm H_2^\mp H_2^\mp$	See I & II
–	$H_2^+ H_2^+ H_2^- H_2^-$	See II
–	$W_i^+ W_i^+ W_j^- W_j^-$	depends on W 's decay modes
IV. $H_2^{++} H_2^{--}$	–	$\ell^+ \ell^+ \ell^- \ell^-$
–	$H_2^+ H_2^+ H_2^- H_2^-$	See II
–	$H_1^\pm H_1^\pm H_2^\mp H_2^\mp$	See I & II
–	$H_1^+ H_1^+ H_1^- H_1^-$	See I
–	$W_i^+ W_i^+ W_j^- W_j^-$	depends on W 's decay modes
V. $H_1^{\pm\pm} H_1^\mp$	–	$\ell^\pm \ell^\pm \ell^\mp \nu_L$
VI. $H_2^{\pm\pm} H_2^\mp$	–	$\ell^\pm \ell^\pm \ell^\mp \nu_L$
VII. $H_1^\pm Z_i, H_1^\pm W_i$	–	See I & Z_i, W_i decay modes
VIII. $H_2^\pm Z_i, H_2^\pm W_i$	–	See II & Z_i, W_i decay modes
IX. $H_1^\pm \gamma$	–	See I
X. $H_2^\pm \gamma$	–	See II

Table 1. Phenomenologically interesting MLRSM processes at the LHC with primarily produced charged scalar particles and possible final signals. Here γ denotes a photon. $\nu_L = \nu_1, \nu_2, \nu_3$ are SM-like light massive neutrino states and $N_R = N_{4,5,6}$ are heavy neutrino massive states dominated by right-handed weak neutrinos. From now on we will denote $N_R \equiv N$. Here ℓ represents light charged leptons e, μ .

on those plots is that in MLRSM not all four charged Higgs bosons can simultaneously be light. It is a case for $H_1^\pm, H_1^{\pm\pm}$ and $H_2^{\pm\pm}$, for details, see the appendix. The remaining charged scalar H_2^\pm is of the order of the v_R scale, so its effects at LHC is negligible, to make it lighter would require to go beyond MLRSM. For a book keeping, we keep this particle in further discussion. If its mass at some points is assumed to be small (so we go beyond MLRSM), we denote it with a tilde, \tilde{H}_2^\pm . Its coupling is kept all the time as in MLRSM (why it can be so is discussed shortly in the appendix).

In this paper we consider only the processes where charged Higgs particles can be produced directly as shown in the table 1, first column.

The decay branching ratios for heavy neutrino states N and heavy gauge bosons (W_2, Z_2) in MLRSM which determine both secondary production and final signals in the last column of this table are given in [7]. However, with assumed light charged

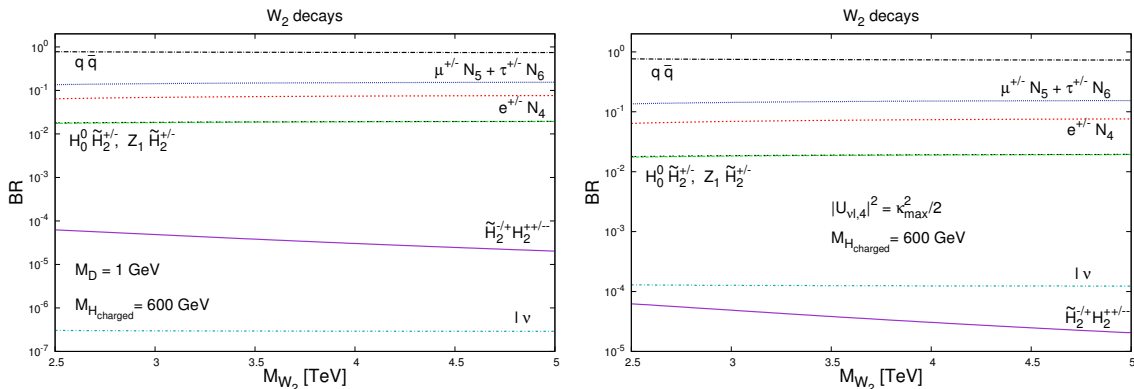


Figure 2. Branching ratio for W_2 decay with relatively light charged scalars. Here we put $M_{N_4} = M_{N_5} = 1 \text{ TeV}$, $M_{N_6} = 800 \text{ GeV}$. Symbol $q\bar{q}$ on this and next plots stands for a sum of all quark flavours, $q\bar{q} \equiv \sum_{i,i'=u,d,s,b,c,t} q_i \bar{q}_{i'}$. Similarly, $l\nu \equiv \sum_{i=1}^3 l_i \nu_i$.

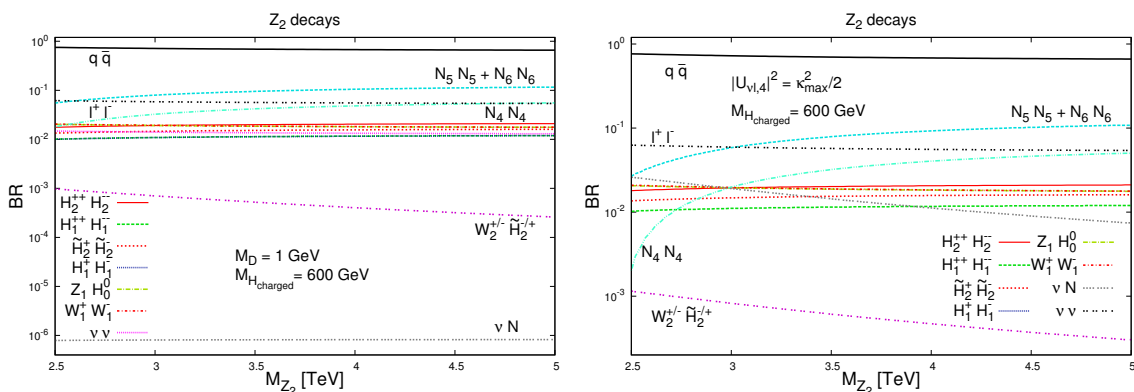


Figure 3. Branching ratio for Z_2 decay with relatively light charged scalars. Here $\nu\nu \equiv \sum_{i=1}^3 \nu_i \nu_i$ and $\nu N \equiv \sum_{i=1}^3 \nu_i N_{i+3}$.

Higgs particles, new decay modes are potentially open, and discussion must be repeated. Results are given in figures 2, 3, and 4. As can be seen from figure 2, contribution of charged scalars to the total decay width of W_2 is at the percent level. Here more important are heavy neutrino decay modes.² Different scenarios for LH neutrino mixings [7] are discussed, i.e., see-saw mechanisms where $|U_{\nu i j}| \simeq \frac{|(M_D)|}{M_{N_j}} \delta_{i,j-3}$, $i = 1, 2, 3$, $j = 4, 5, 6$ and scenarios where LH neutrino mixings are independent of neutrino masses: $\sum_{j=4,5,6} U_{\nu 1,j-3} U_{\nu 1,j-3}^* = U_{\nu 1,4} U_{\nu 1,4}^* \leq 0.003 \equiv \kappa_{\max}^2$ [49]. In a case of many heavy neutrino states (as in MLRSM), taking into account constraints coming from neutrinoless double-beta decay experiment, this limit becomes $\kappa_{\max}^2/2$ [50–52]. For W_2 decays different LH neutrino mixing scenarios affect only light neutrino νl channel for which BR is small, anyway.

For the Z_2 decays, figure 3, four channels with charged Higgs bosons, namely $H_1^{++} H_1^{--}$, $H_1^+ H_1^-$, $H_2^{++} H_2^{--}$, and $\tilde{H}_2^+ \tilde{H}_2^-$, contribute to the decay rate in a percentage level. The

²Some processes in the table 1 depend strongly on the light-heavy (LH) neutrino mixing scenarios.

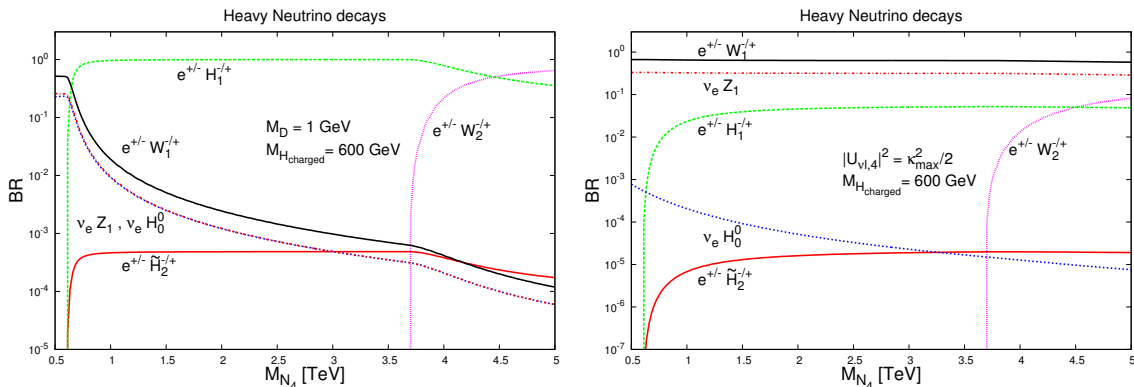


Figure 4. Branching ratios for N_4 decay with relatively light charged scalars.

quark decay modes dominate, and the second important are the heavy neutrino decay modes.

The most interesting situation is for the decays of heavy neutrinos. Here H_1^+ decay mode is the largest in see-saw scenarios. The reason is that in case of Yukawa coupling, say $H_1^+ - N - e$, the change in LH neutrino mixing is compensated by the proportionality of the coupling to the heavy neutrino mass, which is not the case for the gauge $N - e - W$ and $N - \nu - Z$ couplings. That is why eW and νZ decay modes are relevant only in scenarios where LH neutrino mixings are independent of the heavy neutrino masses and are close to the present experimental limits. Large charged Higgs boson decay mode of the heavy neutrino can influence the “golden” $pp \rightarrow eN$ process [3, 4, 6, 7, 53, 54].

For typical see-saw cases when charged Higgs boson masses are very large, standard model modes dominate: $N \rightarrow eW_1$ and $N \rightarrow \nu_L Z_1$ if $M_N < M_{W_2}$ whereas $N \rightarrow eW_2$ if $M_N > M_{W_2}$. In scenarios with large LH neutrino mixings the standard modes dominates independently of the heavy neutrino and W_2 masses.³ Finally, let us note that in typical Type I see-saw scenarios the TeV scale of heavy neutrino masses implies $m_D \sim 10^{-6}$ GeV to accomplish light neutrino masses at the eV level. In this situation nothing happens to the left plots in figures 2, 3, and 4 apart from the fact that $l\nu$, lN and νZ channels will disappear completely there.

In the case of heavy gauge boson decays, quarks dominate and jets will be produced while for SM-like gauge bosons hadronic decay branching is around 70%. That is why typical final signals for reactions I and II in table 1 are two or four jets plus missing energy. There are only two cases without missing energy:

$$H_{1(2)}^+ H_{1(2)}^- \rightarrow \ell^+ \ell^- N N \rightarrow \ell^+ \ell^- W_m^\pm \ell^\mp W_n^\pm \ell^\mp \rightarrow jjjj \ell^+ \ell^- \ell^\mp \ell^\mp, \quad (2.2)$$

and

$$H_{1(2)}^+ H_{1(2)}^- \rightarrow \ell^+ \ell^- N N \rightarrow \ell^+ \ell^- W_m^\pm \ell^\mp W_n^\mp \ell^\pm \rightarrow jjjj \ell^+ \ell^- \ell^\pm \ell^\mp. \quad (2.3)$$

However, as we can see from the table, the cleanest signals are connected with doubly charged Higgs particles, that is why we focus on them in this paper. For some related

³Relevance of see-saw LH mixings at the LHC has been discussed lately in [54].

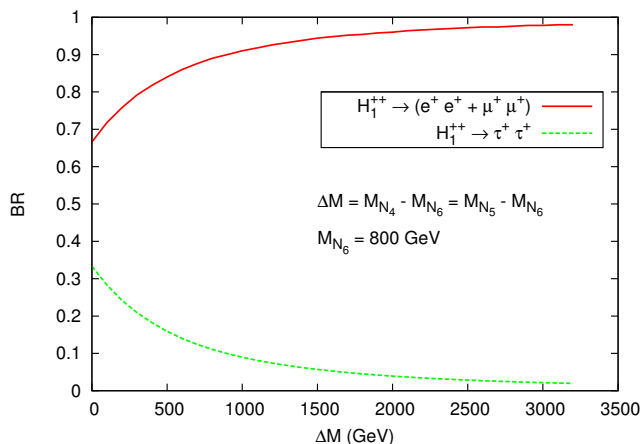


Figure 5. Branching ratios for the decay modes $(e^+e^+ + \mu^+\mu^+)$ and $\tau^+\tau^+$ of the doubly charged scalars as a function of ΔM , where $\Delta M = M_{N_4} - M_{N_6} = M_{N_5} - M_{N_6}$. We have kept fixed $M_{N_6} = 800$ GeV. Note that the BRs of both the doubly charged scalars (H_1^{++} and H_2^{++}) are the same in scenarios where $M_{W_2} \gg M_{H^{\pm\pm}}$ and $M_{H^{\pm\pm}} \simeq M_{H^\pm}$.

discussions on doubly charged scalars, see e.g. [55–63]. The processes eqs. (2.2) and (2.3) with four charged leptons plus jets will be considered elsewhere.

For processes III–X important are charged Higgs boson decay modes. For doubly charged Higgs particles possible decay modes are

$$\begin{aligned}
 \text{(i)} \quad & H_1^{\pm\pm} \rightarrow l^\pm l^\pm, \\
 \text{(ii)} \quad & H_1^{\pm\pm} \rightarrow H_1^\pm W_1^\pm; \\
 \text{(iii)} \quad & H_2^{\pm\pm} \rightarrow l^\pm l^\pm, \\
 \text{(iv)} \quad & H_2^{\pm\pm} \rightarrow H_2^\pm W_2^\pm; \\
 \text{(v)} \quad & H_2^{\pm\pm} \rightarrow W_2^\pm W_2^\pm; \\
 \text{(vi)} \quad & H_2^{\pm\pm} \rightarrow H_2^\pm W_1^\pm;
 \end{aligned}
 \tag{2.4}$$

where $l = e, \mu, \tau$.

Apart from the above decay modes, the other possibilities for the doubly charged scalars can be

$$\begin{aligned}
 \text{(vii)} \quad & H_2^{\pm\pm} \rightarrow H_1^\pm H_1^\pm, \\
 \text{(viii)} \quad & H_2^{\pm\pm} \rightarrow H_2^\pm H_2^\pm;
 \end{aligned}
 \tag{2.5}$$

when they are not degenerate with the singly charged ones. But for nearly or exact degenerate case, the charged scalars dominantly decay through leptonic modes and here kinematics play a role too.

Figure 5 shows a scenario in which pure leptonic decay modes can be realised. The crucial factor is the Yukawa coupling which depends (indirectly) on heavy right-handed neutrino mass. If heavy neutrino masses are degenerate then democratic scenario is understood where all leptonic channels are the same (i.e. $\text{BR}(H^{\pm\pm} \rightarrow e^\pm e^\pm) \simeq 33\%$).

Typically, as can be seen from figure 5, for right-handed neutrino masses to be 1 TeV, 1 TeV and 800 GeV for N_4, N_5, N_6 respectively, the branching ratios are the following

$$\begin{aligned} \text{BR}(H_{1/2}^{\pm\pm} \rightarrow e^\pm e^\pm) &= 37.9\%, \\ \text{BR}(H_{1/2}^{\pm\pm} \rightarrow \mu^\pm \mu^\pm) &= 37.9\%, \\ \text{BR}(H_{1/2}^{\pm\pm} \rightarrow \tau^\pm \tau^\pm) &= 24.2\%. \end{aligned} \tag{2.6}$$

If the first two generations neutrinos (N_4, N_5) have masses above ~ 4 TeV, τ decay mode is practically irrelevant. From the discussion it is also clear, that *one of the decay modes can dominate if only one of the right-handed neutrino masses is much bigger than remaining two heavy neutrino states*. Limits in eq. (1.3) assume 100% leptonic decays, in our case, taking into account figure 5, eq. (2.6) and results given in [22, 23], mass limits are much weaker, at about 300 GeV, see e.g. figure 3 in [23].

For decays of singly charged H_1^\pm scalars situation is analogical as for doubly charged scalars (possible decay modes to neutral H_1^0 and A_1^0 scalars are negligible for $M_{H_1^0}, M_{A_1^0} \gg M_{H_1^\pm}$, as dictated by FCNC constraints).

\tilde{H}_2^\pm decays hadronically, namely, for $100 \text{ GeV} < M_{\tilde{H}_2^\pm} < 200 \text{ GeV}$

$$\begin{aligned} \text{BR}(\tilde{H}_2^+ \rightarrow c\bar{s}) &= 95\%, \\ \text{BR}(\tilde{H}_2^+ \rightarrow c\bar{d}) &= 5\%, \end{aligned} \tag{2.7}$$

and $\text{BR}(\tilde{H}_2^+ \rightarrow t\bar{b}) \sim 100\%$ for $M_{\tilde{H}_2^\pm} > 200 \text{ GeV}$.

2.1 Primary production of heavy charged Higgs bosons at the LHC

Below different processes involving solely charged scalar productions are classified. In analysis which follow $v_R = 8000 \text{ GeV}$ to respect with a large excess the present exclusion limits on W_2^\pm , and Z_2 masses. SM-Higgs like mass is set to 125 GeV, masses of neutral scalar particles are set at very high limit ($\sim 10 \text{ TeV}$). In this way, as already discussed, scenarios are realised with relatively light (hundreds of GeV) charged Higgs bosons while remaining non-standard particles within MLRSM are much heavier. All cross sections given in this section are without any kinematic cuts, those will be considered with final signals and distributions in section 3.

2.1.1 $pp \rightarrow H_1^+ H_1^-$ and $pp \rightarrow H_2^+ H_2^-$

The cross section for singly charged scalar pair production as a function of their mass is given in figure 6. This process is dominated by s-channel γ, Z_1 and t-channel quark exchange diagrams. Contributions coming from s-channel H_0^0, Z_2 and H_1^0 bosons are negligible for considered MLRSM parameters. For singly charged scalar mass equals to 400 GeV, the cross sections are (as discussed in section 2, H_2^\pm Higgs boson is assumed to be light and we denote it here with a tilde, for $M_{H_2^\pm} \gg 1 \text{ TeV}$ the considered cross section is negligible, $\sigma(pp \rightarrow \tilde{H}_2^\pm \tilde{H}_2^\mp) \simeq 0$)

$$\sigma(pp \rightarrow H_1^\pm H_1^\mp) = 0.12 \text{ (0.52) fb}, \tag{2.8}$$

$$\sigma(pp \rightarrow \tilde{H}_2^\pm \tilde{H}_2^\mp) = 0.27 \text{ (1.12) fb}, \tag{2.9}$$

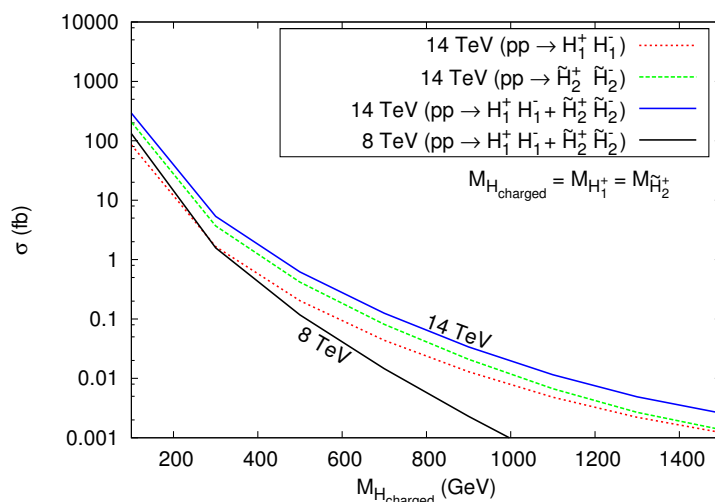


Figure 6. Production cross sections for $pp \rightarrow H_1^+ H_1^-$ and $pp \rightarrow \tilde{H}_2^+ \tilde{H}_2^-$ processes without imposing kinematic cuts.

while for singly charged scalar mass equals to 600 GeV are

$$\sigma(pp \rightarrow H_1^\pm H_1^\mp) = 0.01 \text{ (0.09) fb}, \quad (2.10)$$

$$\sigma(pp \rightarrow \tilde{H}_2^\pm \tilde{H}_2^\mp) = 0.03 \text{ (0.18) fb}, \quad (2.11)$$

with $\sqrt{s} = 8 \text{ (14) TeV}$.

Increasing center of mass energy from $\sqrt{s} = 8 \text{ TeV}$ to $\sqrt{s} = 14 \text{ TeV}$ the cross sections grow by factors $\sim 4 \div 7$, depending on masses of charged Higgs bosons. In general cross sections fall down below 0.1 fb for masses of charged scalars above approximately 730 (420) GeV for $\sqrt{s} = 14 \text{ (8) TeV}$.

2.1.2 $pp \rightarrow H_1^{++} H_1^{--}$ and $pp \rightarrow H_2^{++} H_2^{--}$

The dominant contribution to these processes is via neutral s-channel current, i.e., via Z_1 and γ . Contributions coming from s-channel H_0^0, Z_2 and H_1^0 are negligible for considered MLRSM parameters.

To explore the phenomenological aspects of the doubly charged scalars in the MLRSM model we consider two scenarios. *Scenario I* when the doubly charged scalars are degenerated in mass, i.e., $M_{H_1^{\pm\pm}} = M_{H_2^{\pm\pm}}$. This scenario is motivated by analysis of the Higgs potential (a detailed study of the Higgs potential and scalar mass spectrum will be presented elsewhere). In *Scenario II* masses are different, i.e., $M_{H_1^{\pm\pm}} \neq M_{H_2^{\pm\pm}}$.

Scenario I, degenerate mass spectrum. In our analysis we set our benchmark point with both of the doubly charged scalars at the same mass $M_{H_1^{++}} = M_{H_2^{++}} = 400 \text{ GeV}$. In this case, the cross section at the LHC without imposing any cut at $\sqrt{s} = 8 \text{ (14) TeV}$ is

$$\sigma(pp \rightarrow (H_1^{++} H_1^{--} + H_2^{++} H_2^{--}) \rightarrow \ell_i^+ \ell_i^+ \ell_j^- \ell_j^-) = 1.44 \text{ (6.06) fb}. \quad (2.12)$$

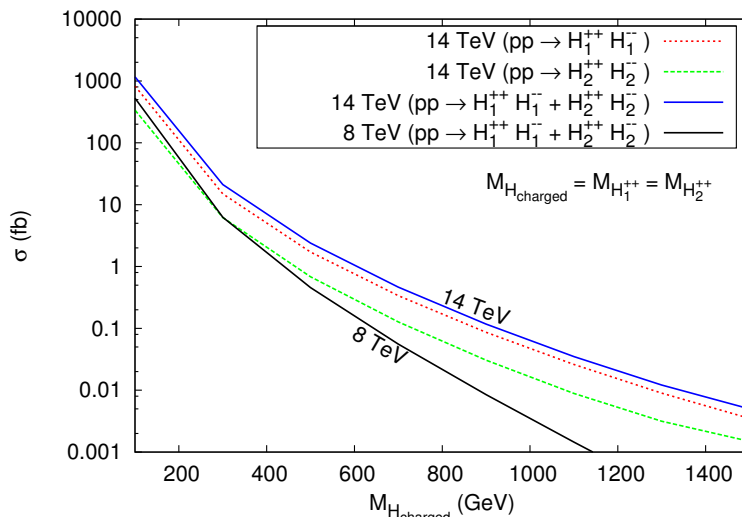


Figure 7. Scenario I. Cross sections for $pp \rightarrow H_1^{++}H_1^{--}$ and $pp \rightarrow H_2^{++}H_2^{--}$ processes without imposing kinematic cuts.

The contributions to the cross sections from two possible channels are noted for $\sqrt{s} = 8(14)$ TeV as

$$\sigma(pp \rightarrow H_1^{++}H_1^{--}) = 1.09 (4.58) \text{ fb}, \quad (2.13)$$

$$\sigma(pp \rightarrow H_2^{++}H_2^{--}) = 0.45 (1.86) \text{ fb}, \quad (2.14)$$

where $\ell_{i,j} = e, \mu$.

For $M_{H_1^{++}} = M_{H_2^{++}} = 600$ GeV it is

$$\sigma(pp \rightarrow (H_1^{++}H_1^{--} + H_2^{++}H_2^{--}) \rightarrow \ell_i^+ \ell_i^+ \ell_j^- \ell_j^-) = 0.14 (0.95) \text{ fb}, \quad (2.15)$$

for $\sqrt{s} = 8(14)$ TeV. The contributions to the cross sections from individual channels for $\sqrt{s} = 8(14)$ TeV are as following:

$$\sigma(pp \rightarrow H_1^{++}H_1^{--}) = 0.11 (0.73) \text{ fb}, \quad (2.16)$$

$$\sigma(pp \rightarrow H_2^{++}H_2^{--}) = 0.04 (0.28) \text{ fb}. \quad (2.17)$$

The cross sections for pair productions of doubly charged scalars at the LHC with 14 and 8 TeV are given in figure 7. From the figure we can see that cross sections fall very rapidly as the masses of the doubly charged scalars increase. Also the production cross section for $H_1^{\pm\pm}$ is much larger than that for $H_2^{\pm\pm}$ as shown in the figure. The cross section at $\sqrt{s} = 14(8)$ TeV for scalar masses above 920 (640) GeV is ≤ 0.1 fb.

Scenario II, non-degenerated mass spectrum. Here we choose another set of benchmark points where the doubly charged scalars are non-degenerated. The cross section for the same process with $M_{H_1^{\pm\pm}} = 400$ GeV and $M_{H_2^{\pm\pm}} = 500$ GeV at $\sqrt{s} = 14$ TeV is

$$\sigma(pp \rightarrow (H_1^{++}H_1^{--} + H_2^{++}H_2^{--}) \rightarrow \ell_i^+ \ell_i^+ \ell_j^- \ell_j^-) = 4.95 \text{ fb}. \quad (2.18)$$

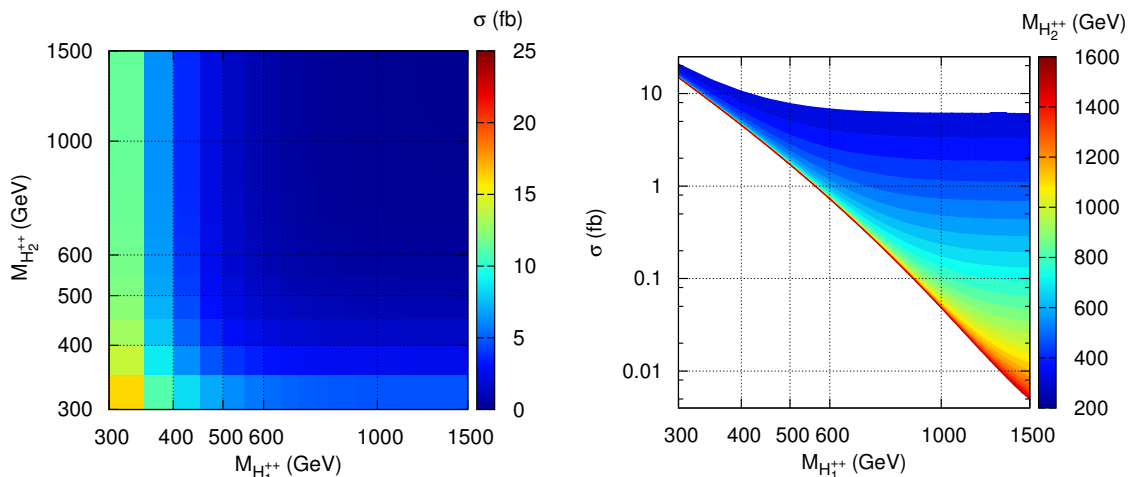


Figure 8. Scenario II. Contour plots for the $pp \rightarrow (H_1^{++}H_1^{--} + H_2^{++}H_2^{--})$ cross section. $\sqrt{s} = 14$ TeV, no kinematic cuts imposed.

The contributions to the cross sections from individual channels are given as:

$$\sigma(pp \rightarrow H_1^{++}H_1^{--}) = 1.09 (4.58) \text{ fb}, \tag{2.19}$$

$$\sigma(pp \rightarrow H_2^{++}H_2^{--}) = 0.13 (0.69) \text{ fb}, \tag{2.20}$$

for $\sqrt{s} = 8 (14)$ TeV.

Contour plots for the $pp \rightarrow (H_1^{++}H_1^{--} + H_2^{++}H_2^{--})$ cross section as a function of doubly charged scalar masses is shown in figure 8 (left). On the right figure of figure 8 different projections are used where X and Y axes are for $M_{H_1^{++}}$ and the cross section, respectively, whereas $M_{H_2^{++}}$ is projected as a contour. As can be seen from these figures, cross sections at the level of 1 fb can be obtained for doubly charged scalar masses up to approximately 600 GeV.

2.1.3 $pp \rightarrow H_1^{\pm\pm}H_1^\mp$ and $pp \rightarrow H_2^{\pm\pm}H_2^\mp$

The production of a doubly charged in association with a singly charged scalar goes through the charged s-channel interaction where $W_{1,2}^\pm$ gauge bosons are exchanged. Diagrams with s-channel exchanged singly charged scalar H_2^\pm is negligible (its coupling to W_1 is proportional to v_L which is zero). As W_2^\pm is very heavy, the dominant contribution originates from the process via W_1^\pm .

To give yet another benchmark, we set $v_R = 8$ TeV and the following charged scalar masses: $M_{H_1^{\pm\pm}} = 483$ GeV, $M_{H_2^{\pm\pm}} = 527$ GeV, $M_{H_1^\pm} = 355$ GeV, $M_{H_2^\pm} = 15066$ GeV. The choice is for the following Higgs potential parameters (for the mass formulas, see the appendix): $\rho_1 = 0.2397$, $\rho_2 = 0.0005$, $\rho_3 = 0.48$, $\lambda_1 = 0.13$, $\lambda_2 = -0.87$, $\lambda_3 = -5.17$, $\alpha_3 = 7.09$. This example shows that a wide spectrum of charged scalar masses can be easily obtained, still keeping reasonable small potential parameters (important for higher order perturbation analysis). To reduce τ channel decays, the masses for the heavy right handed neutrinos are set at 4 TeV for the first two generations and 800 GeV for the third

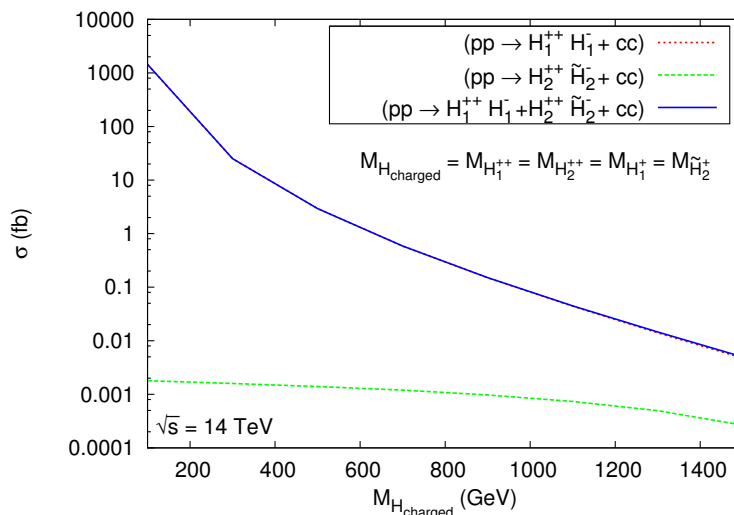


Figure 9. Production cross sections for $pp \rightarrow H_1^{++} H_1^-$ and $pp \rightarrow H_2^{++} \tilde{H}_2^-$ processes at $\sqrt{s} = 14$ TeV and no kinematic cuts are imposed. Mass of H_2^\pm is allowed to be small and denoted with a tilde.

generation, see figure 5. The cross section for the process before any kinematic cuts with centre of mass energy $\sqrt{s} = 8$ (14) TeV at the LHC is

$$\sigma(pp \rightarrow (H_1^{\pm\pm} H_1^\mp + H_2^{\pm\pm} H_2^\mp) \rightarrow \ell\ell\nu_\ell) = 1.44 (6.05) \text{ fb}. \quad (2.21)$$

The contributions to the cross sections from individual channels are noted as:

$$\sigma(pp \rightarrow H_1^{\pm\pm} H_1^\mp) = 1.48 (6.24) \text{ fb}, \quad (2.22)$$

$$\sigma(pp \rightarrow H_2^{\pm\pm} H_2^\mp) \sim 0 (0) \text{ fb}, \quad (2.23)$$

with $\sqrt{s} = 8$ (14) TeV.

For the model consistency (i.e. chosen potential parameters), the second singly charged scalar has been chosen with very high mass $M_{H_2^\pm} = 15066$ GeV. Even if it has low mass (~ 400 GeV) then also the cross section for the processes $pp \rightarrow H_2^{\pm\pm} H_2^\mp$ is very low compared to $pp \rightarrow H_1^{\pm\pm} H_1^\mp$ as $H_2^{\pm\pm} H_2^\mp W_1^\mp$ coupling is proportional to $\sin \xi$ and $H_2^{\pm\pm} H_2^\mp W_2^\mp$ coupling is proportional to $\cos \xi$. On the other hand, $H_1^{\pm\pm} H_1^\mp W_1^\mp$ coupling is proportional to $\cos \xi$ and $H_1^{\pm\pm} H_1^\mp W_2^\mp$ coupling is proportional to $\sin \xi$. In both cases W_2^\pm mediated processes are much less dominant than the W_1^\pm mediated processes. But as the charged gauge boson mixing angle ξ is neglected, the $H_2^{\pm\pm} H_2^\mp W_1^\mp$ vertex is much more suppressed compare to $H_1^{\pm\pm} H_1^\mp W_1^\mp$.

It appears that in MLRSM mixed processes, $pp \rightarrow H_1^{++} H_2^-$ and $pp \rightarrow H_2^{++} H_1^-$, vanishes as $v_L = 0$. In figure 9 the total cross section for two considered processes are given. The mass of H_2^\pm is allowed to be small and because, as discussed before, this is not natural in the MLRSM, its contribution is denoted with a tilde. Anyway, its contribution (keeping a form of its couplings as dictated by MLRSM) is negligible. Final comparison of cross sections of different processes discussed in sections 2.1.1, 2.1.2 and 2.1.3 is given in

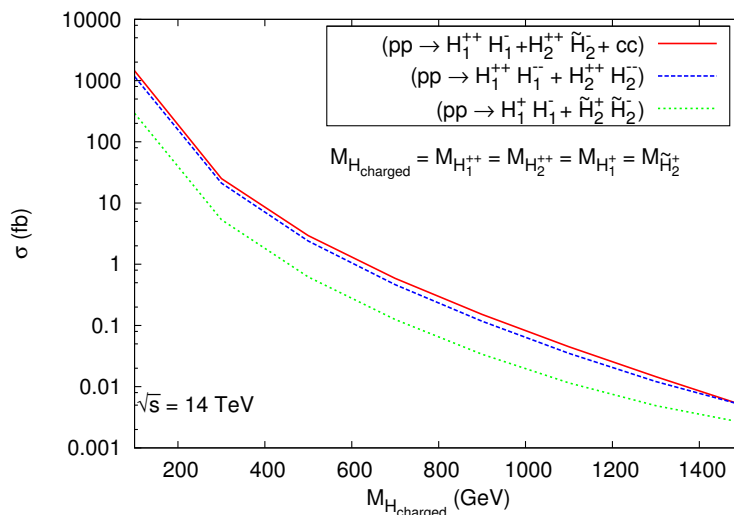


Figure 10. Summary of various MLRSM LHC production cross sections considered in the paper is shown with charged scalars at $\sqrt{s} = 14$ TeV and without kinematic cuts. We have taken degenerate mass $M_{H_{charged}}$ for $M_{H_1^{++}}$, $M_{H_2^{++}}$, $M_{H_1^+}$ and $M_{H_2^+}$.

figure 10. We can see that the largest cross sections are for a pair production of singly with doubly charged scalars, and the cross sections for production of doubly charged scalar pair is slightly lower, while the smallest cross section is for pair production of singly charged scalars. Contributions from processes where H_2^\pm is involved are negligible or at most much smaller than corresponding results where H_1^\pm is involved. Keeping in mind the status of the SM background (analysed for our purposes in section 3.3) we look for multi lepton signals for three or more leptons. Thus we focus in the following sections on the processes which involve primary production of at least one doubly charged scalar.

2.2 Primary production of a heavy Higgs and gauge bosons

2.2.1 $pp \rightarrow W_{1/2}^\mp H_{1/2}^\pm$, $pp \rightarrow Z_{1/2} H_{1/2}^\pm$ and $pp \rightarrow \gamma H_{1/2}^\pm$

In our scenarios the production cross sections for these processes are very small and can be ignored. This is because the W_2/Z_2 propagator diagrams are suppressed as they are as heavy as few TeV. For the other light propagators the scalar-gauge boson-gauge boson vertices are proportional to $\sin \xi$ and/or v_L , which are zero here.

3 Simulations and results for final lepton signals

In this paper we are interested in tri- and four-lepton signal events. To enhance such signals, suitable kinematic cuts are applied in order to decrease the SM backgrounds.

3.1 Events selection criteria

The detailed simulation criteria used in our study are following:

- The Parton Distribution Function (PDF): CTEQ6L1 [64].

- Initial selection (identification) criteria of a lepton: pseudorapidity $|\eta| < 2.5$ and p_T (transverse momentum $p_T = \sqrt{p_x^2 + p_y^2}$) of that lepton should be > 10 GeV.
- Detector efficiency for leptons:
 - ◊ For electron (either e^- or e^+) detector efficiency is 0.7 (70%);
 - ◊ For muon (either μ^- or μ^+) detector efficiency is 0.9 (90%).
- Smearing of electron energy and muon p_T are considered. All these criteria are implemented in PYTHIA and for details see [65].
- Lepton-lepton separation: the separation between any two leptons should be $\Delta R_{ll} \geq 0.2$.
- Lepton-photon separation: $\Delta R_{l\gamma} \geq 0.2$ with all the photons having $p_{T\gamma} > 10$ GeV.
- Lepton-jet separation: the separation of a lepton with all the jets should be $\Delta R_{lj} \geq 0.4$, otherwise that lepton is not counted as lepton. Jets are constructed from hadrons using PYCELL within the PYTHIA.
- Hadronic activity cut: this cut is applied to take only pure kind of leptons that have very less hadronic activity around them. Each lepton should have hadronic activity, $\frac{\sum p_{T\text{hadron}}}{p_{Tl}} \leq 0.2$ within the cone of radius 0.2 around the lepton.
- Hard p_T cuts: $p_{Tl_1} > 30$ GeV, $p_{Tl_2} > 30$ GeV, $p_{Tl_3} > 20$ GeV, $p_{Tl_4} > 20$ GeV.
- Missing p_T cut: this cut is not applied for four-lepton final states while for three-lepton case due to the presence of neutrino, a missing p_T cut (> 30 GeV) is applied.
- Z-veto⁴ is also applied to suppress the SM background. This has larger impact while reducing the background for four-lepton without missing energy.

3.2 Signal events for doubly charged Higgs particles in MLRSM

Doubly charged scalars decay mainly to either a pair of same sign charged leptons or charged gauge bosons depending on the choice of parameters. As already discussed, we have chosen the parameter space in such a way that the doubly charged scalars decay to charged leptons with almost 100% branching ratio.

This decay is lepton number violating and can also be possibly lepton flavour violating. In our scenarios we assume no lepton flavour violation as the Yukawa couplings are considered to be flavour diagonal. Thus, the four lepton final state contains two pairs of same sign and same flavoured charged leptons where each pair has opposite charges to each other. As there is no neutrino (missing energy) or jet involved it is easy to reconstruct the momentum of the final state particles. We have reconstructed invariant masses⁵ for

⁴Same flavoured but opposite sign lepton pair invariant mass $m_{\ell_1\ell_2}$ must be sufficiently away from Z_1 mass, such that, typically, $|m_{\ell_1\ell_2} - M_{Z_1}| \geq 6\Gamma_{Z_1} \sim 15$ GeV [65].

⁵The invariant mass for a lepton pair is defined as $m_{\ell_1\ell_2} = \sqrt{(E_1 + E_2)^2 - (\vec{P}_1 + \vec{P}_2)^2}$, where E_i and \vec{P}_i are the energy and three momentum of ℓ_i , respectively.

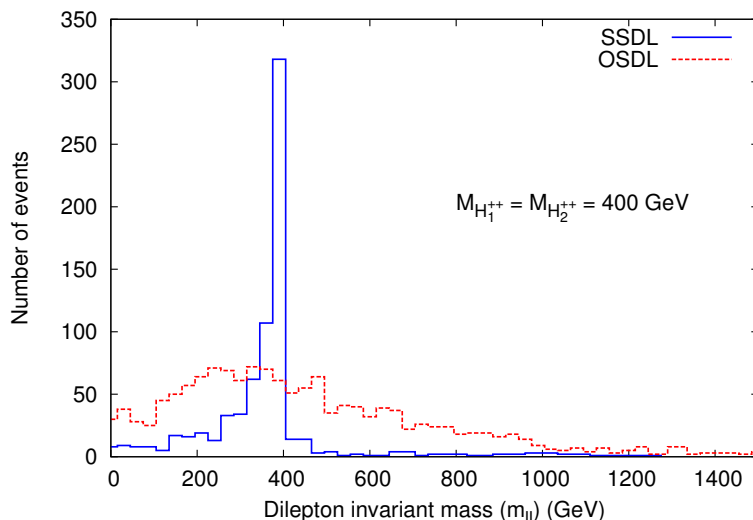


Figure 11. Invariant mass for SSDL and OSDL for $(pp \rightarrow H_{1,2}^{++} H_{1,2}^{--} \rightarrow 4l)$ with $M_{H_1^{++}} = M_{H_2^{++}} = 400$ GeV for $\sqrt{s} = 14$ TeV and $L = 300$ fb $^{-1}$. As the doubly charged scalars are degenerate in mass both the invariant mass peaks occur at the same place and thus cannot be distinguished.

same sign di-leptons (SSDL) and opposite sign di-leptons (OSDL). As the doubly charged scalars are the parents of the di-lepton pairs, invariant mass of the SSDL is expected to give a clean peak around the mass of the doubly charged scalar, which is not necessarily a case for OSDL.

3.2.1 $pp \rightarrow H_1^{++} H_1^{--}$ and $pp \rightarrow H_2^{++} H_2^{--}$

Scenario I, degenerated doubly charged mass spectrum. As calculated in section 2, eq. (2.12), if $M_{H_1^{++}} = M_{H_2^{++}} = 400$ GeV, the cross section at the LHC with centre of mass energy $\sqrt{s} = 14$ TeV is $\sigma(pp \rightarrow (H_1^{++} H_1^{--} + H_2^{++} H_2^{--}) \rightarrow \ell_i^+ \ell_i^+ \ell_j^- \ell_j^-) = 6.06$ fb, where $\ell_{i,j} = e, \mu$. After implementing all the cuts, as described in section 3.1, the four lepton events with no missing energy can be estimated. Each pair of SSDL originates from different doubly charged scalars. We have plotted the reconstructed invariant mass distributions for both SSDL and OSDL in figure 11 with anticipated integrated luminosity $L = 300$ fb $^{-1}$. As both the doubly charged scalars are degenerate the invariant mass peaks occur at around 400 GeV. *This clean reconstruction of the invariant mass is indeed possible even in the hadronic environment and can be a smoking gun feature indicating the presence of doubly charged scalars.*

We have computed this process also with centre of mass energy 8 TeV. In this case we find that the cross section, with $\sqrt{s} = 8$ TeV at the LHC, is 1.06 fb, about 6 times smaller than for $\sqrt{s} = 14$ TeV. If we take present integrated luminosity to be 25 fb $^{-1}$ then total number of the events even before all the cuts, is statistically insignificant to analyse this particular process at the LHC after implementing all the selection criteria. Thus to justify this four lepton signal for this scenario needs more data in future.

To select the doubly charged scalar signal properly and in an independent way, there is another interesting variable which can be used for determination of signals as sug-

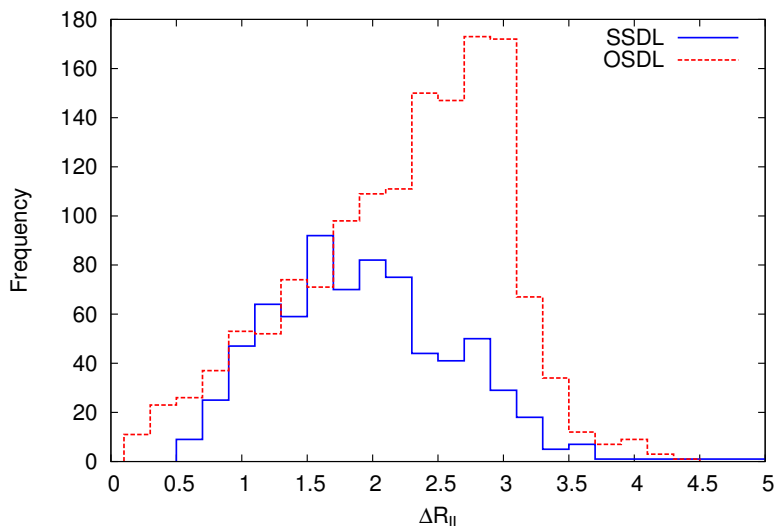


Figure 12. Lepton-lepton separations for the same sign lepton pairs ($\Delta R_{\ell\pm\ell\pm}$) and opposite sign lepton pairs ($\Delta R_{\ell\pm\ell\mp}$) for $(pp \rightarrow H_{1,2}^{++} H_{1,2}^{--} \rightarrow 4l)$ within the degenerate scenario with $M_{H_1^{++}} = M_{H_2^{++}} = 400$ GeV for $\sqrt{s} = 14$ TeV and $L = 300$ fb $^{-1}$.

gested in [62]

$$\Delta R_{\ell_1\ell_2} = \sqrt{(\eta_1 - \eta_2)^2 + (\phi_1 - \phi_2)^2}, \tag{3.1}$$

where η_i and ϕ_i denote pseudorapidity and azimuth of ℓ_i , respectively. $\Delta R_{\ell\ell}$ amounts the separation between two light charged leptons (ℓ) in azimuth-pseudorapidity plane. Its physical importance is that in the detector if $\Delta R_{\ell\ell}$ is smaller than the specified value then one can not distinguish whether the deposited energy is really by one or two leptons. So, one chooses only events for which leptons are well separated. *We expect that the leptons originated from a single doubly charged scalar will be less separated than the leptons coming from different charged scalars.* In our considered processes and decays the doubly charged scalars decay mainly into pair of same flavoured same sign leptons. Thus in a case of opposite sign di-lepton pair each of them are coming from different doubly charged scalars must be well separated. We have plotted the $\Delta R_{\ell\ell}$ distribution to address this feature. It is pretty clear from figure 12 that the distribution peaks at smaller $\Delta R_{\ell\ell}$ for same sign lepton pair while that for the oppositely charged lepton pair peaks at larger value of $\Delta R_{\ell\ell}$, as expected. This implies that most of the leptons in the SSDL pairs are less separated than the leptons which belong to the OSDL pair.

Scenario II, non degenerated doubly charged mass spectrum. Here we choose another set of benchmark points where the doubly charged scalars are non-degenerate. In section 2, eq. (2.18), the cross section at $\sqrt{s} = 14$ TeV has been calculated for the same process with $M_{H_1^{\pm\pm}} = 400$ GeV and $M_{H_2^{\pm\pm}} = 500$ GeV, $\sigma = 4.95$ fb. As $M_{H_2^{\pm\pm}} > M_{H_1^{\pm\pm}}$, the production cross section for $H_1^{\pm\pm}$ is much larger than that for $H_2^{\pm\pm}$. *Thus the four lepton events will be generated mostly from the leptonic decays of the $H_1^{\pm\pm}$ pair than $H_2^{\pm\pm}$ decays.* This statement is very distinctively clear from the invariant mass distributions

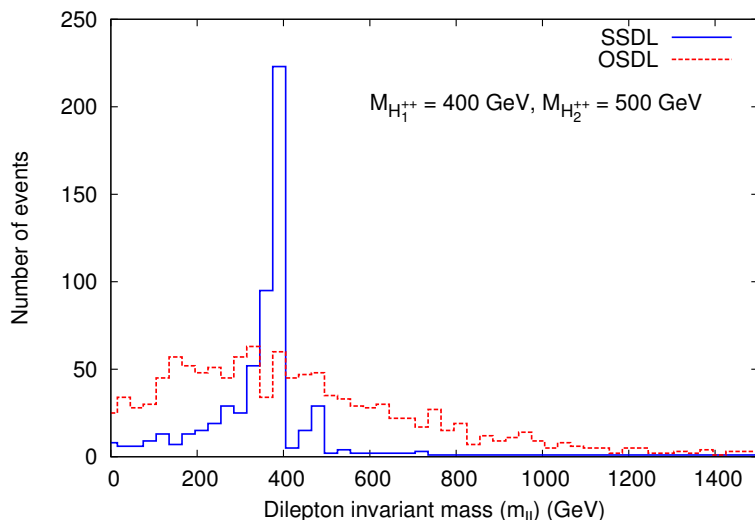


Figure 13. Invariant mass for SSDL and OSDL signals in the $(pp \rightarrow H_{1,2}^{++} H_{1,2}^{--} \rightarrow 4l)$ process in the non-degenerate mass scenario with $M_{H_1^{\pm\pm}} = 400$ GeV and $M_{H_2^{\pm\pm}} = 500$ GeV for $\sqrt{s} = 14$ TeV and $L = 300 \text{ fb}^{-1}$.

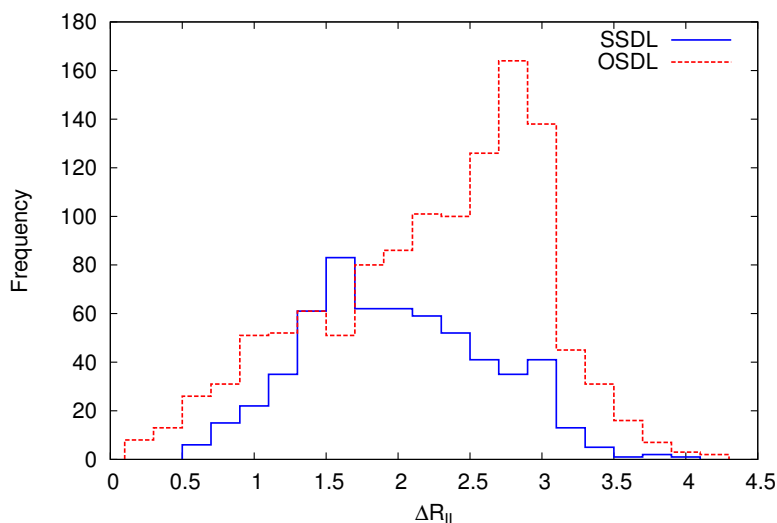


Figure 14. Lepton-lepton separations for same sign lepton pairs ($\Delta R_{\ell\pm\ell\pm}$) and opposite sign lepton pairs ($\Delta R_{\ell\pm\ell\mp}$) in the $(pp \rightarrow H_{1,2}^{++} H_{1,2}^{--} \rightarrow 4l)$ process for non-degenerate mass scenario having $M_{H_1^{\pm\pm}} = 400$ GeV and $M_{H_2^{\pm\pm}} = 500$ GeV with $\sqrt{s} = 14$ TeV and $L = 300 \text{ fb}^{-1}$.

of the same sign di-leptons, as shown in the figure 13. Maximum number of same dilepton events are with an invariant mass peak around $M_{H_1^{\pm\pm}} = 400$ GeV and that around $M_{H_2^{\pm\pm}} = 500$ GeV is much smaller, as expected.

We also performed the $\Delta R_{\ell\ell}$ distribution for the same benchmark point. For the same reason as explained before our expectation is reflected in figure 14.

3.2.2 $pp \rightarrow H_1^{\pm\pm} H_1^\mp$ and $pp \rightarrow H_2^{\pm\pm} H_2^\mp$

These processes lead to the tri-lepton events with missing p_T , see table 1. For chosen MLRSM parameters, eq. (2.21), the cross section for the process $pp \rightarrow (H_1^{\pm\pm} H_1^\mp + H_2^{\pm\pm} H_2^\mp) \rightarrow \ell\ell\nu_\ell$ before cuts with centre of mass energy $\sqrt{s} = 14$ TeV is $\sigma = 6.05$ fb. The tri-lepton events can be classified into two categories: either $\ell^+\ell^+\ell^-$ or $\ell^-\ell^-\ell^+$. The first and second types of signals are originated from W_1^+ and W_1^- mediated processes, respectively. Thus, it is indeed possible to estimate the charge asymmetry, define as the ratio of the number of events of $\ell^+\ell^+\ell^-$ type to the number of events of $\ell^-\ell^-\ell^+$ type at the LHC. This is very similar to the forward-backward asymmetry at Tevatron. This charge asymmetry depends on Parton Distribution Functions (PDF) and thus is a special feature of LHC. We have estimated this ratio (R_\pm^+) with the above choices of charged scalar masses with $\sqrt{s} = 14$ TeV and integrated luminosity 300 fb^{-1} . We find 554 tri-lepton signal events after all the cuts and that leads to

$$R_\pm^+ = \frac{\# \text{ of events for } \ell^+\ell^+\ell^-}{\# \text{ of events for } \ell^-\ell^-\ell^+} = \frac{396}{158} \simeq 2.51. \quad (3.2)$$

In SM the corresponding value calculated for the main processes given in the next section in table 2 is $(R_\pm^+)_{\text{SM}} = \frac{17.751}{14.962} = 1.186$. This value is slightly different from the calculated values in [66] where higher order corrections are taken into account and the specific kinematic cuts are different. Nevertheless, MLRSM value given in eq. (3.2) differs substantially from its SM counterpart to signify its presence.

As discussed in section 2, the $H_2^{\pm\pm} H_2^\mp W_1^\mp$ vertex is much more suppressed compare to $H_1^{\pm\pm} H_1^\mp W_1^\mp$. Thus, in this case most of the tri-lepton events are originated from $pp \rightarrow H_1^{\pm\pm} H_1^\mp$ process. This is clearly visible from the invariant mass distributions. Here we have plotted the same and opposite sign di-lepton invariant mass distributions, see figure 15. As similar to the earlier discussions *in the opposite sign lepton pairs two leptons have different origin thus their invariant mass distribution is continuous while the same sign di-lepton invariant mass distributions always peak around the mass of the doubly charged scalars.*

Here, from figure 15, it is distinctly seen that the significant amount of same sign di-lepton pair peaks at $M_{H_1^{\pm\pm}} = 483$ GeV rather than $M_{H_2^{\pm\pm}} = 527$ GeV. This implies that the dominant contribution to this tri-lepton events are generated through $pp \rightarrow H_1^{\pm\pm} H_1^\mp$ process (cf. figure 9) and the further leptonic decays of the charged scalars.

In the figure 16, separations between leptons are plotted. As can be seen from this figure the SSDL separations peak at lower value of $\Delta R_{\ell\ell}$, while OSDL separations peak at larger value of $\Delta R_{\ell\ell}$. This is because same-sign leptons pair has the origin from the same mother, while opposite sign leptons pair has both the leptons from different mothers.

For $\sqrt{s} = 8$ TeV and the same benchmark point the production cross section $\sigma(pp \rightarrow (H_1^{\pm\pm} H_1^\mp + H_2^{\pm\pm} H_2^\mp) \rightarrow \ell\ell\nu_\ell) = 1.44$ fb is about four times smaller than for $\sqrt{s} = 14$ TeV, eq. (2.21). With an integrated luminosity 25 fb^{-1} at $\sqrt{s} = 8$ TeV and 300 fb^{-1} at $\sqrt{s} = 14$ TeV, total number of events is about 50 times smaller in the former case, so the difference is substantial.

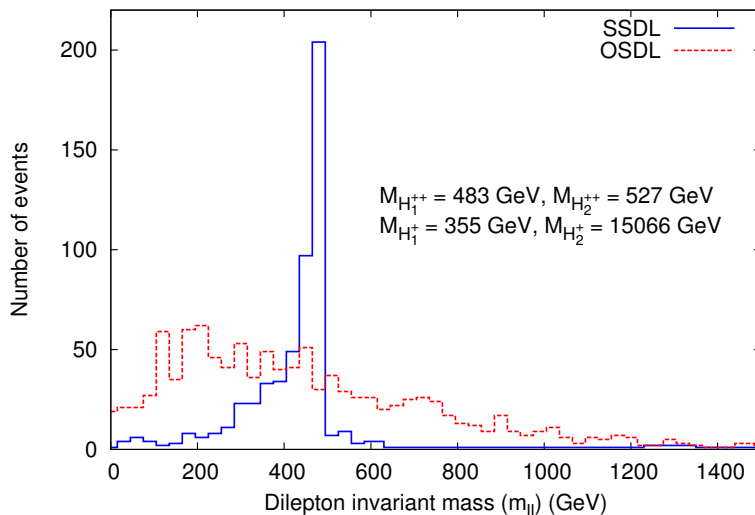


Figure 15. Invariant mass plots for SSDL and OSDL for the signals $\ell^\pm\ell^\pm\ell^\mp + \text{missing } p_T$, at the LHC with $\sqrt{s} = 14 \text{ TeV}$ and integrated luminosity 300 fb^{-1} .

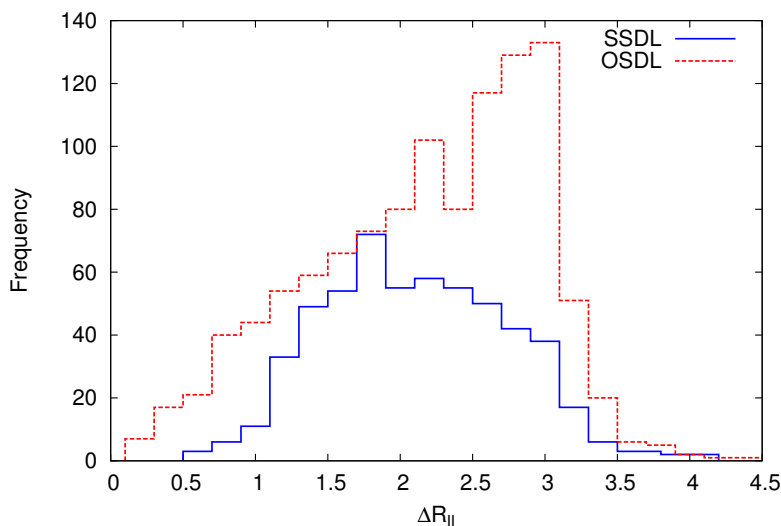


Figure 16. Lepton-lepton separation plot for same sign leptons ($\Delta R_{\ell^\pm\ell^\pm}$) and opposite sign leptons ($\Delta R_{\ell^\pm\ell^\mp}$) in the process $(pp \rightarrow (H_1^{\pm\pm}H_1^\mp + H_2^{\pm\pm}H_2^\mp) \rightarrow 3\ell)$. Here $\sqrt{s} = 14 \text{ TeV}$ and integrated luminosity 300 fb^{-1} at the LHC.

Distributions presented so far show that it is possible to extract clear signals for doubly charged scalars at the LHC. However, for signal identification crucial is how large the SM background effects are and the significance too.

3.3 Background estimation and significance of signals

Kinematic cuts are used which have been investigated and established for the first time in [65]. The cuts are optimised in a way such that we can reduce the SM background

<i>Processes</i>	3 ℓ (fb)	$\ell^+\ell^+\ell^-$ (fb)	$\ell^-\ell^-\ell^+$ (fb)	4 ℓ (fb)
$t\bar{t}$	18.973	9.522	9.451	–
$t\bar{t}(Z/\gamma^*)$	1.103	0.549	0.552	0.0816
$t\bar{t}W^\pm$	0.639	0.422	0.214	–
$W^\pm(Z/\gamma^*)$	10.832	6.664	4.164	–
$(Z/\gamma^*)(Z/\gamma^*)$	1.175	0.594	0.581	0.0362
<i>TOTAL</i>	32.722	17.751	14.962	0.1178

Table 2. Dominant Standard Model background contributions (in fb) for tri- and four-lepton signals at the LHC with $\sqrt{s} = 14$ TeV after obeying suitable selection criteria defined in the text. The $t\bar{t}$ cross section is presented here after the inclusion of k-factor. While computing the SM contributions to 4 ℓ final state, no missing p_T cut has been applied.

and enhance the signal events.⁶ Standard Model background cross sections for tri- and four-lepton signals are given in table 2. In this table we have also separately computed the backgrounds for $\ell^+\ell^+\ell^-$ and $\ell^-\ell^-\ell^+$.

In principal the tri-lepton contributions can come also from $H_1^{++}H_1^{--}$ and $H_2^{++}H_2^{--}$ involved processes if during simulations one of the four-leptons does not satisfy the cuts. But in our case this contribution is negligible due to the extra missing energy cut applied as one of the gate pass for the tri-lepton events. Thus all the productions together are considered and all the intermediate particles are allowed to decay. After passing through the cuts, tri-lepton and four-lepton events are counted.

In table 3 we present the total background and signal events for 25 and 300 fb⁻¹ integrated luminosities. It is clear that four-lepton signals are well beyond the SM background. The tri-lepton signal is also very prominent over the background (what matters is the signal excess over the background fluctuations). To see it properly, in table 4 the significance of different signals is shown.

Assuming the significance at the level of 5 as a comfortable discovery limit, we can see that LHC will be in the next run sensitive to masses of MLRSM doubly charged Higgs bosons up to approximately 600 GeV.

4 MLRSM charged Higgs bosons contribution to $H_0^0 \rightarrow \gamma\gamma$

In LR symmetric models there are (singly-, doubly-) charged scalars and charged gauge boson (W_2^\pm) which couple to photons and hence they can contribute to $H_0^0 \rightarrow \gamma\gamma$ channel where H_0^0 is the SM-like neutral Higgs taken to be 125 GeV. Since W_2^\pm are heavy, their

⁶In our analysis while computing the tri-lepton events (signal and background), the p_T of the third hardest lepton needs to be greater than 20 GeV, and also a missing p_T cut (> 30 GeV) must be satisfied, see section 3.1. Thus the tri-lepton background for process like $t\bar{t}$ where one of the lepton is coming from semi-leptonic decays of B 's is reduced. Here the hadronic activity cut also reduces the hadronic activity around the selected leptons and plays a crucial role in this case. All these cuts reduces the efficiency of misidentification of b-jets as leptons. In our case this is less than 0.05%.

<i>Luminosity</i>	Background 3 ℓ events	Signal 3 ℓ events	Background 4 ℓ events	Signal 4 ℓ events	
				scenario I	scenario II
25 fb $^{-1}$	797.5	46.2	2.9	(i) 30 (ii) 4.4	24.8
300 fb $^{-1}$	9569.7	554	34.8	(i) 360 (ii) 53	298

Table 3. Number of background and signal events at 25 fb $^{-1}$ and 300 fb $^{-1}$ as an anticipated integrated luminosity at next 14 TeV run of LHC. The tri-lepton signal is computed for following charged scalar masses: $M_{H_1^{\pm\pm}} = 483$ GeV, $M_{H_2^{\pm\pm}} = 527$ GeV, $M_{H_1^\pm} = 355$ GeV, $M_{H_2^\pm} = 15066$ GeV. Scenario I reflects degeneracy of doubly charged scalar masses with (i) $M_{H_1^{\pm\pm}} = M_{H_2^{\pm\pm}} = 400$ GeV and (ii) $M_{H_1^{\pm\pm}} = M_{H_2^{\pm\pm}} = 600$ GeV, while Scenario II realises their non-degenerate spectrum, namely $M_{H_1^{\pm\pm}} = 400$ and $M_{H_2^{\pm\pm}} = 500$ GeV. Here we have used the same kinematical cuts as applied while estimating the SM background events. We have not implemented other extra cuts, like invariant mass ($m_{\ell\ell}$) and lepton separation ($\Delta R_{\ell\ell}$) to estimate the signal and background events in this table.

Significance	3 ℓ events	4 ℓ events	
		scenario I	scenario II
S/\sqrt{B}	5.66	(i) NA (ii) NA	NA
$S/\sqrt{(S+B)}$	5.51	(i) 18.11 (ii) 5.65	16.34

Table 4. The significance of the signals given in table 3 is given using two definitions of significance: (i) S/\sqrt{B} , and (ii) $S/\sqrt{(S+B)}$, where S and B are the total number of signal and background events for 300 fb $^{-1}$ integrated luminosity, respectively. The parameters are the same as given in table 3. Here ‘NA’ implies that S/\sqrt{B} can not be used as the definition of significance in these cases as $S \ll B$ is not justified.

contributions are suppressed compared to charged scalars, so we look for charged scalar contributions. They contribute to the channel via a loop shown in the figure 17.

Following [67–69] we can write the enhancement factor for this channel, which is nothing but a ratio of partial decay width in the new model to that in the SM

$$R_{\gamma\gamma} = \left| 1 + \sum_{S=H_{1,2}^{\pm\pm}, H_1^\pm} Q_S^2 \frac{c_S}{2} \frac{k_+^2}{M_S^2} \frac{A_0(\tau_S)}{A_1(\tau_{W_1}) + N_c Q_t^2 A_{1/2}(\tau_t)} \right|^2. \quad (4.1)$$

In the above equation Q_S is electric charge of charged scalars in unit of e , M_S is a mass of scalars. N_c is colour factor which is 1 for colour singlet scalars and $\tau_i = 4m_i^2/m_{H_0^0}^2$ ($i = W_1, t, S$). c_S are the coupling of the Higgs boson with the charged scalars and $k_+ = \sqrt{k_1^2 + k_2^2}$ where k_1, k_2 are the vacuum expectation values of the bi-doublet. The expressions

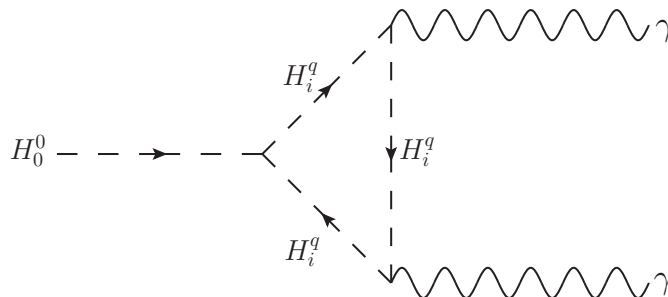


Figure 17. Charged scalar contribution to the $H_0^0 \rightarrow \gamma\gamma$ channel at the LHC. In the loop there are three contributions coming from the charged scalars $H_i^q \equiv H_1^{\pm\pm}, H_2^{\pm\pm}, H_1^\pm$. In MLRSM H_2^\pm is very heavy and its contribution is negligible.

for c_S are as follows

$$c_{H_0^0 H_1^+ H_1^-} = - \left[\frac{2\alpha_1 k_+^2 + 8\alpha_2 k_1 k_2 + \alpha_3 (k_+^2)}{2k_+^2} \right], \tag{4.2}$$

$$c_{H_0^0 H_1^{++} H_1^{--}} = - \left[\frac{\alpha_1 k_+^2 + k_1 (4\alpha_2 k_2 + \alpha_3 k_1)}{k_+^2} \right], \tag{4.3}$$

$$c_{H_0^0 H_2^{++} H_2^{--}} = - \left[\frac{\alpha_1 k_+^2 + k_1 (4\alpha_2 k_2 + \alpha_3 k_1)}{k_+^2} \right]. \tag{4.4}$$

Here the parameters that are involved in the above eqs. (4.2)–(4.4), are contained in the scalar potential and following the convention as suggested in [36].

$A_{1/2}, A_1$ and A_0 are loop functions for fermions, vector bosons and scalars respectively, given as

$$A_{1/2}(x) = 2x^2 [x^{-1} + (x^{-1} - 1)f(x^{-1})], \tag{4.5}$$

$$A_1(x) = -x^2 [2x^{-2} + 3x^{-1} + 3(2x^{-1} - 1)f(x^{-1})], \tag{4.6}$$

$$A_0(x) = -x^2 [x^{-1} - f(x^{-1})]. \tag{4.7}$$

For the SM-like Higgs mass below threshold, i.e., $m_{H_0^0} < 2m_{\text{loop}}$ (m_{loop} is a mass of a particle in the loop) $f(x) = \text{arcSin}^2(\sqrt{x})$.

In figure 18 we present a contour plot to grab the contributions from the charged scalars to $R_{\gamma\gamma}$. We have assumed $M_{H_1^{++}} = M_{H_1^+}$ to reduce number of free parameters.

Experimental observations of the Higgs to di-photon decay normalised to the SM prediction, as pointed out by ATLAS and CMS is given as in [70, 71]:

$$R_{\gamma\gamma} = 1.65 \pm 0.24 \text{ (stat)}_{-0.18}^{+0.25} \text{ (syst)} \quad \text{(ATLAS)}, \tag{4.8}$$

$$R_{\gamma\gamma} = 0.78_{-0.26}^{+0.28} \quad \text{(CMS)}. \tag{4.9}$$

As errors are still very large, it is too early to make any conclusive remarks on these results, especially that tendency seems to be that anomaly systematically approaches 1. However, MLRSM can accommodate wide range of $R_{\gamma\gamma}$ values by the charged Higgs boson effects, for related discussions, see e.g. in [72].

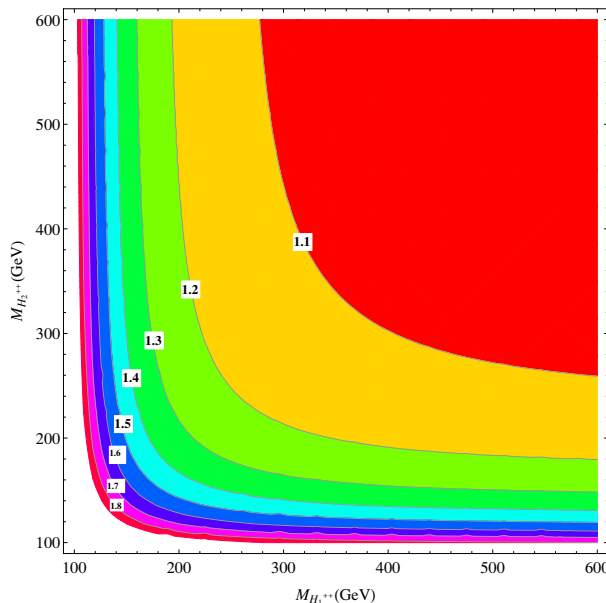


Figure 18. $R_{\gamma\gamma}$ with the variation of charged scalar masses.

5 Conclusions and outlook

After discovery of the SM-like neutral Higgs boson in July 2012 at the LHC, the next big issue is what is the actual shape of the Higgs potential. Thus a question is asked to reveal the further query regarding possible gauge symmetry behind the existence of elementary Higgs boson. Here we have concentrated on studies connected with LHC potential discovery of charged Higgs bosons within classical MLRSM which is already phenomenologically rich enough and worth of separate investigations. Though different low energy data and the LHC exclusion plots constrain already W_2 and Z_2 very much, still the charged scalars can be relatively light. It has been shown which of singly and doubly charged Higgs bosons can be light, in agreement with FCNC limits on neutral Higgs bosons particles, as both charged and neutral scalar sectors are connected through the Higgs potential parameters. They can be produced at the LHC with non-negligible cross sections. However, their production cross sections decrease rapidly with their masses, that is why we have undertaken here more detailed and systematic studies including the production and decays of charged scalars. We have concentrated on the single and pair production of doubly charged scalars. We have chosen the benchmark points in such a way that signals connected with doubly charged scalars can dominate over non-standard signals coming from both heavy gauge and neutral Higgs bosons. We have analysed the four-lepton and tri-lepton signals at the LHC. As a rule of thumb, for all considered processes with doubly charged scalars cross sections are about 1 fb for their masses in vicinity of $400 \div 500$ GeV, which is about the present lowest limit on their masses. If planned integrated luminosity in the next LHC run at $\sqrt{s} = 14$ TeV is about 10 times larger than present values, clear signals with four-leptons without missing energy and tri-lepton signals can be detected. It will be an indication

for doubly charged scalar effects. These multi lepton final states possess very small SM background. We have shown that MLRSM model can give such signals for doubly charged masses up to approximately 600 GeV. In our analysis we have used the di-lepton invariant mass and lepton-lepton separation distributions. We also estimate the amount of charge asymmetry in signal as well as background events, and show that this might be a smoking gun feature for future discovery. The same and opposite sign charged lepton signals have been analysed using proper kinematic cuts and the clear impact of doubly charged scalars are noted carefully.

Finally, as in the Left-Right symmetric models charged gauge bosons are very heavy, they do not contribute significantly to the Higgs to di-photon process, however, the relatively light charged scalars can contribute easily. We have incorporated the impact of the light charged scalars in this process and estimated the strength of this contribution over the SM one.

As an outlook, several interesting things can still be done, e.g.

1. More detailed comparison studies including also lepton spin correlations and their angular distributions with other non-standard models where doubly charged scalars exist (e.g. Higgs Triplet Model [73]);
2. Studies of dedicated distributions for processes involving doubly charged Higgs bosons with both jets and missing energy;
3. Theoretical studies of general Higgs potentials which can realise relatively light charged Higgs bosons keeping at the same time a few TeV scale of neutral Higgs bosons (e.g. [48]);
4. To release theoretical assumptions on equality of left and right gauge boson couplings, diagonal neutrino light-heavy mixings and possible see-saw scenarios, take into account relations between model parameters in the Higgs, gauge and neutrino sectors, e.g. [11].

In summary, we are in a very exciting moment and the next LHC run should be decisive if our scenario with relatively light charged Higgs bosons can be realised. Still there is a room for Left-Right gauge symmetry signals discovery at the LHC, including MLRSM doubly charged Higgs bosons effects as long as long as their masses will be well below 1 TeV range ($m_{H_{1/2}^{\pm\pm}} \leq 600$ GeV).

Acknowledgments

Work of JC is supported by Department of Science & Technology, Government of INDIA under the Grant Agreement number IFA12-PH-34 (INSPIRE Faculty Award). Work of MK is supported by the Świder fellowship. Work of JG is supported by the Research Executive Agency (REA) of the European Union under the Grant Agreement number PITN-GA-2010-264564 (LHCPhenoNet). Work of RS is supported by Science and Engineering Research Canada (NSERC).

A Reconciling FCNC effects and large v_R with relatively light charged Higgs mass spectrum within MLRSM

A scan of potential parameters based on the numerical diagonalisation and minimisation of the complete MLRSM Higgs potential within our own implementation of the FeynRules package [46] has been performed. This leads to the figure 1. Here, just for illustration, we discuss it in a simplified form based on approximations discussed in [74]. In MLRSM there is one neutral SM-like Higgs boson having mass proportional to the vacuum expectation value (VEV) κ_1 (\sim electro-weak breaking scale). The other Higgs bosons are much heavier. A natural mass scale for them is driven by v_R which decides about the $SU(2)_R \otimes U(1)_{B-L}$ breaking scale. As discussed in the main text of the paper, we assume large v_R (~ 8 TeV), to be consistent with the experimental constraints.

The minimisation and diagonalisation of the MLRSM Higgs potential have been investigated in [35] and explicit correlations among physical and unphysical scalar fields are given in [74]. For the sake of completeness, here we have depicted them along with their mass relations considering $\kappa_2 = 0$:

- masses

$$M_{H_0^0}^2 \simeq 2\kappa_1^2 \lambda_1, \tag{A.1}$$

$$M_{H_1^0}^2 \simeq \frac{1}{2} \alpha_3 v_R^2, \tag{A.2}$$

$$M_{H_2^0}^2 \simeq 2\rho_1 v_R^2, \quad M_{H_3^0}^2 \simeq \frac{1}{2} v_R^2 (\rho_3 - 2\rho_1), \tag{A.3}$$

$$M_{A_1^0}^2 \simeq \frac{1}{2} \alpha_3 v_R^2 - 2\kappa_1^2 (2\lambda_2 - \lambda_3), \tag{A.4}$$

$$M_{A_2^0}^2 \simeq \frac{1}{2} v_R^2 (\rho_3 - 2\rho_1), \tag{A.5}$$

$$M_{H_1^\pm}^2 \simeq \frac{1}{2} v_R^2 (\rho_3 - 2\rho_1) + \frac{1}{4} \alpha_3 \kappa_1^2, \quad M_{H_2^\pm}^2 \simeq \frac{1}{2} \alpha_3 \left[v_R^2 + \frac{1}{2} \kappa_1^2 \right], \tag{A.6}$$

$$M_{H_1^{\pm\pm}}^2 \simeq \frac{1}{2} [v_R^2 (\rho_3 - 2\rho_1) + \alpha_3 \kappa_1^2], \quad M_{H_2^{\pm\pm}}^2 \simeq 2\rho_2 v_R^2 + \frac{1}{2} \alpha_3 \kappa_1^2. \tag{A.7}$$

- relations among physical and unphysical fields (“G” stands for Goldstone modes)

$$\phi_1^0 \simeq \frac{1}{\sqrt{2}} [H_0^0 + i\tilde{G}_1^0], \tag{A.8}$$

$$\phi_2^0 \simeq \frac{1}{\sqrt{2}} [H_1^0 - iA_1^0], \tag{A.9}$$

$$\delta_R^0 = \frac{1}{\sqrt{2}} (H_2^0 + iG_2^0), \quad \delta_L^0 = \frac{1}{\sqrt{2}} (H_3^0 + iA_2^0), \tag{A.10}$$

$$\delta_L^+ = H_1^+, \quad \delta_R^+ \simeq G_R^+, \tag{A.11}$$

$$\phi_1^+ \simeq H_2^+, \quad \phi_2^+ \simeq G_L^+, \tag{A.12}$$

$$\delta_R^{\pm\pm} = H_1^{\pm\pm}, \quad \delta_L^{\pm\pm} = H_2^{\pm\pm}. \tag{A.13}$$

As masses of quarks are non-degenerate, FCNC effects appear through the A_0 part of the following Lagrangian [36]

$$L_{\text{quark-Higgs}}(u, d) = -\bar{U} [P_L(M_{\text{diag}}^u B_0^* + U^{\text{CKM}} M_{\text{diag}}^d U^{\text{CKM}\dagger} A_0) + P_R(M_{\text{diag}}^u B_0 + U^{\text{CKM}} M_{\text{diag}}^d U^{\text{CKM}\dagger} A_0^*)] U, \quad (\text{A.14})$$

where A_0 is a linear combination of neutral physical Higgs and Goldstone fields connected with a bi-doublet Φ [35], and taking into account eq. (A.9), we finally have

$$A_0 = \sqrt{2}(\kappa_1 \phi_2^0) = (H_1^0 - iA_1^0). \quad (\text{A.15})$$

To suppress the effects connected with these fields [7, 28, 75–77], their masses needs to be at least ~ 10 TeV. In our analysis we have kept them to be ~ 15 TeV:

$$m_{H_1^0}, m_{A_1^0} > 15 \text{ TeV}. \quad (\text{A.16})$$

It can be easily shown that for defined masses of Higgs bosons, see eqs. (A.2)–(A.7), we can find parameters of the MLRSM Higgs potential within the perturbative limit, and simultaneously satisfy the light charged Higgs bosons and eq. (A.16). This can be achieved even after keeping three charged Higgs bosons $H_1^{\pm\pm}$, $H_2^{\pm\pm}$, H_1^\pm relatively light. For instance, with $v_R = 8$ TeV and $\kappa_1 = 246$ GeV we find the scalar spectrum (in GeV)

$$M_{H_0^0} = 125, \quad (\text{A.17})$$

$$M_{H_1^0} = 15062, \quad M_{H_2^0} = 11313, \quad M_{H_3^0} = 505, \quad (\text{A.18})$$

$$M_{A_1^0} = 15066, \quad (\text{A.19})$$

$$M_{A_2^0} = 505, \quad (\text{A.20})$$

$$M_{H_1^\pm} = 602, \quad M_{H_2^\pm} = 15066, \quad (\text{A.21})$$

$$M_{H_1^{\pm\pm}} = 685, \quad M_{H_2^{\pm\pm}} = 463, \quad (\text{A.22})$$

where

$$\rho_1 = 1, \quad \rho_2 = 0, \quad \rho_3 = 2.008, \quad (\text{A.23})$$

$$\lambda_1 = 0.13, \quad \lambda_2 = 0, \quad \lambda_3 = 1, \quad (\text{A.24})$$

$$\alpha_3 = 7.09. \quad (\text{A.25})$$

We can see that the remaining fourth charged Higgs boson H_2^\pm in MLRSM is naturally very heavy. To make it light, one needs to go beyond MLRSM and incorporate new terms in the scalar potential which would affect MLRSM Higgs boson masses.⁷

⁷Let us imagine that an additional intermediate energy scale is introduced connected with VEV of an additional $SU(2)_L$ and $SU(2)_R$ singlet scalar field (such scalars give for instance heavy neutrino Majorana mass terms but they decouple from other low energy phenomenological effects). If this scalar couple to the MLRSM right handed triplet fields, it would modify eqs. (A.6), (A.7) but because of its large VEV, mixing of MLRSM Higgs scalars with this state would be negligible, so the effective couplings of MLRSM Higgs bosons, including H_2^\pm , would stay the same.

Open Access. This article is distributed under the terms of the Creative Commons Attribution License ([CC-BY 4.0](https://creativecommons.org/licenses/by/4.0/)), which permits any use, distribution and reproduction in any medium, provided the original author(s) and source are credited.

References

- [1] R.N. Mohapatra and J.C. Pati, *A natural left-right symmetry*, *Phys. Rev. D* **11** (1975) 2558 [[INSPIRE](#)].
- [2] G. Senjanović and R.N. Mohapatra, *Exact left-right symmetry and spontaneous violation of parity*, *Phys. Rev. D* **12** (1975) 1502 [[INSPIRE](#)].
- [3] M. Nemevšek, F. Nesti, G. Senjanović and Y. Zhang, *First limits on left-right symmetry scale from LHC data*, *Phys. Rev. D* **83** (2011) 115014 [[arXiv:1103.1627](#)] [[INSPIRE](#)].
- [4] A. Ferrari et al., *Sensitivity study for new gauge bosons and right-handed Majorana neutrinos in pp collisions at $\sqrt{s} = 14$ TeV*, *Phys. Rev. D* **62** (2000) 013001 [[INSPIRE](#)].
- [5] M. Frank, A. Hayreter and I. Turan, *Top quark pair production and asymmetry at the Tevatron and LHC in left-right models*, *Phys. Rev. D* **84** (2011) 114007 [[arXiv:1108.0998](#)] [[INSPIRE](#)].
- [6] S.P. Das, F.F. Deppisch, O. Kittel and J.W.F. Valle, *Heavy neutrinos and lepton flavour violation in left-right symmetric models at the LHC*, *Phys. Rev. D* **86** (2012) 055006 [[arXiv:1206.0256](#)] [[INSPIRE](#)].
- [7] J. Chakraborty, J. Gluza, R. Sevvilano and R. Szafron, *Left-right symmetry at LHC and precise 1-loop low energy data*, *JHEP* **07** (2012) 038 [[arXiv:1204.0736](#)] [[INSPIRE](#)].
- [8] C.-H. Lee, P.S. Bhupal Dev and R.N. Mohapatra, *Natural TeV-scale left-right seesaw for neutrinos and experimental tests*, *Phys. Rev. D* **88** (2013) 093010 [[arXiv:1309.0774](#)] [[INSPIRE](#)].
- [9] X.-G. He and G. Valencia, *B decays with τ -leptons in non-universal left-right models*, *Phys. Rev. D* **87** (2013) 014014 [[arXiv:1211.0348](#)] [[INSPIRE](#)].
- [10] PARTICLE DATA GROUP collaboration, J. Beringer et al., *Review of particle physics*, *Phys. Rev. D* **86** (2012) 010001 [[INSPIRE](#)].
- [11] M. Czakon, J. Gluza and M. Zralek, *Low-energy physics and left-right symmetry: bounds on the model parameters*, *Phys. Lett. B* **458** (1999) 355 [[hep-ph/9904216](#)] [[INSPIRE](#)].
- [12] CMS collaboration, *Search for narrow resonances using the dijet mass spectrum with 19.6fb^{-1} of pp collisions at $\sqrt{s} = 8$ TeV*, *CMS-PAS-EXO-12-059* (2013).
- [13] CMS collaboration, *Search for resonances in the dilepton mass distribution in pp collisions at $\sqrt{s} = 8$ TeV*, *CMS-PAS-EXO-12-061* (2013).
- [14] ATLAS collaboration, *Search for new phenomena in the dijet mass distribution updated using 13.0fb^{-1} of pp collisions at $\sqrt{s} = 8$ TeV collected by the ATLAS detector*, *ATLAS-CONF-2012-148*, ATLAS-COM-CONF-2012-180 (2012).
- [15] ATLAS collaboration, *Search for $W' \rightarrow t\bar{b}$ in proton-proton collisions at a centre-of-mass energy of $\sqrt{s} = 8$ TeV with the ATLAS detector*, *ATLAS-CONF-2013-050*, ATLAS-COM-CONF-2013-022 (2013).

- [16] ATLAS collaboration, *Search for high-mass dilepton resonances in 20fb^{-1} of pp collisions at $\sqrt{s} = 8\text{ TeV}$ with the ATLAS experiment*, [ATLAS-CONF-2013-017](#), ATLAS-COM-CONF-2013-010 (2013).
- [17] CMS collaboration, *Search for a heavy neutrino and right-handed W of the left-right symmetric model in pp collisions at 8 TeV* , [CMS-PAS-EXO-12-017](#) (2012).
- [18] CMS collaboration, *Searches for new physics with leptons and/or jets at CMS*, [CMS-CR-2013-155](#) (2013) [[arXiv:1307.2168](#)] [[INSPIRE](#)].
- [19] LEP HIGGS WORKING GROUP FOR HIGGS BOSON SEARCHES, ALEPH, DELPHI, L3 and OPAL collaborations, *Search for charged Higgs bosons: preliminary combined results using LEP data collected at energies up to 209 GeV* , [hep-ex/0107031](#) [[INSPIRE](#)].
- [20] CMS collaboration, *Search for a light charged Higgs boson in top quark decays in pp collisions at $\sqrt{s} = 7\text{ TeV}$* , *JHEP* **07** (2012) 143 [[arXiv:1205.5736](#)] [[INSPIRE](#)].
- [21] ATLAS collaboration, *Search for charged Higgs bosons in the $\tau + \text{jets}$ final state with pp collision data recorded at $\sqrt{s} = 8\text{ TeV}$ with the ATLAS experiment*, [ATLAS-CONF-2013-090](#) (2013).
- [22] CMS collaboration, *Inclusive search for doubly charged Higgs in leptonic final states with the 2011 data at 7 TeV* , [CMS-PAS-HIG-12-005](#) (2012).
- [23] ATLAS collaboration, *Search for doubly-charged Higgs bosons in like-sign dilepton final states at $\sqrt{s} = 7\text{ TeV}$ with the ATLAS detector*, *Eur. Phys. J. C* **72** (2012) 2244 [[arXiv:1210.5070](#)] [[INSPIRE](#)].
- [24] CMS collaboration, *Search for heavy neutrinos and W_R bosons with right-handed couplings in a left-right symmetric model in pp collisions at $\sqrt{s} = 7\text{ TeV}$* , *Phys. Rev. Lett.* **109** (2012) 261802 [[arXiv:1210.2402](#)] [[INSPIRE](#)].
- [25] ATLAS collaboration, *ATLAS search for a heavy gauge boson decaying to a charged lepton and a neutrino in pp collisions at $\sqrt{s} = 7\text{ TeV}$* , *Eur. Phys. J. C* **72** (2012) 2241 [[arXiv:1209.4446](#)] [[INSPIRE](#)].
- [26] R.N. Mohapatra and G. Senjanović, *Neutrino mass and spontaneous parity violation*, *Phys. Rev. Lett.* **44** (1980) 912 [[INSPIRE](#)].
- [27] R.N. Mohapatra and G. Senjanović, *Neutrino masses and mixings in gauge models with spontaneous parity violation*, *Phys. Rev. D* **23** (1981) 165 [[INSPIRE](#)].
- [28] A. Maiezza, M. Nemevšek, F. Nesti and G. Senjanović, *Left-right symmetry at LHC*, *Phys. Rev. D* **82** (2010) 055022 [[arXiv:1005.5160](#)] [[INSPIRE](#)].
- [29] V. Tello, M. Nemevšek, F. Nesti, G. Senjanović and F. Vissani, *Left-right symmetry: from LHC to neutrinoless double beta decay*, *Phys. Rev. Lett.* **106** (2011) 151801 [[arXiv:1011.3522](#)] [[INSPIRE](#)].
- [30] M. Nemevšek, F. Nesti, G. Senjanović and V. Tello, *Neutrinoless double beta decay: low left-right symmetry scale?*, [arXiv:1112.3061](#) [[INSPIRE](#)].
- [31] J. Chakraborty, H.Z. Devi, S. Goswami and S. Patra, *Neutrinoless double- β decay in TeV scale left-right symmetric models*, *JHEP* **08** (2012) 008 [[arXiv:1204.2527](#)] [[INSPIRE](#)].
- [32] P.S. Bhupal Dev, S. Goswami, M. Mitra and W. Rodejohann, *Constraining neutrino mass from neutrinoless double beta decay*, *Phys. Rev. D* **88** (2013) 091301 [[arXiv:1305.0056](#)] [[INSPIRE](#)].

- [33] N.T. Shaban and W.J. Stirling, *Minimal left-right symmetry and SO(10) grand unification using LEP coupling constant measurements*, *Phys. Lett. B* **291** (1992) 281 [[INSPIRE](#)].
- [34] J. Chakraborty and A. Raychaudhuri, *Grand unified theories with dimension-5 interactions: gauge unification and intermediate scales*, *Phys. Rev. D* **81** (2010) 055004 [[arXiv:0909.3905](#)] [[INSPIRE](#)].
- [35] J.F. Gunion, J. Grifols, A. Mendez, B. Kayser and F.I. Olness, *Higgs bosons in left-right symmetric models*, *Phys. Rev. D* **40** (1989) 1546 [[INSPIRE](#)].
- [36] P. Duka, J. Gluza and M. Zralek, *Quantization and renormalization of the manifest left-right symmetric model of electroweak interactions*, *Annals Phys.* **280** (2000) 336 [[hep-ph/9910279](#)] [[INSPIRE](#)].
- [37] M. Czakon, J. Gluza and J. Hejczyk, *Muon decay to one loop order in the left-right symmetric model*, *Nucl. Phys. B* **642** (2002) 157 [[hep-ph/0205303](#)] [[INSPIRE](#)].
- [38] J. Gluza, *On teraelectronvolt Majorana neutrinos*, *Acta Phys. Polon. B* **33** (2002) 1735 [[hep-ph/0201002](#)] [[INSPIRE](#)].
- [39] J. Gluza and M. Zralek, *Neutrino production in e^+e^- collisions in a left-right symmetric model*, *Phys. Rev. D* **48** (1993) 5093 [[INSPIRE](#)].
- [40] R.N. Mohapatra and S. Nussinov, *Constraints on decaying right-handed Majorana neutrinos from SN1987a observations*, *Phys. Rev. D* **39** (1989) 1378 [[INSPIRE](#)].
- [41] M. Czakon, M. Zralek and J. Gluza, *Left-right symmetry and heavy particle quantum effects*, *Nucl. Phys. B* **573** (2000) 57 [[hep-ph/9906356](#)] [[INSPIRE](#)].
- [42] A. Belyaev, N.D. Christensen and A. Pukhov, *CalcHEP 3.4 for collider physics within and beyond the standard model*, *Comput. Phys. Commun.* **184** (2013) 1729 [[arXiv:1207.6082](#)] [[INSPIRE](#)].
- [43] M.L. Mangano, M. Moretti, F. Piccinini, R. Pittau and A.D. Polosa, *ALPGEN, a generator for hard multiparton processes in hadronic collisions*, *JHEP* **07** (2003) 001 [[hep-ph/0206293](#)] [[INSPIRE](#)].
- [44] T. Sjöstrand, S. Mrenna and P.Z. Skands, *PYTHIA 6.4 physics and manual*, *JHEP* **05** (2006) 026 [[hep-ph/0603175](#)] [[INSPIRE](#)].
- [45] J. Alwall, M. Herquet, F. Maltoni, O. Mattelaer and T. Stelzer, *MadGraph 5: going beyond*, *JHEP* **06** (2011) 128 [[arXiv:1106.0522](#)] [[INSPIRE](#)].
- [46] N.D. Christensen and C. Duhr, *FeynRules — Feynman rules made easy*, *Comput. Phys. Commun.* **180** (2009) 1614 [[arXiv:0806.4194](#)] [[INSPIRE](#)].
- [47] C. Degrande et al., *UFO — the Universal FeynRules Output*, *Comput. Phys. Commun.* **183** (2012) 1201 [[arXiv:1108.2040](#)] [[INSPIRE](#)].
- [48] D. Guadagnoli and R.N. Mohapatra, *TeV scale left right symmetry and flavor changing neutral Higgs effects*, *Phys. Lett. B* **694** (2011) 386 [[arXiv:1008.1074](#)] [[INSPIRE](#)].
- [49] F. del Aguila, J. de Blas and M. Pérez-Victoria, *Effects of new leptons in electroweak precision data*, *Phys. Rev. D* **78** (2008) 013010 [[arXiv:0803.4008](#)] [[INSPIRE](#)].
- [50] J. Gluza, J. Maalampi, M. Raidal and M. Zralek, *Heavy neutrino mixing and single production at linear collider*, *Phys. Lett. B* **407** (1997) 45 [[hep-ph/9703215](#)] [[INSPIRE](#)].

- [51] J. Gluza and M. Zralek, *On possibility of detecting the $e^-e^- \rightarrow W^-W^-$ process in the standard model with additional right-handed neutrinos*, *Phys. Lett. B* **362** (1995) 148 [[hep-ph/9507269](#)] [[INSPIRE](#)].
- [52] J. Gluza and M. Zralek, *Inverse neutrinoless double beta decay in gauge theories with CP-violation*, *Phys. Rev. D* **52** (1995) 6238 [[hep-ph/9502284](#)] [[INSPIRE](#)].
- [53] W.-Y. Keung and G. Senjanović, *Majorana neutrinos and the production of the right-handed charged gauge boson*, *Phys. Rev. Lett.* **50** (1983) 1427 [[INSPIRE](#)].
- [54] C.-Y. Chen, P.S. Bhupal Dev and R.N. Mohapatra, *Probing heavy-light neutrino mixing in left-right seesaw models at the LHC*, *Phys. Rev. D* **88** (2013) 033014 [[arXiv:1306.2342](#)] [[INSPIRE](#)].
- [55] K. Huitu, J. Maalampi, A. Pietila and M. Raidal, *Doubly charged Higgs at LHC*, *Nucl. Phys. B* **487** (1997) 27 [[hep-ph/9606311](#)] [[INSPIRE](#)].
- [56] M.L. Swartz, *Limits on doubly charged Higgs bosons and lepton flavor violation*, *Phys. Rev. D* **40** (1989) 1521 [[INSPIRE](#)].
- [57] T.G. Rizzo, *Doubly charged Higgs bosons and lepton number violating processes*, *Phys. Rev. D* **25** (1982) 1355 [*Addendum ibid.* **D 27** (1983) 657] [[INSPIRE](#)].
- [58] J. Maalampi and N. Romanenko, *Single production of doubly charged Higgs bosons at hadron colliders*, *Phys. Lett. B* **532** (2002) 202 [[hep-ph/0201196](#)] [[INSPIRE](#)].
- [59] F. del Aguila and J.A. Aguilar-Saavedra, *Distinguishing seesaw models at LHC with multi-lepton signals*, *Nucl. Phys. B* **813** (2009) 22 [[arXiv:0808.2468](#)] [[INSPIRE](#)].
- [60] A. Melfo, M. Nemevšek, F. Nesti, G. Senjanović and Y. Zhang, *Type II seesaw at LHC: the roadmap*, *Phys. Rev. D* **85** (2012) 055018 [[arXiv:1108.4416](#)] [[INSPIRE](#)].
- [61] F. del Aguila, M. Chala, A. Santamaria and J. Wudka, *Discriminating between lepton number violating scalars using events with four and three charged leptons at the LHC*, *Phys. Lett. B* **725** (2013) 310 [[arXiv:1305.3904](#)] [[INSPIRE](#)].
- [62] K.S. Babu, A. Patra and S.K. Rai, *New signals for doubly-charged scalars and fermions at the Large Hadron Collider*, *Phys. Rev. D* **88** (2013) 055006 [[arXiv:1306.2066](#)] [[INSPIRE](#)].
- [63] F. del Aguila and M. Chala, *LHC bounds on lepton number violation mediated by doubly and singly-charged scalars*, *JHEP* **03** (2014) 027 [[arXiv:1311.1510](#)] [[INSPIRE](#)].
- [64] J. Pumplin et al., *New generation of parton distributions with uncertainties from global QCD analysis*, *JHEP* **07** (2002) 012 [[hep-ph/0201195](#)] [[INSPIRE](#)].
- [65] G. Bambhaniya, J. Chakraborty, S. Goswami and P. Konar, *Generation of neutrino mass from new physics at TeV scale and multi-lepton signatures at the LHC*, *Phys. Rev. D* **88** (2013) 075006 [[arXiv:1305.2795](#)] [[INSPIRE](#)].
- [66] C.-H. Kom and W.J. Stirling, *Charge asymmetry in W^+ jets production at the LHC*, *Eur. Phys. J. C* **69** (2010) 67 [[arXiv:1004.3404](#)] [[INSPIRE](#)].
- [67] R. Martinez, M.A. Perez and J.J. Toscano, *The two photon decay width of the Higgs boson in left-right symmetric theories*, *Phys. Rev. D* **40** (1989) 1722 [[INSPIRE](#)].
- [68] I. Picek and B. Radovic, *Enhancement of $h \rightarrow \gamma\gamma$ by seesaw-motivated exotic scalars*, *Phys. Lett. B* **719** (2013) 404 [[arXiv:1210.6449](#)] [[INSPIRE](#)].
- [69] M. Carena, I. Low and C.E.M. Wagner, *Implications of a modified Higgs to diphoton decay width*, *JHEP* **08** (2012) 060 [[arXiv:1206.1082](#)] [[INSPIRE](#)].

- [70] ATLAS collaboration, *Measurements of the properties of the Higgs-like boson in the two photon decay channel with the ATLAS detector using 25 fb^{-1} of proton-proton collision data*, [ATLAS-CONF-2013-012](#), ATLAS-COM-CONF-2013-015 (2013).
- [71] CMS collaboration, *Updated measurements of the Higgs boson at 125 GeV in the two photon decay channel*, [CMS-PAS-HIG-13-001](#) (2013).
- [72] P.S. Bhupal Dev, D.K. Ghosh, N. Okada and I. Saha, *125 GeV Higgs boson and the type-II seesaw model*, *JHEP* **03** (2013) 150 [Erratum *ibid.* **05** (2013) 049] [[arXiv:1301.3453](#)] [[INSPIRE](#)].
- [73] A.G. Akeroyd and S. Moretti, *Enhancement of $H \rightarrow \gamma\gamma$ from doubly charged scalars in the Higgs triplet model*, *Phys. Rev. D* **86** (2012) 035015 [[arXiv:1206.0535](#)] [[INSPIRE](#)].
- [74] J. Gluza and M. Zralek, *Higgs boson contributions to neutrino production in e^-e^+ collisions in a left-right symmetric model*, *Phys. Rev. D* **51** (1995) 4695 [[hep-ph/9409225](#)] [[INSPIRE](#)].
- [75] G. Ecker, W. Grimus and H. Neufeld, *Higgs induced flavor changing neutral interactions in $SU(2)_L \times SU(2)_R \times U(1)$* , *Phys. Lett. B* **127** (1983) 365 [Erratum *ibid.* **B 132** (1983) 467] [[INSPIRE](#)].
- [76] R.N. Mohapatra, G. Senjanović and M.D. Tran, *Strangeness changing processes and the limit on the right-handed gauge boson mass*, *Phys. Rev. D* **28** (1983) 546 [[INSPIRE](#)].
- [77] M.E. Pospelov, *FCNC in left-right symmetric theories and constraints on the right-handed scale*, *Phys. Rev. D* **56** (1997) 259 [[hep-ph/9611422](#)] [[INSPIRE](#)].

Looking for hints of a reconstructible seesaw model at the Large Hadron Collider

Gulab Bambhaniya,^{1,*} Srubabati Goswami,^{1,†} Subrata Khan,^{1,‡} Partha Konar,^{1,§} and Tanmoy Mondal^{1,2,||}

¹*Physical Research Laboratory (PRL), Ahmedabad 380009, Gujarat, India*

²*Indian Institute of Technology, Gandhinagar, Ahmedabad 382424, Gujarat, India*

(Received 27 October 2014; revised manuscript received 17 March 2015; published 9 April 2015)

We study the production of heavy neutrinos at the Large Hadron Collider through the dominant s -channel production mode as well as the vector boson fusion process. We consider the TeV scale minimal linear seesaw model containing two heavy singlets with the opposite lepton number. This model is fully reconstructible from oscillation data apart from an overall normalization constant which can be constrained from the metastability of the electroweak vacuum and bounds coming from lepton flavor violation searches. The Dirac nature of heavy neutrinos in this model implies suppression of the conventional same-sign-dilepton signal at the Large Hadron Collider. We analyze the collider signatures with the trilepton final state and missing transverse energy as well as vector boson fusion type signals which are characterized by two additional forward tagged jets. Our investigation reveals that due to stringent constraints on light-heavy mixing coming from lepton flavor violation and metastability bounds, the model can be explored only for a light to moderate mass range of heavy neutrinos. We also note that in case of a positive signal, flavor counting of the final trilepton channel can give information about the mass hierarchy of the light neutrinos.

DOI: 10.1103/PhysRevD.91.075007

PACS numbers: 12.60.-i, 13.35.Hb, 13.85.Qk, 14.60.St

I. INTRODUCTION

The discovery of the Higgs boson at the Large Hadron Collider by both ATLAS [1] and CMS [2] Collaborations has put the Standard Model (SM) on a firm footing. However, no signal of physics beyond the Standard Model has been found so far at the LHC. On the other hand, convincing indications of physics beyond the Standard Model have already emerged from the phenomenon of neutrino oscillation observed in terrestrial experiments. These results have conclusively established that neutrinos have nonzero mass and flavor mixing. Oscillation data together with the cosmological bound on sum of neutrino masses ($\Sigma m_i < 0.23$ eV including the PLANCK data [3]) indicate that neutrino masses are much smaller as compared to the other fermions in the SM. Such small masses can be generated naturally by the seesaw mechanism. The origin of seesaw is the dimension 5 effective operator $\frac{c_5}{M} LLHH$, where $L(H)$ being the SM lepton (Higgs) doublet and c_5 is a dimensionless coupling, M is the mass scale at which the effective operator gets generated [4]. Such operators arise by integrating out heavy fields added to the SM Lagrangian and they violate the lepton number by two units. The smallness of the neutrino mass in these models is related to the scale of lepton number violation which is required to be very high

$\sim \mathcal{O}(10^{15}$ GeV) to generate neutrino masses in the right ballpark. The most economical in terms of particle contents is the type-I seesaw in which heavy singlet right-handed neutrinos are added to the SM Lagrangian [5–9]. However, the natural seesaw scale is far beyond the reach of the LHC. To have signatures of seesaw models at the LHC, the heavy neutrino (N) mass needs to be $\sim \mathcal{O}$ (TeV). However, if one lowers the scale of the seesaw to TeV then it also requires much smaller neutrino Yukawa couplings ($\sim 10^{-6}$) to obtain correct light neutrino masses. Such small Yukawa couplings lead to suppression of the production of the heavy neutrinos in natural TeV scale type-I seesaw models. This leads to the question of whether it is possible to achieve both the requirements simultaneously, i.e. having TeV scale heavy neutrinos along with large Yukawa coupling leading to large light-heavy mixing. Such possibilities can be realized in some specific mass textures [10–18]. Other options include models with higher-dimensional operators arising due to the exchange of new particles belonging to larger representations [19–27], radiative mass generations [28–35], etc. One of the most popular options to generate TeV scale seesaw is through the inverse seesaw models in which one includes additional singlet states. These models were first proposed in the context of E(6) grand unified theories [36]. In these models the seesaw scale is decoupled from the scale of lepton number violation and the smallness of the neutrino mass originates from the small lepton number violating terms in the Lagrangian.

In the type-I seesaw model the heavy and light neutrinos are both Majorana particles. It is well known that the Majorana nature of neutrinos can be established by observing a positive signal in neutrinoless double beta

*gulab@prl.res.in
 †sruba@prl.res.in
 ‡subrata@prl.res.in
 §konar@prl.res.in
 ||tanmoym@prl.res.in

decay experiments. It was noticed in [37], in the context of the left-right symmetric model that resonant production of N and its subsequent decay giving the same-sign-dilepton (SSDL) signal in colliders can also constitute evidence for the Majorana nature of neutrinos. Given the importance of this signal, there have been several studies of this channel at the hadron colliders [38–43] including searches at the LHC [44]. Enhanced contribution from the infrared t -channel, especially for heavier masses, was proposed [45,46] together with s -channel production.

The heavy neutrinos in the inverse seesaw model are of the pseudo-Dirac nature and in this case the SSDL signal is suppressed by the small lepton number violating coupling. For such models the heavy neutrinos are produced by the s -channel process along with a charged lepton. This neutrino further decays to a second lepton (of sign opposite to the first lepton to conserve the lepton number) together with a W -boson. The W -boson can further decay leptonically to produce a lepton and a neutrino. Thus, the final signal consists of trilepton and missing energy which is expected to have a tiny contamination from the Standard Model backgrounds. Detailed studies including the SM background in the context of pseudo-Dirac neutrinos have been done in [42,47]. Similar studies in the context of the left-right symmetric model, nonminimal supersymmetric inverse seesaw models, and the type-III seesaw model have been performed in [48,49], and [50], respectively. Experimental searches for multilepton signals have been carried out by the CMS Collaboration using an integrated luminosity of 19.5 fb^{-1} with center of mass energy $\sqrt{s} = 8 \text{ TeV}$ at the LHC [51]. They considered at least three leptons in the final state using a search strategy not specific to any particular model.

In this work, we consider the minimal linear seesaw model (MLSM) studied in [52,53] as an example of the TeV scale seesaw model. This is a variant of the inverse seesaw model but in this case the minimal scheme consists of adding just two heavy singlets with the opposite lepton number as opposed to four heavy neutrinos in canonical minimal inverse seesaw models [54]. It was shown in [52] that the Yukawa coupling matrices for this model can be fully reconstructed in terms of the oscillation parameters apart from an overall normalization factor. It was further shown in [53] that this normalization constant can be constrained from consideration of the metastability of the electroweak vacuum and lepton flavor violation bounds. The heavy neutrinos in this model are of Dirac type and the SSDL signal is suppressed.¹ In the context of this model, we consider two possible production channels for the heavy neutrinos resulting in two different classes of signals. The first one of this is the s -channel process to produce heavy Dirac neutrinos associated with a lepton and finally giving

¹Because of the same reason the heavy neutrino contribution towards $0\nu\beta\beta$ is suppressed [53].

the trilepton and missing energy signal. The second one is the production of heavy neutrinos through vector boson fusion (VBF) in which two electroweak vector bosons coming from two partons “fuse” to produce the signal under consideration (trileptons) along with two highly forward jets. It becomes important in the context of hadron colliders since the tagging of forward jets allows us to reduce the background considerably. Also the lack of color exchange between these jets makes the central region free from the color activities and this is exploited by vetoing central jets; see [55] and references therein in the context of the Higgs search. This helps in minimizing the backgrounds further. For these reasons VBF remains an important channel to look for new physics [56–58] at hadron colliders.

We consider both normal hierarchy (NH) as well as inverted hierarchy (IH) for the light neutrino mass spectra. We also estimate the corresponding Standard Model backgrounds for the 14 TeV LHC. In each case, we perform a realistic simulation with extensive event selections using MadGraph and PYTHIA.

The paper is organized as follows: Sec. II contains a brief description of the model. The production and decay of the right-handed neutrino at the LHC are discussed in Sec. III. Simulation details and results are presented in Sec. IV, while in Sec. V we discuss the discovery potential of the signals at the LHC. Finally, we conclude in Sec. VI.

II. THE LINEAR SEESAW MODEL

The most general Lagrangian containing heavy singlet fields N_R and S with opposite lepton numbers is given by

$$-\mathcal{L} = \bar{N}_R Y_\nu \tilde{\phi}^\dagger l_L + \bar{S} Y_S \tilde{\phi}^\dagger l_L + \bar{S} M_N N_R^c + \frac{1}{2} \bar{S} \mu S^c + \frac{1}{2} \bar{N}_R \mu_N N_R^c + \text{H.c.}, \quad (1)$$

where $l_L = (\nu_x, x)^T$, $x = e, \mu, \tau$.

Once the symmetry is broken spontaneously, the Higgs field ϕ obtains a vacuum expectation value equal to $v/\sqrt{2}$. This generates the Dirac mass term $m_D = Y_\nu v/\sqrt{2}$ and the lepton number breaking mass term $m_S = Y_S v/\sqrt{2}$. In the linear seesaw models [59–61] one assumes m_S to be small and nonzero while the μ and the μ_N terms are set to zero. This can be done since they contribute towards the light neutrino mass in the subleading orders [62]. Since lepton number violating mass terms are set to zero, the heavy neutrinos are purely Dirac type. Then the mass matrix takes the form

$$\mathcal{M}_\nu = \begin{pmatrix} 0 & m_D^T & m_S^T \\ m_D & 0 & M_N \\ m_S & M_N^T & 0 \end{pmatrix}, \quad (2)$$

in the (ν_L, N_R^c, S^c) basis.

TABLE I. Allowed 3σ ranges of oscillation parameters and benchmark values of these parameters used in our analysis to get the signal allowed by LFV and vacuum metastability. Case I corresponds to the peak in Fig. 1 (left panel), while case II corresponds to a lower value of y_ν/M_N , for which $V_{\mu N}$ is maximum. The value of the Majorana phase α is set at $3\pi/2(3\pi/4)$ for the NH (IH) scenario.

Bound	Parameter					δ
	$\Delta_\odot^2 [10^{-5} \text{ eV}^2]$	$\Delta_{\text{atm}}^2 [10^{-3} \text{ eV}^2]$	$\sin^2\theta_{12}$	$\sin^2\theta_{23}$	$\sin^2\theta_{13}$	
3σ range (NH)	7.12–8.20	2.31–2.74	0.27–0.37	0.36–0.68	0.017–0.033	0– 2π
(IH)		2.21–2.64		0.37–0.67		
Used value (NH: case I)	7.15	2.73	0.27	0.36	0.033	0.0
Used value (NH: case II)	7.13	2.73	0.27	0.68	0.033	0.0
Used value (IH)	7.25	2.40	0.34	0.57	0.021	0.0

The minimal model which can successfully generate two light neutrinos with nonzero mass is when only two extra heavy singlets are added to the SM Lagrangian. This is called the MLSM [52,53]. The full mass matrix has dimension 5×5 and can be written as

$$\mathcal{M}_\nu = \begin{pmatrix} 0 & m'_D{}^T \\ m'_D & M \end{pmatrix}, \quad (3)$$

where $m'_D{}^T = (m'_D, m'_S)$ and

$$M = \begin{pmatrix} 0 & M_N \\ M_N & 0 \end{pmatrix}. \quad (4)$$

For the minimal case, M_N is just a number, not a matrix. \mathcal{M}_ν can be diagonalized by a 5×5 unitary matrix U_0 as

$$U_0^T \mathcal{M}_\nu U_0 = \mathcal{M}_\nu^{\text{diag}}, \quad (5)$$

where $\mathcal{M}_\nu^{\text{diag}} = \text{diag}(m_1, m_2, m_3, M_1, M_2)$. Following a two-step diagonalization procedure [63], U_0 can be expressed as

$$U_0 = \begin{pmatrix} (1 - \frac{1}{2}\epsilon)U_\nu & m'_D{}^\dagger(M^{-1})^*U_R \\ -M^{-1}m'_D U_\nu & (1 - \frac{1}{2}\epsilon')U_R \end{pmatrix} \equiv \begin{pmatrix} U_L & V \\ S & U_H \end{pmatrix}, \quad (6)$$

where U_L is the U_{PMNS} mixing matrix, and V, S are the light-heavy mixing matrices. Interaction of heavy neutrinos with the SM fields is determined by the mixing matrix V , whose elements will be denoted as V_{IN} hereafter. We would notice afterwards that the strong constraints on some elements of this matrix, i.e. V_{eN} and $V_{\mu N}$, would restrict the production signal. The diagonalizing matrix is now nonunitary which is characterized by the factor $(1 - \epsilon/2)$. The nonunitary corrections ϵ and ϵ' are given in [63,64]. U_ν is the unitary component of U_{PMNS} which is same as U_{PMNS} for $\epsilon \ll 1$. We use the standard parametrization for this:

$$U_\nu = \begin{pmatrix} c_{12}c_{13} & s_{12}c_{13} & s_{13}e^{-i\delta} \\ -c_{23}s_{12} - s_{23}s_{13}c_{12}e^{i\delta} & c_{23}c_{12} - s_{23}s_{13}s_{12}e^{i\delta} & s_{23}c_{13} \\ s_{23}s_{12} - c_{23}s_{13}c_{12}e^{i\delta} & -s_{23}c_{12} - c_{23}s_{13}s_{12}e^{i\delta} & c_{23}c_{13} \end{pmatrix} P, \quad (7)$$

where $c_{ij} = \cos\theta_{ij}$, $s_{ij} = \sin\theta_{ij}$, and δ denotes the Dirac CP phase. The Majorana phase matrix P is expressed as $P = \text{diag}(e^{-i\alpha}, e^{i\alpha}, 1)$; there is only one Majorana phase because one of the mass eigenvalues is zero. In Table I, we have presented the 3σ allowed range of oscillation parameters. Note that the phases are completely unconstrained at present.

Using the seesaw approximation, one obtains the light neutrino mass matrix,

$$m_{\text{light}} = m'_D{}^T M^{-1} m'_D. \quad (8)$$

This being a rank 2 matrix, the light neutrinos belonging to this model are hierarchical. Thus, there are two possible mass spectra:

- (i) NH: ($m_1 < m_2 < m_3$)
- (ii) IH: ($m_3 \ll m_2 \approx m_1$).

In the MLSM, Y_ν and Y_S are 3×1 matrices [cf. Eq. (1)] and can be considered as two independent vectors

$$Y_\nu \equiv y_\nu \hat{\mathbf{a}}; \quad Y_S \equiv y_S \hat{\mathbf{b}}, \quad (9)$$

where $\hat{\mathbf{a}}$ and $\hat{\mathbf{b}}$ denote complex vectors with unit norm while y_ν and y_S represent the norms of the Yukawa matrices Y_ν and Y_S , respectively. Using Eqs. (8) and (9) one can reconstruct the Yukawa matrices Y_ν and Y_S in terms of the oscillation parameters barring an overall normalization factor. The parametrization of the Yukawa matrices depends on the mass hierarchy and can be expressed as [52,53]

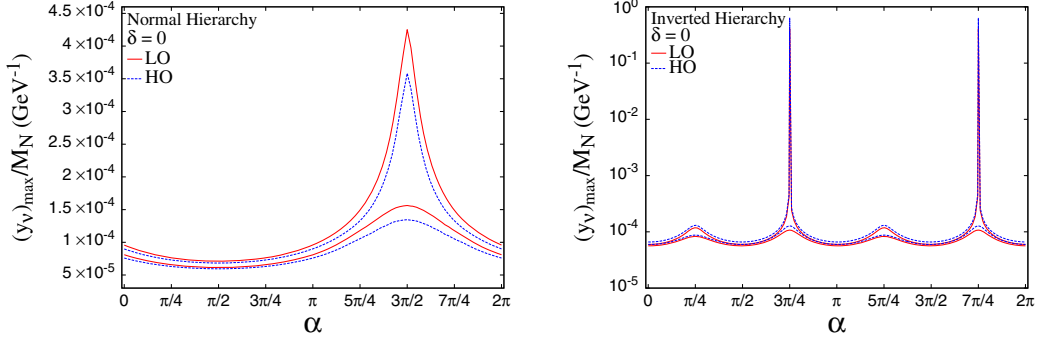


FIG. 1 (color online). Bound on y_ν/M_N as a function of the Majorana phase α , varying the oscillation parameters in the allowed 3σ range. The red-solid (blue-dashed) curve corresponds to the atmospheric angle (θ_{23}) residing in the LO (HO) region. (Left plot) The plot is for the NH scenario, where the highest allowed value of y_ν/M_N lies in the LO region. (Right plot) The same plot for the IH scenario.

$$\begin{aligned}
 Y_\nu &= \frac{y_\nu}{\sqrt{2}} \left(\sqrt{1+\rho} U_j^\dagger + e^{i\frac{\pi}{2}} \sqrt{1-\rho} U_k^\dagger \right), \\
 Y_S &= \frac{y_s}{\sqrt{2}} \left(\sqrt{1+\rho} U_j^\dagger - e^{i\frac{\pi}{2}} \sqrt{1-\rho} U_k^\dagger \right), \quad (10)
 \end{aligned}$$

where $j = 2, k = 3$ for NH and $j = 2, k = 1$ for IH. U_j 's denote the columns of the unitary matrix U_ν that diagonalizes the light neutrino mass matrix m_{light} in Eq. (8). The parameter ρ is given as

$$\rho = \frac{\sqrt{1+r} - \sqrt{r}}{\sqrt{1+r} + \sqrt{r}} \text{(NH)}, \quad \rho = \frac{\sqrt{1+r} - 1}{\sqrt{1+r} + 1} \text{(IH)}. \quad (11)$$

Here r denotes the ratio of the solar and atmospheric mass squared differences, $r = \Delta m_\odot^2 / \Delta m_{\text{atm}}^2$, with $\Delta m_\odot^2 \equiv m_2^2 - m_1^2$ and $\Delta m_{\text{atm}}^2 \simeq m_3^2 - m_1^2$ ($m_2^2 - m_3^2$) for NH (IH).

The overall coupling y_ν can be constrained from the metastability of the electroweak vacuum and LFV [53]. For NH the most stringent constraint comes from LFV, whereas for the IH case the vacuum metastability constraint is more restrictive. This is because of cancellations occurring for the IH for LFV processes [53]. The dependence of the bound on y_ν from metastability and LFV on the heavy neutrino mass has been shown in [53]. The metastability bound on y_ν varies approximately in the range 0.4–0.5 for M_N varying in the range 100–1000 GeV. This bound is independent of the oscillation parameters. However, significant variation on the bound on y_ν from the LFV

constraint is possible within the allowed range of oscillation parameters, mostly due to unconstrained phases, δ and α . Details of these dependences can be followed from Fig. 1. For a particular M_N , the strength of the signal at the LHC would depend on the value of y_ν . To maximize the signal, we therefore choose the value of y_ν at the peak for the NH case. However, for the IH case the peak value is much above the vacuum metastability bound and therefore we choose the maximum allowed value of y_ν satisfying the metastability bound. The corresponding parameter values are depicted in Table I for NH (case I) and IH. Note that, the above mentioned cancellations within the terms, ensure the peak position corresponds to $\alpha + \delta = 3\pi/2$ ($3\pi/4$) for NH (IH), which is also evident in Fig. 1. We have chosen $\delta = 0$ in our analysis. For some other values of δ , the phase α has to be chosen so that one is at the peak. In Fig. 1 we also show the variation of this bound with respect to the θ_{23} mixing angle in the lower octant (LO, $\theta_{23} < \pi/4$) and higher octant (HO, $\theta_{23} > \pi/4$). The y_ν value 0.4 (0.075) corresponds to the IH (NH: case I) scenario for $M_N = 100$ GeV, which we will use in our analysis. These will be translated into the bounds on the mixing matrix elements, V_{IN} , depending on the heavy neutrino mass M_N . Since y_s is extremely small [$\mathcal{O}(10^{-10})$], Y_S does not play any role in determining V_{IN} . The elements of the matrix V (or V_{IN}) can be expressed in terms of the U_{PMNS} matrix, ρ and y_ν as follows:

$$\begin{aligned}
 V_{eN_1} &= \frac{-i}{\sqrt{2}M_N} \frac{y_\nu v}{2} [\sqrt{1+\rho}(U_{\text{PMNS}})_{12}^* + i\sqrt{1-\rho}(U_{\text{PMNS}})_{11}^*] \\
 &\simeq \frac{y_\nu v}{4M_N} [e^{i(\alpha+\delta)}(-2 + \sqrt{r})r^{\frac{1}{4}}s_{12} - 2is_{13}] + \mathcal{O}((\sqrt{r}, s_{13})^2) \\
 V_{\mu N_1} &= \frac{-i}{\sqrt{2}M_N} \frac{y_\nu v}{2} (\sqrt{1+\rho}(U_{\text{PMNS}})_{22}^* + i\sqrt{1-\rho}(U_{\text{PMNS}})_{21}^*) \\
 &\simeq \frac{y_\nu v}{4M_N} [(-2 + \sqrt{r})(e^{i\alpha}r^{\frac{1}{4}}c_{12}c_{23} + is_{23}) + 2e^{i(\alpha+\delta)}r^{\frac{1}{4}}s_{12}s_{23}s_{13}] + \mathcal{O}((\sqrt{r}, s_{13})^2). \quad (12)
 \end{aligned}$$

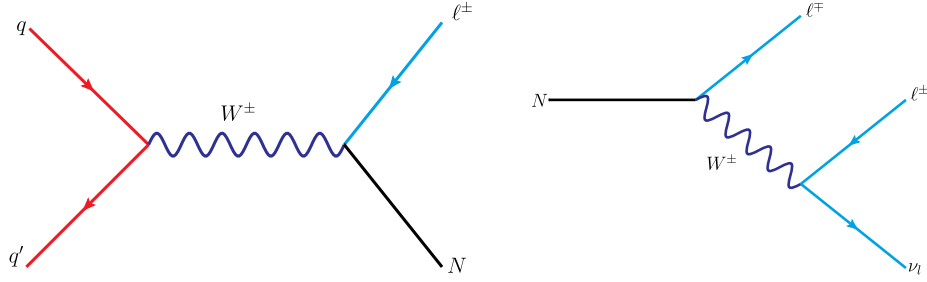


FIG. 2 (color online). (Left plot) Leading order s -channel diagram for heavy neutrino production at hadron colliders, and (right plot) representative diagram for one of the decay modes of the heavy neutrino. These two figures lead to the trilepton $+E_T$ signal considered in the analysis.

The above expressions are for the NH scenario and similar expressions can be computed for IH also. The element V_{eN_2} ($V_{\mu N_2}$) differs from V_{eN_1} ($V_{\mu N_1}$) by a phase factor. Note that in Table I, we also consider a second set of oscillation parameters for NH (NH: case II) corresponding to a lower value of y_ν of 0.056 with θ_{23} in the higher octant. This value is chosen such that $V_{\mu N}$ is the maximum and the muon signal may be larger, since the muon has higher efficiency for detection.

To get some perspective on the degree of suppression in the cross section coming from these constraints, we note down the corresponding V_{lN} values for $M_N = 100$ GeV as $V_{eN} = 1.95 \times 10^{-3}$, $V_{\mu N} = 2.93 \times 10^{-2}$, and $V_{\tau N} = 8.83 \times 10^{-2}$ for the NH (case I) scenario, whereas, $V_{eN} = 1.43 \times 10^{-3}$, $V_{\mu N} = 4.14 \times 10^{-2}$, and $V_{\tau N} = 5.48 \times 10^{-2}$ for the NH (case II), respectively. For IH these values are $V_{eN} = 0.48$, $V_{\mu N} = 4.15 \times 10^{-9}$, and $V_{\tau N} = 0.109$. Note that since our model is fully reconstructible and the only unknown parameter is y_ν , which can be constrained from LFV and metastability bounds, we have definite predictions for the parameters V_{lN} and these values are different for NH and IH scenarios. Bounds on V_{lN} can also come from electroweak precision data [65]. Our bounds for NH are consistent with these bounds. For IH we get a larger value for V_{eN} . However, it is to be noted that the electroweak precision data bounds are obtained assuming mixing with a single charged lepton and can be evaded in the presence of cancellations or mixing with the other charged leptons [42].

III. PHENOMENOLOGY AT THE LHC

The dominant production channel of the heavy neutrinos at the LHC is the s -channel process through virtual W -boson exchange. At the leading order the parton level process ($q\bar{q}' \rightarrow W^\pm \rightarrow \ell^\pm N$) is depicted in Fig. 2 (left plot). The heavy neutrinos can also be produced through the VBF process where production of N is associated with two forward jets. Figure 3 contains the representative

parton level Feynman diagrams for VBF processes.² Estimated total production cross sections of these heavy Dirac neutrinos at the 14 TeV LHC in the IH scenario are shown in Fig. 4 for both s -channel (solid-line) as well as VBF (dashed-line). For the NH scenario the s -channel production cross sections are shown in the same figure for two different cases (cf. Table I), case I (red dot-dashed line) and case II (black double dotted line). Basic cuts such as $p_{T\ell} > 20$ GeV and $|\eta_\ell| < 2.5$ are applied and y_ν values mentioned in the previous section are used. It is seen from the figure that although case II corresponds to a lower value of y_ν since $V_{\mu N}$ is larger, the production cross section is slightly larger. Since the VBF cross section is much lower, we do not present the VBF cross section for the NH case. In these analyses CTEQ6L1 [68], parton distribution functions have been used with the factorization scale set at the heavy neutrino mass M_N .

Heavy neutrinos N can decay into charged leptons or neutrinos associated with the gauge (or Higgs) boson.

$$N \rightarrow W^\pm l^\mp / Z\nu_l / H\nu_l, \quad \text{where } l \equiv e, \mu, \tau. \quad (13)$$

A representative diagram for the decay of N ($N \rightarrow \ell^\mp W^\pm$) is shown in Fig. 2 (right plot).

In Fig. 5 we present the branching ratios (BRs) for these decay channels as a function of heavy neutrino mass M_N both in the case of normal hierarchy (left) and inverted hierarchy (right). Total decay widths in each case are also demonstrated with the solid line in each figure. Identifying that the charged lepton decay modes for the heavy neutrino, i.e. $N \rightarrow W^\pm l^\mp$ are the main channel for the search at the hadron collider, we discuss the corresponding decay modes in detail for both scenarios. The figure clearly shows that for NH,

²Note that there are some diagrams which are not truly the VBF type, i.e. two gauge boson are not fused via the t -channel (e.g. bottom right diagram in Fig. 3), but they can lead to the same final states. These diagrams are necessary for the requirements of gauge invariance and included both for background [66,67] and signal calculations.

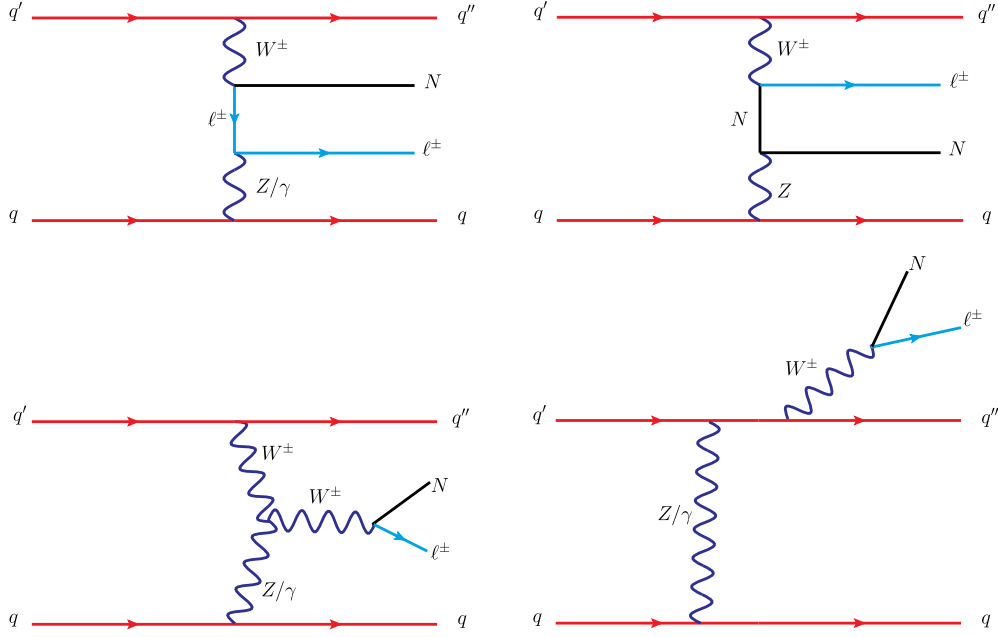


FIG. 3 (color online). Representative parton level diagrams contributing to $N\ell jj$ production through vector boson fusion at hadron colliders. Mirror diagrams are not shown here and also the last diagram is one of the four diagrams with W^\pm emitting from each of the quark legs.

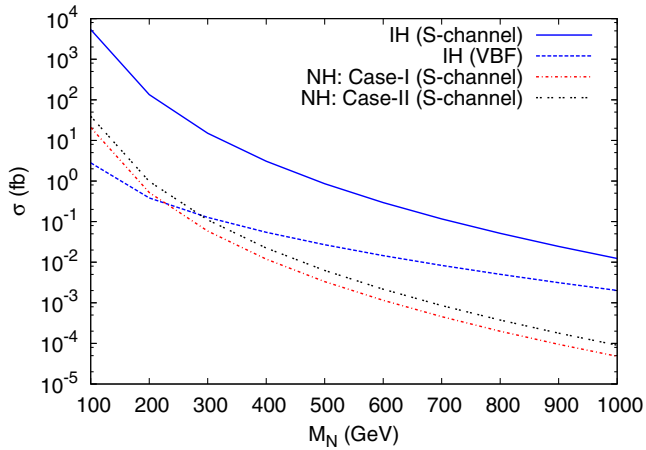


FIG. 4 (color online). The total cross section is shown for the production of the heavy neutrino associated with the light lepton ($pp \rightarrow N\ell$, where $\ell = e, \mu$) at the 14 TeV LHC through the leading order s -channel process, while dotted lines represent VBF production cross section.

case I,³ heavy neutrinos mostly decay into the tau lepton (τ) and W -boson. On the other hand for IH, decay into the first generation lepton (e) possesses the maximum branching ratio. For NH the decay to μ is low and decay

³For case II, although branching ratios to different channels are likely to change, we do not show the corresponding plot as the final production cross section for both the cases, after putting all the selection criteria, is very low for NH and beyond the reach of the LHC at 14 TeV even with a luminosity of 3000 fb^{-1} .

to e is severely suppressed, while for IH, the decay to τ has a lower ratio and decay to μ is negligible. The W^\pm can have hadronic decay modes ($W^\pm \rightarrow jj$) or leptonic decay modes ($W^\pm \rightarrow l^\pm \nu$). The trilepton signal $pp \rightarrow l^\pm l^\mp l^\pm \nu$ comes from the later decay mode.⁴

Other than the charged lepton decay mode, N can also decay to the Z -boson or Higgs boson associated with the neutrinos as listed in Eq. (13). The corresponding branching ratios are also shown in Fig. 5. Note that the branching ratio for $Z\nu$ is suppressed for lower values of the masses of the heavy neutrinos essentially because of the W mass threshold. For the $H\nu$ decay mode, the Higgs mass threshold suppresses the decay rate for lower values of $M_N \sim 100$ GeV. However, as M_N increases, these branching ratios increase to retain a $\sim 25\%$ level. Both these channels can contribute to the trilepton signal via leptonic decays and we have considered their contributions in our simulation. However, since we will apply the Z -veto (to minimize the SM background), the contribution coming

⁴Evidently, the former decay mode leads to opposite sign dileptons (OSDL), also suppressed by $|V_{lN}|^4$, but slightly larger compare to the trilepton signal. However, significant irreducible backgrounds can come from $t\bar{t}$, VV (with $V = W, Z$), as well as $Z + \text{Jets}$ after vetoing the dilepton invariant mass at Z -pole. Hence, we are not considering the OSDL as a signal. An estimate of these backgrounds for OSDL can be found in [69]. Note that their more specific selection criteria are not applicable for our present signal. Similarly, OSDL through VBF is suppressed by $|V_{lN}|^4$ and is beset with a large background coming from WW , $\tau\tau$, and ZZ production at VBF [57].

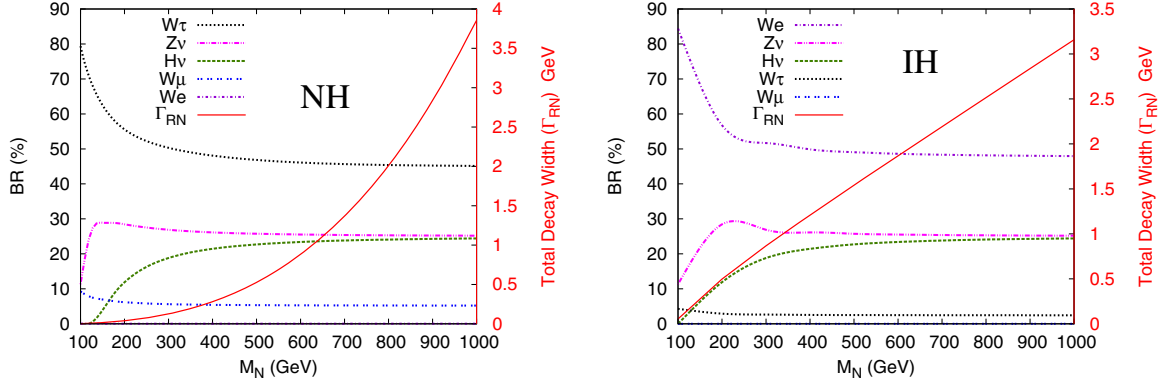


FIG. 5 (color online). The decay branching ratios of the heavy neutrino (N) in different channels as a function of its mass in the case of normal hierarchy, case I, (left) and inverted hierarchy (right). Total decay widths in each case are also demonstrated with the solid line in the same figure.

from the $Z\nu$ decay mode will be suppressed after final event selection.

As the lepton Yukawa is small, the $H\nu$ mode is also not going to contribute to our signal even for higher values of M_N .

IV. SIMULATION AND RESULTS

We have implemented the model in FeynRules [70] and generated the Feynman rules compatible with MadGraph5 [71]. After generating the Les Houches Event [72] file from MadGraph, we have passed that to PYTHIA6 [73] for showering and hadronization.

A. Selection criteria

To get enhancement in signal over background, we use the following selection criteria [74,75]:

- (1) Identification criteria of a lepton: Pseudorapidity $|\eta_\ell| < 2.5$ and $p_{T\ell} > 20$ GeV have been used.
- (2) Detector efficiency for leptons [76,77]:
 - (a) For the electron (either e^- or e^+), detector efficiency is 0.7 (70%);
 - (b) For the muon (either μ^- or μ^+), detector efficiency is 0.9 (90%).
- (3) Smearing⁵ of electron energy and muon p_T are incorporated.
- (4) Lepton-lepton separation: For this, $\Delta R_{ll} \geq 0.2$ is used⁶ (due to the detector resolution of leptons).
- (5) Lepton-photon separation: This is taken as $\Delta R_{l\gamma} \geq 0.2$ with all the photons having $p_{T\gamma} > 10$ GeV.

⁵The choice of corresponding η dependent parameters is similar to one of our earlier work [74].

⁶Here $\Delta R_{ij} = \sqrt{(\eta_i - \eta_j)^2 - (\phi_i - \phi_j)^2}$ quantifies the separation between particles i and j in the pseudorapidity (η)-azimuth (ϕ) plane.

- (6) Lepton-jet separation: The separation of a lepton with all the jets is set at $\Delta R_{lj} \geq 0.4$; otherwise that lepton is not counted as a lepton. Jets are constructed from hadrons using PYCELL within the PYTHIA.
- (7) Hadronic activity cut: This cut is applied to take only the pure kind of leptons that have very less hadronic activity around them. The hadronic activity within the cone of radius 0.2 around the lepton should be small, $\sum \frac{p_{T\text{hadron}}}{p_{Tl}} \leq 0.2$.
- (8) Hard p_T cuts used are $p_{Tl_1} > 30$ GeV, $p_{Tl_2} > 30$ GeV, and $p_{Tl_3} > 20$ GeV.
- (9) Missing p_T cut: Because of the presence of the neutrino, a missing p_T cut (> 30 GeV) is applied.
- (10) Z-veto⁷ is applied to suppress the SM background.
- (11) VBF cuts [55,78]:
 - (a) Central jet veto is also applied, in which we consider any jet with $E_{T3} > 20$ GeV and compute the rapidity with respect to the average of the two forward jets: $\eta_0 = \eta_3 - (\eta_1 + \eta_2)/2$. We veto the event if $|\eta_0| < 2$. The central jet veto is applied to suppress the QCD background substantially.
 - (b) Charged leptons need to fall in between the rapidities of two forward tagging jets, i.e. $\eta_{j,\min} < \eta_\ell < \eta_{j,\max}$.
 - (c) p_T of jets: $p_{Tj_1,j_2} > 20$ GeV.
 - (d) Invariant mass of jets: $M_{j_1,j_2} > 600$ GeV.
 - (e) Pseudorapidity of jets: $\eta_{j_1}, \eta_{j_2} < 0$ and $|\eta_{j_1} - \eta_{j_2}| > 4$. Demanding both the tagged jets in the opposite hemisphere and a large rapidity separation among them significantly reduces the background for VBF.

⁷The same flavored but opposite sign lepton pair invariant mass $m_{\ell_1\ell_2}$ must be sufficiently away from the Z mass, such that, typically, $|m_{\ell_1\ell_2} - M_Z| \geq 6\Gamma_Z \sim 15$ GeV.

TABLE II. Dominant Standard Model background cross sections contributing to trilepton and missing transverse energy. These are calculated satisfying all the cuts (except VBF cuts) for the 14 TeV LHC. For each process we also classify the trilepton background into four different flavor combinations and present the cross section in each case along with the total contribution.

Process	Cross section (<i>fb</i>)				
	$\ell\ell\ell$	eee	$e\mu\mu$	$e\mu\mu$	$\mu\mu\mu$
$t\bar{t}$	18.972	1.1383	7.0831	8.2214	2.5297
$W^\pm(Z/\gamma^*)$	10.832	0.0677	0.1311	5.9891	4.6440
$(Z/\gamma^*)(Z/\gamma^*)$	1.175	0.0734	0.0525	0.6400	0.4090
$t\bar{t}(Z/\gamma^*)$	1.103	0.0429	0.1329	0.4997	0.4275
$t\bar{t}W^\pm$	0.639	0.0328	0.2655	0.2424	0.0983
TOTAL	32.721	1.3551	7.6651	15.5926	8.1085

TABLE III. Dominant Standard Model background cross section contributing to the trilepton and missing transverse energy associated with two forward jets. These are calculated satisfying all the cuts including VBF cuts for the 14 TeV LHC. Cross sections of four different flavor combinations as well as the total cross section are listed.

Process	Cross section (<i>fb</i>)				
	$\ell\ell\ell$	eee	$e\mu\mu$	$e\mu\mu$	$\mu\mu\mu$
W^+Zjj	0.04068	0.00073	0.00105	0.02157	0.01734
W^-Zjj	0.01923	0.00038	0.00055	0.00994	0.00836
$ZZjj$	0.00094	0.00002	0.00002	0.00066	0.00024
TOTAL	0.06085	0.00113	0.00162	0.03216	0.02594

B. Background

1. For the s -channel signal

To calculate the SM background we consider all channels that can produce or mimic the trilepton production with missing P_T . We closely follow the reference [74,79] where a similar background analysis was done with the event selection criteria listed as above except the cuts related to the VBF. Events are generated using ALPHGEN [80] for the processes coming from $t\bar{t}$, $t\bar{t}(Z/\gamma^*)$, $t\bar{t}W^\pm$, $W^\pm(Z/\gamma^*)$, $(Z/\gamma^*)(Z/\gamma^*)$ at the parton level and passed into PYTHIA. As expected $t\bar{t}$ and $W^\pm(Z/\gamma^*)$ contribute dominantly. These and other SM backgrounds are listed in Table II. For each process, we classify the trilepton signals into four different flavor combinations and compute the cross section in each case along with the total contribution.

2. For VBF signal

The trilepton signal with missing P_T and two forward jets in VBF can be faked by different SM backgrounds. Processes like $t\bar{t}$ would produce b -jets and are mostly effective in the central region. Vetoing on jet activities in the central region can eliminate most of the non-VBF type SM processes. However, the most important irreducible background comes from $W^\pm Z$ and ZZ together with two extra forward jets once the gauge bosons decay leptonically. These processes can construct a dominant SM

background for the VBF production of $3\ell + E_T$ since they include the typical VBF topology and hence can easily pass the central jet veto criteria. These backgrounds are calculated⁸ using MadGraph5 and PYTHIA6. In Table III the dominant background cross sections, after satisfying all the cuts including VBF cuts at 14 TeV LHC, are tabulated. Like the case of s -channel backgrounds, for each process we also classify the trilepton signals into four different flavor combinations and compute the cross section in each case as well as the total contribution.

C. Signal

Earlier in Sec. III we have presented the total heavy neutrino production cross sections for different light neutrino hierarchies with basic selection criteria. The cross section for the NH scenario was found to be much lower than the IH scenario for the s -channel. The branching ratios for decays of N to final states with μ and e are also very small for NH. Therefore, we will concentrate only on the IH scenario henceforth. For this we consider both s -channel and VBF process. Although the VBF cross section for IH is lower or comparable to the s -channel cross section for NH for lower values of M_N , the background for VBF processes are much smaller. Hence, we study this channel also for IH. In this section we consider all leptonic decay modes of

⁸Next to leading order QCD corrections are available in [66,67].

TABLE IV. Cross section for the IH case. Final trilepton signal cross section through s -channel heavy neutrino production at the 14 TeV LHC for the benchmark point $M_N = 100$ GeV including all event selection cuts except VBF cuts. We classify the trilepton signals into four different flavor combinations and present the cross section in each case along with the total light lepton contribution.

Hierarchy	Cross section (fb)				
	$\ell\ell\ell$	eee	$e\mu\mu$	$e\mu\mu$	$\mu\mu\mu$
IH	27.07	10.297	16.314	0.459	0.0

heavy neutrinos for a benchmark mass of M_N at 100 GeV with the cuts discussed in Sec. IV A.

1. Signal for s -channel

The signal coming from the decay of heavy neutrinos

$$pp \rightarrow \ell^\pm N \rightarrow \ell^\pm(\ell^\mp W^\pm) \rightarrow \ell^\pm \ell^\mp \ell^\pm + \cancel{E}_T,$$

where $\ell \equiv e, \mu$.

Table IV lists the final trilepton signal cross section through s -channel heavy neutrino production at 14 TeV LHC for the benchmark point $M_N = 100$ GeV incorporating all event selection criteria except VBF cuts as described earlier. The total contribution from the light leptons as well as the contributions from the four different flavor combinations are presented.

As we can see from the Table IV, the cross section in terms of flavors has the ordering: $e\mu\mu > eee > e\mu\mu > \mu\mu\mu$. We can understand this in the following way. There are a total of 8 possibilities which can produce $\ell\ell\ell$ events. There is only one way to produce $\mu\mu\mu$ and eee final states. However, there are three possible ways to get the $e\mu\mu$ channel depending on which one of ℓ_i 's in Fig. 2 is associated with e and μ . Similarly for the $e\mu\mu$ final state also we get 3 possibilities. The amplitude for the eee channel $\sim V_{eN}^4$, the $e\mu\mu$ channel goes as $\sim V_{eN}^2 + 2V_{eN}V_{\mu N}$, the $e\mu\mu$ channel goes as $\sim V_{\mu N}^2 + 2V_{eN}V_{\mu N}$, while the $\mu\mu\mu$ channel goes as $\sim V_{\mu N}^4$. Since $V_{eN} \gg V_{\mu N}$, the eee and $e\mu\mu$ cross sections are much larger, whereas the $\mu\mu\mu$ cross section is negligible. The $e\mu\mu$ cross section is higher than the eee cross section because of higher muon efficiency in the detector, whereas the small $e\mu\mu$ cross section is due to a very tiny value of $V_{\mu N}$.

One can also compute the ratios of events with different flavor compositions in which some of the common systematic uncertainties can get canceled. For example $e\mu\mu/eee \sim \epsilon$ where ϵ denotes the relative efficiency of detection of the muon over the electron, $e\mu\mu/\mu\mu\mu \sim \epsilon V_{eN}^4/V_{\mu N}^4$, $eee/e\mu\mu \sim \epsilon^2 V_{eN}^4/V_{\mu N}^4$, etc. Since for a fixed y_ν , which in turn implies specific values for phases, the variation of the light-heavy mixing angles is not very much with oscillation parameters, these ratios vary within a very

TABLE V. Final trilepton signal through VBF production of heavy neutrinos for the benchmark point $M_N = 100$ GeV at 14 TeV LHC for IH after all event selection cuts.

Hierarchy	Cross section (fb)				
	$\ell\ell\ell$	eee	$e\mu\mu$	$e\mu\mu$	$\mu\mu\mu$
IH	0.018068	7.09×10^{-3}	1.06×10^{-2}	4.06×10^{-4}	0.00

narrow range⁹ and hence can be used to test the model. Of course, for different phase choices a different y_ν and hence different predictions can be obtained. However, a smaller value in y_ν would result in a lower event rate and hence it would be difficult to test at the LHC.

2. Signal for VBF

In this section we present the results for the case where N is produced by VBF:

$$pp \rightarrow \ell^\pm N jj \rightarrow \ell^\pm(\ell^\mp W^\pm)jj \rightarrow \ell^\pm \ell^\mp \ell^\pm + \cancel{E}_T + jj(\text{forward jets}), \quad \text{where } \ell \equiv e, \mu.$$

In Table V we present the final trilepton signal cross sections through VBF production of heavy neutrinos at the 14 TeV LHC for the benchmark point $M_N = 100$ GeV, after including all cuts. Here we have only shown the case of inverted hierarchy and signal is found to be quite small. Although VBF backgrounds are small, the tiny production cross sections are insufficient for giving any signal with an integrated luminosity of 300 fb^{-1} . Some indications from VBF can appear only at the HL-LHC (3000 fb^{-1}). However, 5σ significance cannot be reached even for $M_N = 100$ GeV.

V. DISCOVERY POTENTIAL

After numerical computation of all necessary signals and backgrounds, results are better represented in terms of significance, defined as $S/\sqrt{S+B}$, where $S(B) = \mathcal{L}\sigma_{S(B)}$. Here, \mathcal{L} is the integrated luminosity available for the collider at a certain machine energy and $\sigma_{S(B)}$ is the final cross section after all event selections, for given parameters like heavy neutrino mass and corresponding allowed couplings. Figure 6 (left) demonstrates the expected significance coming from the s -channel production of the heavy Dirac neutrino of mass 100 GeV as a function of

⁹Note that, the allowed magnitude of mixings are as following: For a fixed value of $y_\nu (= 0.4)$, $\alpha (= 3\pi/4)$, $\delta (= 0)$, and $M_N (= 100)$ GeV, the magnitude of $|V_{eN}|$ and $|V_{\mu N}|$ vary in a very small range for 3σ variation of oscillation parameters; $|V_{eN}| = 0.471-0.484$, $|V_{\mu N}| = 1.236 \times 10^{-4}-1.272 \times 10^{-4}$. However, $|V_{\tau N}|$ varies little higher; $|V_{\tau N}| = 0.092-0.147$. Since we are considering modes involving only e and μ , the cross sections are likely to vary by a small amount for different set of oscillation parameters.

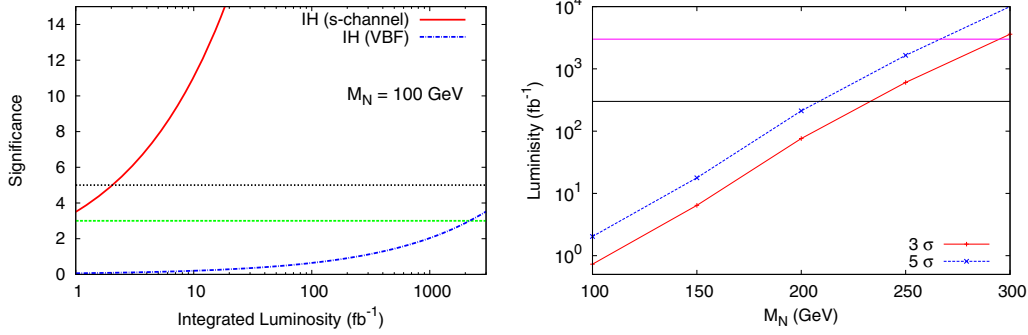


FIG. 6 (color online). (Left) The variation of significance $S/\sqrt{S+B}$ for the s -channel production signal for benchmark point $M_N = 100$ GeV with the integrated luminosity available for the low luminosity option at 14 TeV LHC. Black-dotted (green-dashed) line parallel to the x axis represents the 5σ (3σ) significance. (Right) The lines for the 3σ (red) and 5σ (blue) significance in terms of heavy neutrino mass and integrated luminosity. With 300 fb^{-1} luminosity at LHC14, the heavy neutrino mass in this model can be probed up to $\sim 210(230)$ GeV with $\sim 5\sigma$ (3σ) significance. For a very high luminosity of 3000 fb^{-1} this can reach up to $\sim 270(295)$ GeV.

integrated luminosity at 14 TeV LHC. In the figure, the black-dotted (green-dashed) line shows 5σ (3σ) significance. From the figure it is clear that for the case of the s -channel signal in the IH scenario, the 3σ (5σ) significance can be achieved within the integrated luminosity $\sim 0.73(2.03) \text{ fb}^{-1}$. In the case of the VBF channel 3σ significance can be achieved with 2175 fb^{-1} luminosity, while 5σ significance is not achievable within 3000 fb^{-1} luminosity which is planned for the HL-LHC.

Figure 6 (right) shows the lines for 3σ (red) and 5σ (blue) significance in terms of heavy neutrino mass and integrated luminosity. With 300 fb^{-1} luminosity at LHC14 the heavy neutrino mass in this model can be probed up to $\sim 210(230)$ GeV with $\sim 5\sigma$ (3σ) significance. For very high luminosity of 3000 fb^{-1} this can reach up to $\sim 270(295)$ GeV. For the VBF signal, since $M_N = 100$ GeV, it requires a very large integrated luminosity; higher values of M_N are not possible to explore.

VI. SUMMARY AND CONCLUSION

In this work we have considered a TeV scale minimal linear seesaw model which generates the correct order of light neutrino masses and has sizable light-heavy mixing to produce heavy neutrinos at colliders like LHC. One of the important features of this model is that it can be fully reconstructible from oscillation data excepting an overall factor y_ν characterizing the Dirac Yukawa matrix. However, this parameter gets constrained by LFV and vacuum metastability bounds. The neutral fermion mass spectrum of this model consists of one massless, two light, and two heavy neutrinos.

We have studied the collider phenomenology of the TeV scale linear seesaw at 14 TeV LHC. The heavy neutrinos in this model can be dominantly produced through the s -channel. In a leading order calculation, subsequent decay of these leads to the characteristic trilepton signal with missing p_T . We also consider the production of heavy neutrinos through the VBF process. The signal for this is

trileptons with additional two forward jets which can be tagged. Both these signals as well as the SM backgrounds have been estimated with realistic simulations using MadGraph and PYTHIA.

We found that s -channel trilepton production processes have the potential to be discovered at the LHC for the IH scenario. However, due to severe constraint on the light-heavy mixing coming from LFV in the case of the NH scenario, both the s -channel and VBF cannot be probed at the 14 TeV LHC with proposed luminosity. For a benchmark point with a heavy neutrino mass $M_N = 100$ GeV, 3σ significance can be achieved with an integrated luminosity of $\sim 0.73(2175) \text{ fb}^{-1}$ for the s -channel (VBF) signal in the IH scenario. 5σ significance can be reached for the s -channel signal with an integrated luminosity of $\sim 2 \text{ fb}^{-1}$; however, for the VBF signal the required luminosity is $\sim 6042 \text{ fb}^{-1}$, which is beyond the reach of the projected luminosity at the LHC. The discovery reach in the trilepton channel can be achieved up to the heavy neutrino mass of $\sim 210(230)$ GeV with $\sim 5\sigma$ (3σ) significance at the low luminosity (300 fb^{-1}) option of 14 TeV LHC. In the high luminosity (3000 fb^{-1}) search, the reach is up to $\sim 270(295)$ GeV. Whereas, the VBF channel can only reach up to $\sim 3\sigma$ for M_N at 100 GeV. Our analysis uses values for the elements, V_{IN} , of the light-heavy mixing matrix, which are consistent with the constraints coming from vacuum metastability and LFV. Any freedom of choosing larger values [e.g. $\sim \mathcal{O}(1)$] for these parameters can extend the discovery limit by a very significant amount. With the constraints used in this work, for V_{IN} , a detectable trilepton signal can only be obtained for the inverted hierarchical scenario with particular choices of phases leading to large y_ν . One can also compute the ratios of events with different flavor compositions which are proportional to the elements V_{IN} . They vary only within a narrow range with the 3σ variations of oscillation parameters and thus the model has very definite predictions for these ratios.

- [1] G. Aad *et al.* (ATLAS Collaboration), *Phys. Lett. B* **716**, 1 (2012).
- [2] S. Chatrchyan *et al.* (CMS Collaboration), *Phys. Lett. B* **716**, 30 (2012).
- [3] P. Ade *et al.* (Planck Collaboration), *Astron. Astrophys.* **571**, A16 (2014).
- [4] S. Weinberg, *Phys. Rev. Lett.* **43**, 1566 (1979).
- [5] P. Minkowski, *Phys. Lett.* **67B**, 421 (1977).
- [6] T. Yanagida, *Conf. Proc.* **C7902131**, 95 (1979).
- [7] M. Gell-Mann, P. Ramond, and R. Slansky, *Conf. Proc.* **C790927**, 315 (1979).
- [8] S. Glashow, *NATO Adv. Study Inst. Ser. B Phys.* **59**, 687 (1980).
- [9] R. N. Mohapatra and G. Senjanovic, *Phys. Rev. Lett.* **44**, 912 (1980).
- [10] A. Pilaftsis, *Z. Phys. C* **55**, 275 (1992).
- [11] J. Gluza, *arXiv:hep-ph/0201002*
- [12] A. Pilaftsis, *Phys. Rev. Lett.* **95**, 081602 (2005).
- [13] J. Kersten and A. Y. Smirnov, *Phys. Rev. D* **76**, 073005 (2007).
- [14] Z.-z. Xing, *Prog. Theor. Phys. Suppl.* **180**, 112 (2009).
- [15] X.-G. He, S. Oh, J. Tandean, and C.-C. Wen, *Phys. Rev. D* **80**, 073012 (2009).
- [16] A. Ibarra, E. Molinaro, and S. Petcov, *J. High Energy Phys.* **09** (2010) 108.
- [17] F. F. Deppisch and A. Pilaftsis, *Phys. Rev. D* **83**, 076007 (2011).
- [18] R. Adhikari and A. Raychaudhuri, *Phys. Rev. D* **84**, 033002 (2011).
- [19] I. Gogoladze, N. Okada, and Q. Shafi, *Phys. Lett. B* **672**, 235 (2009).
- [20] K. Babu, S. Nandi, and Z. Tavartkiladze, *Phys. Rev. D* **80**, 071702 (2009).
- [21] F. Bonnet, D. Hernandez, T. Ota, and W. Winter, *J. High Energy Phys.* **10** (2009) 076.
- [22] S. Kanemura and T. Ota, *Phys. Lett. B* **694**, 233 (2010).
- [23] Y. Liao, G.-Z. Ning, and L. Ren, *Phys. Rev. D* **82**, 113003 (2010).
- [24] I. Picek and B. Radovicic, *Phys. Lett. B* **687**, 338 (2010).
- [25] Y. Liao, *J. High Energy Phys.* **06** (2011) 098.
- [26] K. Kumericki, I. Picek, and B. Radovicic, *Phys. Rev. D* **86**, 013006 (2012).
- [27] K. L. McDonald, *J. High Energy Phys.* **07** (2013) 020.
- [28] A. Zee, *Phys. Lett.* **93B**, 389 (1980).
- [29] A. Zee, *Nucl. Phys.* **B264**, 99 (1986).
- [30] K. Babu, *Phys. Lett.* **B203**, 132 (1988).
- [31] L. M. Krauss, S. Nasri, and M. Trodden, *Phys. Rev. D* **67**, 085002 (2003).
- [32] E. Ma, *Phys. Rev. D* **73**, 077301 (2006).
- [33] M. Aoki, S. Kanemura, and O. Seto, *Phys. Rev. Lett.* **102**, 051805 (2009).
- [34] P. B. Dev and A. Pilaftsis, *Phys. Rev. D* **86**, 113001 (2012).
- [35] M. Gustafsson, J. M. No, and M. A. Rivera, *Phys. Rev. D* **90**, 013012 (2014).
- [36] R. Mohapatra and J. Valle, *Phys. Rev. D* **34**, 1642 (1986).
- [37] W.-Y. Keung and G. Senjanovic, *Phys. Rev. Lett.* **50**, 1427 (1983).
- [38] A. Datta, M. Guchait, and A. Pilaftsis, *Phys. Rev. D* **50**, 3195 (1994).
- [39] T. Han and B. Zhang, *Phys. Rev. Lett.* **97**, 171804 (2006).
- [40] S. Bray, J. S. Lee, and A. Pilaftsis, *Nucl. Phys.* **B786**, 95 (2007).
- [41] F. del Aguila, J. Aguilar-Saavedra, and R. Pittau, *J. High Energy Phys.* **10** (2007) 047.
- [42] F. del Aguila and J. Aguilar-Saavedra, *Nucl. Phys.* **B813**, 22 (2009).
- [43] A. Atre, T. Han, S. Pascoli, and B. Zhang, *J. High Energy Phys.* **05** (2009) 030.
- [44] S. Chatrchyan *et al.* (CMS Collaboration), *Phys. Lett. B* **717**, 109 (2012).
- [45] P. S. B. Dev, A. Pilaftsis, and U.-k. Yang, *Phys. Rev. Lett.* **112**, 081801 (2014).
- [46] A. Das, P. B. Dev, and N. Okada, *Phys. Lett. B* **735**, 364 (2014).
- [47] F. del Aguila and J. Aguilar-Saavedra, *Phys. Lett. B* **672**, 158 (2009).
- [48] C.-Y. Chen and P. B. Dev, *Phys. Rev. D* **85**, 093018 (2012).
- [49] A. Das and N. Okada, *Phys. Rev. D* **88**, 113001 (2013).
- [50] O. Eboli, J. Gonzalez-Fraile, and M. Gonzalez-Garcia, *J. High Energy Phys.* **12** (2011) 009.
- [51] S. Chatrchyan *et al.* (CMS Collaboration), *Phys. Rev. D* **90**, 032006 (2014).
- [52] M. Gavela, T. Hambye, D. Hernandez, and P. Hernandez, *J. High Energy Phys.* **09** (2009) 038.
- [53] S. Khan, S. Goswami, and S. Roy, *Phys. Rev. D* **89**, 073021 (2014).
- [54] M. Malinsky, T. Ohlsson, Z.-z. Xing, and H. Zhang, *Phys. Lett. B* **679**, 242 (2009).
- [55] D. L. Rainwater, *arXiv:hep-ph/9908378*.
- [56] A. Datta, P. Konar, and B. Mukhopadhyaya, *Phys. Rev. Lett.* **88**, 181802 (2002).
- [57] D. Choudhury, A. Datta, K. Huitu, P. Konar, S. Moretti, and B. Mukhopadhyaya, *Phys. Rev. D* **68**, 075007 (2003).
- [58] G.-C. Cho, K. Hagiwara, J. Kanzaki, T. Plehn, D. Rainwater, and T. Stelzer, *Phys. Rev. D* **73**, 054002 (2006).
- [59] P.-H. Gu and U. Sarkar, *Phys. Lett. B* **694**, 226 (2010).
- [60] H. Zhang and S. Zhou, *Phys. Lett. B* **685**, 297 (2010).
- [61] M. Hirsch, S. Morisi, and J. Valle, *Phys. Lett. B* **679**, 454 (2009).
- [62] F. Bazzocchi, *Phys. Rev. D* **83**, 093009 (2011).
- [63] W. Grimus and L. Lavoura, *J. High Energy Phys.* **11** (2000) 042.
- [64] S. Khan, *Nucl. Phys.* **B864**, 38 (2012).
- [65] J. de Blas, *Europhys. J. Web Conf.* **60**, 19008 (2013).
- [66] G. Bozzi, B. Jager, C. Oleari, and D. Zeppenfeld, *Phys. Rev. D* **75**, 073004 (2007).
- [67] B. Jager, C. Oleari, and D. Zeppenfeld, *Phys. Rev. D* **73**, 113006 (2006).
- [68] J. Pumplin, D. Stump, J. Huston, H. Lai, P. M. Nadolsky, P. Nadolsky, and W.-K. Tung, *J. High Energy Phys.* **07** (2002) 012.
- [69] J. Eckel, M. J. Ramsey-Musolf, W. Shepherd, and S. Su, *J. High Energy Phys.* **11** (2014) 117.
- [70] N. D. Christensen and C. Duhr, *Comput. Phys. Commun.* **180**, 1614 (2009).
- [71] J. Alwall, M. Herquet, F. Maltoni, O. Mattelaer, and T. Stelzer, *J. High Energy Phys.* **06** (2011) 128.
- [72] J. Alwall, A. Ballestrero, P. Bartalini, S. Belov, E. Boos *et al.*, *Comput. Phys. Commun.* **176**, 300 (2007).

- [73] T. Sjostrand, S. Mrenna, and P. Z. Skands, *J. High Energy Phys.* **05** (2006) 026.
- [74] G. Bambhaniya, J. Chakraborty, S. Goswami, and P. Konar, *Phys. Rev. D* **88**, 075006 (2013).
- [75] B. Mukhopadhyaya and S. Mukhopadhyay, *Phys. Rev. D* **82**, 031501 (2010).
- [76] G. Aad *et al.* (ATLAS Collaboration), [arXiv:0901.0512](https://arxiv.org/abs/0901.0512).
- [77] G. Bayatian *et al.* (CMS Collaboration), *J. Phys. D* **34**, 995 (2007).
- [78] E. Yazgan, J. Damgov, N. Akchurin, V. Genchev, D. Green, S. Kunori, M. Schmitt, W. Wu, and M. T. Zeyrek *et al.*, *Eur. Phys. J. C* **53**, 329 (2008).
- [79] G. Bambhaniya, J. Chakraborty, J. Gluza, M. Kordiaczynska, and R. Szafron, *J. High Energy Phys.* **05** (2014) 033.
- [80] M. L. Mangano, M. Moretti, F. Piccinini, R. Pittau, and A. D. Polosa, *J. High Energy Phys.* **07** (2003) 001.